AD-A141 998 COMPUTER SIMULATION STUDIES OF SPUTTERING AND MULTIMER 1/3
FORMATION FROM CLE..(U) NAVAL POSTGRADUATE SCHOOL
MONTEREY CA M G MATHIS DEC 83

UNCLASSIFIED F/G 20/12 NL

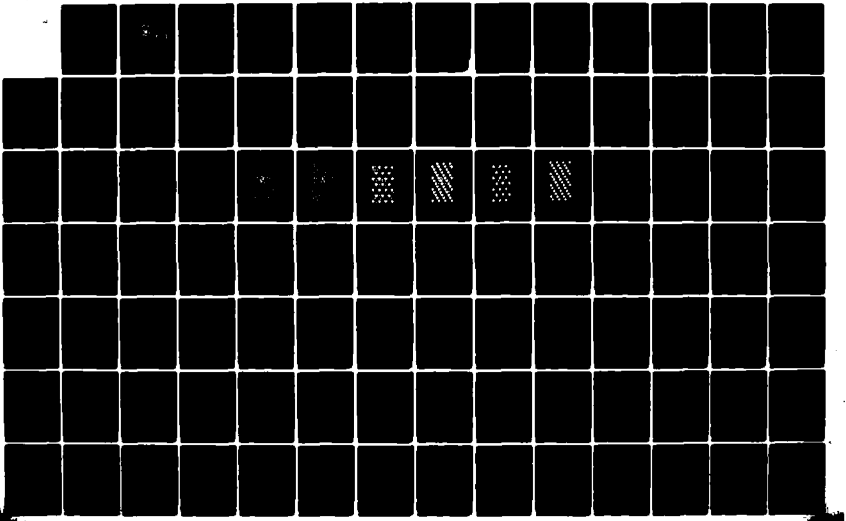

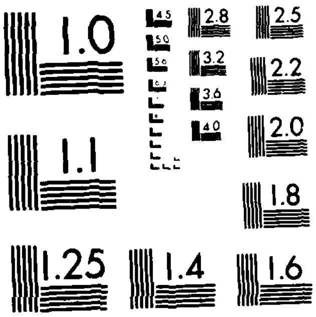

MICROCOPY RESOLUTION TEST CHART
NATIONAL BUREAU OF STANDARDS-1963 A

②

NAVAL POSTGRADUATE SCHOOL
Monterey, California

THESIS

COMPUTER SIMULATION STUDIES OF SPUTTERING AND MULTIMER FORMATION FROM CLEAN AND OXYGEN REACTED SURFACES OF TITANIUM, VANADIUM AND NIOBIUM

by

Michael G. Mathis

December 1983

Thesis Advisor: D.E. Harrison,Jr.

Approved for public release; distribution unlimited.

REPORT DOCUMENTATION PAGE

READ INSTRUCTIONS
BEFORE COMPLETING FORM

1. REPORT NUMBER

2. GOVT ACCESSION NO.

3. RECIPIENT'S CATALOG NUMBER

4. TITLE (and Subtitle)
Computer Simulation Studies of Sputtering and Multimer Formation from Clean and Oxygen Reacted Surfaces of Titanium, Vanadium and Niobium

5. TYPE OF REPORT & PERIOD COVERED
Master's Thesis;
December 1983

6. PERFORMING ORG. REPORT NUMBER

7. AUTHOR(s)
Michael G. Mathis

8. CONTRACT OR GRANT NUMBER(s)

9. PERFORMING ORGANIZATION NAME AND ADDRESS
Naval Postgraduate School
Monterey, California 93943

10. PROGRAM ELEMENT, PROJECT, TASK AREA & WORK UNIT NUMBERS

11. CONTROLLING OFFICE NAME AND ADDRESS
Naval Postgraduate School
Monterey, California 93943

12. REPORT DATE
December 1983

13. NUMBER OF PAGES
220

14. MONITORING AGENCY NAME & ADDRESS (if different from Controlling Office)

15. SECURITY CLASS. (of this report)
Unclassified

15a. DECLASSIFICATION/DOWNGRADING SCHEDULE

16. DISTRIBUTION STATEMENT (of this Report)

Approved for public release; distribution unlimited.

17. DISTRIBUTION STATEMENT (of the abstract entered in Block 20, if different from Report)

18. SUPPLEMENTARY NOTES

19. KEY WORDS (Continue on reverse side if necessary and identify by block number)

Sputtering; Computer Simulation; Ion Bombardment; Titanium; Vanadium; Niobium

20. ABSTRACT (Continue on reverse side if necessary and identify by block number)

The NPS computer simulation model was used to investigate the sputtering by 1.0 keV argon bombardment of clean and oxygen reacted monocrystalline titanium, vanadium and niobium. Variations in yield, energy and angular distributions and in particular, multimer formation, were studied as a function of oxygen density and location. Simulation results show a significant decline in substrate yield as the oxygen coverage

DD FORM 1 JAN 73 1473 EDITION OF 1 NOV 65 IS OBSOLETE
S/N 0102-LF-014-6601

(20. ABSTRACT Continued)

is increased, regardless of location. Further, there is a marked preference for multimer formation by lattice fragmentation, rather than by recombination, for all three metals. The percentages of multimers formed by fragmentation were found to increase with increasing oxygen density for all three metals. Previous results on face-centered cubic crystals concerning the yield per layer and the effects of channeling were confirmed for body-centered cubic and hexagonal closed-packed crystals. For comparison, simulation runs were repeated at ion energies of 0.5 and 2.0 keV for titanium with oxygen atoms located in three-fold sites with a C(2x2) density.

Approved for public release; distribution unlimited.

COMPUTER SIMULATION STUDIES OF SPUTTERING AND MULTIMER FORMATION FROM CLEAN AND OXYGEN REACTED SURFACES OF TITANIUM, VANADIUM AND NIOBIUM

by

Michael G. Mathis
Lieutenant Commander, United States Navy
B.S., Seattle University, 1970

Submitted in partial fulfillment of the
requirements for the degree of

MASTER OF SCIENCE IN PHYSICS

from the

NAVAL POSTGRADUATE SCHOOL
December 1983

Author: Michael G. Mathis

Approved by: D E Harrison
Thesis Advisor

Kathryn C. Dimiduk
Second Reader

G E Schacher
Chairman, Department of Physics

J N Dyer
Dean of Science and Engineering

ABSTRACT

The NPS computer simulation model was used to investigate the sputtering by 1.0 keV argon bombardment of clean and oxygen reacted monocrystalline titanium, vanadium and niobium. Variations in yield, energy and angular distributions and in particular, multimer formation, were studied as a function of oxygen density and location. Simulation results show a significant decline in substrate yield as the oxygen coverage is increased, regardless of location. Further, there is a marked preference for multimer formation by lattice fragmentation, rather than by recombination, for all three metals. The percentages of multimers formed by fragmentation were found to increase with increasing oxygen density for all three metals. Previous results on face-centered cubic crystals concerning the yield per layer and the effects of channeling were confirmed for body-centered cubic and hexagonal closed-packed crystals. For comparison, simulation runs were repeated at ion energies of 0.5 and 2.0 keV for a titanium with oxygen atoms located in three-fold sites with a C(2x2) density.

TABLE OF CONTENTS

LIST OF TABLES

I. BACKGROUND

A. OVERVIEW

Sputtering is the ejection of atoms from a target by bombardment with an energetic projectile ion. The incoming ion collides with atoms of the solid, thereby losing a portion of its energy and momentum. If the energy gained by a struck atom exceeds the binding energy holding it in position in the lattice a primary recoil atom will be created. This recoil atom will then collide with other atoms in the material, distributing its energy via a collision cascade. An atom at or near the surface will be sputtered if the energy associated with the normal component of its velocity exceeds the surface binding energy of the material.

The phenomenon of sputtering can be subdivided into two principle categories. Transmission sputtering is the ejection of atoms from the rear of a thin target following penetration by the ion. Sufficient energy must be transported through the target to allow atoms to overcome their binding energy and escape. Back-sputtering is the ejection of atoms from the front of the target and depends upon sufficient energy being deposited in the surface layers to allow ejection. This thesis will be concerned with the latter.

First discovered by Grove in 1853 and Faraday in 1854 as the deposition of metal atoms on the glass walls of a gas discharge tube, it was not until 1902 that Goldstein

[Ref. 1] presented evidence that the sputtering effect was caused by positive ions of the discharge impacting on the metal cathode. Since its principle effect was to contaminate experimental environments and to erode apparatus, the majority of early work centered around ways to control or eliminate what was considered to be an undesirable side effect. The necessity of increasing the life expectancies of high voltage vacuum tubes and the recognition of the possible applications of sputtering to thin film coatings gradually spurred interest in understanding the mechanics involved.

Early theoretical work was hampered by a paucity of experimental data. Reproducibility of results was also a major problem due to an incomplete understanding of the factors involved. Since the sputtering yield, Y (defined as the number of atoms ejected per incident ion), is critically sensitive to ambient pressure and surface contamination, as well as the flux density and angle of incidence of the beam, progress was dependent on the development and refinement of experimental techniques.

B. EARLY EXPERIMENTAL WORK

The effect of pressure on yield was first demonstrated by Penning and Moubis [Ref. 2]. They found that an increase in pressure increased the collision frequency between the ejected atoms and surrounding gases, resulting in the backscattering of the escaping atoms back onto the target surface. By keeping background pressure below 10^{-5} Torr, they were able to obtain reproducible results for ion energies in excess of 500 eV. Below 500 eV, the scouring action of the incident beam was insufficient to maintain a clean surface.

The elimination of adsorbed gases and surface oxide layers as a critical factor in determining the true yield was described by Arifov, et al., in 1963 [Ref. 3]. Yonts and Harrison also presented evidence [Ref. 4] that surface recontamination from background gases was a significant factor in quantitative sputtering yield measurements. Criteria were therefore developed for conducting 'clean' experiments.

In addition to pressure and surface cleanliness, the following conditions must be met in order to obtain reproducible yields:

(1) The ions must strike the target at a known angle of incidence.

(2) The energy spread of the beam must be small.

(3) All ions must be uniformly charged and mass separated.

(4) On monocrystalline surfaces the lattice orientation must be adequately described.

C. THEORETICAL DEVELOPMENT

Pioneering work on the concept of an individual sputtering event on an atomic scale was conducted by Stark [Ref. 5]. Applying the conservation laws governing elastic collisions, he proposed two theories to explain known experimental results. One, the "Hot-Spot" model, considered the sputtered atoms to be the result of evaporation of target material from an atomically small region due to ion induced local heating. In his "Collision" model, sputtering events were the result of a series of binary collisions initiated by a single ion. His models were modestly successful in predicting the energy distribution of the sputtered particles. Further refinements on the hot-spot model were attempted by von Hipple [Ref. 6], but only after the demonstration by Wehner [Ref. 7] of the effects of crystal structure on the yield did it become apparent that local heating alone could not explain the mechanisms involved in sputtering.

Wehner's observation of spot patterns (angular distribution patterns characteristic of the crystallographic properties of the substrate) obtained from sputtering of monocrystalline targets revived interest in the collision approach. In 1952 Keywell [Ref. 8] made a first attempt to formulate Stark's collision model in terms of the neutron transport model developed for nuclear work. Harrison then developed a theory based on probability concepts as expressed by the idea of collision cross-sections [Ref. 9]. However, due to the large number of unknown parameters, these theories were limited in their quantitative application.

As a further attempt to account for the angular distribution of ejecta, Silsbee [Ref. 10] proposed a focused collision model which allowed the transport of momentum in crystals along preferred directions. Available experimental results showed that the yield from monocrystals depended sensitively on the crystallographic orientation of the incident beam. This was explained in terms of the "holes" seen in crystal models when viewed from different planes and led to the development of various "Transparency" models. While focusing has been shown to be a contributing factor in cascade development within a crystal, it is inadequate to explain Wehner spots.

As an alternative to the focusing collision theory, Lehmann and Sigmund [Ref. 10] proposed a model based on the Boltzman transport equations that required the target surface to have an ordered structure, but not long straight rows of atoms intersecting the surface as in the focusing model. Emphasis is placed on the role of the surface structure and in particular, surface binding energies in monocrystalline sputtering. As an ion strikes the surface a collision cascade is created via binary interactions. An atom in the cascade will sputter if its momentum component normal to the surface has sufficient energy associated with it to overcome the surface potential barrier. Thompson [Ref. 12] expanded on this idea and proposed that the surface attraction for the escaping particle causes a refraction of its velocity vector away from the normal, resulting in a distorted angular distribution of ejected particles. Significant agreement with experimental results was found when projectile energies were much greater than the surface binding energy. This approach also provided correct information concerning both the angular and the energy distributions from polycrystalline targets. Thompson's [Ref. 12] work also incorporated the idea of focusons (momentum transport without mass displacement) into the theory. Robinson [Ref. 13] has taken a similar approach while accounting for channeling.

While these theories have provided mathematical tools to aid experimentalists, they have been rather unsuccessful in predicting yields at low projectile energies and from single crystal targets. Binary collision models have thus far been unable to account for the predominance of sputtered atoms from surface layers of the target.

In general, these theories have attempted to reduce what is essentially a many-body, multiple interaction process into forms that are analytically tractable. An assortment of refinements followed, attempting to explain observed behavior. Full scale attack on the multiple interaction problem had to await the arrival of high speed computers with sufficient storage to handle the hundreds or thousands of atoms in a cascade.

D. COMPUTER SIMULATION MODELS

Paralleling the theoretical and experimental progress in the understanding of sputtering was the effort to model the basic mechanisms through the use of computer simulation. In 1960 Gibson, Goland, Milgram and Vineyard [Ref. 14] developed a computer model to simulate the motion of atoms in a copper monocrystal following the impact of an ion on a single target atom. Atomic interactions were treated as binary collisions and the resulting cascades were developed by applying Newton's equations of motion. Ion penetration studies by Robinson and Oen [Ref. 15] using a similar program led to the discovery of channeling which was later experimentally verified.

In 1967, based on earlier preliminary studies, Harrison, Levy, Johnson and Effron [Ref. 16] used a computer to simulate the bombardment of a single copper crystal by argon. An important finding of this work was that the yield was almost entirely confined to the first three layers of the top surface. Subsequent refinements of the model [Refs. 17-20] included the addition of potential functions that allowed for attractive, as well as repulsive interactions, creating a dynamically stable crystal. Harrison's results showed that focusons were not a major contributor to the yield.

In 1978 Garrison, Winograd and Harrison [Ref. 21] published the results of a comprehensive study of atomic and molecular ejection from a copper crystal with adsorbed oxygen atoms. Their simulation of the system provided a detailed picture of the mechanisms of ejection and enabled them to determine whether molecules were ejected as a cluster from the surface or combined together in the space above the target. They were also able to determine the effects of adatom placement on molecule formation. Such results, when coupled with laboratory data, should lead to a better understanding of actual adatom locations on chemically reacted surfaces.

While much work remains to be done, particularly with respect to constructing interatomic potentials that accurately represent the physical processes involved, computer simulation permits the study of sputtering phenomena with a precision and flexibility that is impossible to duplicate in the laboratory. While it cannot replace actual experimentation, it can lead to a better understanding of experimental results and provide a testing ground for theoretical concepts.

II. OBJECTIVES

The primary objective of this thesis is to study the sputtering of titanium, vanadium and niobium monocrystals using the NPS computer simulation model, QRAD. In addition, changes in the yield and multimer formation are studied when the surface is reacted with oxygen.

Yu [Refs. 22,23] has conducted comprehensive research on clean and oxygen reacted titanium, niobium and vanadium in an attempt to link several earlier theories on the mechanisms responsible for ionic multimer formation. In the Lattice Fragmentation Model first proposed by Benninghoved [Ref. 24] molecular species (multimers) are emitted as complete fragments of the surface lattice during ion bombardment. In the Recombination Model [Refs. 18,25] only single atoms are ejected. Molecules are then formed through the attractive interaction between sputtered atoms from the same sputtering event, establishing their identities above the surface. The charge state of the molecules is not taken into account in these models.

Yu has reported experimental evidence [Ref. 23] that the emission mechanism for a sputtered molecular species may be a function of its charge state. He proposed that for low oxygen coverages (< one monolayer) the formation of positively charged titanium and niobium molecules (MO^+, MO_2^+) favored the recombination model, while the formation of negatively charged species (MO^-, MO_2^- and MO_3^-) followed the fragmentation process in all three metals. In the case of vanadium it appeared that the positive oxide species were not formed exclusively by recombination, but by a combination of the two methods.

Formation of positively charged ions was also found to be strongly dependent on oxygen coverage. When the number of oxygen atoms neighboring a metal atom increases, the frequency of sputtering an M^+ and O^0 adjacent to each other naturally increases. Consequently the percentage of MO^+ produced by fragmentation will increase.

The formation of negative molecular ions by lattice fragmentation was found to be insensitive to oxygen coverage due to the kinetics involved in the formation proces. A molecule formed by recombination is usually left with excess energy. If this energy approaches the electron affinity of the molecule the negative ion will attempt to stabilize itself by ejecting an electron. If the excess energy is much greater than this, one approaches the dissociation energy, and the molecule will be prevented from forming at all. Thus the formation of a stable negative ion is most favorable when the components are close neighbors on the surface and eject with small relative velocities as in the lattice fragmentation process. Increasing the oxygen coverage will only increase the probability of forming higher order oxide multimers.

Some discrepancies were noted in Yu's results for positive ions and were attributed to the recombination of metal atoms and oxygen from adjacent sites. Thus the results were indistinguishable from fragmentation at higher oxygen coverages. All nine of the negative molecular ion species investigated by Yu showed strong evidence of formation by fragmentation. Since the energy balance for recombined negatively charged ions indicates that they tend to neutralize by electron ejection, this leaves fragmentation as the principal source of molecule formation.

It should be noted that Yu's experimental procedure utilized an ion beam with a 45 degree angle of incidence to the polycrystalline surface. The mass spectrometer detector was also positioned at 45 degrees with respect to the surface, at right angles to the ion beam. Thus only a portion of the total yield was sampled. The data from the simulation studies that follow are based on the total yield from ion bombardment perpendicular to monocrystal surface. These data include neutral atoms, as well as ions, which are not collected by the mass spectrometer.

While determination of the charge state of molecules is not possible with the computer model, the various mechanisms of ejection can be studied in detail to determine whether recombination or fragmentation is the major contributor to the multimer yield. Ejection times of the various constituents are also available for correlation.

Some discrepancies were noted in Yu's results for positive ions and were attributed to the recombination of metal atoms and oxygen from adjacent sites. Thus the results were indistinguishable from fragmentation at higher oxygen coverages. All nine of the negative molecular ion species investigated by Yu showed strong evidence of formation by fragmentation. Since the energy balance for recombined negatively charged ions indicates that they tend to neutralize by electron ejection, this leaves fragmentation as the principal source of molecule formation.

It should be noted that Yu's experimental procedure utilized an ion beam with a 45 degree angle of incidence to the polycrystalline surface. The mass spectrometer detector was also positioned at 45 degrees with respect to the surface, at right angles to the ion beam. Thus only a portion of the total yield was sampled. The data from the simulation studies that follow are based on the total yield from ion bombardment perpendicular to monocrystal surface. These data include neutral atoms, as well as ions, which are not collected by the mass spectrometer.

While determination of the charge state of molecules is not possible with the computer model, the various mechanisms of ejection can be studied in detail to determine whether recombination or fragmentation is the major contributor to the multimer yield. Ejection times of the various constituents are also available for correlation.

Additionally the energy and angular distributions of ejected particles, which can be related to experimental SIMS data, will be studied. Since the actual sites of adatom adsorption have yet to be determined, the effects of oxygen coverage and location on yield and multimer formation will also be investigated.

III. MODEL DEVELOPMENT AND SIMULATION

A. COMPUTER MODEL

QRAD is a computer simulation program designed to track the motions of atoms in a microcrystal following ion bombardment. Trajectories are calculated by solving Hamilton's equations of motion using an average force method [Ref. 26]. It is a multiple interaction (MI) simulation following time step logic. Once the atomic masses, crystal characteristics, interatomic potentials and ion energy have been initialized, the program will develop and follow the resulting collision cascade until the energy of the atoms reaches a predetermined minimum. (See reference 24 for a comprehensive discussion of sputtering simulations.)

Initially an ion of given mass is projected toward a surface impact point with a specified energy and angle of incidence. As the cascade develops, the positions and velocities of the ion and lattice atoms are calculated at the end of each timestep. A timestep is determined by the velocity of the most energetic particle so that its displacement does not exceed 0.1 lattice unit (LU).[1] To expedite calculations, particles are classified as either moving or non-moving depending on their energies and the forces exerted on them

---

[1] The lattice unit is a convenient method of expressing distances when dealing with different crystal types. An LU is equal to the lattice constant 'a' divided by root two for hcp crystals and is equal to a/2 for bcc crystals.

by neighbor atoms. Atoms which rise above the surface with sufficient momentum are reclassified and assigned to a tentative list of ejected atoms. A trajectory is terminated when the energy of the most energetic atom is such that the probability that either it, or other atoms, will escape the surface is very small. Final positions and velocities are then recorded. Multiple trajectories, simulating bombardment by an ion beam, can be run by computing trajectories for a set of impact points chosen to sample a representative area of the crystal surface as a function of its symmetry. Data on the sputtered atoms is then analyzed by separate programs (AN83 and PLOTAN) to determine multimer formation, ejection angle information, etc.

As mentioned previously, multimers may result either from lattice fragmentation or by recombination above the surface. A multimer is considered formed when its constituent atoms are in a favorable spatial position with sufficiently low relative kinetic energy to permit bonding. The total energy of the resulting system must be negative and is an indication of the group's binding stability. Absolute multimer yield is strongly dependent on the pair-potential in use and the range specified for atomic interactions (R_C), however the mechanisms for cluster formation have been found to be insensitive to the choice of the potential function [Ref. 27].

Global results, suitable for comparison with experimental data, are obtained by averaging the yields from each run over a number of trajectories. While the number of trajectories is quite small (100-200, depending on symmetry considerations), the results have been found to vary by less than 10% when compared with other independently chosen sets of impact points [Ref. 28]. These global results are used in determining the number of atoms ejected per single ion (ASI yield), energy and angular distributions, as well as the spatial distribution of yield from the impact zone.

The remainder of this chapter is devoted to the development of the potential functions and other parameters used by QRAD. Adatom nomenclature and placement are discussed in Section D. Trajectory sets and crystal impact points are covered in Sections F and G. The chemical properties of titanium, vanadium and niobium are covered in the following sections.

B. TITANIUM

Titanium is a dimorphic transition metal ranking ninth in abundance of the elements making up the earth's crust. Below about 880°C it exists as a silvery gray hexagonal close-packed (hcp) crystalline material, while above 880°C it undergoes a phase transformation to a face-centered cubic (fcc) structure. The important physical and chemical properties of titanium are listed in Table 1.

Titanium reacts with oxygen to produce four well defined oxides, the monoxide TiO, the sesquioxide Ti_2O_3, the dioxide or titanic acid TiO_2 and the trioxide or pertitanic acid

TiO_3. Ti_2O_5, Ti_3O_5 and Ti_7O_{12} have also been reported, but may in fact be metastable combinations of the others [Ref. 29].

At least two distinct forms of oxygen coverage have been observed on Ti(001) surfaces.

1. Type 1 begins to form at low oxygen exposures of approximately 1.0 L[2] and is characterized by a low work function, very low electron stimulated desorption (ESD) and photon stimulated desorption (PSD) yields and a surface binding energy of 5.9 eV as determined by UV photoemission spectroscopy (UPS). Plateau, et al., had previously determined this value to be 5.7 ± 0.2 eV, also using UPS and ESCA [Ref. 38].
2. As the oxygen exposure is increased (~50 L) a second type of oxygen coverage is observed which has a higher work function, high PSD yield and additional binding energy in UPS. The effects of oxygen adsorption appear to saturate at about 70 L.

Hanson [Ref. 37] concluded that type 1 may correspond to oxygen adatoms lying below the surface plane or in high coordination sites, possibly the three-fold hollows, which would account for the low desorption rate.

Jonker [Ref. 39] has also observed two states of oxygen on the surface. The first is detected at low coverages and produces a well-ordered P(2x2) low energy diffraction

---

[2] 1.0 L (Langmuir) = 10^{-6} Torr-sec = 1.33×10^{-4} Pa-sec.

(LEED) pattern. At higher oxygen exposures a second state emerges which has a disordered appearance. This was explained by assuming that the sticking probability coefficient for oxygen is relatively constant up to a quarter monolayer coverage. At this point interference from previously adsorbed oxygens would cause it to change abruptly. The sticking coefficient would then remain constant for increasing exposures until the density of oxygen favored a change in the chemical bonding, resulting in the formation of a more stable metal oxide in the upper layers of the crystal.

Kawasaki, et al. [Ref. 40], have also reached the conclusion that oxygen is first adsorbed on the surface at low doses, but as the exposure is increased, it is slowly adsorbed into the surface. This corresponds to the formation of an oxide, and is accompanied by changes in the crystal structure. Their results also indicate that at the lower exposures oxygen occupies either a doubly bonded A-top or a two-fold bridge position. The A-top position is also supported by PSD experiments [Ref. 41] in which the oxygen atoms were observed to desorb normal to the surface, implying that the Ti-O bonds are perpendicular to the surface.

Experimental work by Singh, et al. [Ref. 43], confirms the formation of an oxide as saturation is reached, with oxygen atoms incorporated extensively into the metal lattice. (Here saturation is defined as the point where increasing the oxygen exposure no longer has an effect on the metal crystal, i.e., the sticking probability is equal to zero.) Since the sputtering yield comes mainly from the top three layers, modeling of an oxygen saturated surface would have to be accomplished by using a titanium oxide crystal rather than titanium with oxygen adatoms.

In view of the uncertainty of the actual locations of the oxygen atoms, a complete set of trajectories was run for the A-top, two-fold (bridge) and three-fold locations, in addition to those on the clean surface. Figures 1 through 8 present the various adatom locations on the metal crystal surface. (See Section D for a description of adatom notation.)

C. VANADIUM AND NIOBIUM

Vanadium and niobium are also transition metals, but unlike titanium, they have a body-centered cubic (bcc) structure. Their (110) planes, while not as close packed, do however have a hexagonal arrangement of atoms similar to the titanium (001) plane (Fig. 9). Their physical and chemical properties (Tables 2 and 3) are also quite similar to titanium, hence their sputtering mechanisms should bear some correlation to that of titanium.

Haas, Jackson and Hooker [Ref. 44] in their LEED experiments on niobium, tantalum and vanadium have found that oxygen adsorption is the same on all three metals and is a function of oxygen exposure. At low oxygen coverages the oxygen patterns clearly indicate a six-fold symmetry characteristic of the substrate lattice. But, as in the case of

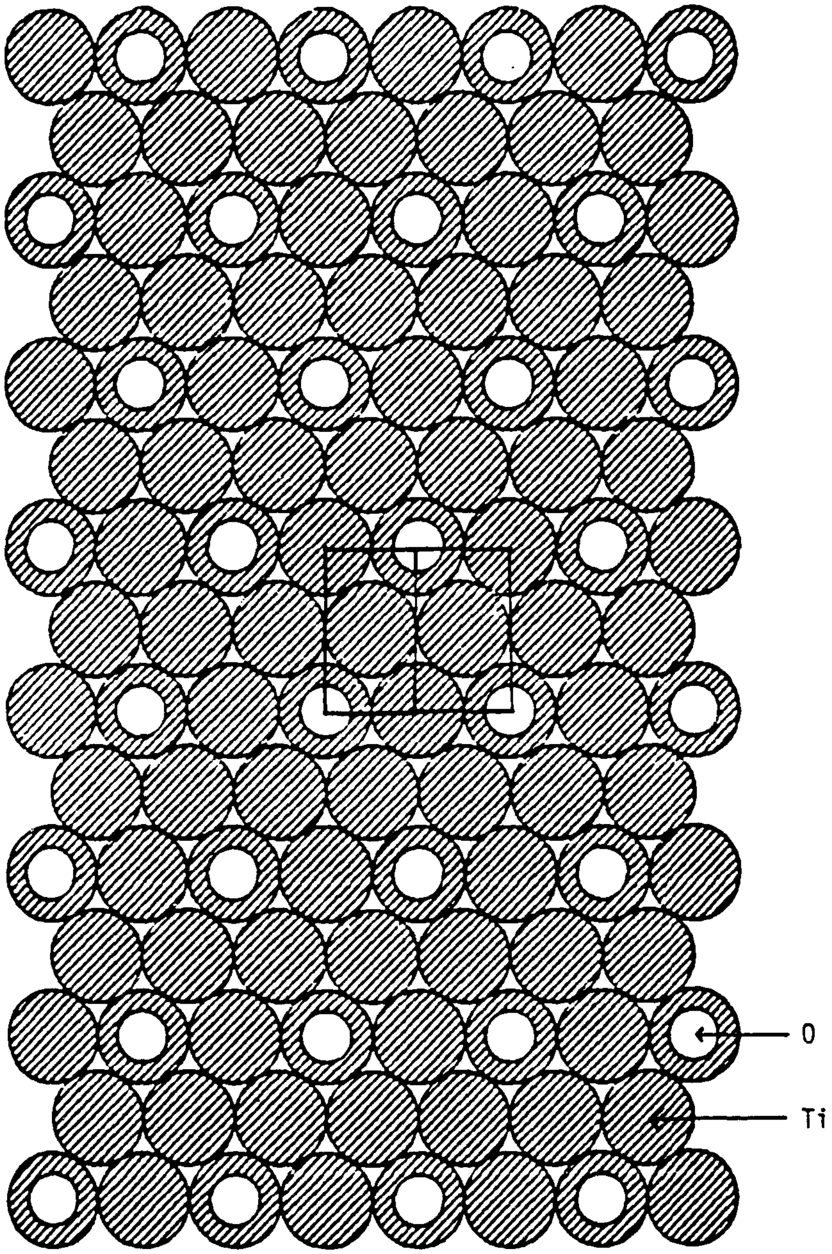

Fig. 1. Titanium (001) surface with adatoms in a P(2x2) A-top configuration. Rectangles in this and subsequent figures indicate impact zones used in the simulation runs.

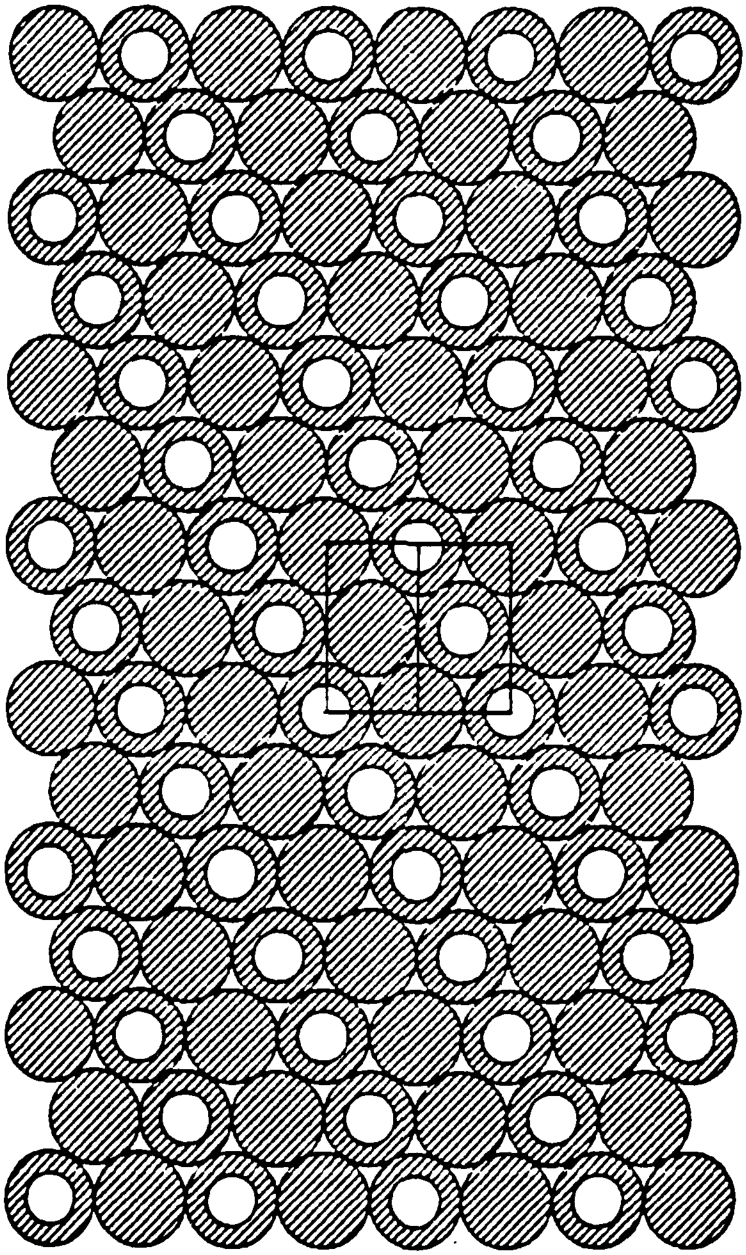

Fig. 2. Titanium with adatoms in a C(2x2) A-top configuration.

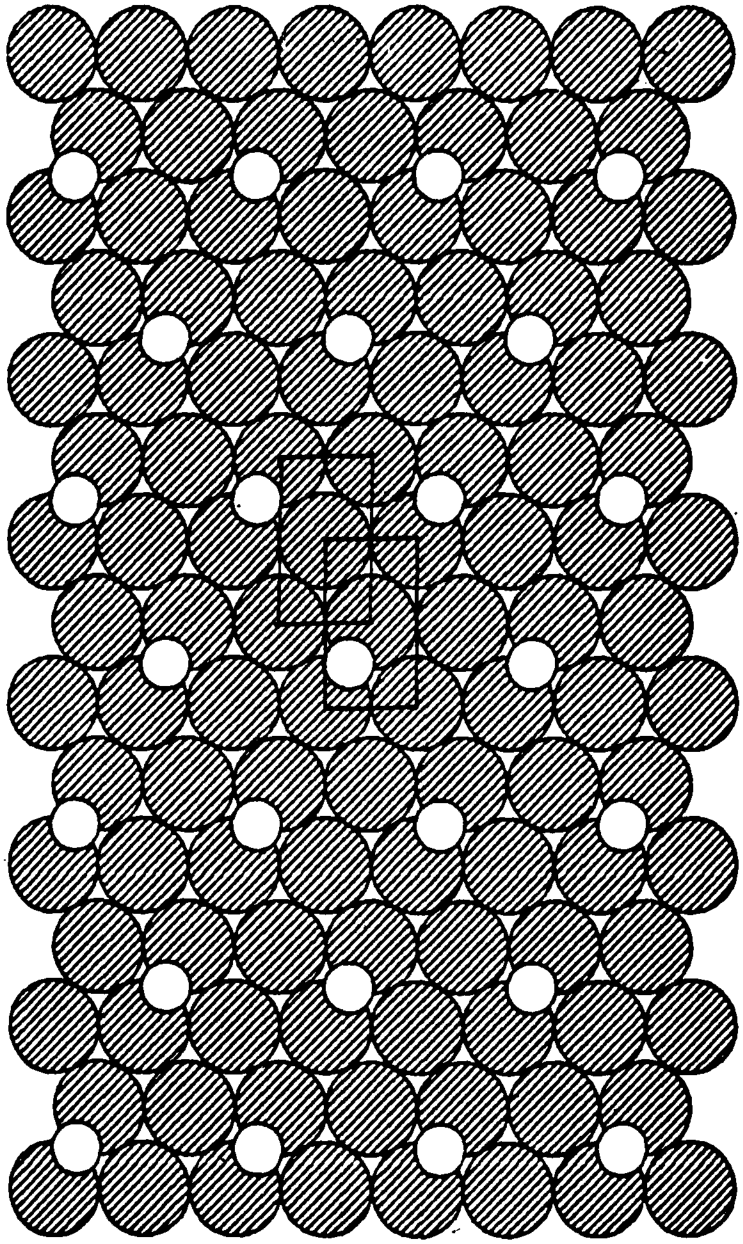

Fig. 3. Titanium with adatoms in P(2x2) bridge configuration.

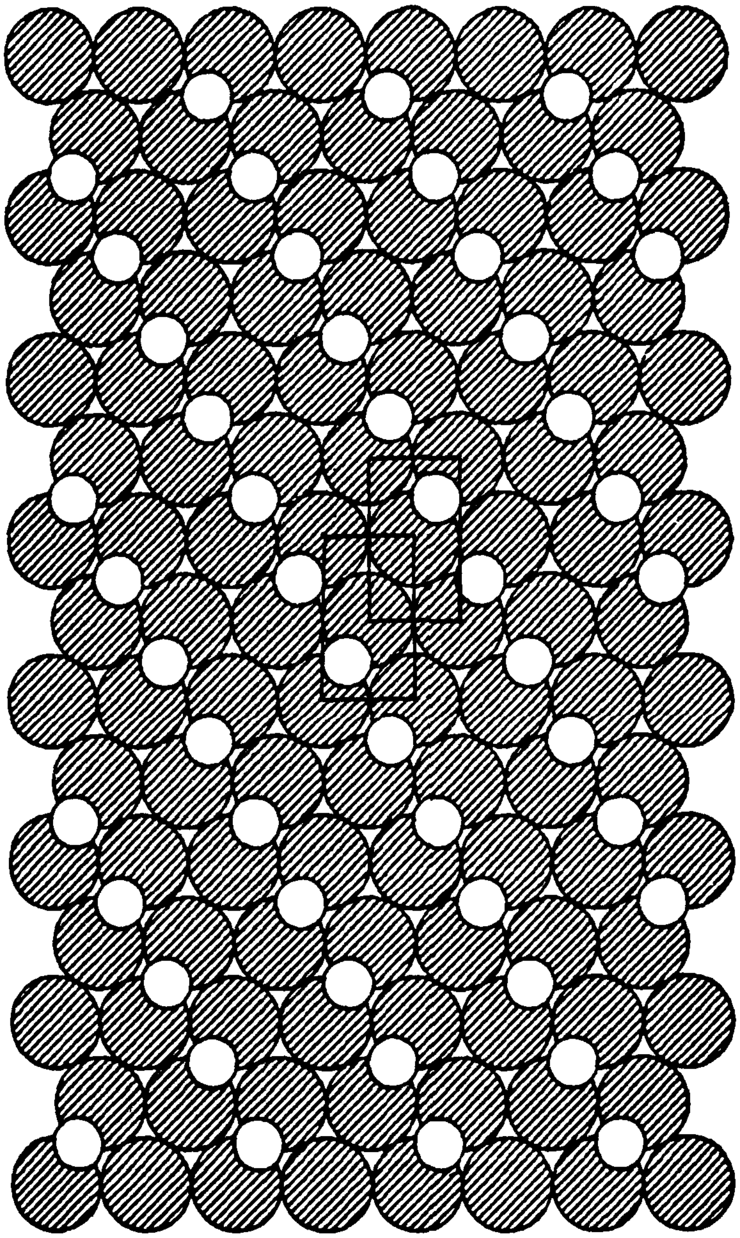

Fig. 4. Titanium with adatoms in C(2x2) bridge configuration.

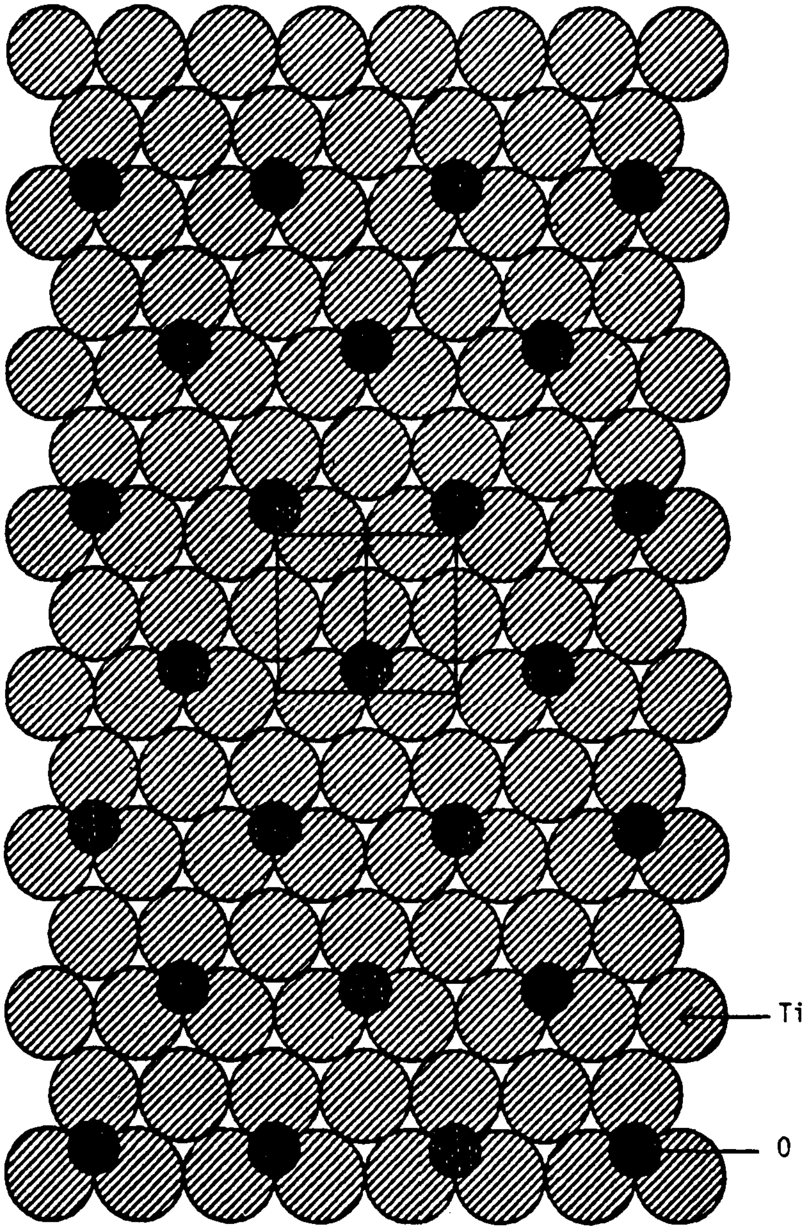

Fig. 5. Titanium with adatoms in P(2x2) three-fold "A" position.

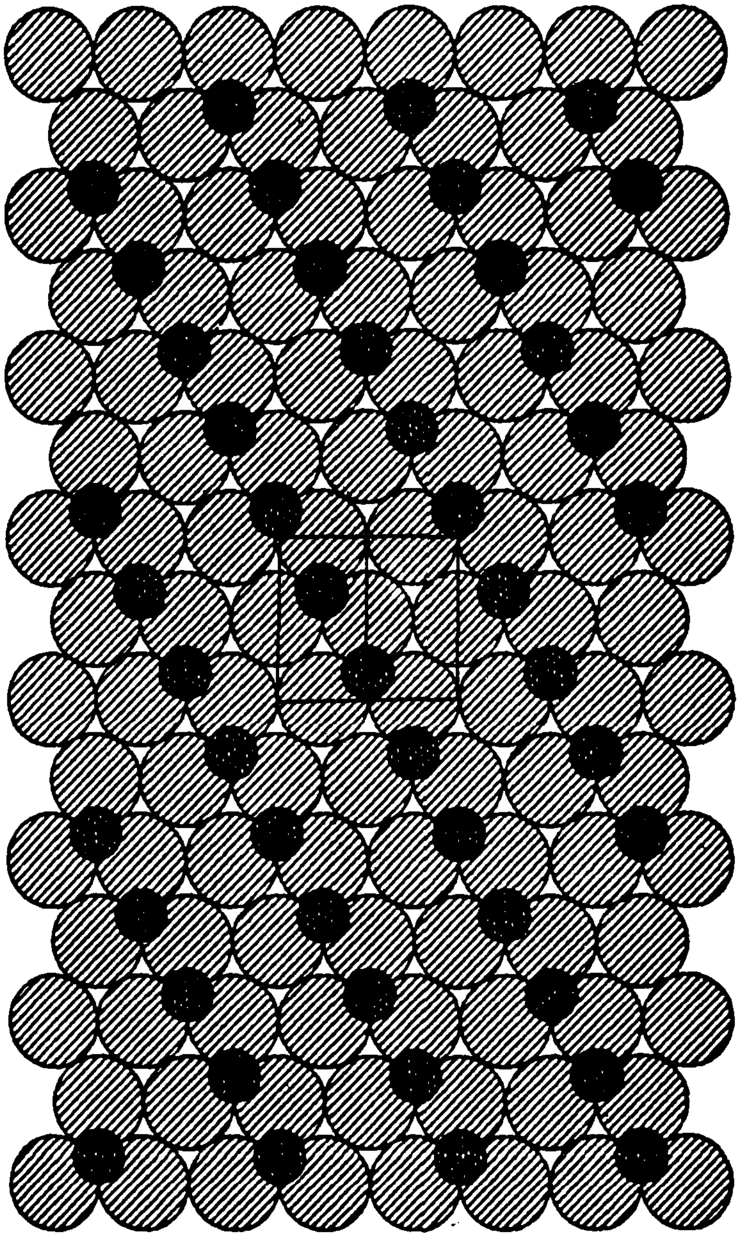

Fig. 6. Titanium with adatoms in C(2x2) three-fold "A" position.

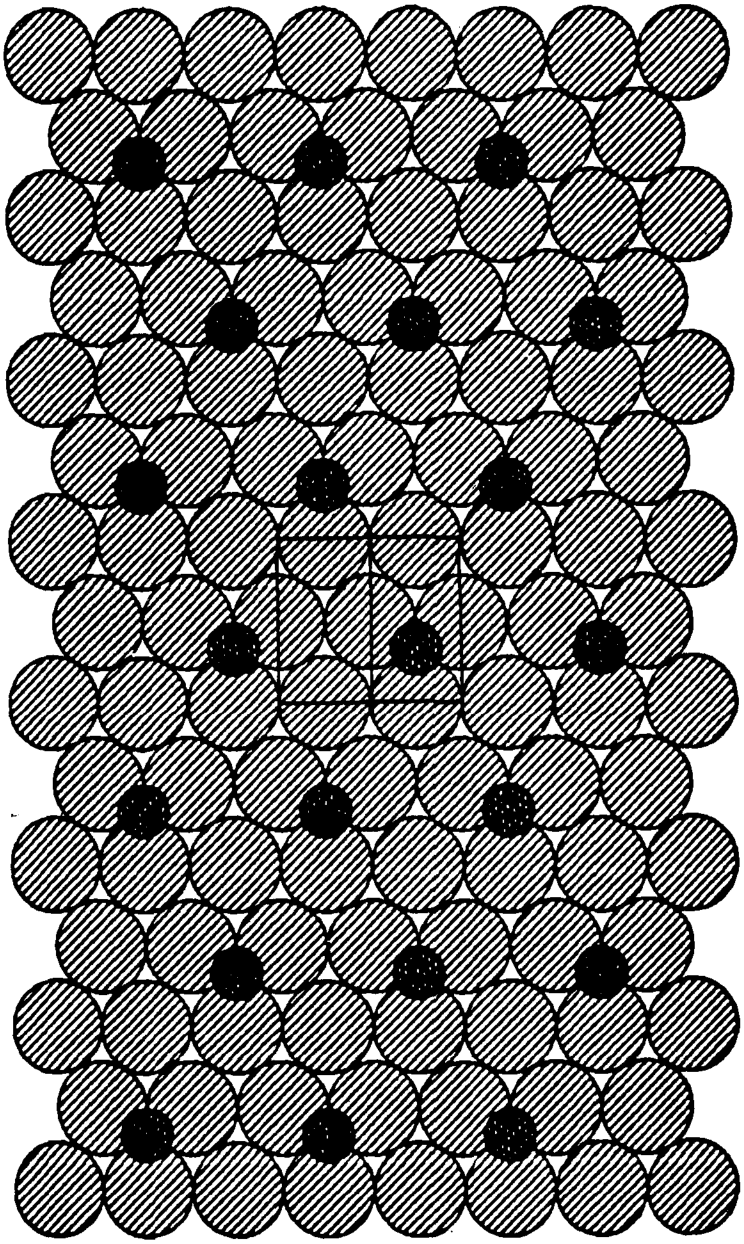

Fig. 7. Titanium with adatoms in P(2x2) three-fold "B" position.

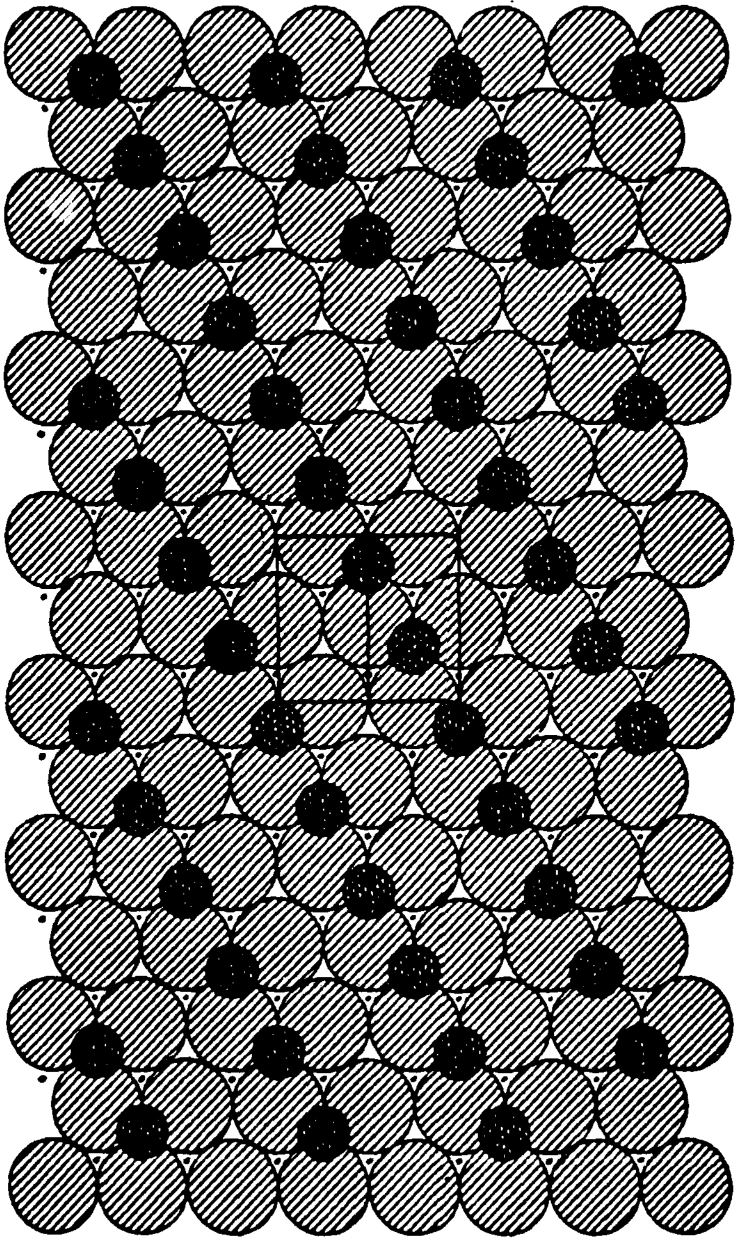

Fig. 8. Titanium with adatoms in C(2x2) three-fold "B" position. Small dots indicate centers of atoms in the second layer.

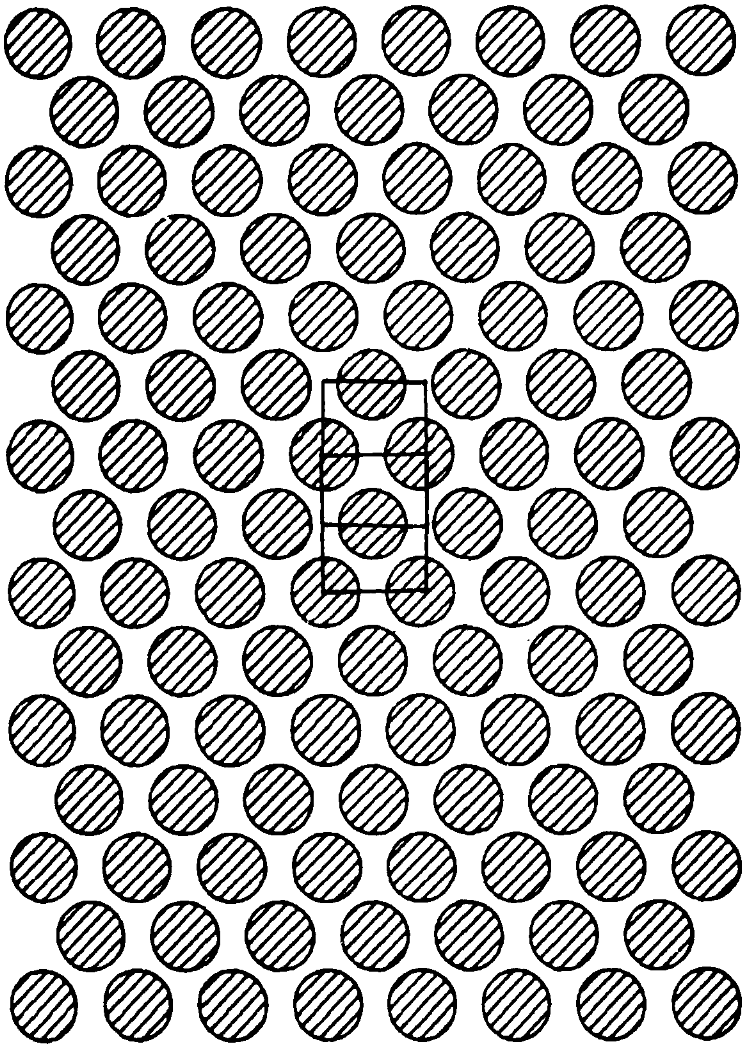

Fig. 9. Vanadium and Niobium clean (110) surface.

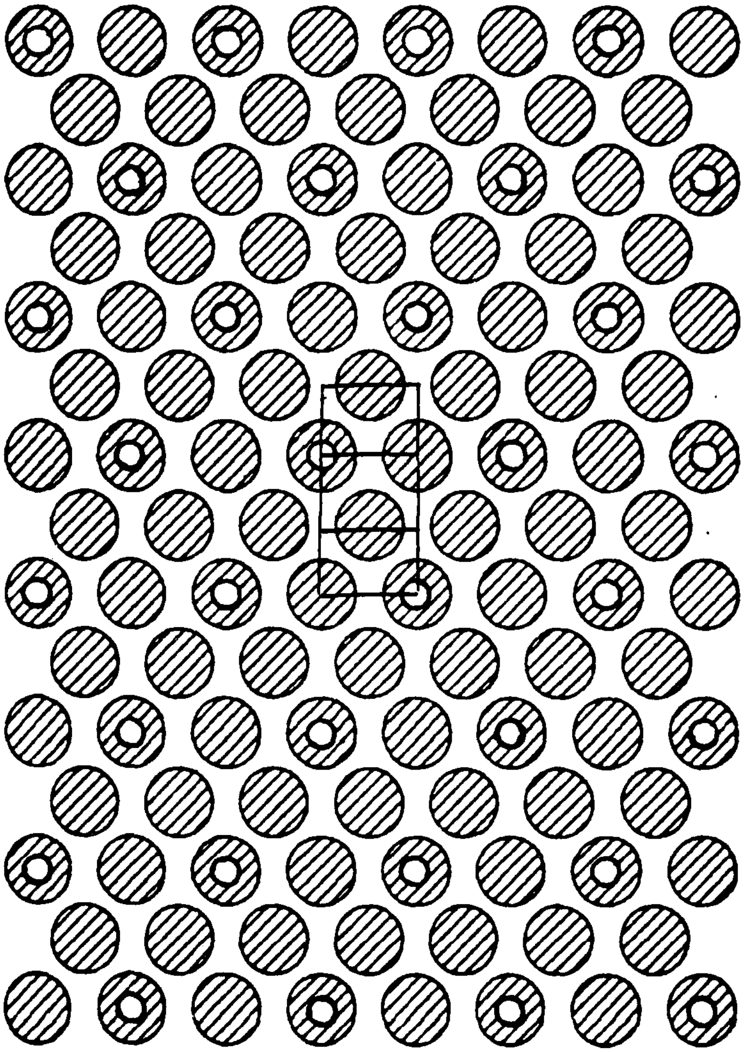

Fig. 10. Vanadium and niobium with adatoms in P(2x2) A-top position.

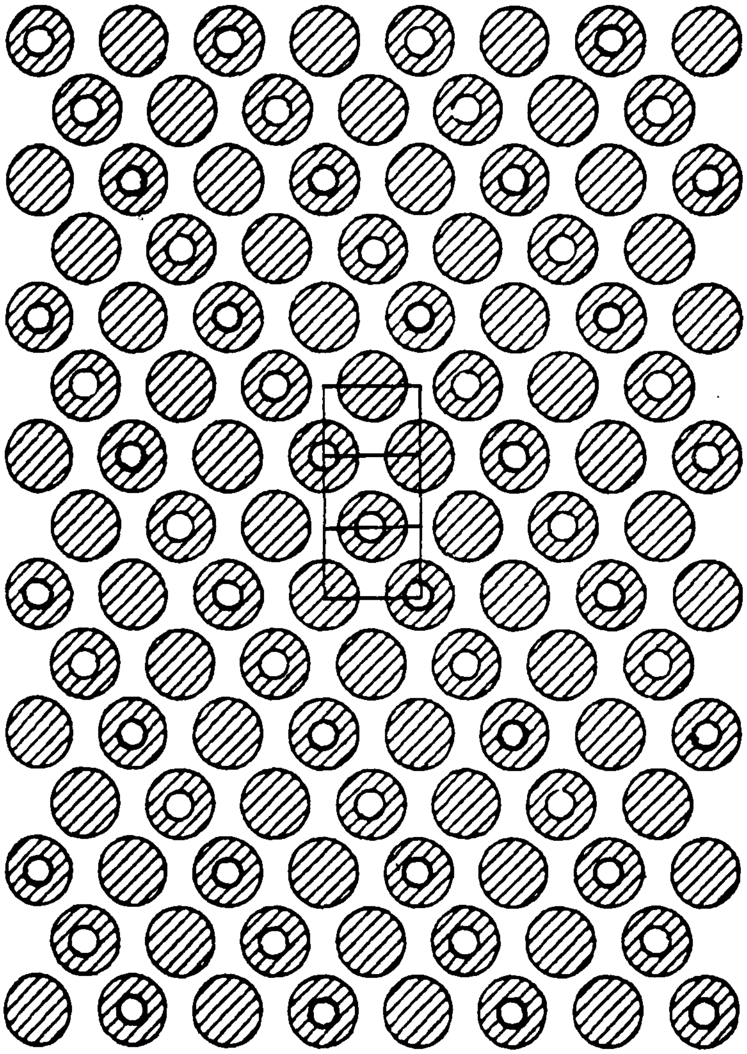

Fig. 11. Vanadium and niobium with adatoms in C(2x2) A-top position.

TABLE 2

Physical Properties of Vanadium and Parameters of Associated Potential Functions

Atomic Number	23	REF
Atomic Weight	50.9415	30
Melting Point	1890 ± 10° C	30
Boiling Point	3380° C	30
Valance	+2,3,4,5	30
Crystal Type	bcc	31
a	3.0399 ± 0.0003 Å	
Lattice Unit	1.51995 Å	Calc.
R_e	2.6326 Å	31
Cohesive Energy	5.31 eV	33
Gas Phase Bond Lengths (Å)		
V-V	2.6224	30
Ti-O	1.56 ± .04	34
O-O	1.20752	35
Ar-O	3.31	35
Gas Phase Bond Strengths (eV)		
V-V	2.511	30
V-O	6.462	30
O-O	5.1545	35
Ar-O	0.0049	30
Surface Binding Energy		
V-O	5.52 eV	Calculated, see text.

TABLE 3

Physical Properties of Niobium and Parameters of Associated Potential Functions

Atomic'Number	41	REF
Atomic Weight	92.9064	30
Melting Point	2468 ± 10° C	30
Boiling Point	4742° C	30
Valance	+2,3,4(?),5	30
Crystal Type	bcc	31
a	3.30656 ± 0.00002 Å	
Lattic Unit	1.65328 Å	Calc.
R_e	2.8636 Å	Calc.
Cohesive Energy	7.57 eV	33
Gas Phase Bond Lengths (Å)		
Nb-Nb	2.8584	30
Nb-O	1.69	34
O-O	1.20752	35
Ar-O	3.31	35
Gas Phase Bond Strengths (eV)		
Nb-Nb	2.83	34
Nb-O	7.805	35
O-O	5.1545	35
Ar-O	0.0049	30
Surface Binding Energy		
Nb-O	6.67 eV	Calculated, see text.

titanium, the reference index for the adatom mesh is uncertain. Two locations are possible on the vanadium and niobium (110) faces; the A-top and a rectangular four-fold site not present in titanium. In the four-fold position the adatoms could be placed either equidistant from the two pairs of neighbor atoms, or off to one side in a three-fold 'plus' position. Both would result in a high degree of bonding asymmetry. Since there is no corresponding site on the Ti (001) surface, the A-top position was chosen for comparison with titanium.

No information is available on the binding energies of chemisorbed oxygen on vanadium or niobium. Since all three metals possess similar chemical properties, surface binding energies were calculated by scaling the gas phase M-O binding energies to the known SBE of oxygen on titanium. This resulted in estimated SBE's of 5.52 and 6.67 eV respectively.

D. ADATOM COVERAGE

Computations were run at two specific coverages, P(2x2) and C(2x2), for each of the adatom locations. These coverages correspond roughly to a quarter and a half monolayer of oxygen respectively.

The designations for surface coverages were standardized in an article by E.A. Wood in 1964 [Ref. 45]. In this notation the three dimensional unit cell is reduced to a diperiodic structure referred to as a net in which the unit area is the unit mesh. The fourteen Bravais space lattices are thus reduced to five basic nets pictured below.

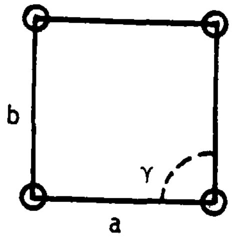

Square

$\gamma = 90^\circ$, $a = b$

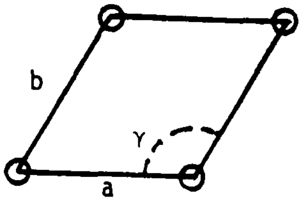

Hexagonal

$\gamma = 120^\circ$, $a = b$

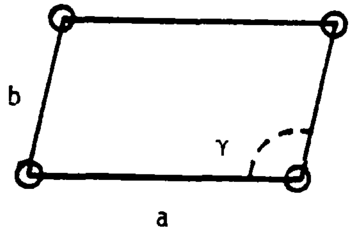

Oblique

$\gamma \neq 90^\circ$, $a \neq b$

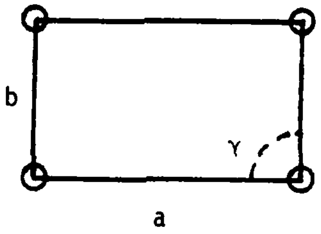

Rectangle

$\gamma = 90^\circ$, $a \neq b$

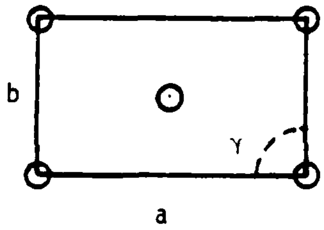

Centered Rectangle

$\gamma = 90^\circ$, $a \neq b$

The letter "P" is used to denote the primative mesh with equivalent points at the four corners, but none within the mesh itself. The letter "C" is used to identify a unit mesh that contains a central point. Numerals are used to indicate the repetition interval in the X and Z directions, referenced to the substrate unit mesh. Meshes rotated from the substrate principal directions are designated as above followed by the angle of rotation. NaCl(100) P(5xl)-45 would represent a primative mesh located on the (100) surface of NaCl, five units by one unit in area and oriented in the <110> direction. Meshes formed on other than substrate atoms are further identified by their origin point, two-fold bridge, etc. (For simplicity the four number designation normally used for hcp crystals has been abbreviated to three digits; i.e., (0001) = (001). The numbers themselves refer to the principal crystal directions (hkil) where i = h + k.)

In the case of the titanium (001) surface and the (110) surfaces of vanadium and niobium, the unit mesh is a 120 degree rhombus. The unit mesh for the A-top positions is centered above the substrate atoms and is displaced for the two and three-fold positions. Figures 1-11 depict the various coverages used, with the adatoms scaled according to their covalent radii. The two-fold locations are abbreviated "BR" (bridge) and the three-fold sites by "TF". Since there are two different three-fold sites on the hcp (001) surface, the additional identifier "TFA" or "TFB" is used to denote whether the adatom is fixed "above" an atom in the second layer of the substrate or centered over a channel.

E. POTENTIAL FUNCTIONS

1. General

A variety of potential function forms are available in this program to describe the interatomic forces. The merits of each have been hotly debated in the literature, but Harrison has found [Ref. 42] that the global results are not strongly dependent on the particular form in use. Individual parameters may be adjusted, if necessary, so that absolute values match experimental results, but the basic mechanisms involved remain unchanged. The four potential functions used are as follows:

a. Born-Mayer, which is strictly repulsive having the form

$$V(r) = A \exp(-br) \; ;$$

b. Moliere, which is an approximation to the Thomas-Fermi screening function, and is also repulsive

$$V(r) = (Z_1 Z_2 e^2/r)\{0.35 \exp(-0.3r/a) + 0.55 \exp(-1.2r/a) + 0.1 \exp(-6.0r/a)\} \; ,$$

where:

$$a = 0.8853 a_0/(Z_1^{1/2} + Z_2^{1/2})^{2/3} \quad \text{(Firsov radius)}$$

and

$$a_0 = h^2/4\pi^2 m e^2 = 0.5292 \text{ Å}. \quad \text{(Bohr radius)}$$

The parameter "a" may be varied to produce a "modified" Moliere function.

c. Morse, which is both repulsive and attractive having the form

$$V(r) = D_e \exp\{-2\alpha(r-r_e)\} - 2D_e \exp\{-\alpha(r-r_e)\} ,$$

where r_e is the equilibrium separation distance between atoms, D_e is the well depth and alpha is used to scale the distance in the potential function; and

d. Composite Moliere-Morse, which consists of the two potential functions joined together smoothly by a cubic spline.

The adjustable parameters can be related to the ion "size" and a collision "hardness", which in the case of the Born-Mayer potential correspond to the A and b constants. Thus one can tailor the frequency and hardness of collisions by appropriate selection of the parameters. At large separations the Moliere and Born-Mayer functions have similar shapes. In all of the potentials the repulsive wall dominates the dynamics of collisions, while the attractive well determines whether an atom will escape the surface and be sputtered. Reference [42] contains a detailed discussion on potential function selection.

2. Solid Phase Potentials

The Ti-Ti interactions within the crystal were modeled using a standard Moliere-Morse spline (a = 0.10529 Å) to allow for the anticipated hard collisions in the experiment. R_e was set at the lattice parameter value of 2.95 Å and D_e was adjusted to give the correct crystal cohesive energy of 4.855 eV. The Morse alpha was set at 1.33 $Å^{-1}$ so that the slope closely matched that of the Moliere. The two were then connected by a spline between $R_A = 0.68$ and $R_B = 0.72$ LU. R_C, the distance at which the potential is truncated, was set at 2.20 LU to allow only interactions between nearest and next-nearest neighbor atoms. Since the forces produced at greater separations are very weak, this selection of R_C allows calculation time to be minimized with negligible effect on the results.

The Nb-Nb and V-V potentials were similarly chosen with alpha equal to 1.34$Å^{-1}$ and 1.62 $Å^{-1}$ respectively. R_C was set at 2.2 LU in both cases. R_e was calculated as $\sqrt{3}/2$ times the lattice constant for the bcc structure.

The metal (M)-Ar potential functions used for the bombardment of the crystal by argon were chosen as standard Moliere potentials since no binding is to be expected. R_C was set at 1.7 LU for all runs.

Morse potentials were used for the M-O surface interactions. Lacking any specific data in the literature, adatoms in the A-top position were placed at the M-O gas phase equilibrium separation distance above the substrate, although this is known to be too high. The well depth and alpha were then adjusted so that the correct surface binding energy was obtained. For the titanium two-fold bridge, gas phase equilibrium separation was maintained between the oxygen and its two neighbor titaniums which necessitated placing the oxygens 0.322 LU above the surface plane. The well depth was again adjusted for the correct SBE. Adatoms in the three-fold sites were placed in the center of the titanium triangles on the surface plane, which required increasing r_e to 1.70 Å. R_C for all was set just outside the nearest neighbor distance to prevent O-O interference. Parameter values for the various adatom positions are summarized in Table 4.

The Ar-O potential used is a Born-Mayer with A = 14.67 keV and b = -4.593 $Å^{-1}$. This choice gave good results in previous work by Harrison, et al. [Ref. 21].

The O-O potential is another Morse with D_e = 5.1545 eV, r_e = 1.208 A and alpha = 2.691 $Å^{-1}$; values which were obtained from gas phase data and were also used by Harrison, et al.

TABLE 4

Solid Phase Potential Function Parameters

		D_e (eV)	r_e (Å)	Alpha ($Å^{-1}$)	R_C (Å)
Ti	ATOP	5.90	1.62	2.0	2.086
Ti	BRIDGE	2.95	1.62	2.0	2.086
Ti	TF	1.97	1.70	2.0	2.086
V	ATOP	5.52	1.56	2.0	2.584
Nb	ATOP	6.67	1.69	2.0	2.810

3. Gas Phase Potentials

The potentials used for interactions above the surface, as well as in determining multimer formation, are all of the pure Morse type. Parameters were selected from References 27, 32 and 33 and are summarized in Table 5. Appendix A (Figs. 15-22), contain plots of potential energy versus separation for most of the potential functions.

TABLE 5

Gas Phase Potential Function Parameters

	D_e (eV)	r_e (Å)	Alpha (Å^{-1})
Ti-Ti	1.466	2.896	1.330
Ti-O	6.870	1.620	2.000
Nb-Nb	2.830	2.858	1.340
Nb-O	7.805	1.690	2.000
V-V	2.511	2.622	1.620
V-O	6.462	1.560	2.000
O-O	5.155	1.208	2.691

F. MICROCRYSTAL

Microcrystals composed of 676 atoms were used for each computer run. The atoms are placed by a lattice generator into the proper hcp or bcc arrangement, resulting in a crystal 15 planes wide by 15 planes long by six planes deep (15x6x15). The first atom in the crystal is number two, one being the ion, and is located at (0,0,0,0). Atoms 2-114 comprise the top layer, 115-226 layer two, 227-339 layer three, 340-451 layer four, 452-564 layer five and 565-676 layer six. Atom numbers above 676 correspond to oxygen adatoms.

Crystal size selection is based on the problem of confinement which is the attempt to encompass the entire surface sensitive portion of the collision cascade within the target lattice. As the target size is increased the yield will asymptotically approach a maximum value. Past this point further increases in size will only affect computer run times. The 15x6x15 crystal size was selected after making a series of runs on clean titanium using a high yield impact point. Yield versus ion energy and crystal size is depicted in Figures 12 and 13. As can be seen containment is effectively achieved for ion energies up to 3.0 keV.

G. IMPACT AREA

The impact area for each simulation is a rectangular array of 104 uniformly distributed impact points adapted from previous work [Ref. 46]. Figure 14 is a graphical representation of the points and their coordinates. The actual length and height of the grid is automatically scaled by the program so that its dimensions match those of the interatomic spacing in the X and Z directions. Thus a grid positioned on planes RBX = 6.0 and RBZ = 6.0 would have its four corners located on the centers of the atoms at (6,6), (8,6), (6,8) and (8,8).

The impact points are slightly offset in the X and Z directions from true center to prevent repetitive sampling of symmetrically equivalent points.

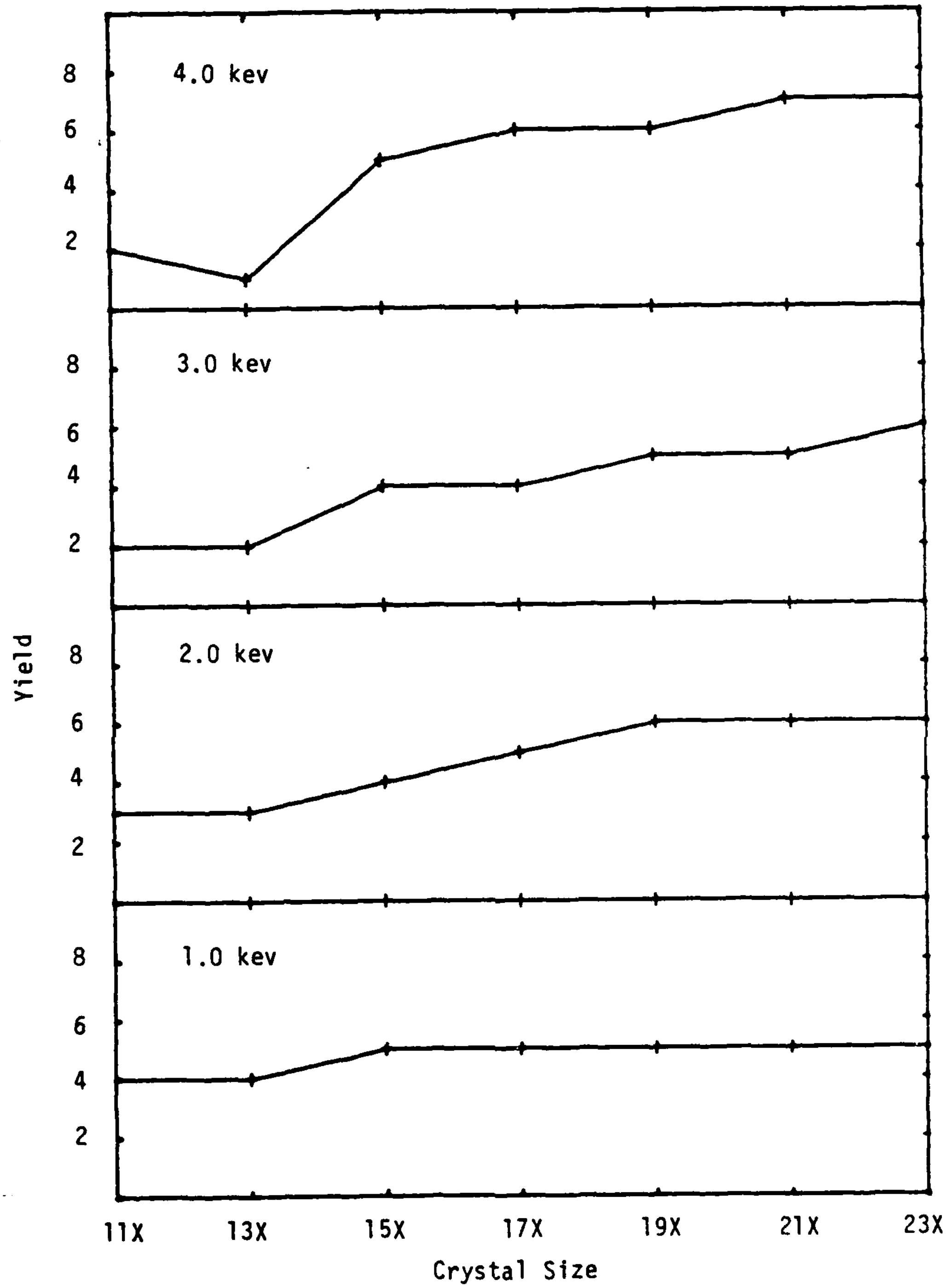

Fig. 12. Yield versus crystal size at various ion energies.

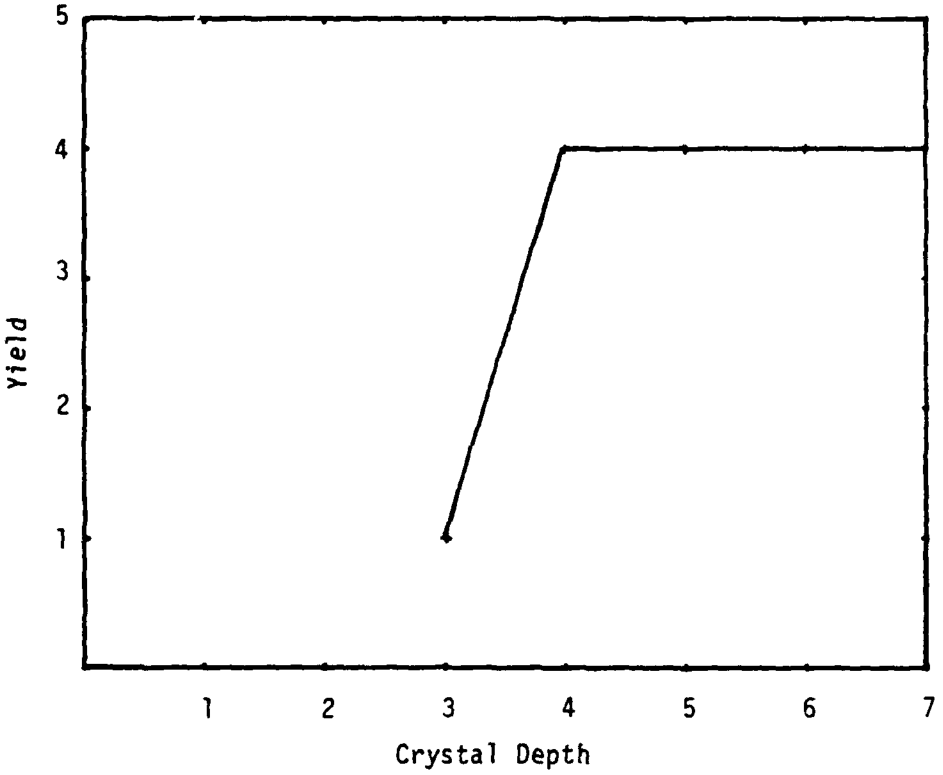

Fig. 13 Yield versus crystal depth.

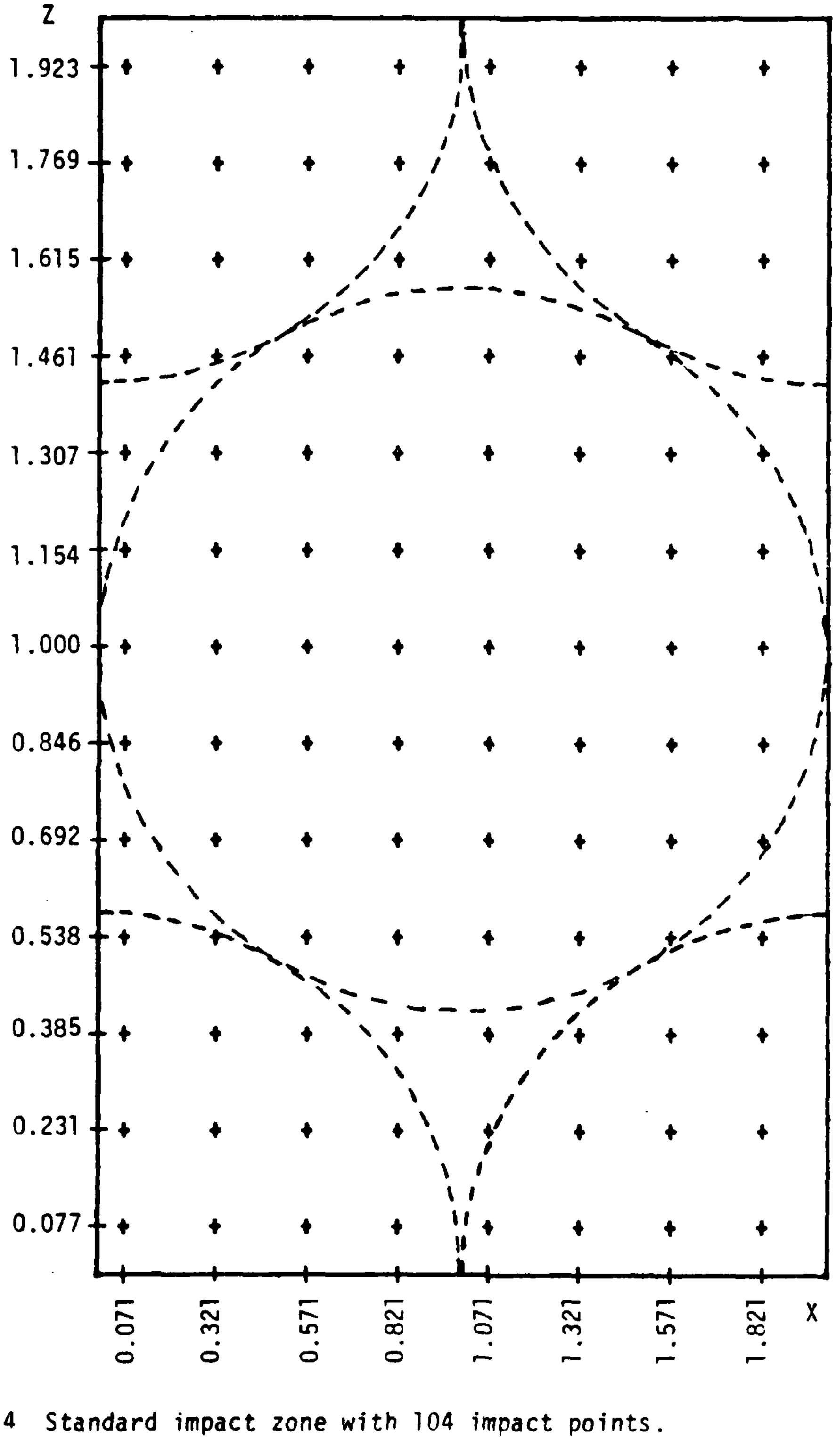

Fig. 14 Standard impact zone with 104 impact points.

Independent data sets can be generated by simply moving the origin of the grid. Selection of grid position is based on the surface symmetry resulting from adatom density and placement. Generally two sets of impact points are required to sample a completely representative area of the target surface. Surfaces which could be mapped into one grid were still run with two sets, shifted by one plane, so that all runs consisted of 208 impact points.

H. ION ENERGY

All simulations were conducted with an ion energy equal to 1.0 keV. This energy produced a reasonable sputtering yield and allowed the runs to be conducted on a moderate sized crystal. Additional runs were conducted on the titanium C(2x2)TFB surface at 0.5 and 2.0 keV, for comparison. This coverage produced the highest yield at 1.0 keV and therefore the differences in results as the ion energy is varied should be more pronounced.

I. PROGRAM MODIFICATIONS

1. QRAD

During the early stages of this investigation Harrison completed extensive modifications to QRAD resulting in improved energy conservation, timestep logic and output format. Considerable effort was expended proofing and debugging the new version. Additional code was also inserted to identify registered pairs, metal-oxygen pairs on the undamaged surface, for later use in tracking multimer origins.

2. AN83

This is the analyzer program used to determine various yield distributions and multimer data. Changes were made to make the program compatible with the new output format of QRAD.

3. PLOTAN

This program used the output from QRAD to generate graphic displays of the results. The program was modified to permit separate analyses of each atom type. It was also expanded to accommodate additional crystal types. The logic was modified to allow determination of the angular distributions from data generated by the non-symmetric sets of impact points in use. Plot scaling routines were also changed to handle the additional crystal types.

4. ADPLOT

ADPLOT is used to generate the pictorial representation of adatoms and steps on the crystal surface. Modifications were made to permit real time changes to the scaling of the plot size and to adjust adatom radii.

IV. RESULTS

A. GENERAL

Detailed information on each run has been assembled into appendices following the main body of this thesis. Included are graphical displays of the ejection time distributions, atoms ejected per single ion (ASI), energy distributions, spot patterns, and the ejection time differences between multimer components. Where applicable these have been broken down into separate substrate and adatom plots. Plot headings are generally self-explanatory, indicating ion energy, metal type and crystal face used for the particular run. For example "1.0 keV Ti(001)/Ar + Ox P(2x2)" indicates that the data pertains to bombardment of the 001 face of titanium by 1.0 keV argon ions. Ox P(2x2) denotes the presence of oxygen adatoms in a P(2x2) configuration. (M) or (OX) are used to identify whether the plot is for the substrate or for the adatoms in the particular configuration. The plots contain information based on a standard run of 208 impact points. On occasion data from a multiple set of 520 impact points is included to amplify significant characteristics. These are identified by the notation (IPX5). Combined plots of adatoms in the TFA and TFB positions are identified by TF(A+B). Discussions of the more noteworthy results of the experiments are contained in the remainder of this chapter.

B. YIELD AND ASI

The yields from the runs conducted on the clean crystal surfaces are summarized in Tables 6 and 7. All runs consisted of the standard set of 208 impact points with the exception of the expanded run on titanium which was composed of 520 impact points. This larger run was used to test the statistical validity of findings from the smaller sets. Of particular interest is the fact that the yield from the representative sample of 208 impact points for titanium is within 1.6% of the yield from a much larger run of 520 impact points, demonstrating the validity of this rather small set. The significantly higher yield of argon from the bombardment of niobium and vanadium is to be expected in view of the lower mass ratio, 0.429 (versus 0.834 and 0.784 for Ti and V respectively) and the increase in the collision cross-section which is a function of the atomic number.

The increased yield of V and Nb, as compared to Ti, may be explained by two characteristics:

1. The more open nature of the bcc (110) face. While the overall cohesive energy is greater, the surface layer has fewer nearest neighbors and therefore fewer bonds must be broken for an atom to escape the surface.
2. The fact that there are no channels present in the bcc (110) face for bombardment at normal angles of incidence. Hence all the ion energy is deposited in the top layers of the crystal from which the vast majority of sputtered atoms

TABLE 6

Yield and ASI (by Coverage)

COVERAGE	N_M (%)	N_O (%)	N_{AR}	Y_M	Y_O
CLEAN					
Ti (520)	945	-	10	1.8	-
Ti (208)	374	-	2	1.8	-
V	946	-	8	4.5	-
Nb	682	-	52	3.3	-
P(2x2)					
Ti ATOP	291 (79)	77 (21)	2	1.4	0.4
V ATOP	616 (83)	126 (17)	6	3.0	0.6
Nb ATOP	522 (82)	112 (18)	37	2.5	0.5
Ti BR	331 (80)	82 (20)	4	1.6	0.4
Ti TFA	324 (90)	38 (10)	2	1.6	0.2
Ti TFB	386 (87)	58 (13)	4	1.9	0.3
C(2x2)					
Ti ATOP	215 (62)	133 (38)	2	1.0	0.6
V ATOP	457 (70)	198 (30)	6	2.2	0.9
Nb ATOP	374 (70)	159 (30)	41	1.8	0.7
Ti Br	271 (65)	148 (35)	4	1.3	0.7
Ti TFA	290 (77)	86 (23)	4	1.4	0.4
Ti TFB(0.5)	233 (69)	105 (31)	7	1.1	0.5
Ti TFB(1.0)	368 (75)	124 (25)	6	1.8	0.6
Ti TFB(2.0)	419 (78)	116 (22)	2	2.1	0.6

NOTE: All ion energies are 1.0 keV unless otherwise noted, i.e., (0.5). The designations (208) and (520) refer to a single set of impact points and a combined group of 520 impact points respectively. N_{Ar} is the number of reflected argon ions. N_M and N_O are the actual counts of ejected atoms. Y_M and Y_O are the computed average yields, atoms/ion.

TABLE 7

Yield and ASI (by Substrate)

COVERAGE	N_M (%)	N_O (%)	N_{AR}	Y_M	Y_O
CLEAN					
Ti (520)	945	-	10	1.8	-
Ti (208)	374	-	2	1.8	-
P(2X2)					
Ti ATOP	291 (79)	77 (21)	2	1.4	0.4
Ti BR	331 (80)	82 (20)	4	1.6	0.4
Ti TF <A+B>	355 (88)	48 (12)	3	1.8	0.3
C(2X2)					
Ti ATOP	215 (62)	133 (38)	2	1.0	0.6
Ti BR	271 (65)	148 (35)	4	1.3	0.7
Ti TF <A+B>	329 (76)	105 (24)	5	1.6	0.5
V CLEAN	946	-	8	4.5	-
V P(2X2) ATOP	616 (83)	126 (17)	6	3.0	0.6
V C(2X2) ATOP	457 (70)	198 (30)	6	2.2	0.9
Nb CLEAN	682	-	52	3.3	-
Nb P(2X2) ATOP	522 (82)	112 (18)	37	2.5	0.5
Nb C(2X2) ATOP	374 (70)	159 (30)	41	1.8	0.7

NOTE: The quantity <A+B> for the three-fold sites refers to the combined average of the A and B positions of the adatoms.

originate. The yield per layer data for adatoms in the A-top position is given in Table 8. Yield ratios for the other adatoms locations were found to be essentially identical.

TABLE 8

Sputtering Yield by Layer

COVERAGE	LAYER 1	LAYER 2	LAYER 3	LAYER 4
CLEAN				
Ti (001)	372	0	0	0
V (110)	900	44	8	0
NB (110)	694	26	8	0
P(2x2)				
Ti (001)	285	5	1	0
V (110)	566	41	7	2
Nb (110)	490	24	8	0
C(2x2)				
Ti (001)	213	2	0	0
V (110)	429	24	8	1
Nb (110)	347	24	3	0

With respect to the various adatom coverages the metal yields for the A-top positions are fairly consistent at about 80% for the P(2x2) and 70% for the C(2x2). As the oxygen coverage is increased there are fewer direct impacts on the substrate atoms which begin to look more like a second layer to the incoming ions with a corresponding decrease in yield. This decrease is summarized below where Delta Y_M represents the drop in substrate yield as the coverage is increased from a quarter to a half monolayer.

TABLE 9

Change in Metal Yield as a Function of Adatom Coverage

COVERAGE	DELTA Y_M (%)
Ti P → C ATOP	-17
V P → C ATOP	-13
Nb P → C ATOP	-12
Ti P → C BR	-15
Ti P → C TFA	-13
Ti P → C TFB	-12

As the adatom position is shifted from A-top to bridge to three-fold, the total yield (M + O) fluctuates with the maximum coming from the bridge positions. The metal yields are about the same percentage for both the A-top and bridge, but increase in the three-fold positions. The corresponding decrease in the fraction of oxygens ejected is reasonable in light of the added stability of the triply bonded positions.

The increased metal yield in the bridge, and particularly in the TFB positions, can again be explained in terms of channel blockage. The bridge locations partially obstruct the channel in the hcp (001) plane, while the TFB position above the channel closes it to incoming ions.

The Atoms per Single Ion graphs for selected cases are contained in Appendix B. The distributions for the substrate atoms are in general broader than for the adatoms. As the oxygen density is increased, there is little change in the substrate ASI distribution, but the maximum in the oxygen distributions shifts toward an ASI of two. This is to be expected due to the larger number of oxygen atoms on the surface. The ASI distributions of the substrate broaden somewhat as the adatom positions are changed from the bridge to the three-fold, consistent with the increasing metal yield.

C. EJECTED PARTICLE ENERGY VERSUS COVERAGE

It is interesting to note that as the adatom coverage in the A-top position is increased, the average energy of the ejected substrate atoms also increases. As noted above, this corresponds to a decrease in metal atom yield as well. Lower energy particles are apparently retained in the crystal, thus raising the average ejection energy. The most probable energy of the ejected metal atoms also is significantly higher when there are adatoms in the A-top position and increases with oxygen density as well (Table 10). This trend does not extend to the bridge and three-fold positions in titanium, but the most probable energies of the substrate atoms are more in line with those ejected from clean metal surfaces.

There is a much closer correlation between the metal and oxygen average energies in the bridge and three-fold positions. The multiple bonding involved appears to equalize the energies of the ejected particles to some degree.

As the ion energy is increased there is a corresponding rise in the average ejection energy of the metal atoms, as

TABLE 10

Average and Most Probable Ejection Energies

COVERAGE	$\langle E_M \rangle$ (eV)	$[E_M]$ MP (eV)	$\langle E_O \rangle$ (eV)
CLEAN			
Ti	10.3	3.5	-
V	8.9	4.0	-
Nb	12.3	4.5	-
P(2x2) (ATOP)			
Ti	10.7	7.0	11.9
V	10.7	7.5	11.4
Nb	13.8	9.0	11.9
C(2x2) (ATOP)			
Ti	11.3	7.5	27.5
V	12.2	8.0	10.7
Nb	15.9	9.0	13.8
TITANIUM			
P(2x2) BR	10.057	4.0	10.062
C(2x2) BR	9.815	5.0	9.461
P(2x2) TFA	9.852	5.0	10.997
C(2x2) TFA	10.193	4.5	10.190
P(2x2) TFB	10.230	3.0	8.055
C(2x2) TFB	9.743	3.0	9.384

TABLE 11

Average Ejection Energy Versus Ion Energy

ION ENERGY (keV)	Ti (eV)	Ox (eV)
0.5	8.059	22.514
1.0	9.743	9.348
2.0	13.146	20.316

one would expect. The changes in the oxygen energy match the variation in yield (105, 124, 116). While the ratio of energies between Ti and O is essentially the same for 0.5 and 2.0 keV, the oxygen energy is about double that for the 1.0 keV ions at all coverages except the A-top C(2x2) where there is also an unexpected rise.

The energy distribution curves are contained in Appendix C. The curves for the ejected oxygen atoms are typically flat for the bridge and the three-fold positions, showing no dominant ejection energy. However there is a pronounced Rayleigh-type shape to the curves for oxygen in the A-top position and they bear more of a resemblance to those of the substrate. This agrees with what was found earlier where the multiple bonds tend to cause a more even distribution of ejected particle energy.

D. EJECTION TIME DISTRIBUTIONS

Appendix D contains bar charts of the ejection time distributions for representative runs. The distributions are similar for titanium and vanadium, but the average ejection time for niobium increases about 30 fsec to about 110 fsec

(1 femptosecond = 10^{-15} sec). The distribution is also broader. There is essentially no change in any of the distributions as oxygen is added to the surface, or increased from P(2x2) to C(2x2). Thus the ejection time appears to be mainly a function of the substrate mass and independent of adatom coverage and lattice type.

The oxygen ejection time distributions show the same characteristics as the substrate atoms. The only significant difference was that oxygen ejection started approximately 10 fsec later for titanium than for vanadium or niobium. Again the distribution was broader for niobium, reflecting the influence of the substrate.

E. YIELD VERSUS ENERGY

Since the C(2x2) TFB coverage produced the highest titanium sputtering yield, it was chosen to investigate the effects of changing ion energy. This coverage was therefore run at energies of 0.5 and 2.0 keV in addition to the 1.0 keV trial. The yield results and layer data are contained in Tables 12 and 13.

TABLE 12

Titanium Atoms Ejected and Yield as a Function of Ion Energy

ENERGY (keV)	N_M	Y_M	N_O	Y_O	N_{Ar}
0.5	233	1.1	105	0.5	0
1.0	368	1.8	124	0.6	0
2.0	419	2.0	116	0.6	0

TABLE 13

Titanium Atom Yield per Layer
as a Function of Ion Energy

ENERGY (keV)	LAYER 1	LAYER 2	LAYER 3	LAYER 4
0.5	232	1	0	0
1.0	363	4	1	0
2.0	398	16	1	4

As can be seen the higher the energy, the higher the yield, but the relationship is definitely non-linear. With increasing energy the average ion penetrates further into the crystal. As a consequence a smaller percentage of its energy is deposited in the top layers. More energy is carried deep into the crystal where it is dissipated through collision cascades producing only lattice displacements and vibrations.

The decrease in oxygen yield for the 2.0 keV ions is also probably caused by the deeper deposition of energy. The energy distribution plot for the ejected oxygens (Figs. 54-56) clearly shows a decrease in the energy as compared to the 1.0 keV case. Hence fewer adatoms are receiving enough energy to surmount the surface binding well and escape.

F. MULTIMER YIELD

Tables 14 and 15 present the various multimer yields in terms of total numbers and as percentages. Tables 16 and 17 contain a breakdown by species arranged by substrate type

TABLE 14

Multimer Yield as a Function of Coverage

COVERAGE	1-MER	2-MER	3-MER	4-MER	5-MER	TOTAL MULTIMER
Clean						
Ti (520)	860	43	2	0	0	45
Ti (208)	356	10	2	0	0	12
V	731	74	22	2	0	98
Nb	585	48	13	2	0	63
P(2x2)						
Ti ATOP	304	25	4	0	0	29
V ATOP	529	77	12	5	0	94
Nb ATOP	441	60	18	2	0	80
Ti BR	350	26	3	0	0	29
Ti TFA	337	10	1	0	0	11
Ti TFB	389	23	1	2	0	26
C(2x2)						
Ti ATOP	250	49	2	0	0	51
V ATOP	416	99	3	3	2	107
Nb ATOP	377	59	7	2	0	68
Ti BR	335	31	3	2	0	36
Ti TFA	336	16	2	0	0	18
Ti TFB (.5)	310	14	0	0	0	14
Ti TFB (1.)	437	18	5	0	0	23
Ti TFB (2.)	490	17	3	0	0	20

NOTE: All ion energies are 1.0 keV except as indicated, i.e., (0.5).

TABLE 15

Multimer Yield (Percentage)

COVERAGE	1-MER	2-MER	3-MER	4-MER	5-MER	% YIELD THAT FORMED MULTIMERS
Clean						
Ti (520)	90.4	9.0	0.6	0.0	0.0	9.6
Ti (208)	97.9	5.3	1.6	0.0	0.0	6.9
V	76.9	15.4	6.9	0.8	0.0	23.1
Nb	80.5	13.1	5.3	1.1	0.0	19.5
P(2x2)						
Ti ATOP	83.2	13.5	3.3	0.0	0.0	16.8
V ATOP	71.6	20.8	4.9	2.7	0.0	28.4
Nb ATOP	71.3	18.9	8.5	1.3	0.0	28.7
Ti BR	85.2	12.6	2.2	0.0	0.0	14.8
Ti TFA	93.7	5.5	0.8	0.0	0.0	6.3
Ti TFB	87.1	10.4	0.7	1.8	0.0	12.9
C(2x2)						
Ti ATOP	70.1	28.2	1.7	0.0	0.0	29.9
V ATOP	65.1	30.2	1.4	1.8	1.5	34.9
Nb ATOP	72.5	22.1	3.9	1.5	0.0	27.5
Ti BR	82.2	14.8	2.1	1.9	0.0	18.8
Ti TFA	89.9	8.5	1.6	0.0	0.0	10.1
Ti TFB (.5)	91.7	8.3	0.0	0.0	0.0	8.3
Ti TRB (1.)	89.6	7.3	3.1	0.0	0.0	10.4
Ti TFB (2.)	93.6	6.4	1.7	0.0	0.0	8.1

NOTE: All ion energies are 1.0 keV except as indicated, i.e., (0.5).

TABLE 16

Multimer Species Formed (by Substrate)

COVERAGE	M_2	M_3	M_4	MO	M_2O	M_3O	MO_2	M_2O_2	M_3O_2
Clean									
Ti (520)	43	2	0	-	-	-	-	-	-
Ti (208)	10	2	0	-	-	-	-	-	-
P(2x2)									
Ti ATOP	3	0	0	22	4	0	0	0	0
Ti BR	8	0	0	18	3	0	0	0	0
Ti TF <A+B>	7	0	0	8	1	1	0	0	0
C(2x2)									
Ti ATOP	0	0	0	49	2	0	0	0	0
Ti BR	5	0	0	26	2	1	1	1	0
Ti TF <A+B>	6	1	0	11	2	0	1	0	0
V CLEAN	74	22	2	-	-	-	-	-	-
V P(2x2)	18	0	2	59	12	3	0	0	0
V C(2x2)	9	0	0	90	3	1	0	2	2
Nb CLEAN	48	13	2	-	-	-	-	-	-
Nb P(2x2)	18	6	0	42	12	1	0	1	0
NB C(2x2)	2	2	0	57	5	0	1	2	0

NOTE: The quantity <A+B> refers to the average of the two three-fold positions.

TABLE 17

Multimer Species Formed (by Coverage)

COVERAGE	M_2	M_3	M_4	MO	M_2O	M_3O	MO_2	M_2O_2	M_3O_2
Clean									
Ti (520)	43	2	0	-	-	-	-	-	-
Ti (208)	10	2	0	-	-	-	-	-	-
V	74	22	2	-	-	-	-	-	-
Nb	48	13	2	-	-	-	-	-	-
P(2x2)									
Ti ATOP	3	0	0	22	4	0	0	0	0
V ATOP	18	0	2	59	12	3	0	0	0
Nb ATOP	18	6	0	42	12	1	0	1	0
Ti BR	8	0	0	18	3	0	0	0	0
Ti BFA	6	0	0	4	1	0	0	0	0
Ti TFB	11	0	0	12	1	2	0	0	0
C(2x2)									
Ti ATOP	0	0	0	49	2	0	0	0	0
V ATOP	9	0	0	90	3	1	0	2	2
Nb ATOP	2	2	0	57	5	0	1	2	0
Ti BR	5	0	0	26	2	1	1	1	0
Ti TFA	6	0	0	10	2	0	0	0	0
Ti TFB (.5)	4	0	0	10	0	0	0	0	0
Ti TFB (1.)	7	1	0	11	2	0	2	0	0
Ti TFB (2.)	9	0	0	8	2	0	1	0	0

NOTE: All ion energies are 1.0 keV except as indicated, i.e., (0.5).

and adatom coverage. The multimer yield is seen to increase with oxygen coverage and is due primarily to the ejection of metal atoms with their attached adatoms. There is a good correspondence in the multimer yield between vanadium and niobium in the clean and P(2x2) coverage which then degenerates as the coverage is increased to C(2x2). This can be attributed to the decreasing influence of the crystal lattice and increasing effect of the oxygen on the ejection mechanisms. This will be covered in greater detail in the following section.

G. MULTIMER ORIGINS

One of the primary objectives was to study the origins of multimer components to compare fragmentation and recombination as modes of molecule formation. Table 18 presents data as to whether the constituent atoms were nearest-neighors in the crystal prior to ejection, or in the case of trimers or greater, whether a portion of the molecule was joined. In the table the letter 'C' represents the number of multimers whose components were coupled together on the surface; p--partially connected multimers, N--those multimers whose components were not joined before ejection, %1--the percentage that was formed by fragmentation and %2--the percentage that were formed either through total or partial fragmentation, where a portion of the multimer was joined on the surface. Table 19 contains similar data for trimers and higher order

TABLE 18

Fragmentation versus Recombination (All multimers)

COVERAGE	C	P	N	%1	%2
Clean					
Ti (520)	29	1	15	64.4	66.6
Ti (208)	6	1	5	50.0	58.3
V	71	7	20	72.4	79.6
Nb	41	1	21	65.1	66.7
P(2x2)					
Ti ATOP	24	0	5	82.8	82.8
V ATOP	76	6	12	80.9	87.2
Nb ATOP	52	7	21	65.0	73.8
Ti BR	23	2	4	79.3	86.2
Ti TFA	9	1	1	81.8	90.9
Ti TFB	21	0	5	80.8	80.8
C(2x2)					
Ti ATOP	49	0	2	96.0	96.0
V ATOP	86	2	19	80.4	82.2
Nb ATOP	49	4	15	72.1	77.9
Ti BR	29	2	5	80.6	86.1
Ti TFA	11	0	7	61.6	61.6
Ti TRB (.5)	10	0	4	71.4	71.4
Ti TFB (1.)	17	1	5	73.9	78.3
Ti TFB (2.)	13	1	6	65.0	70.0

NOTE: C represents the number of multimers that were nearest neighbors on the surface prior to ejection; P, those partially connected and N, the number formed by recombination of non-adjacent atoms. %1 is the percent formed by fragmentation, %2 the percent formed by partial fragmentation. All ion energies are 1.0 keV except as indicated, i.e., (0.5).

TABLE 19

Fragmentation versus Recombination (Trimers and Greater)

COVERAGE	C	P	N	%1	%2
Clean					
Ti (520)	1	1	0	50.0	100.0
Ti (208)	1	1	0	50.0	100.0
V	17	7	0	70.8	100.0
Nb	14	1	0	93.3	100.0
P(2x2)					
Ti ATOP	23	0	3	88.5	88.5
V ATOP	11	6	0	64.7	100.0
Nb ATOP	13	7	0	65.0	100.0
Ti BR	1	2	0	33.3	100.0
Ti TFA	0	1	0	0.0	100.0
Ti TFB	3	0	0	100.0	100.0
C(2x2)					
Ti ATOP	1	0	1	50.0	50.0
V ATOP	6	2	0	75.8	100.0
Nb ATOP	5	4	0	55.6	100.0
Ti BR	4	2	0	60.0	100.0
Ti TRA	1	0	1	50.0	50.0
Ti TRB (1.)	3	1	1	60.0	80.0
Ti TFB (2.)	1	1	1	33.3	66.7

NOTE: C represents the number of multimers that were nearest neighbors on the surface prior to ejection; P, those partially connected and N, the number formed by recombination of non-adjacent atoms. %1 is the percent formed by fragmentation, %2 the percent formed by partial fragmentation. All ion energies are 1.0 keV except as indicated, i.e., (0.5).

multimers. Table 20 presents the percentage of multimer species formed by fragmentation.

The general trend is toward more fragmentation as the oxygen coverage is increased. This is due primarily to the fact that substrate atoms are ejected after being hit from underneath and carry off their attached adatoms as they leave. Many partial fragmentation molecules were formed when attached atoms exited the surface obliquely, knocking off oxygens from nieghboring atoms on the way out. This also appears to be one of the principal mechanisms involved in recombination of non-ajoining atoms.

Figures 74-87 of Appendix E and Table 21 give the locations and frequency of occurrence for all of the observed mechanisms involved in multimer formation. (In the table double entries refer to the a and b sections of the particular drawing.) By far the greatest source of multimers is the dimer composed of a substrate atom and its attached adatom which is a fragmentation mechanism. Higher order multimers are a fairly rare occurrence, but over 65% are formed by fragmentation and virtually all involve at least partial fragmentation (Table 20).

As the oxygen coverage is increased, the monoxide is still the prevalent species formed, but there is a shift in the mechanisms that make up the rest of the yield and new mechanisms are added. In the A-top and bridge positions the percentage of multimers resulting from fragmentation

TABLE 20

Percentage of Multimer Species Formed by Fragmentation

COVERAGE	M_2	M_3	M_4	MO	M_2O	M_3O	MO_2	M_2O_2	M_3O_2
Clean									
Ti	67	50	-	-	-	-	-	-	-
V	74	73	100	-	-	-	-	-	-
Nb	56	92	100	-	-	-	-	-	-
P(2x2)									
Ti ATOP	33	-	-	82	100	-	-	-	-
V ATOP	100	-	100	80	50	100	-	-	-
Nb ATOP	83	100	-	57	50	100	-	1P	-
Ti BR	63	-	-	89	33	-	-	-	-
Ti TFA	100	-	-	75	1P	-	-	-	-
Ti TFB	64	-	-	92	100	100	-	-	-
Ti TF(A+B)	82	-	-	84	50	100	-	-	-
C(2x2)									
Ti ATOP	-	-	-	98	50	-	-	-	-
V ATOP	56	-	-	81	67	1P	-	100	100
Nb ATOP	100	100	-	74	40	-	X	X	-
Ti BR	40	-	-	92	100	100	1P	1P	-
Ti TRA	33	-	-	80	50	-	-	-	-
Ti TFB	86	X	-	73	100	-	50	-	-
Ti TR(A+B)	60	X	-	77	75	-	50	-	-

NOTE: A tack (-) indicates that the species was not formed, while "X" indicates that none were formed by fragmentation. 1P indicates that only one of the particular species was formed and that was through partial fragmentation.

TABLE 21

Frequency of Occurrence of the Various Ejection Mechanisms

COVERAGE	1	2	3	4	5	6	7	8	9	10	11	12
Clean												
Ti (520)	20/6	1	2	9/3	1	1	-	-	-	-	-	-
Ti (208)	3/2	2	2	1	-	-	-	-	-	-	-	-
V	37	13	4	9	5	7	-	4	2	2	4	-
Nb	19	8	10	4	6	2	8	-	2	-	-	2
P(2x2)												
Ti ATOP	1	1	19	1/2	2	-	-	-	-	-	-	-
V ATOP	6/0	6	1	-	-	2	47/10	-	-	4	2	3
NB ATOP	5/1	3	3	3	4	-	24/7	7	1	5	1	2
Ti BR	4	1	1	1	1	12	2	1	1	-	-	-
Ti TFA	1	2	1	1	3	1	-	-	-	-	-	-
Ti TFB	1	5	1	1	1	1	1	11	1	1	-	-
C(2x2)												
Ti ATOP	1	45	1	1	-	-	-	-	-	-	-	-
V ATOP	3	1	9	1	2	-	74	5	7	3	-	-
Nb ATOP	2	-	-	-	-	2	42	10	2	-	1	2
Ti BR	1	1	1	1	24	2	1	1	1	1	1	1
Ti TRA	1	3	1	1	1/1	6/2	1	1	-	-	-	-
Ti TFB (.5)	-	-	1/1	-	1	5/2	-	-	-	-	-	1
Ti TFB (1.)	1	1/1	1/0	2	1	4/4	1/1	1	1	1	1	1
Ti TFB (2.)	1	-	3/2	-	-	5/1	-	1	-	-	-	1

NOTE: The column headings refer to surface locations shown in Appendix E. Columns with double entries refer to the a and b sections of the individual figures. Ion energies are 1.0 keV except as indicated, i.e., (.5).

TABLE 21 (CONT.)

COVERAGE	13	14	15	16	17	18	19	20	21	22	23	24
Clean												
Ti (520)	-	-	-	-	-	-	-	-	-	-	-	-
Ti (208)	-	-	-	-	-	-	-	-	-	-	-	-
V	-	-	2	2	4	1	-	-	-	-	-	-
Nb	1	1	-	-	-	-	-	-	-	-	-	-
P(2x2)												
Ti ATOP	-	-	-	-	-	-	-	-	-	-	-	-
V ATOP	2	1	-	1	2	-	3/2	1	1	-	-	-
Nb ATOP	-	-	2	-	-	1	-	-	-	1	2	3
Ti BR	-	-	-	-	-	-	-	-	-	-	-	-
Ti TFA	-	-	-	-	-	-	-	-	-	-	-	-
Ti TFB	-	-	-	-	-	-	-	-	-	-	-	-
C(2x2)												
Ti ATOP	-	-	-	-	-	-	-	-	-	-	-	-
V ATOP	-	-	-	-	-	-	-	-	7	-	1	2
Nb ATOP	-	1	1	2	1	1	1	1	-	1	-	-
Ti BR	-	-	-	-	-	-	-	-	-	-	-	-
Ti TFA	-	-	-	-	-	-	-	-	-	-	-	-
Ti TFB (.5)	1	-	-	-	-	-	-	-	-	-	-	-
Ti TFB (1.)	-	-	-	-	-	-	-	-	-	-	-	-
Ti TFB (2.)	-	3	2	1	1	-	-	-	-	-	-	-

COVERAGE	25	26	27	28
P(2x2)				
Nb ATOP	1	2	1	1

increases, while it decreases for the three-fold positions. Those oxygens, sharing three bonds, tend to be left behind unless at least two of their nearest neighbors are also ejected. The greater oxygen density also presents a larger target to obliquely ejected fragments, increasing the probability of collision and subsequent capture.

H. MULTIMER EJECTION TIMES

Appendix F contains bar charts depicting the differences in ejection times between multimer components, both for metal-metal and metal-oxygen pairs. Essentially none of the pairs in any of the runs were ejected simultaneously, but all but about seven pairs were ejected within 100 fsec of each other and most within 50 fsec. This difference is about the same order of magnitude as the vibrational period of an equivalent diatomic molecule [Ref. 47], 10^{-13} sec (100 fsec), and is not necessarily an indication that the atoms were ever disjoined at some point in time.

Comparison of the charts for the different oxygen coverages reveals a correspondence between ejection time difference and the percentage of multimers that were formed by fragmentation. As one would expect there is an increasing time difference between component ejection as the number of molecules formed by recombination increases.

I. SPOT PATTERNS

The spot patterns produced by ion bombardment of the crystal surfaces are contained in Appendix G. The ejection patterns correspond to the directions of the close-packed rows in the crystal, which for hcp are oriented at 30, 90 and 150 degrees from the <001> direction. For bcc the directions are 0 and 90 degrees. These lead to a six-fold symmetry pattern in hcp and a four-fold rectangular pattern in bcc. The patterns for vanadium and niobium are in quite good agreement with the expected results, but there is considerable deviation in the case of titanium atoms. The spikes at 90, 150 and 330 degrees are present, but there are extra spikes at 0, 60, 180 and 240 degrees, while those at 30 and 210 degrees are missing. A variety of different runs were conducted with additional impact point origins and permutated impact point sets, but all resulted in the same pattern. At present there is no apparent reason for this discrepancy. Second layer contributions would tend to broaden the spikes somewhat, but not change the overall appearance.

The patterns for the metals with adatoms in the A-top position are essentially the same as for those from clean surfaces, even though they have considerably more energy as was pointed out earlier. There is some blurring, presumably due to adatom interference, but it is very minor. This blurring becomes more pronounced as the oxygen density is increased from P to C. The features of the metal spot patterns begin to fade when adatoms are placed in the bridge positions and are completely absent for oxygen in the three-fold sites, leaving a uniform angular distribution.

There is no marked tendency for oxygen to eject perpendicular to the surface in any of the locations, as was found by Hanson [Ref. 37]. The ejection angles were observed to increase slightly with increasing oxygen density, probably caused by the interference of other adatoms and increasing yield. This was also found to be the case for varying ion energy, where the average ejection angle reached a maximum for 1.0 keV bombardment corresponding to the peak in oxygen yield.

J. EJECTION TIME VERSUS ENERGY

The plots of ejection time versus energy are contained in Appendix H. As can been seen, the highest energy atoms are ejected very early in the process. As time progresses, the ejection energy falls rapidly with a few low energy stragglers coming off as the collision cascade dies and recrystallization begins. The distributions are independent of either adatom density or location. The duration of the ejection period is again seen to be a function of the crystal atomic mass as was found earlier in comparing ejection time distributions. Increasing ion energy increases the energy of those atoms which are ejected early, but has no appreciable effect on the bulk of the ejected atoms.

The energy distribution of ejected oxygens mimics that of the substrate, with the most energetic atoms coming off early in the cascade. This close correlation is most likely due to fragmentation where oxygens are ejected with their neighboring metal atom(s). There is, though, a faster drop-off in energy than in the case of the substrate. Some broadening is observed with more energetic atoms being ejected later as the adsorption sites are shifted to those involving a higher degree of bonding.

K. SURFACE LAYER EJECTION FREQUENCY

Appendix I contains diagrams depicting the relative frequency of ejection of surface layer atoms. For simplicity, the plots contain information for a single set of 104 impact points. Also indicated are the locations of the impact zones that produced the ejections.

The most obvious feature is the tendency for the damage area to extend vertically in the Z direction for the hcp crystals, while the pattern for bcc is much more symmetric. This can be explained in terms of the locations of close-packed rows. The two close-packed rows in bcc are in the X and Z directions, however hcp only has one of three in the X direction, with the other two primarily in the Z direction.

The plots also graphically demonstrate the decrease in substrate yield as the oxygen density is increased, as was mentioned in Section B.

L. COMPARISON WITH EXPERIMENTAL DATA

Tables 22 and 23 provide a comparison of experimental data on the ratios of multimer species formed by recombination and fragmentation with that obtained by computer

TABLE 22

Comparison of Experimental and Simulation Results on Multimer Formation Mechanisms for Titanium

RATIO	LU	P (2x2) ATOP	C (2x2) ATOP	P (2x2) BR	C (2x2) BR	P (2x2) TFA+B	C (2x2) TFA+B	P (2x2) ALL	C (2x2) ALL	
O^-/T_i^+	17.5	20.0	50.6	21.0	51.5	11.7	30.3	15.7	38.4	
TiO^+/Ti^+	50.0	1.55	0.60	0.70	0.92	0.43	1.43	0.70	1.07	R
TiO^-/Ti^+	0.01	7.05	29.6	5.40	10.7	1.97	2.16	4.00	8.63	F
TiO_2^+/Ti^+	0.67	-	-	-	0.04	-	0.12	-	0.04	R
TiO_2^-/Ti^+	0.28	-	-	-	0.36	-	0.18	-	0.26	F
TiO^+/O^-	286.	7.80	1.20	3.20	1.80	3.78	4.64	4.47	2.78	R
TiO^-/O^-	0.07	35.3	58.5	26.3	20.8	17.2	6.96	25.3	22.5	F
TiO_2^+/O^-	3.90	-	-	-	0.08	-	0.44	-	0.09	R
TiO_2^-/O^-	1.60	-	-	-	0.82	-	0.66	-	0.71	F

NOTE: All quantities are in percentages. Experimental data taken from Reference 22. "R" and "F" refer to whether the mechanism involved was recombination or fragmentation. The TFA+B entries were obtained by averaging the data from the TFA and TFB positions. The ALL entires represent the average from all three adatom sites.

TABLE 23

Comparison of Experimental and Simulation Results on Multimer Formation Mechanisms for Vanadium and Niobium

RATIO	YU	P (2x2) ATOP	C (2x2) ATOP	RATIO	YU	P (2x2) ATOP	C (2x2) ATOP	
O^-/V^+	10.0	10.8	29.1	O^-/Nb^+	UNK	13.6	30.8	
VO^+/V^+	27.7	2.44	5.19	NbO^+/Nb^+	UNK	4.55	5.01	R
VO^-/V^+	0.02	9.76	22.1	NbO^-/Nb^+	UNK	6.04	14.3	F
VO_2^+/V^+	0.13	-	-	NbO_2^+/Nb^+	UNK	-	0.42	R
VO_2^-/V^+	0.78	-	-	NbO_2^-/Nb^+	UNK	-	0.28	F
VO^+/O^-	278.	22.6	17.8	NbO^+/O^-	UNK	32.7	16.6	R
VO^-/O^-	0.19	90.4	76.0	NbO^-/O^-	0.72	40.3	47.4	F
VO_2^+/O^-	0.14	-	-	NbO_2^+/O^-	UNK	-	1.32	R
VO_2^-/O^-	7.80	-	-	NbO_2^-/O^-	14.0	-	0.88	F

NOTE: All quantities are in percentages. Experimental data taken from Reference 23. "R" and "F" refer to whether the mechanism involved was recombination or fragmentation.

simulation. The experimental data was obtained by Yu [Refs. 22,23] using 500 ev neon and argon to bombard the three metals. His experiments used cesiated-oxygenated polycrystals and through the change in the work function induced by the cesium, he was able to obtain information on the charge state dependence of the two multimer ejection mechanisms. The ion ratios presented in the tables were calculated by extrapolating the relative yield of each species back to a zero change in the work function which should represent the cesium-free case (Appendix J).

No exact comparison can be made due to the uncertainty with respect to relative ionization probability, oxygen placement and density, as well as differences in ion mass and energy. However, if the ratios of ions formed by the two mechanisms were similar, the computer simulations would support Yu's proposed model. This was not found to be the case. In each of the oxygen positions and densities the ratio of fragmentation to recombination was found to be opposite that reported by Yu.

This variance between the simulation and experimental results is probably not due to differences in ion energy since Table 12 indicates that the total multimer yield decreases as the ion energy increases. The percentage of multimers formed by fragmentation also decreases, but this is believed due to the longer-ranged transport of energy which allows more ejection mechanisms to operate. The activation of more mechanisms could then decrease the relative fraction of multimers formed by fragmentation. The simulation yield obtained at 500 eV was, in any case, too small for meaningful comparison.

Failure of the simulations to support Yu's theory may be caused by an inadequate treatment of the ionization probability contribution to the determination of multimer stability. Since the program does not determine charge state, some of the multimers that were classified as stable may, in reality, be unstable and thus reduce the percentage found to be formed by fragmentation.

V. CONCLUSIONS

The program has the inherent flexiblity to permit detailed analysis of virtually any aspect of sputtering. The ease with which parameters may be isolated and varied greatly facilitates the determination of the significant factors involved, as well as the interdependence of these factors.

The results of these simulations support earlier findings concerning the effects of channeling and that the majority of sputtered atoms originate in the top layers of the crystal. The angular distribution of ejected atoms agrees with experimental results in the case of vanadium and niobium, however the discrepancies noted in the ejection patterns for titanium require further study.

The decrease in oxygen yield from crystals with adatoms in the three-fold positions indicates that the oxygens are most stable in these sites. Such positions would also facilitate their incorporation into the metal lattice as the oxygen exposure is increased, resulting in the formation of a stable oxide in the top layers. It is also possible that the oxygens assume an A-top position at low oxygen exposures and as the coverage is increased, oxygen-oxygen repulsion causes a migration to the three-fold sites.

The disagreement between the simulation results and Yu's theory and findings on multimer formation need not be due to a failure of his basic model, but rather to an incomplete understanding and treatment of the chemistry involved after the atoms are ejected from the surface by the simulation model. On the other hand it is somewhat difficult to understand how the yield of TiO^+, presumably formed by recombination as suggested by Yu, can be so much larger than TiO^-, from fragmentation, considering the probabilities involved in two or more atoms finding themselves in the same location with relative velocities favorable enough to permit bonding. It may also be that a significant percentage of the negative ions stabilize themselves by electron ejection prior to their collection in the mass spectrometer. Yu has also pointed out that several discrepancies in his findings may be due to the fact that as the oxygen density is increased TiO^+ and TiO_2^+ may be formed by both mechanisms.

An item that bears further study is the increase in the most probable energy of the ejected substrate atoms when oxygen is introduced in the A-top position. At present there is no apparent reason for such an increase. If this were a model artifact one would expect the effect to carry over, to some degree, to crystals with adatoms in the bridge positions. Instead, the average and most probable energies for the bridge and three-fold sites are essentially the same.

APPENDIX A

POTENTIAL FUNCTION GRAPHS AND PARAMETERS

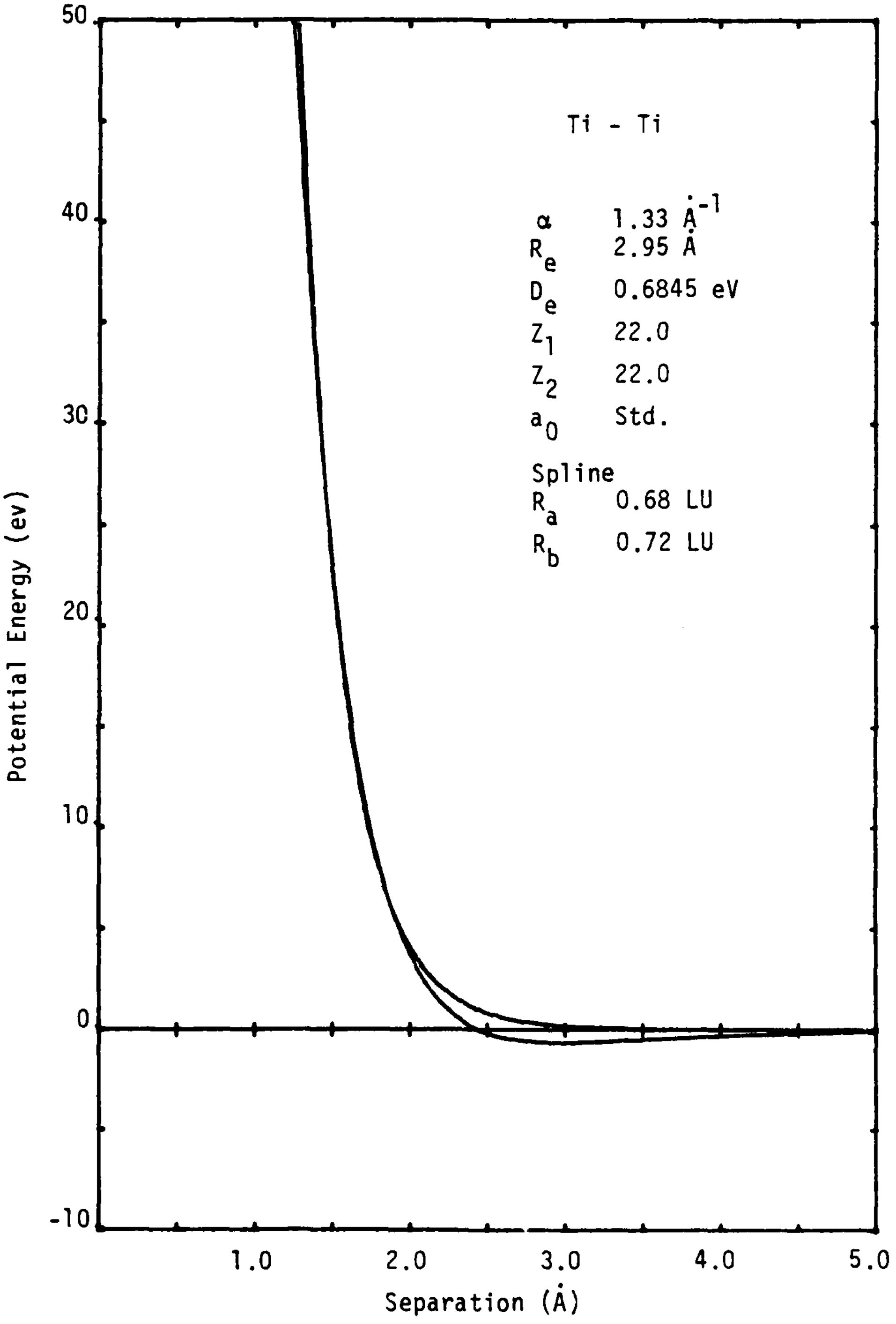

Fig. 15. Ti-Ti solid phase potential function and associated parameters.

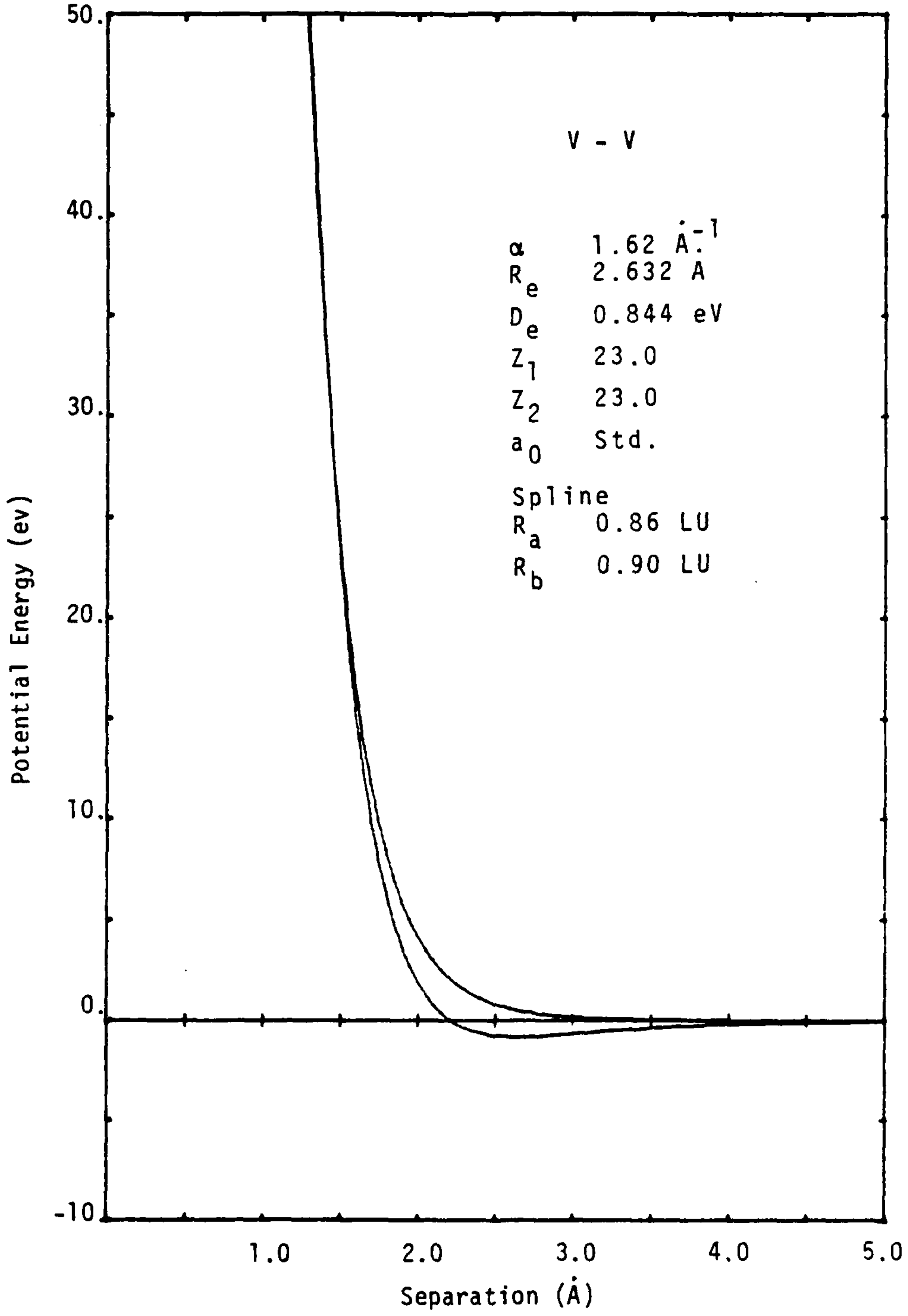

Fig. 16. V-V solid phase potential function and associated parameters.

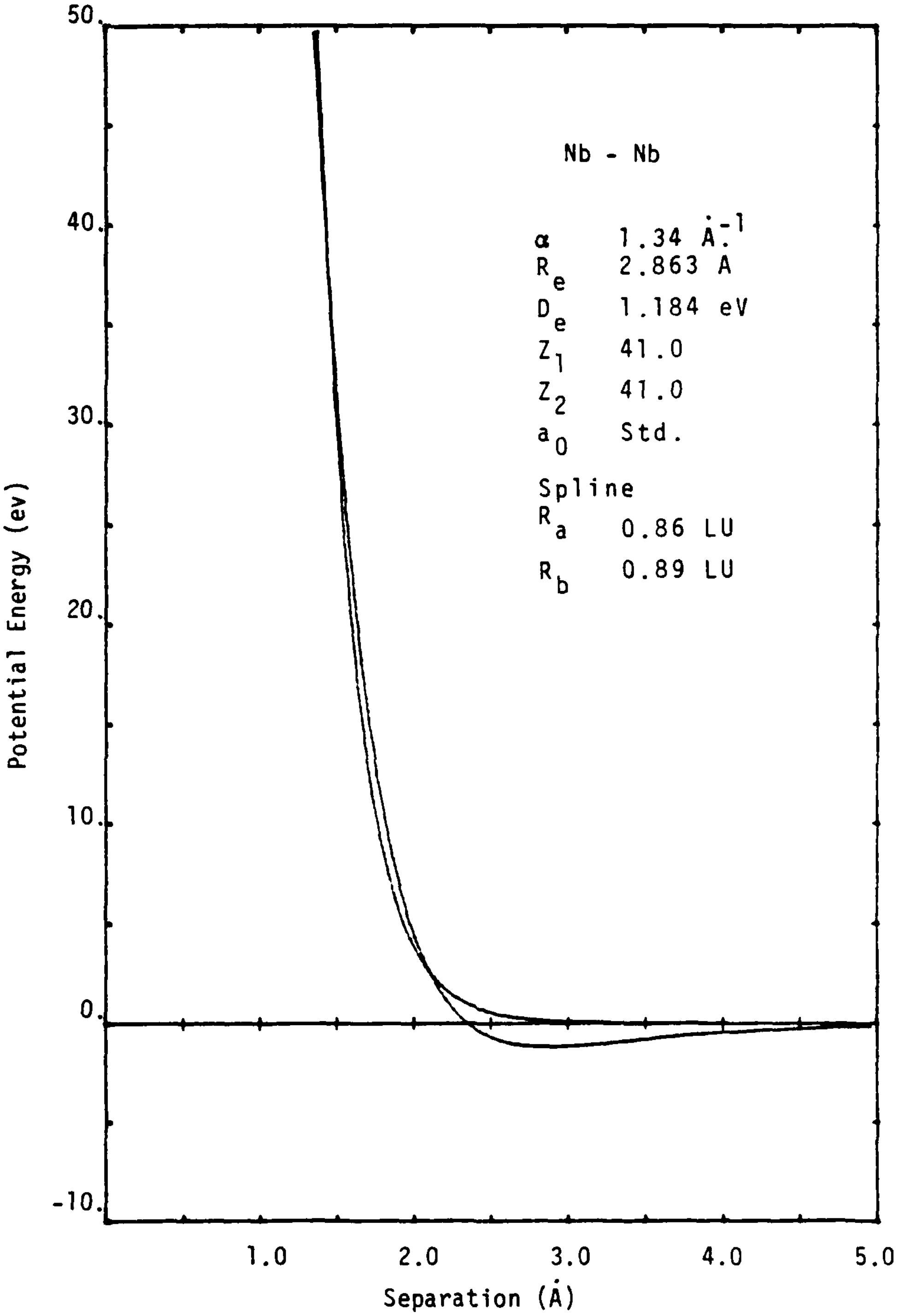

Fig. 17. Nb-Nb solid phase potential function and associated parameters.

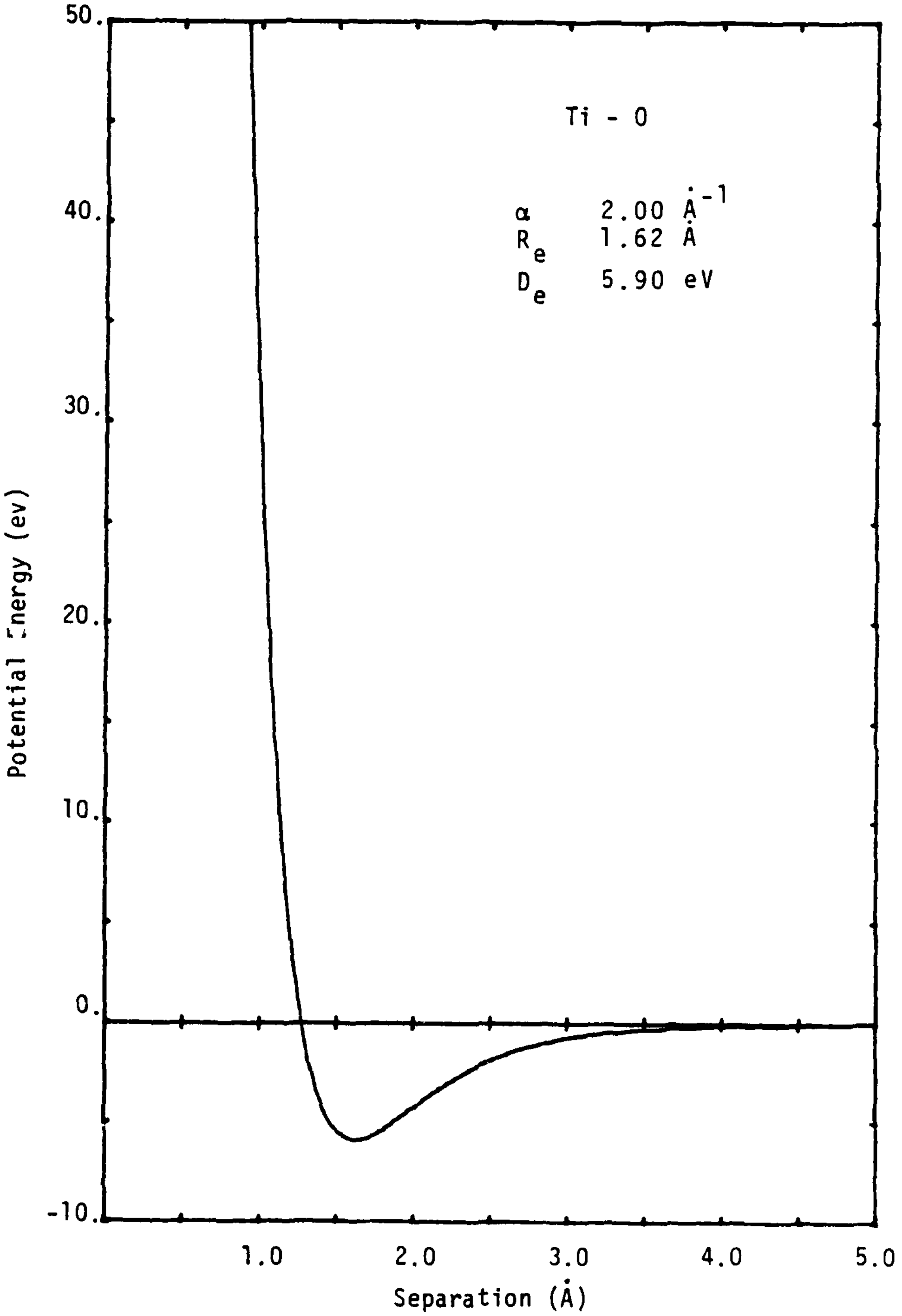

Fig. 18. Ti-O solid phase potential functionand associated parameters.

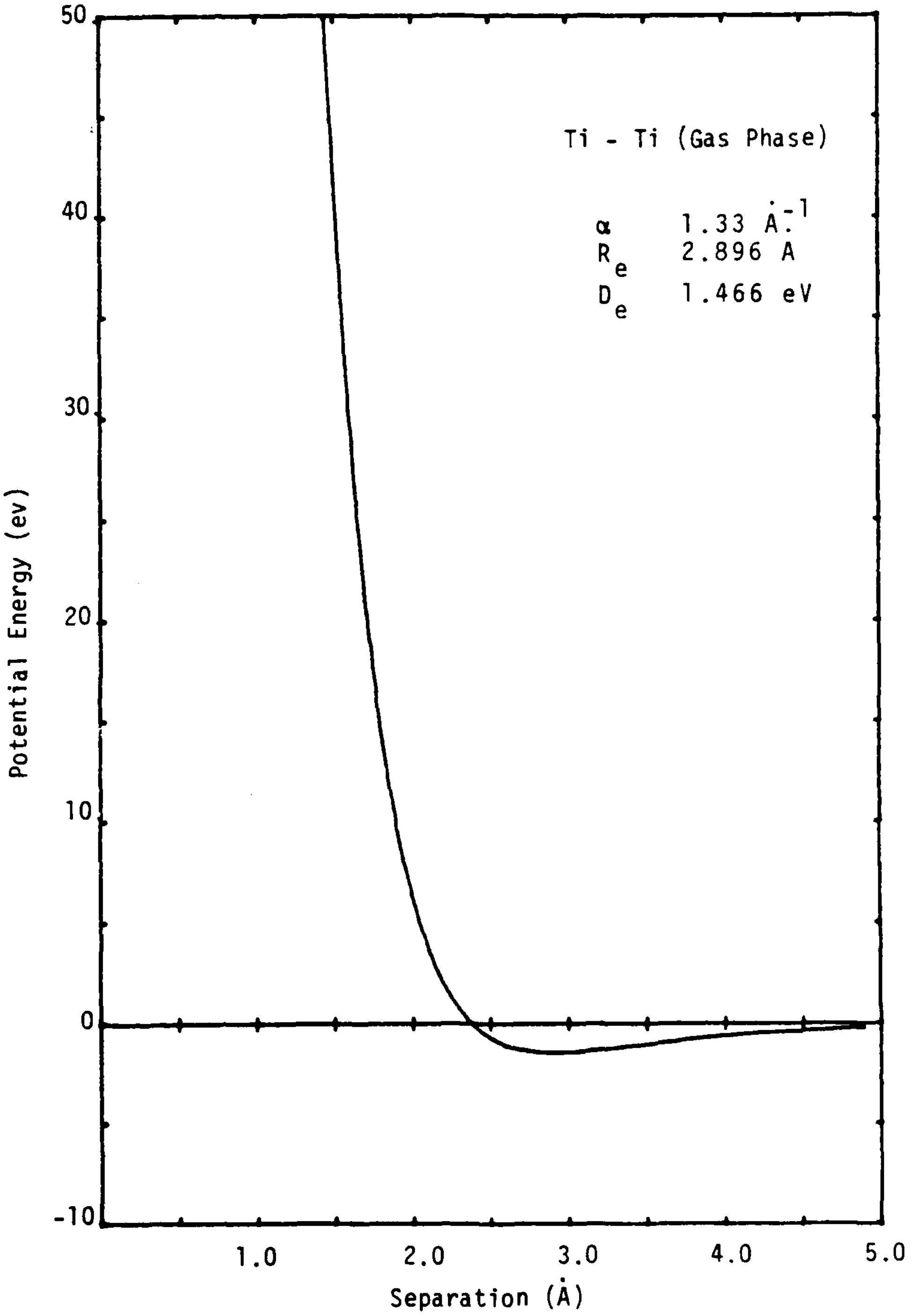

Fig. 19. Ti-Ti gas phase potential function and associated parameters.

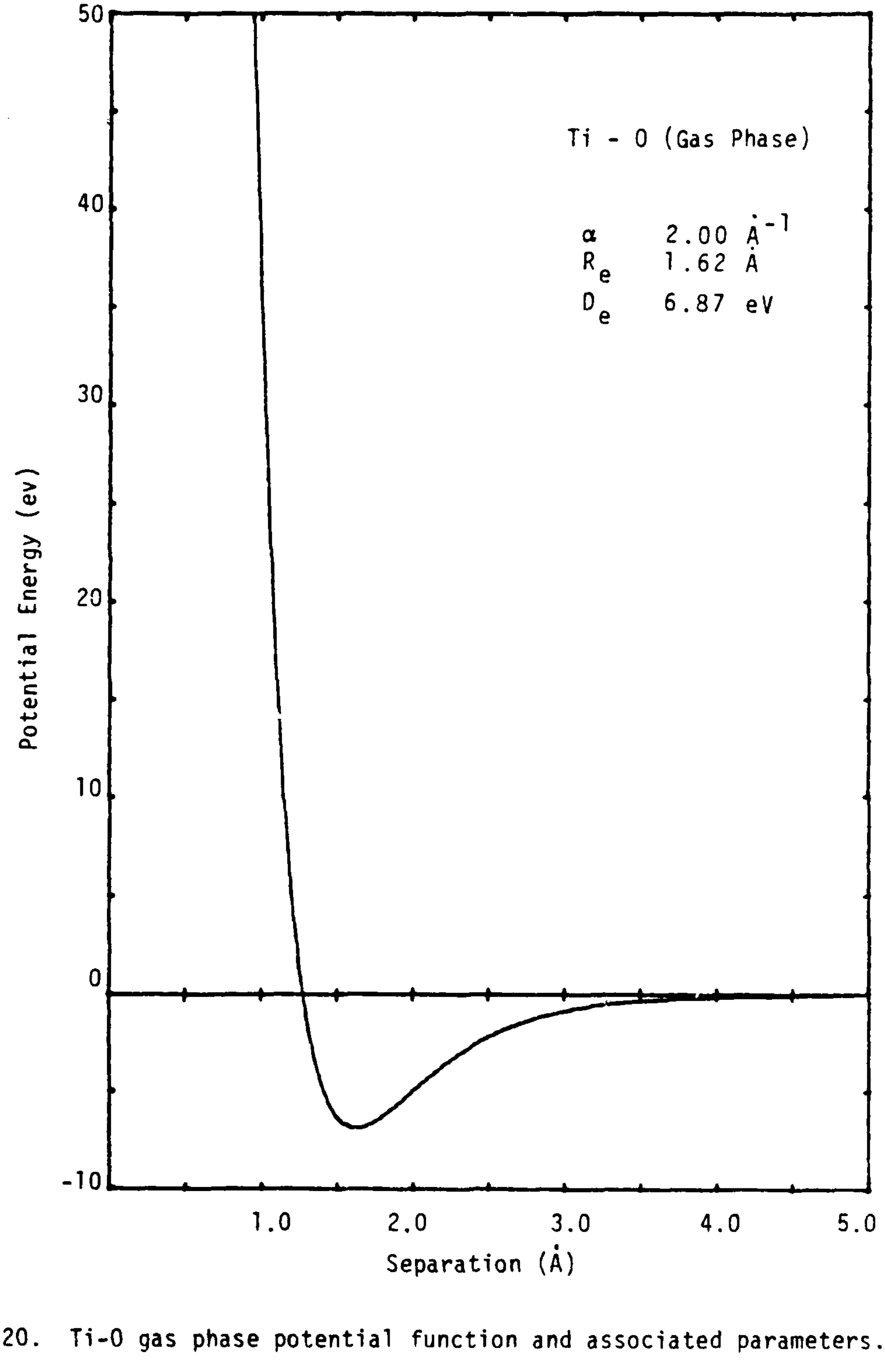

Fig. 20. Ti-O gas phase potential function and associated parameters.

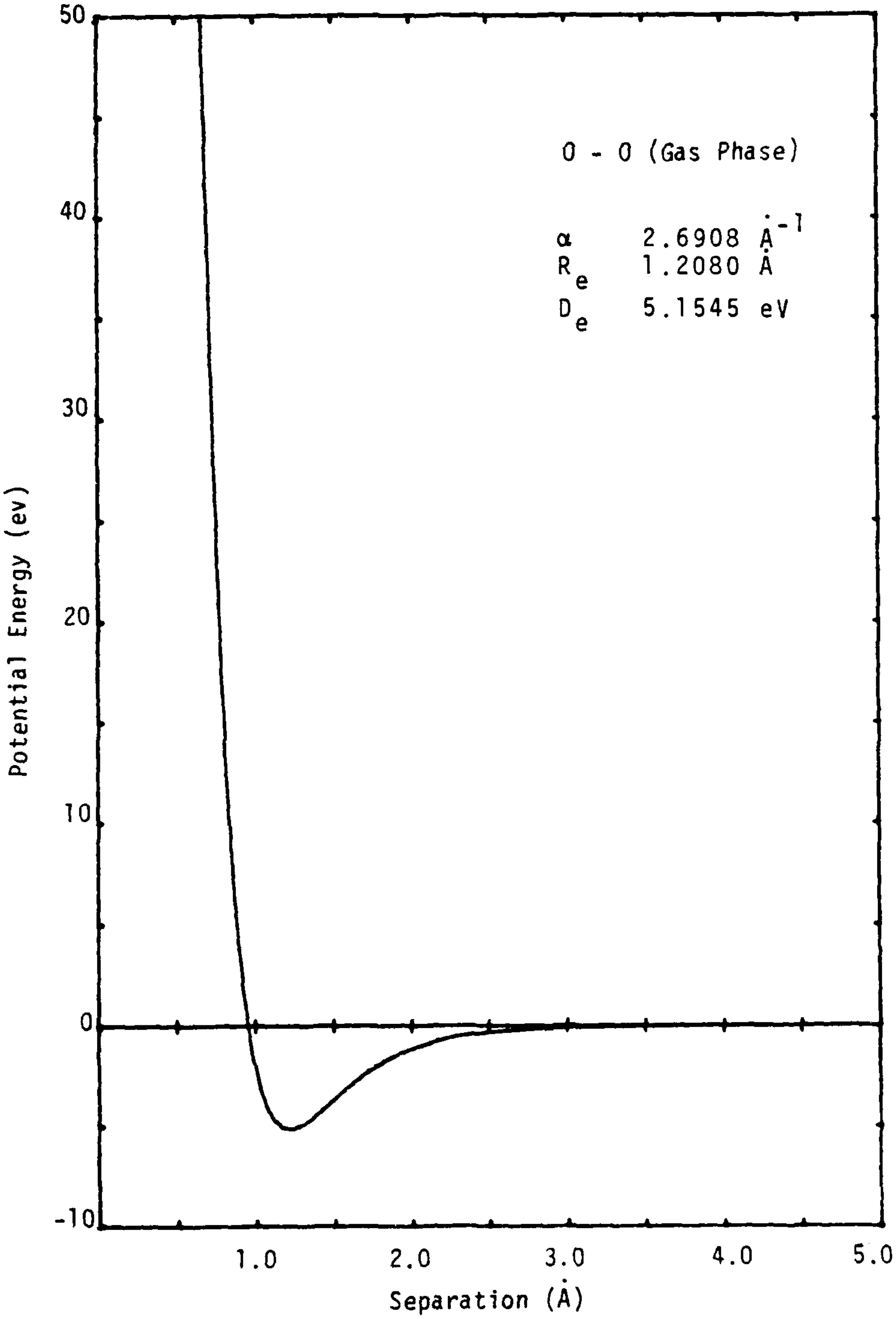

Fig. 21. O-O gas phase potential function and associated parameters.

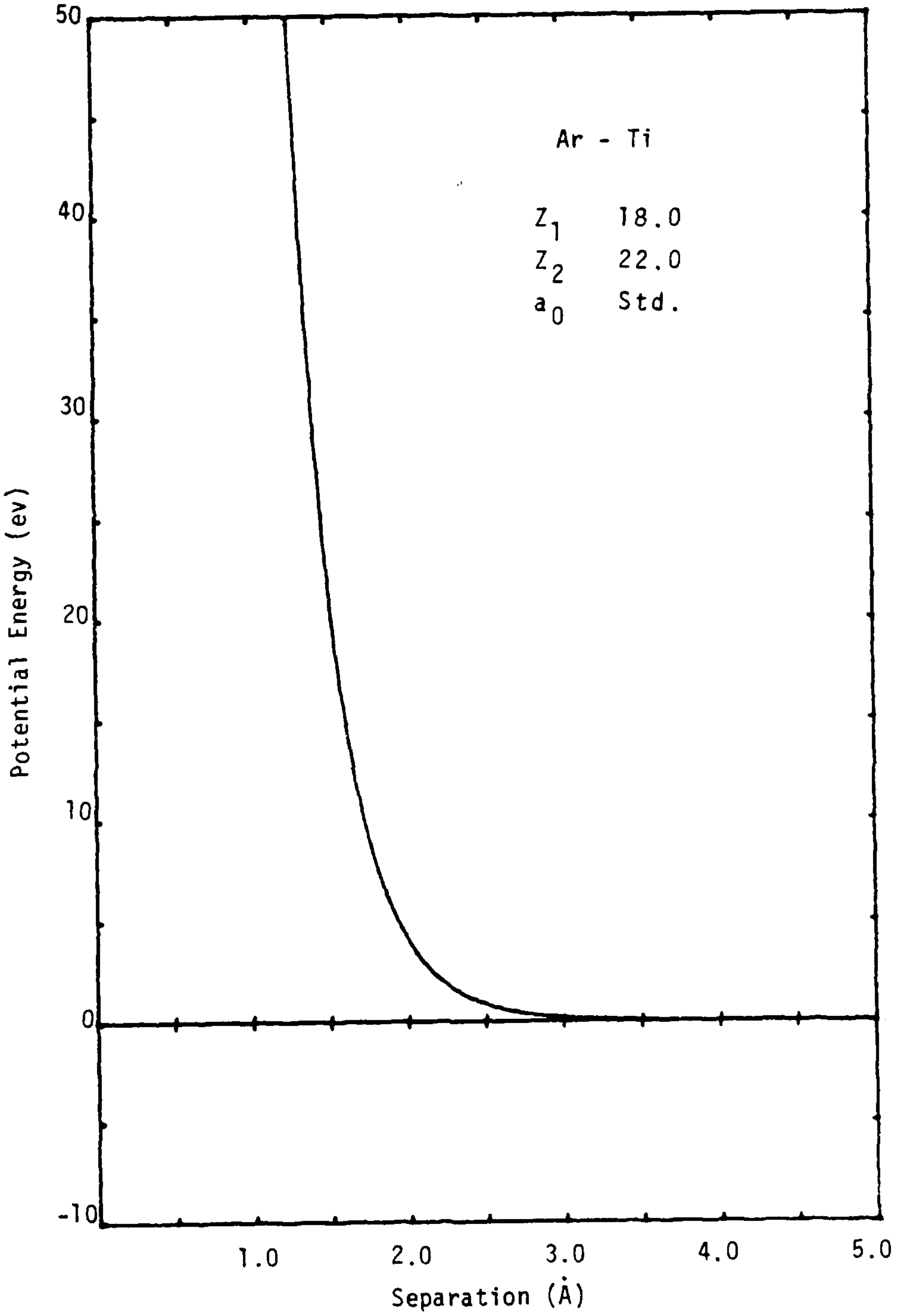

Fig. 22. Ar-Ti potential function and associated parameters.

APPENDIX B

ATOMS PER SINGLE ION CHARTS

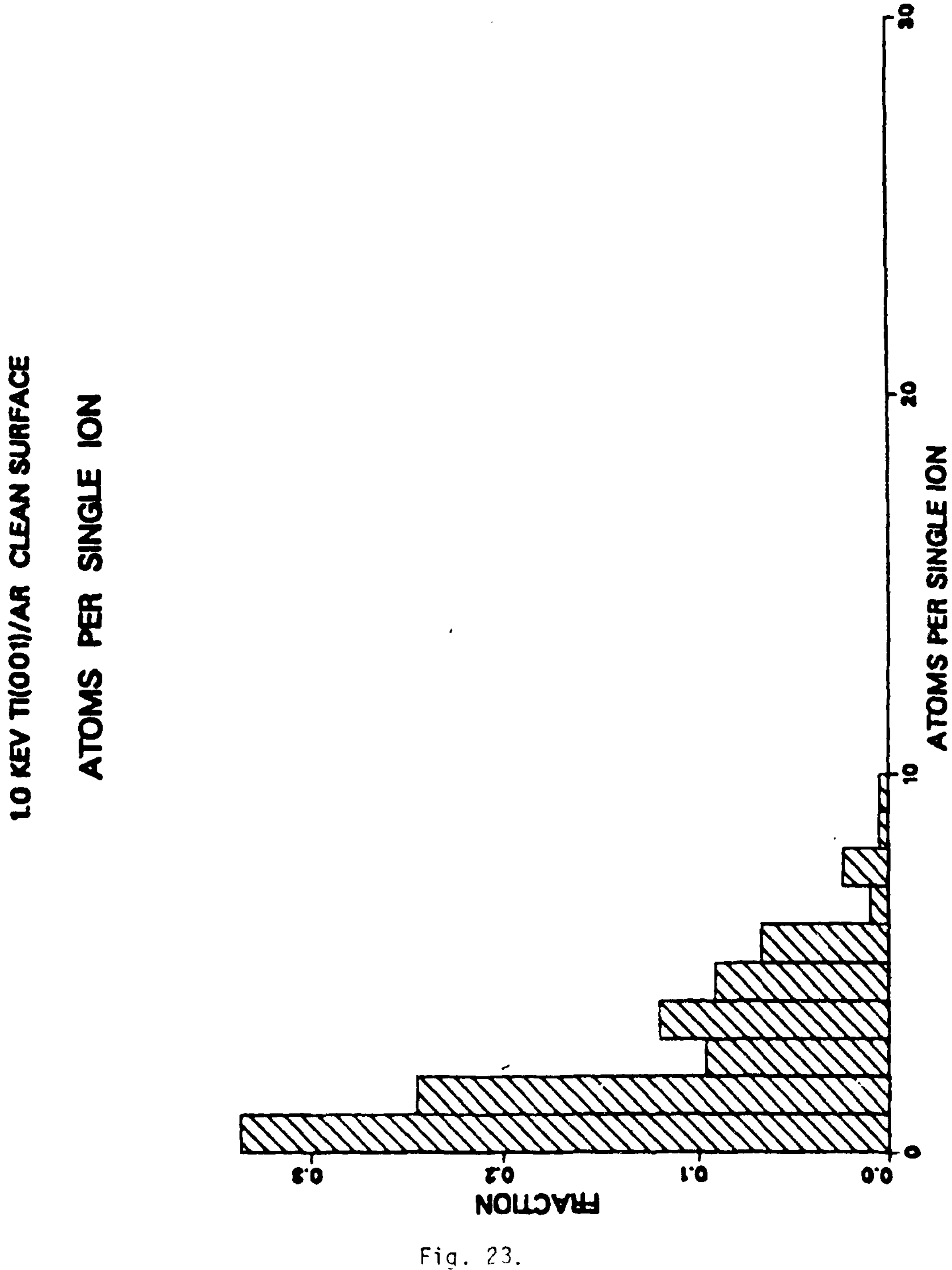

Fig. 23.

AD-A141 998 COMPUTER SIMULATION STUDIES OF SPUTTERING AND MULTIMER FORMATION FROM CLE..(U) NAVAL POSTGRADUATE SCHOOL MONTEREY CA M G MATHIS DEC 83 2/3

UNCLASSIFIED F/G 20/12 NL

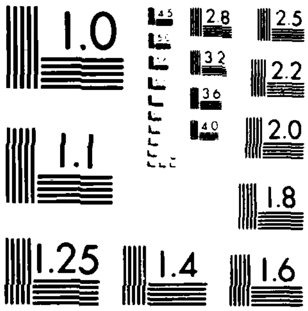

MICROCOPY RESOLUTION TEST CHART
NATIONAL BUREAU OF STANDARDS 1963-A

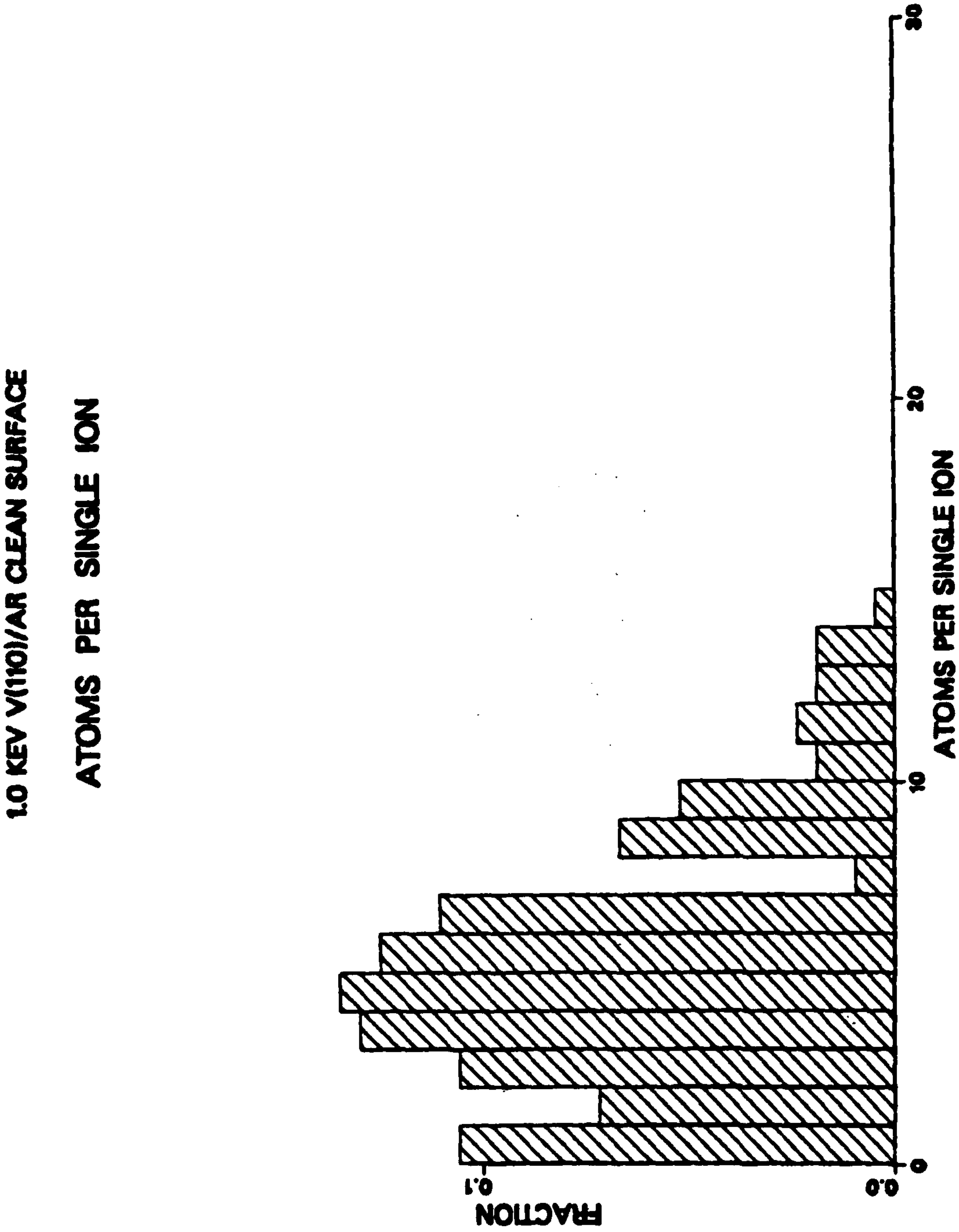
1.0 KEV V(110)/AR CLEAN SURFACE
ATOMS PER SINGLE ION
FRACTION
0.1
0.0
0
10
20
30
ATOMS PER SINGLE ION

Fig. 24.

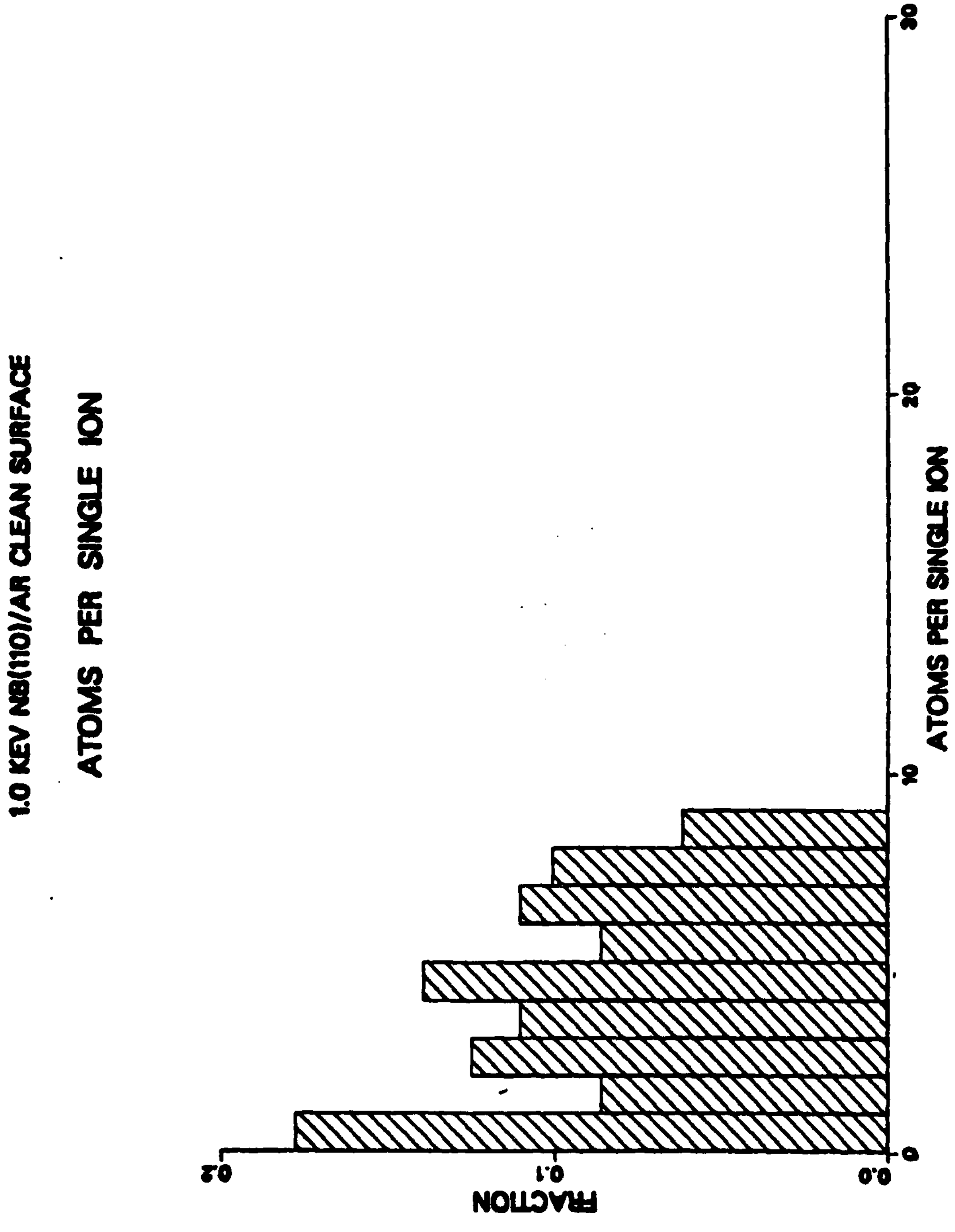
1.0 KEV NB(110)/AR CLEAN SURFACE
ATOMS PER SINGLE ION
FRACTION
0.0
0.1
0.2
0
10
20
30
ATOMS PER SINGLE ION

Fig. 25.

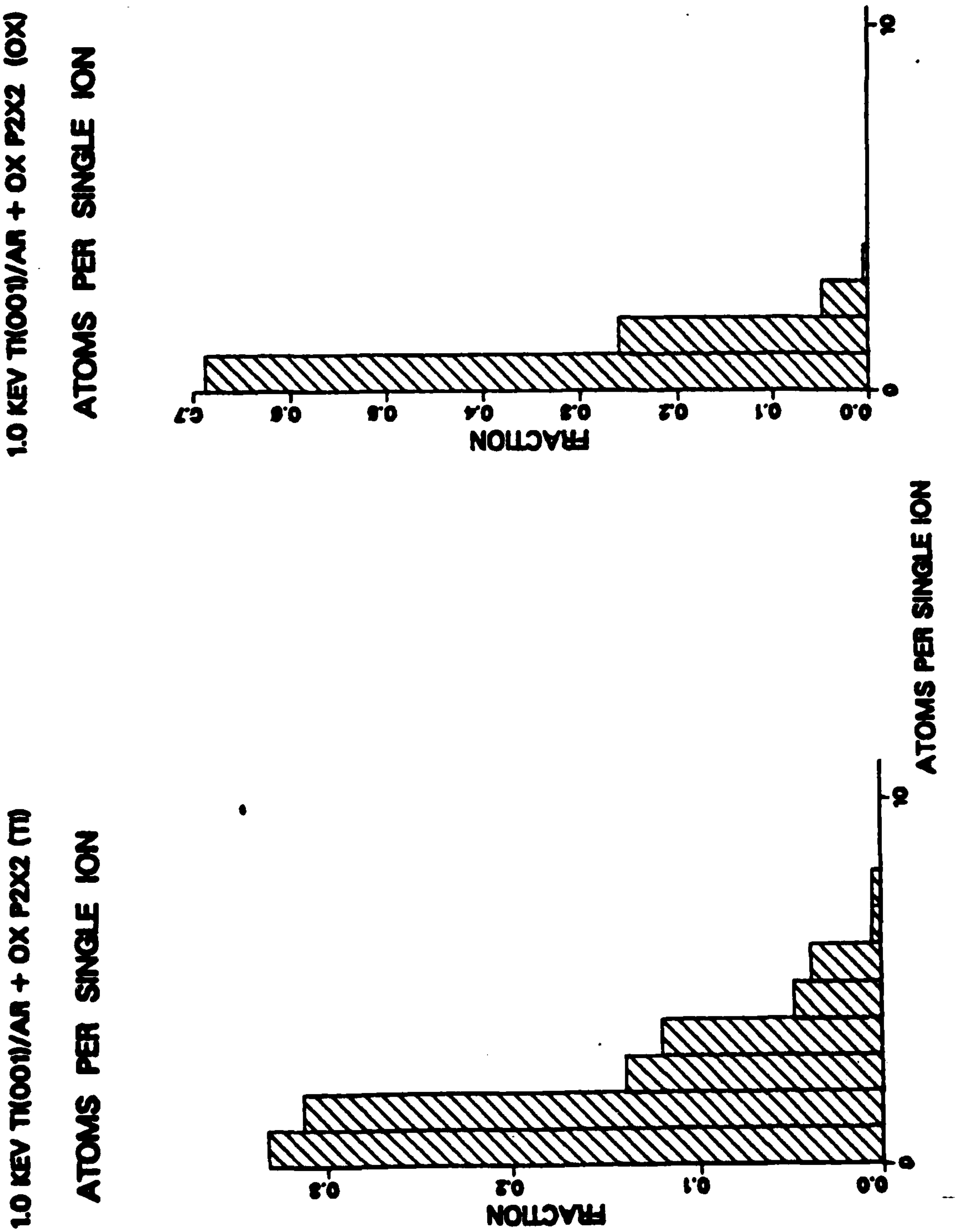
1.0 KEV Ti(001)/AR + OX P2X2 (OX)
ATOMS PER SINGLE ION
FRACTION
0.0
0.1
0.2
0.3
0.4
0.5
0.6
0.7
0
10
1.0 KEV Ti(001)/AR + OX P2X2 (Ti)
ATOMS PER SINGLE ION
FRACTION
0.0
0.1
0.2
0.3
0
10
ATOMS PER SINGLE ION

Fig. 26.

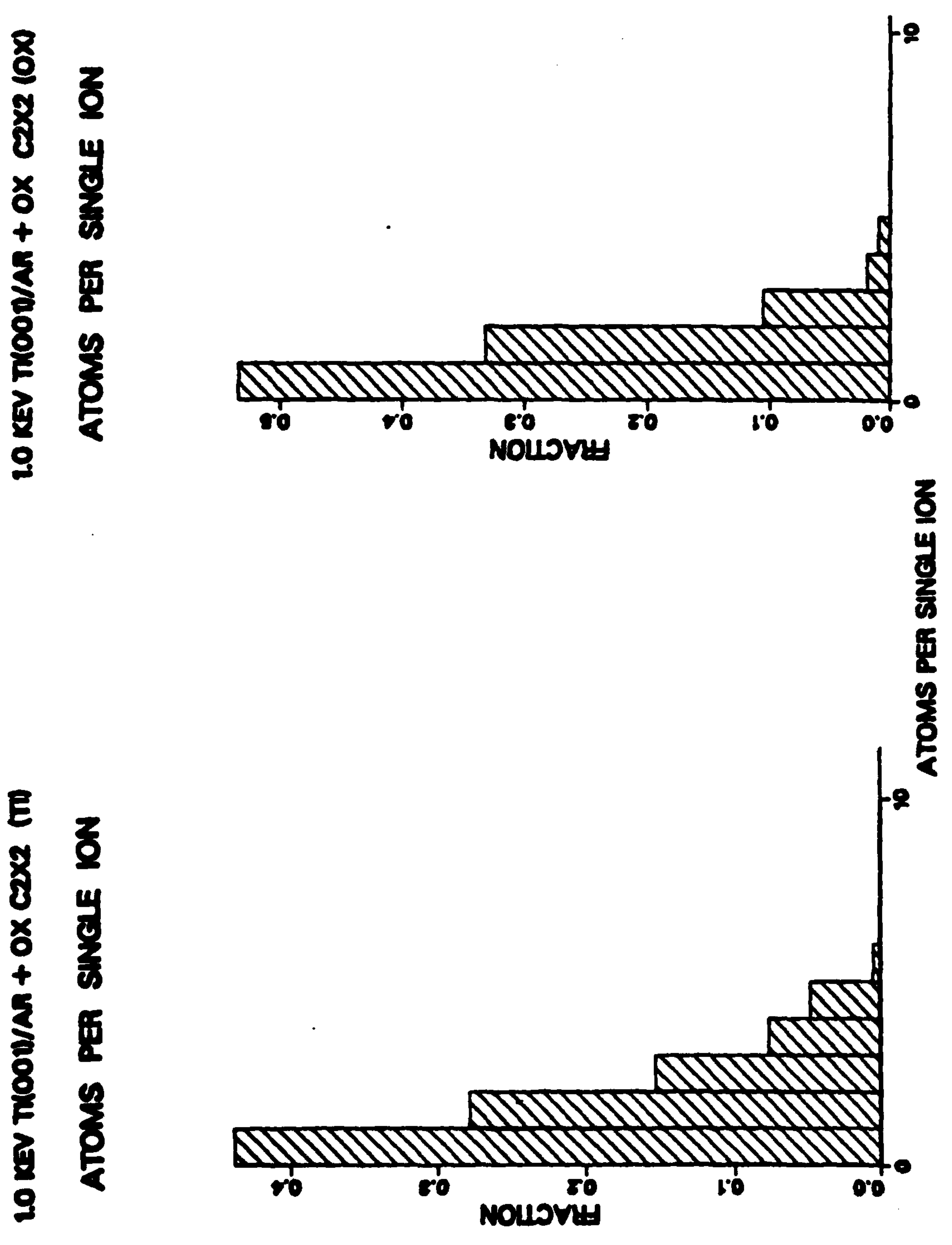
1.0 KEV TI(001)/AR + OX C2X2 (OX)
ATOMS PER SINGLE ION
FRACTION
0.0
0.1
0.2
0.3
0.4
0.5
0
10
ATOMS PER SINGLE ION
1.0 KEV TI(001)/AR + OX C2X2 (TI)
ATOMS PER SINGLE ION
FRACTION
0.0
0.1
0.2
0.3
0.4
0
10

Fig. 27.

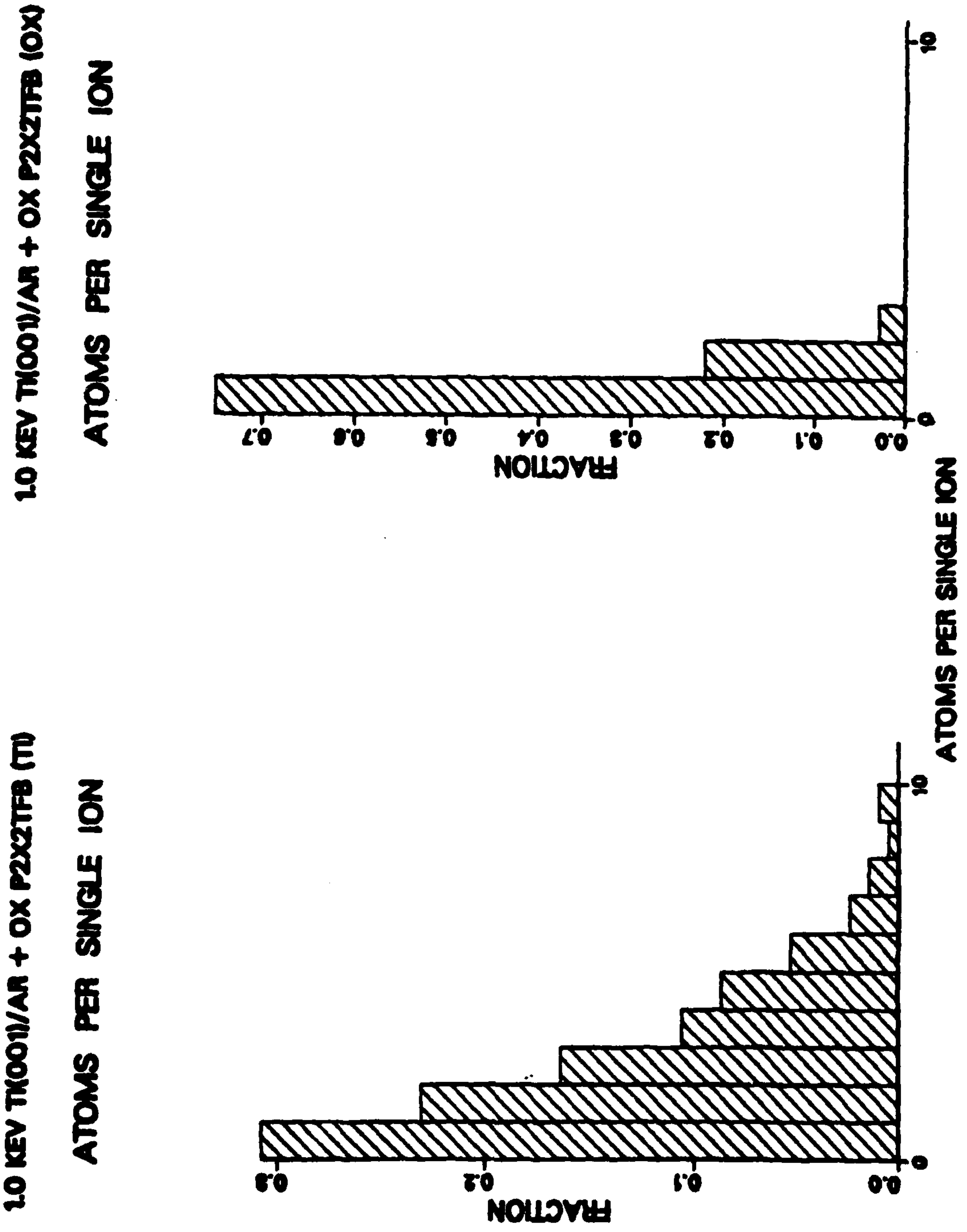
1.0 KEV TI(001)/AR + OX P2X2TFB (OX)
ATOMS PER SINGLE ION
FRACTION
0.0
0.1
0.2
0.3
0.4
0.5
0.6
0.7
0
10
ATOMS PER SINGLE ION
1.0 KEV TI(001)/AR + OX P2X2TFB (TI)
ATOMS PER SINGLE ION
FRACTION
0.0
0.1
0.2
0.3
0
10

Fig. 28.

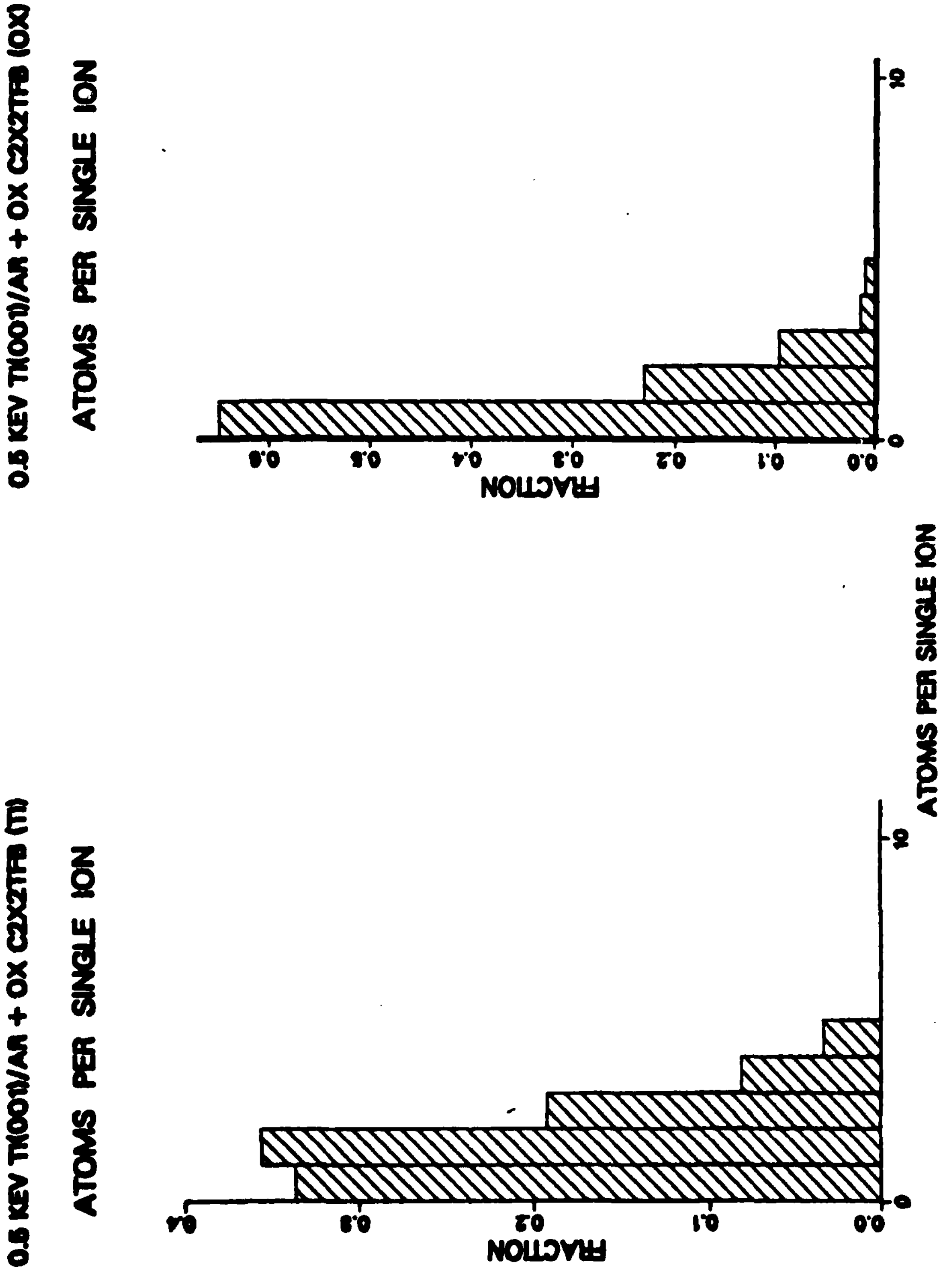
0.5 KEV TI(001)/AR + OX C2X2TFB (OX)
ATOMS PER SINGLE ION
FRACTION
0.0
0.1
0.2
0.3
0.4
0.5
0.6
0
10
ATOMS PER SINGLE ION
0.5 KEV TI(001)/AR + OX C2X2TFB (TI)
ATOMS PER SINGLE ION
FRACTION
0.0
0.1
0.2
0.3
0.4
0
10

Fig. 29.

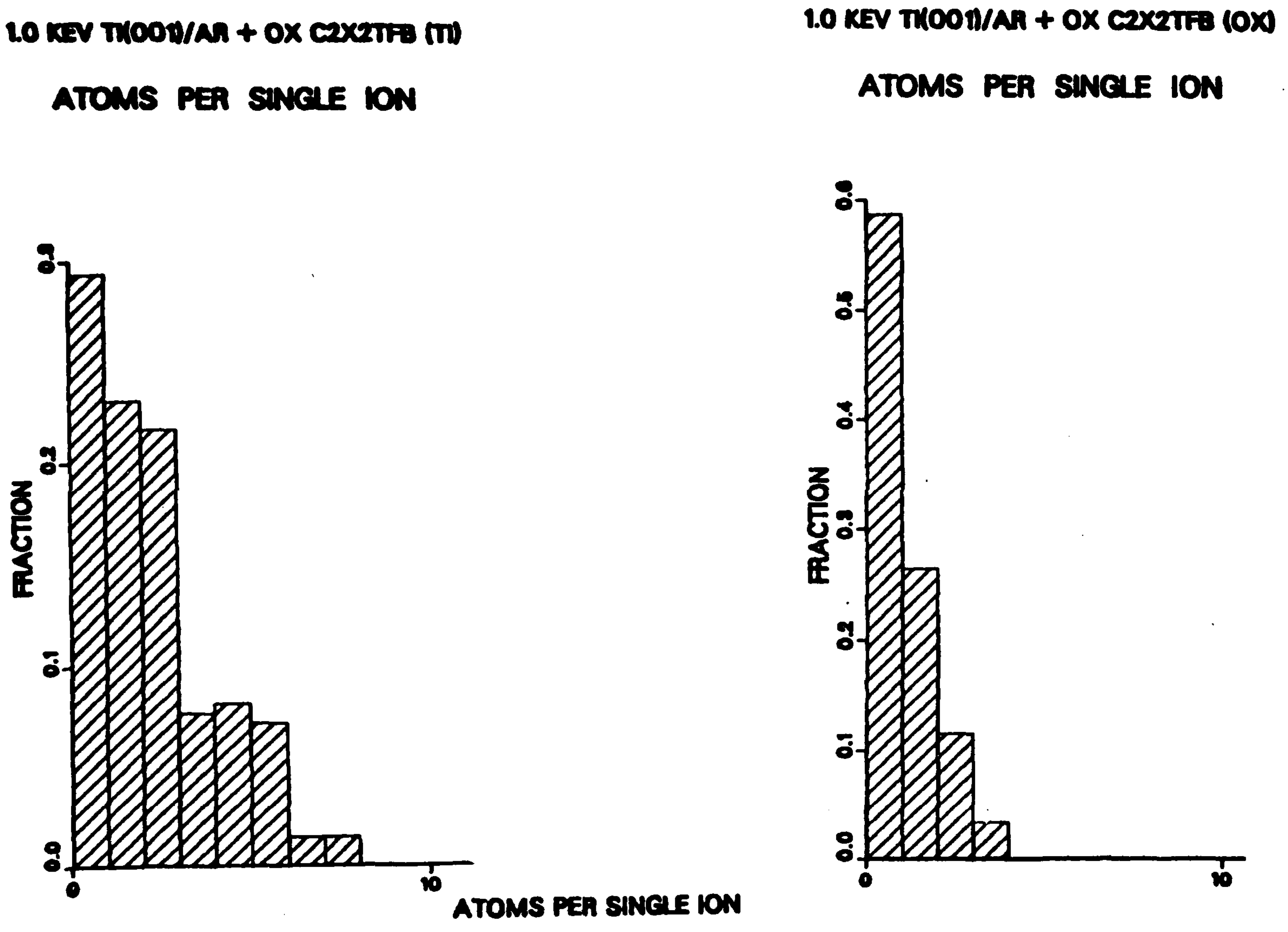

1.0 KEV TI(001)/AR + OX C2X2TFB (TI)

ATOMS PER SINGLE ION

1.0 KEV TI(001)/AR + OX C2X2TFB (OX)

ATOMS PER SINGLE ION

Fig. 30.

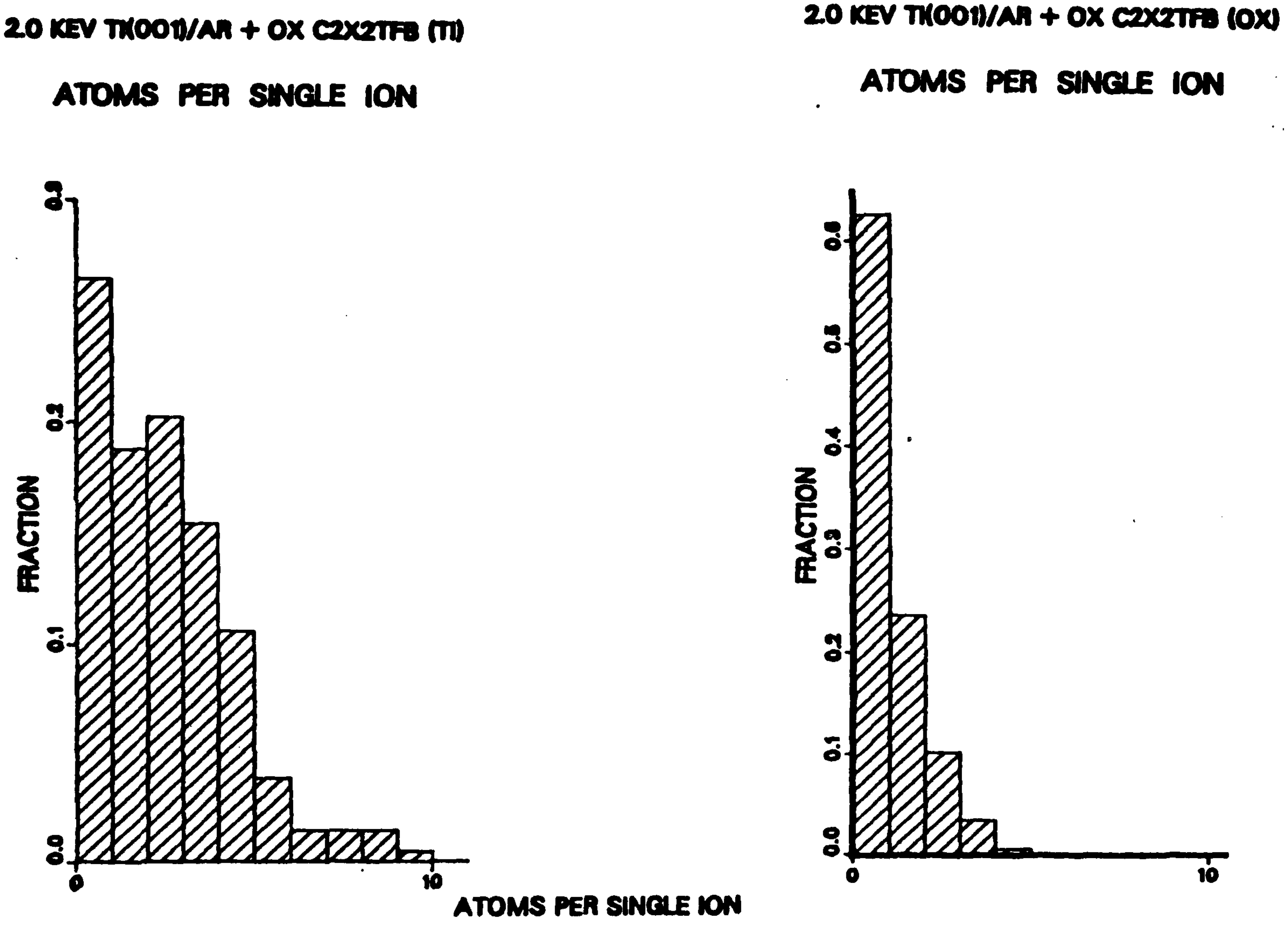
2.0 KEV TI(001)/AR + OX C2X2TFB (TI)
ATOMS PER SINGLE ION
FRACTION
0.0
0.1
0.2
0.3
0
10
ATOMS PER SINGLE ION
2.0 KEV TI(001)/AR + OX C2X2TFB (OX)
ATOMS PER SINGLE ION
FRACTION
0.0
0.1
0.2
0.3
0.4
0.5
0.6
0
10

Fig. 31.

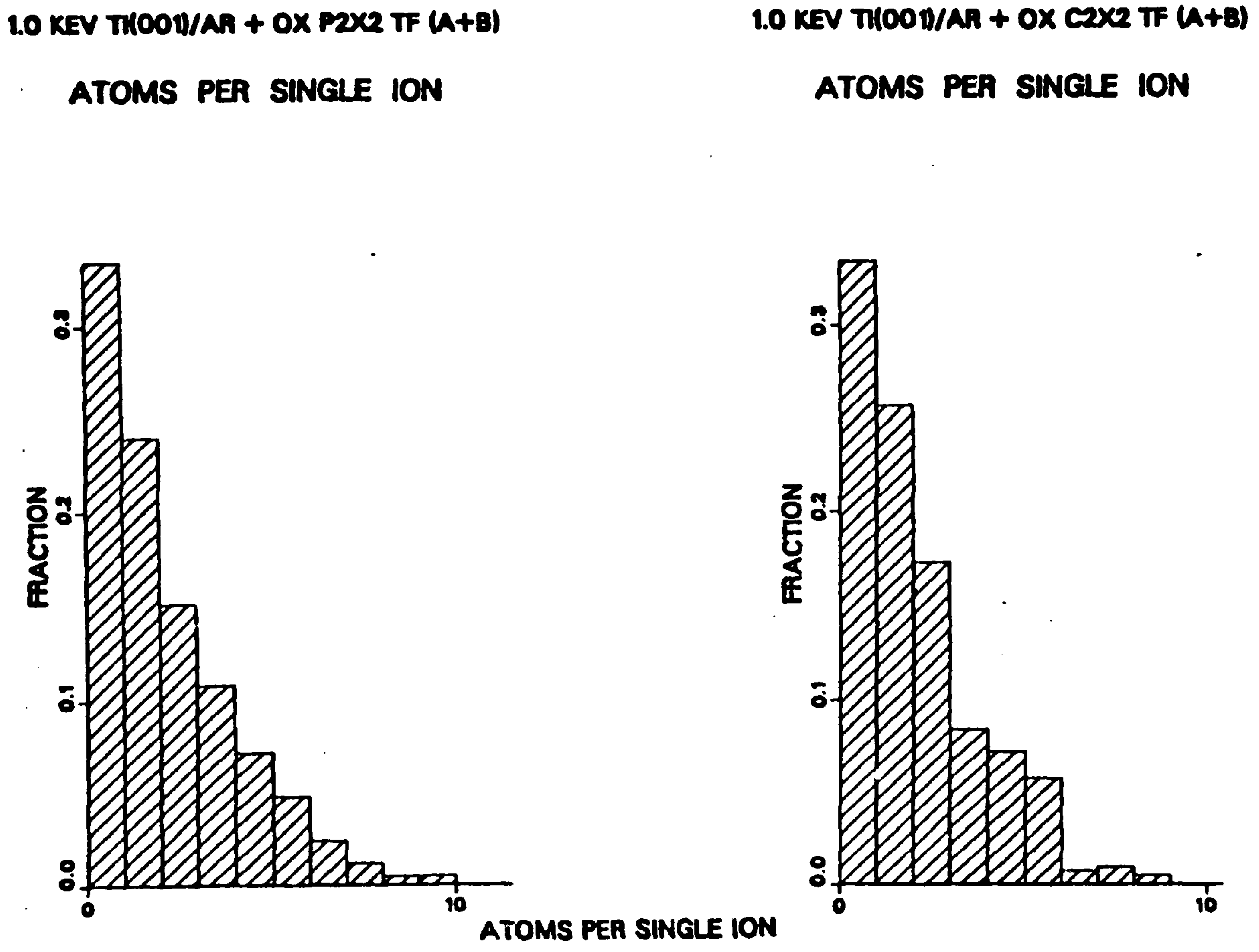
1.0 KEV TI(001)/AR + OX P2X2 TF (A+B)
ATOMS PER SINGLE ION
FRACTION
0.3
0.2
0.1
0.0
0
10
1.0 KEV TI(001)/AR + OX C2X2 TF (A+B)
ATOMS PER SINGLE ION
FRACTION
0.3
0.2
0.1
0.0
0
10
ATOMS PER SINGLE ION

Fig. 32.

APPENDIX C

ENERGY DISTRIBUTION CHARTS

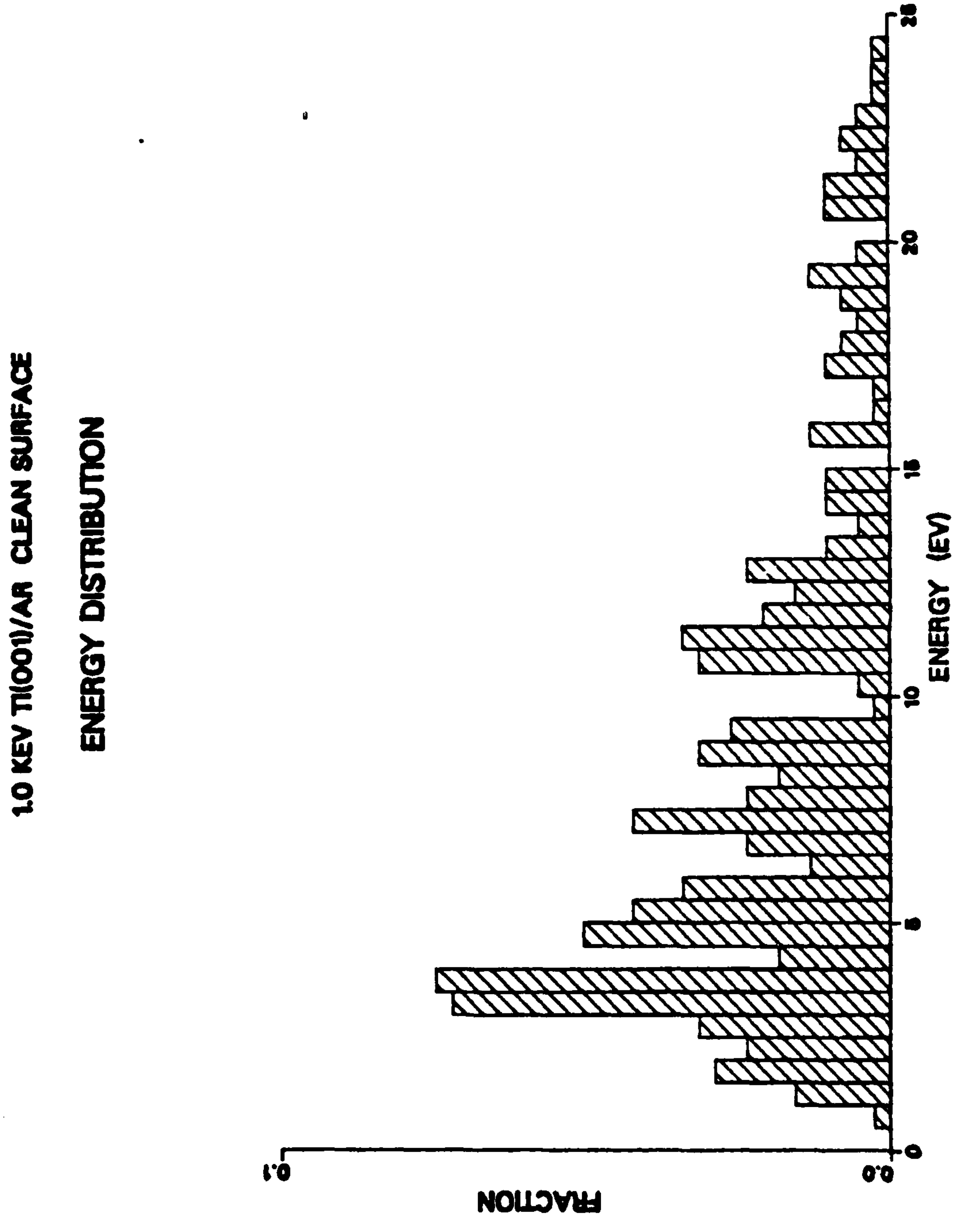

Fig. 33.

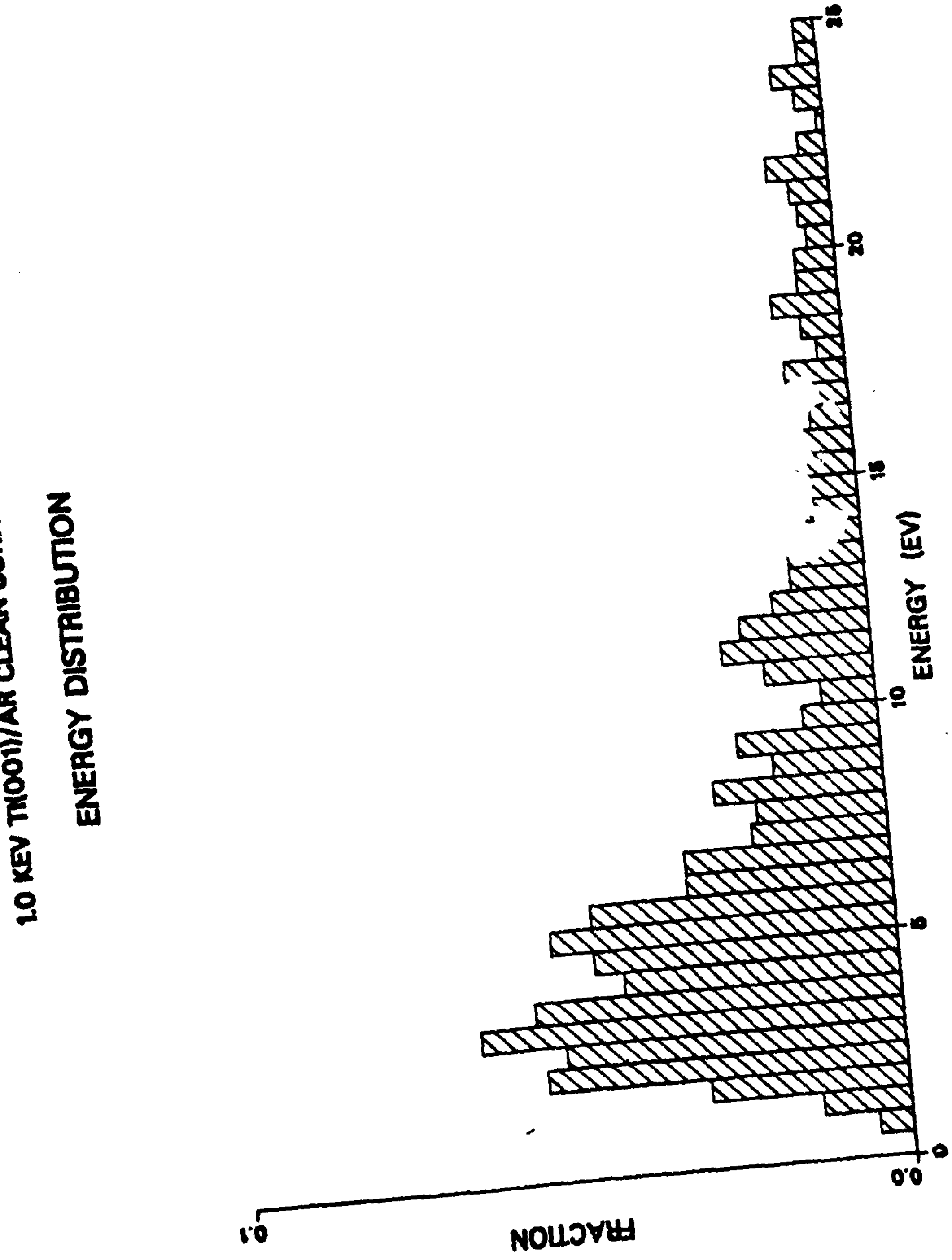

1.0 KEV Ti(001)/AR CLEAN SURFACE IPX5

ENERGY DISTRIBUTION

Fig. 34.

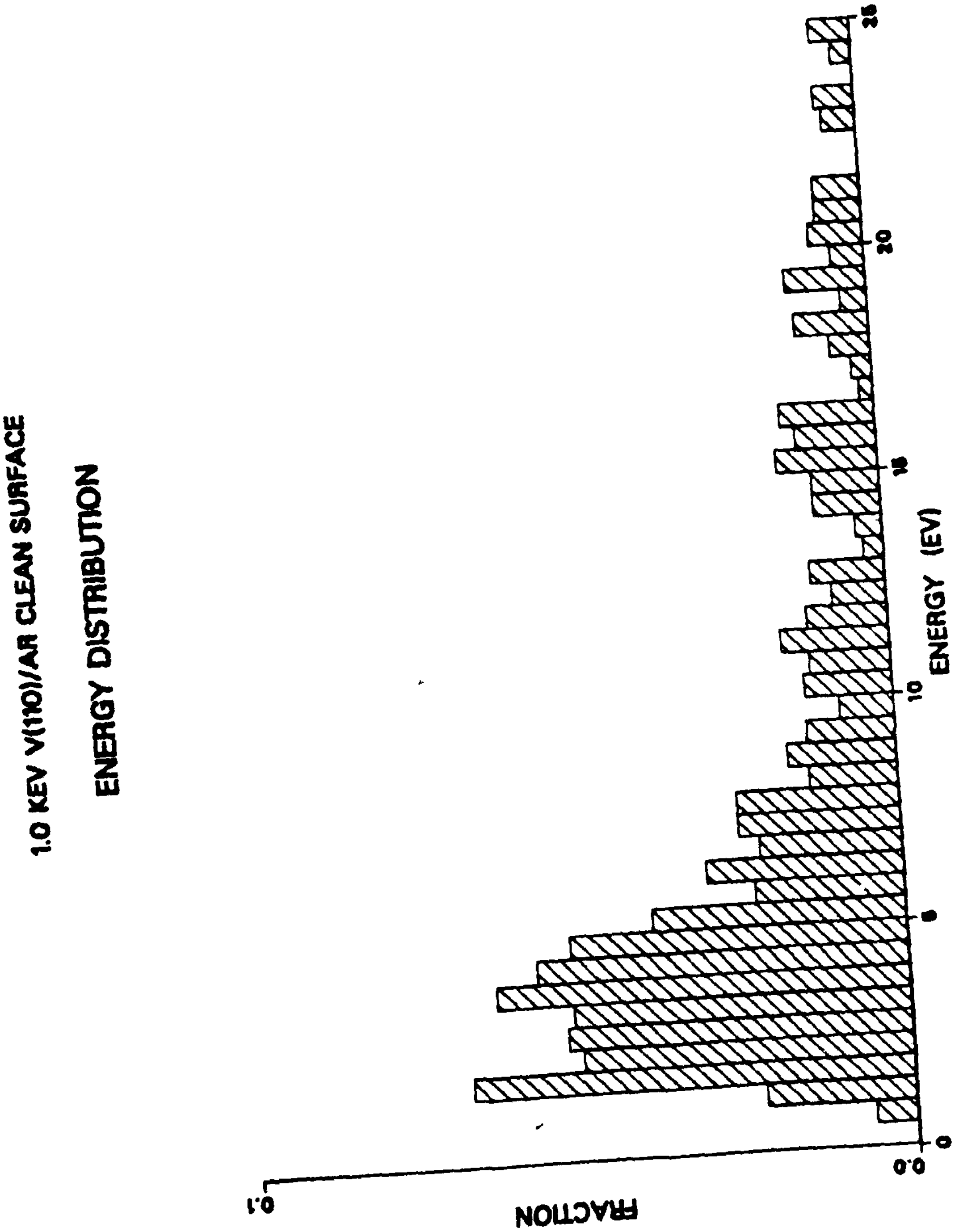
1.0 KEV V(110)/AR CLEAN SURFACE
ENERGY DISTRIBUTION
FRACTION
0.0
0.1
ENERGY (EV)
0
5
10
15
20
25

Fig. 35.

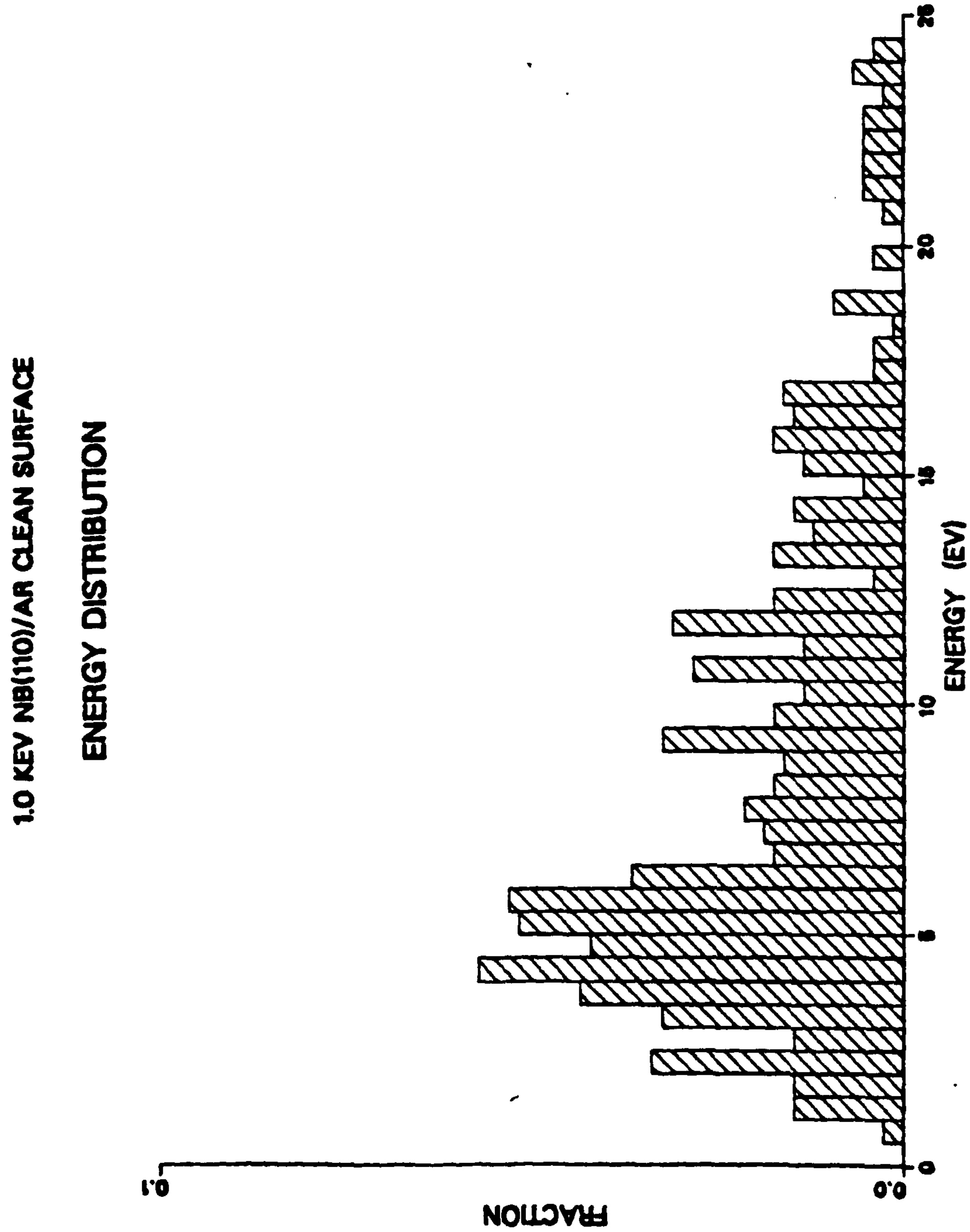
1.0 KEV NB(110)/AR CLEAN SURFACE
ENERGY DISTRIBUTION
FRACTION
0.0
0.1
ENERGY (EV)
0
5
10
15
20
25

Fig. 36.

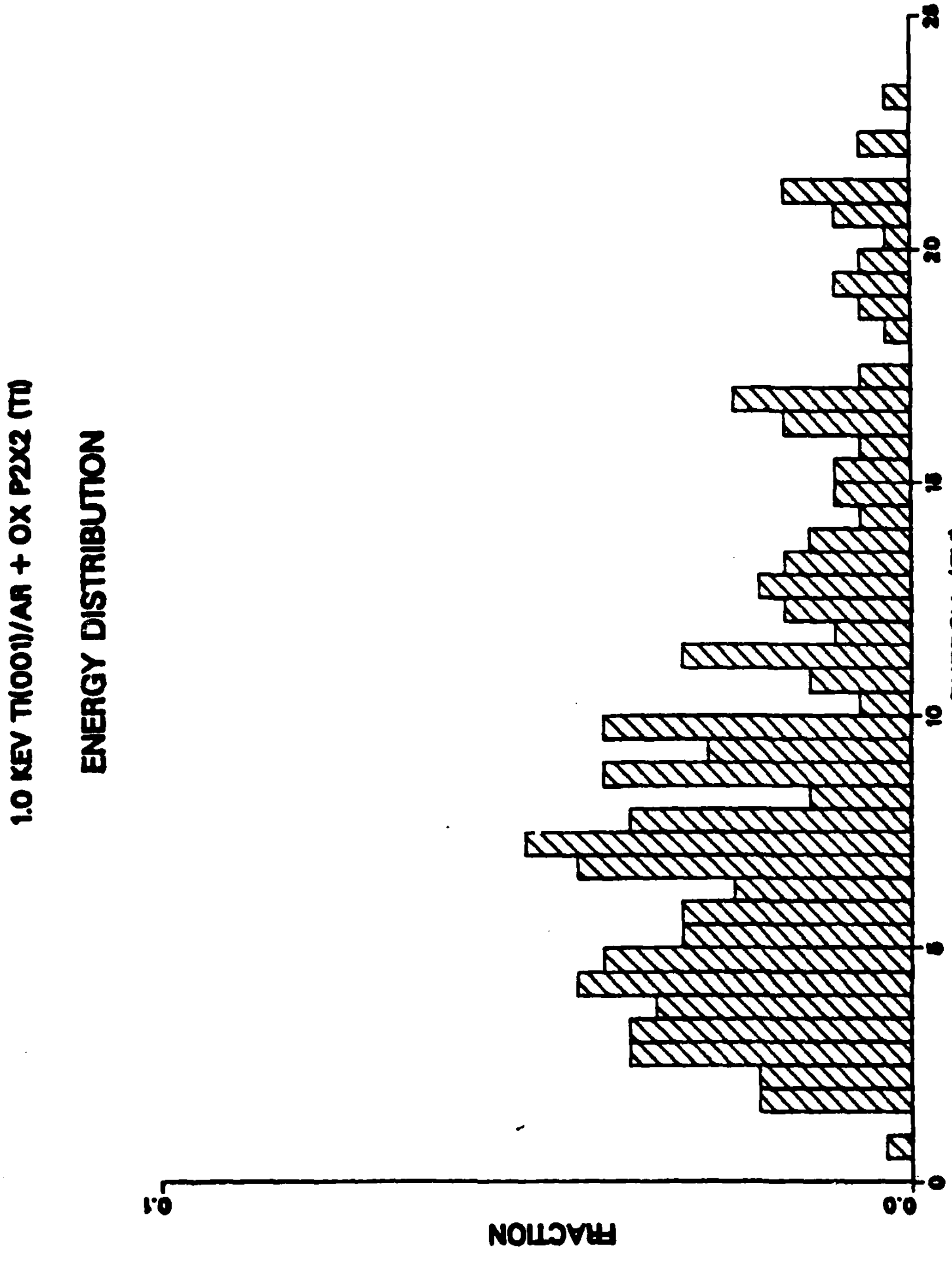
1.0 KEV Ti(001)/AR + OX P2X2 (Ti)
ENERGY DISTRIBUTION
FRACTION
0.0
0.1
ENERGY (EV)
0
5
10
15
20
25

Fig. 37.

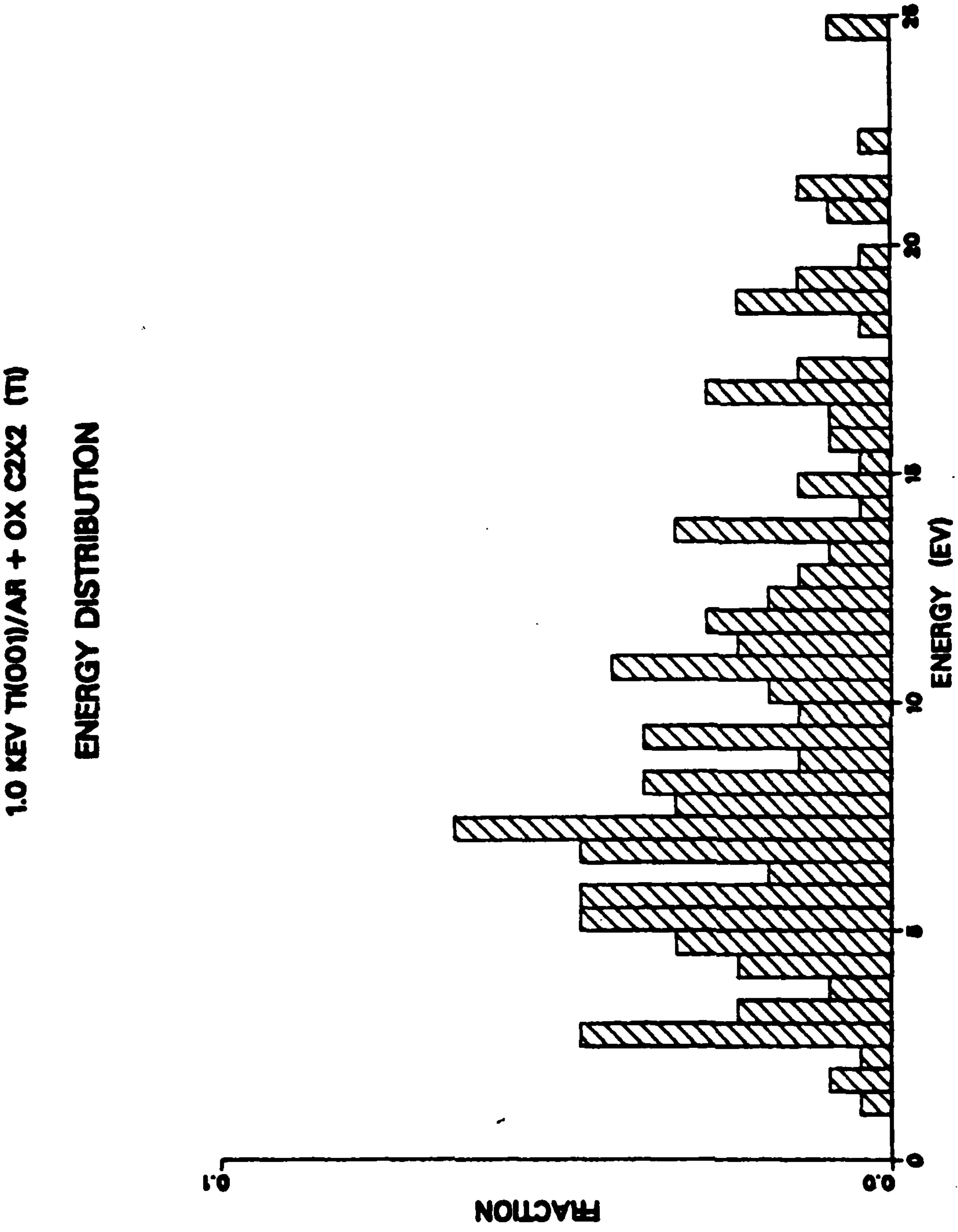
1.0 KEV Ti(001)/AR + OX C2X2 (TI)
ENERGY DISTRIBUTION
FRACTION
0.0
0.1
ENERGY (EV)
0
5
10
15
20
25

Fig. 38.

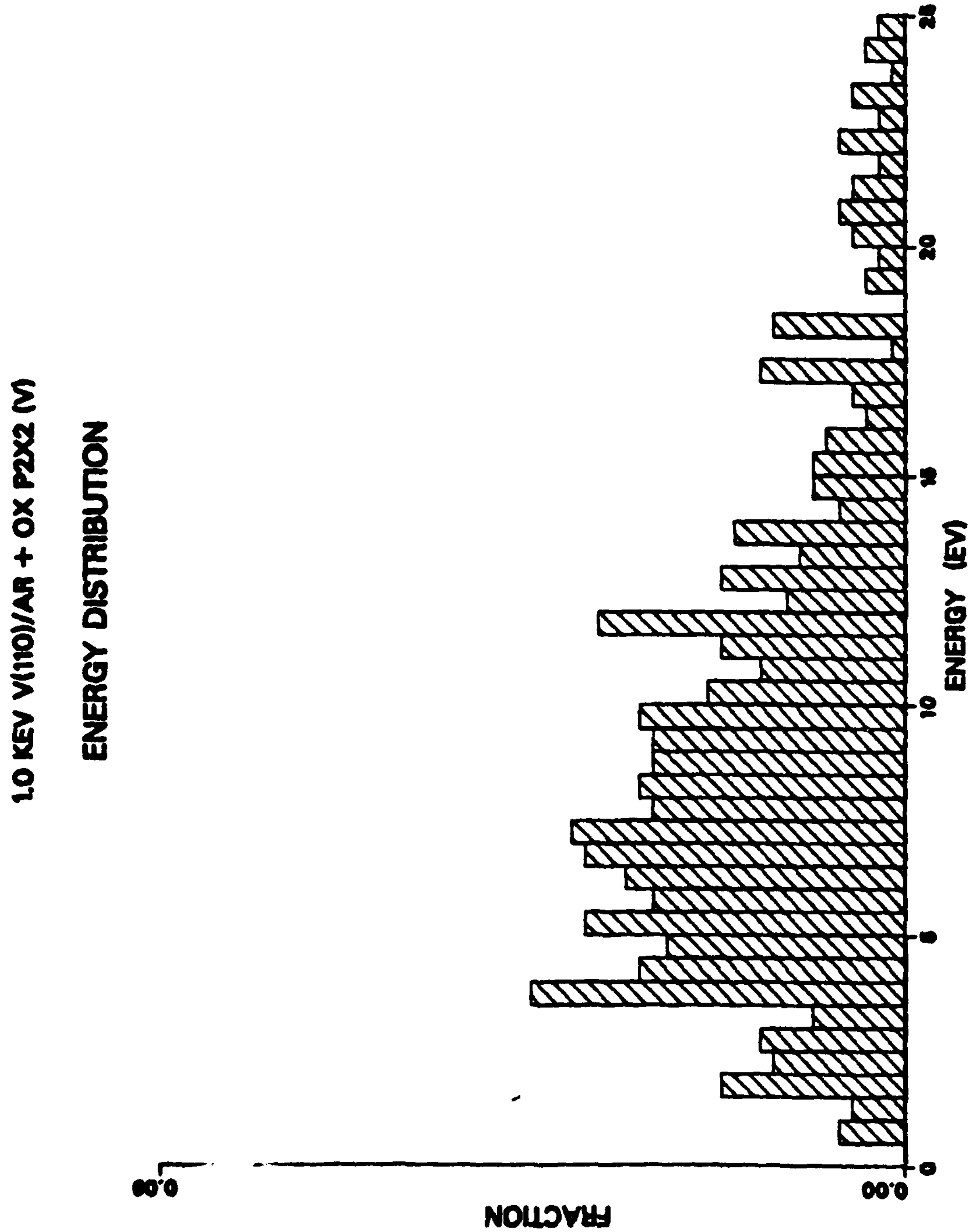1.0 KEV V(110)/AR + OX P2X2 (V)
ENERGY DISTRIBUTION
FRACTION
0.00
0.08
ENERGY (EV)
0
5
10
15
20
25

Fig. 39.

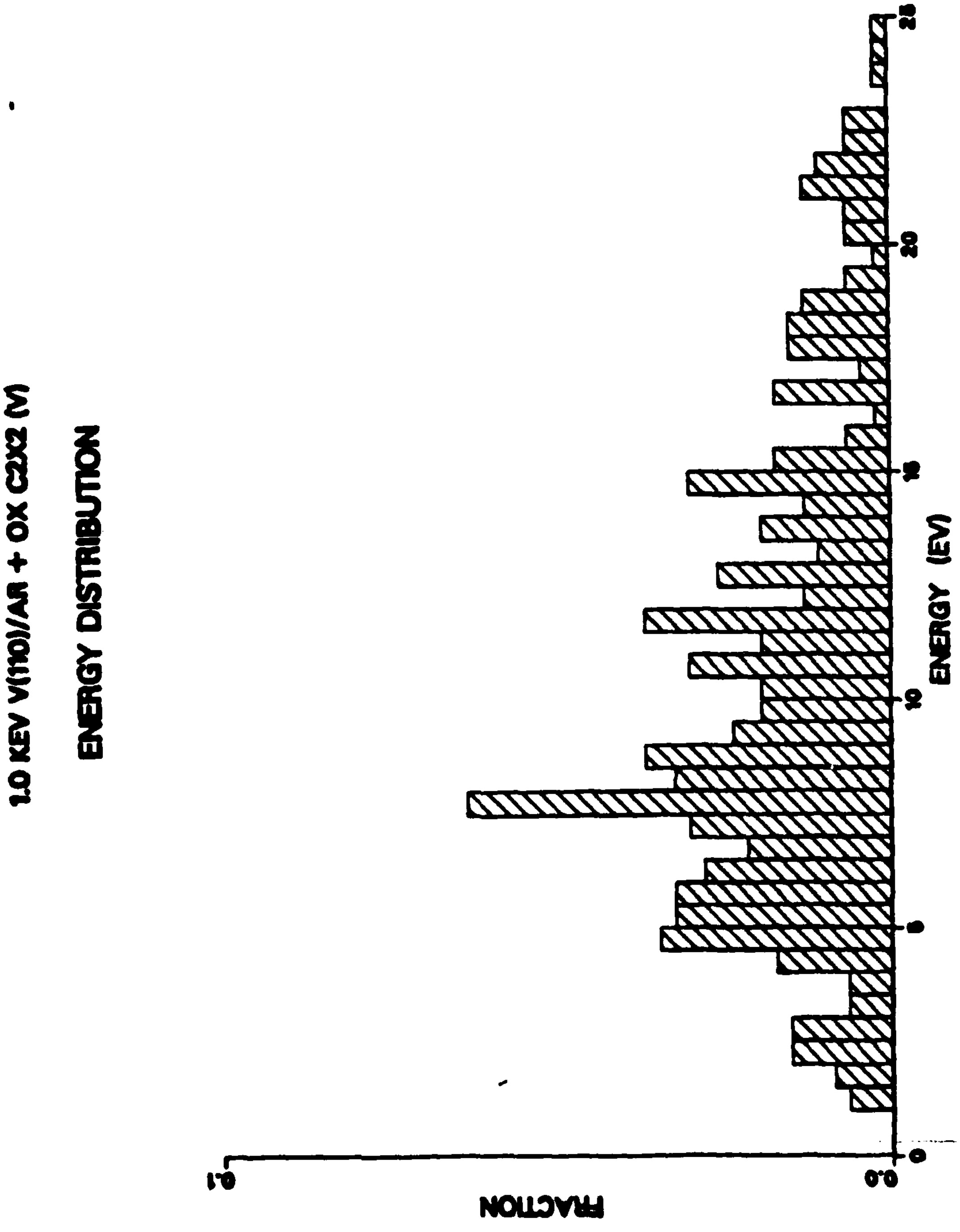
1.0 KEV V(110)/AR + OX C2X2 (V)
ENERGY DISTRIBUTION
FRACTION
0.0
0.1
ENERGY (EV)
0
5
10
15
20
25

Fig. 40.

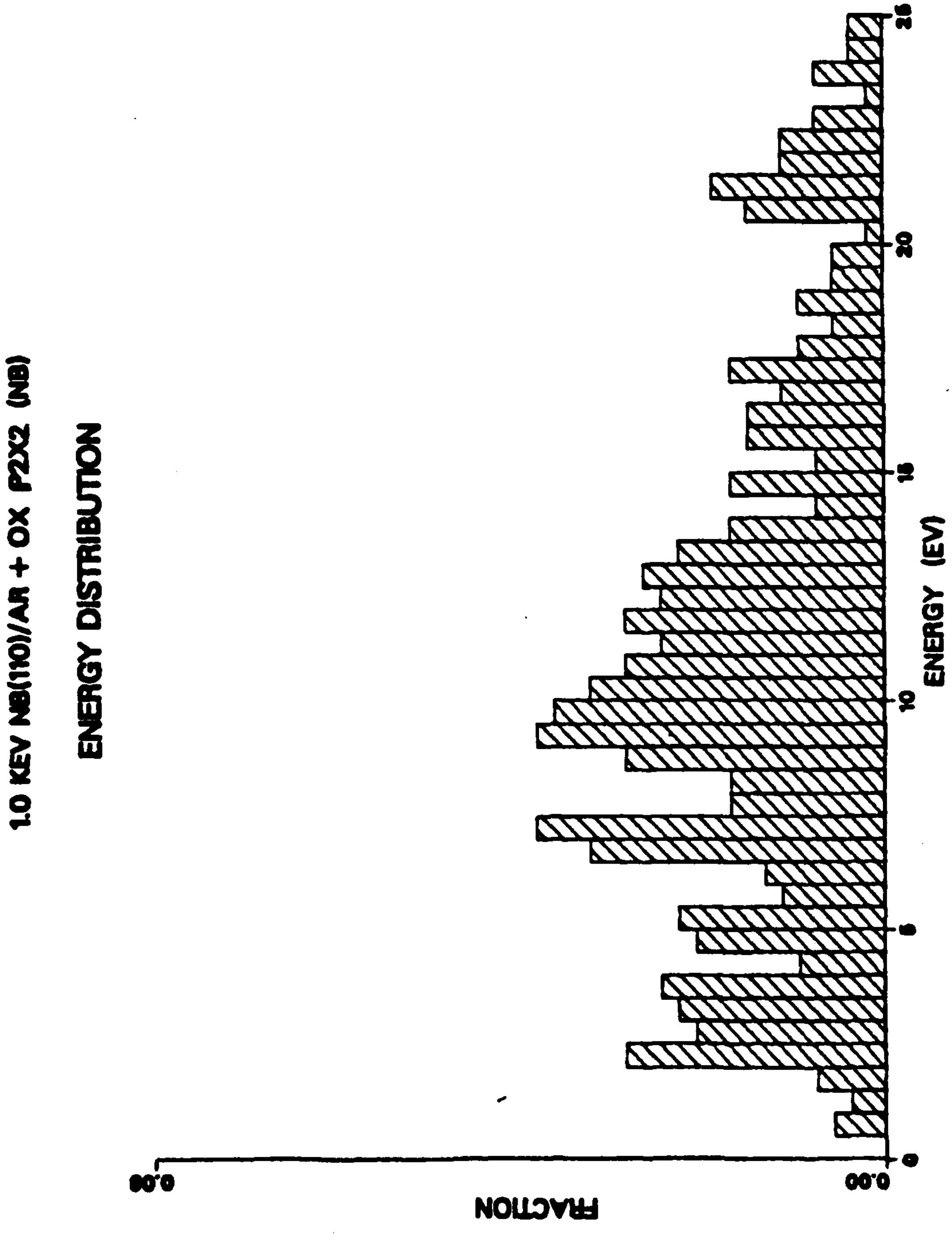
1.0 KEV NB(110)/AR + OX P2X2 (NB)
ENERGY DISTRIBUTION
FRACTION
0.00
0.08
ENERGY (EV)
0
5
10
15
20
25

Fig. 41.

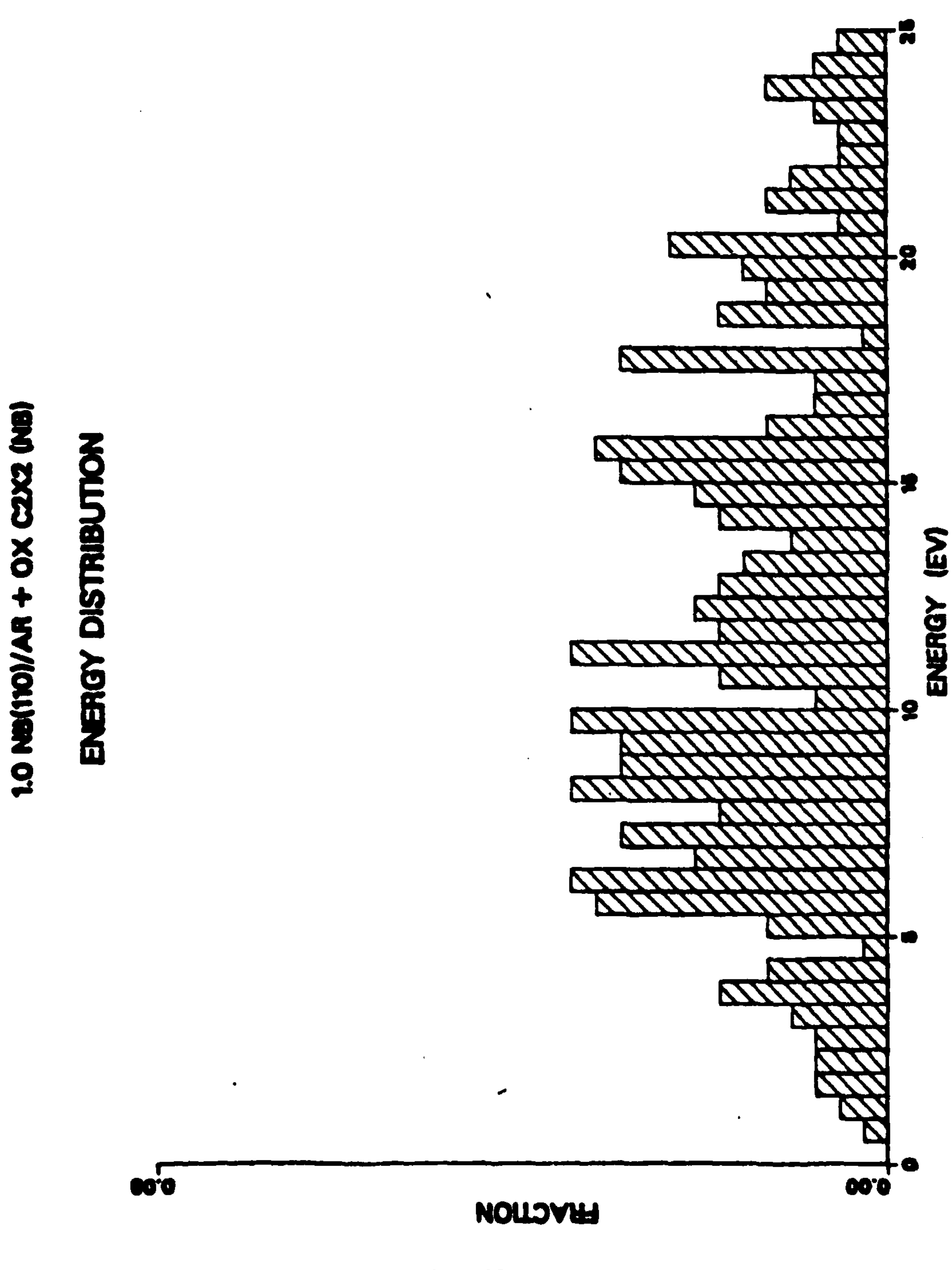
1.0 NB(110)/AR + OX C2X2 (NB)
ENERGY DISTRIBUTION
FRACTION
0.00
0.08
ENERGY (EV)
0
5
10
15
20
25

Fig. 42.

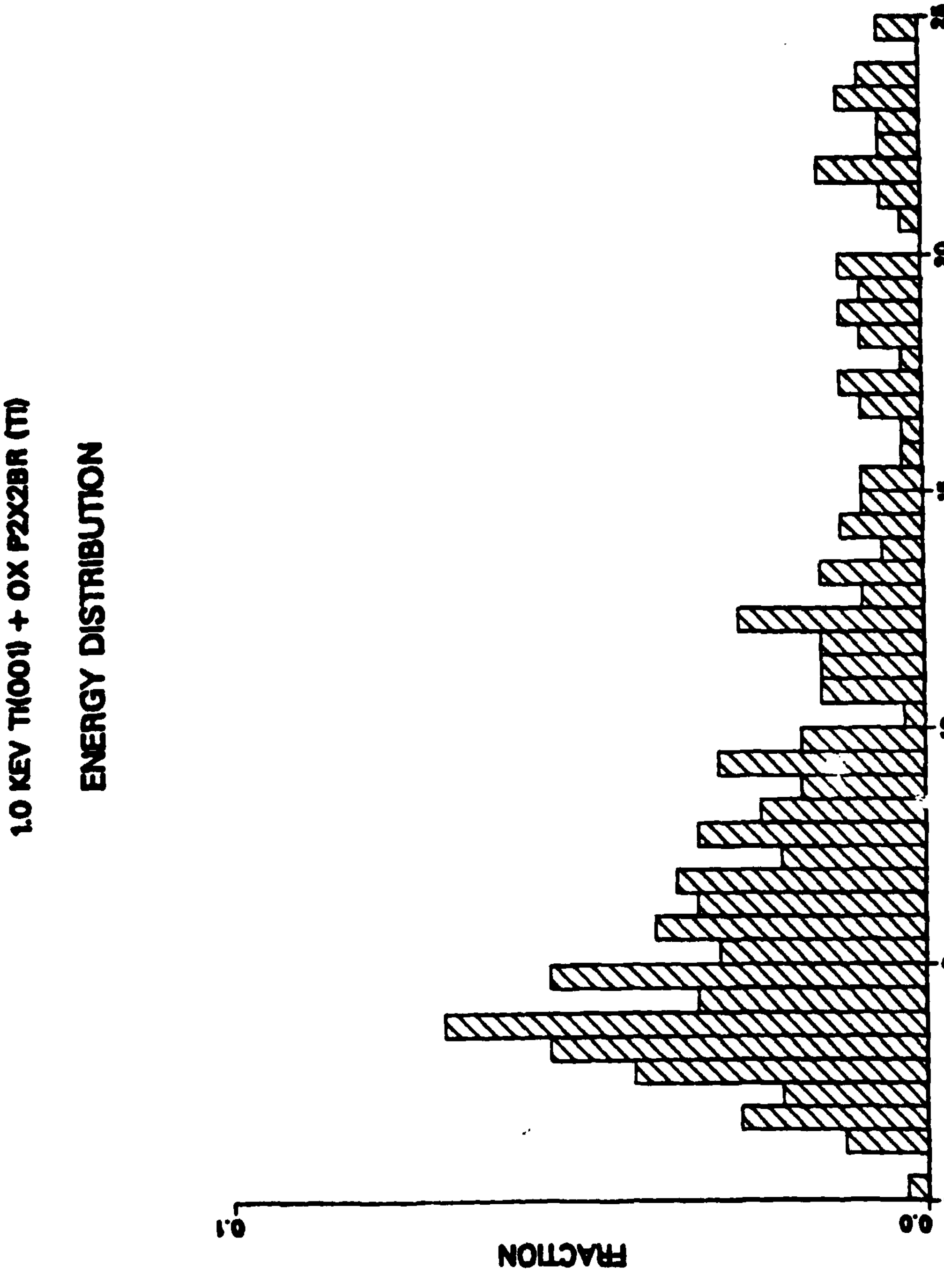
1.0 KEV Ti(001) + OX P2X2BR (Ti)
ENERGY DISTRIBUTION
FRACTION
0.0
0.1
ENERGY (EV)
0
5
10
15
20
25

Fig. 43.

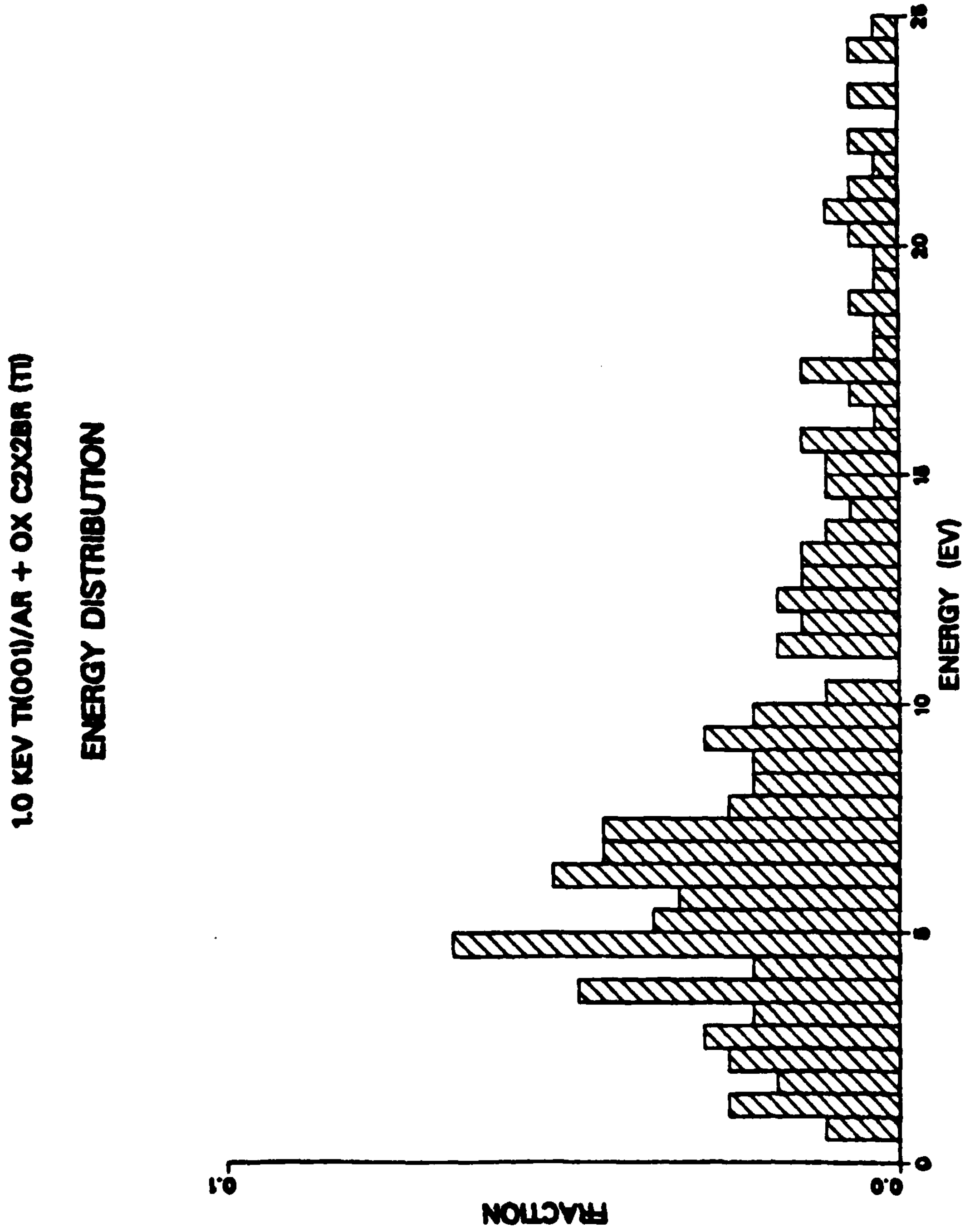
1.0 KEV TI(001)/AR + OX C2X2BR (TI)
ENERGY DISTRIBUTION
FRACTION
0.0
0.1
ENERGY (EV)
0
5
10
15
20
25

Fig. 44.

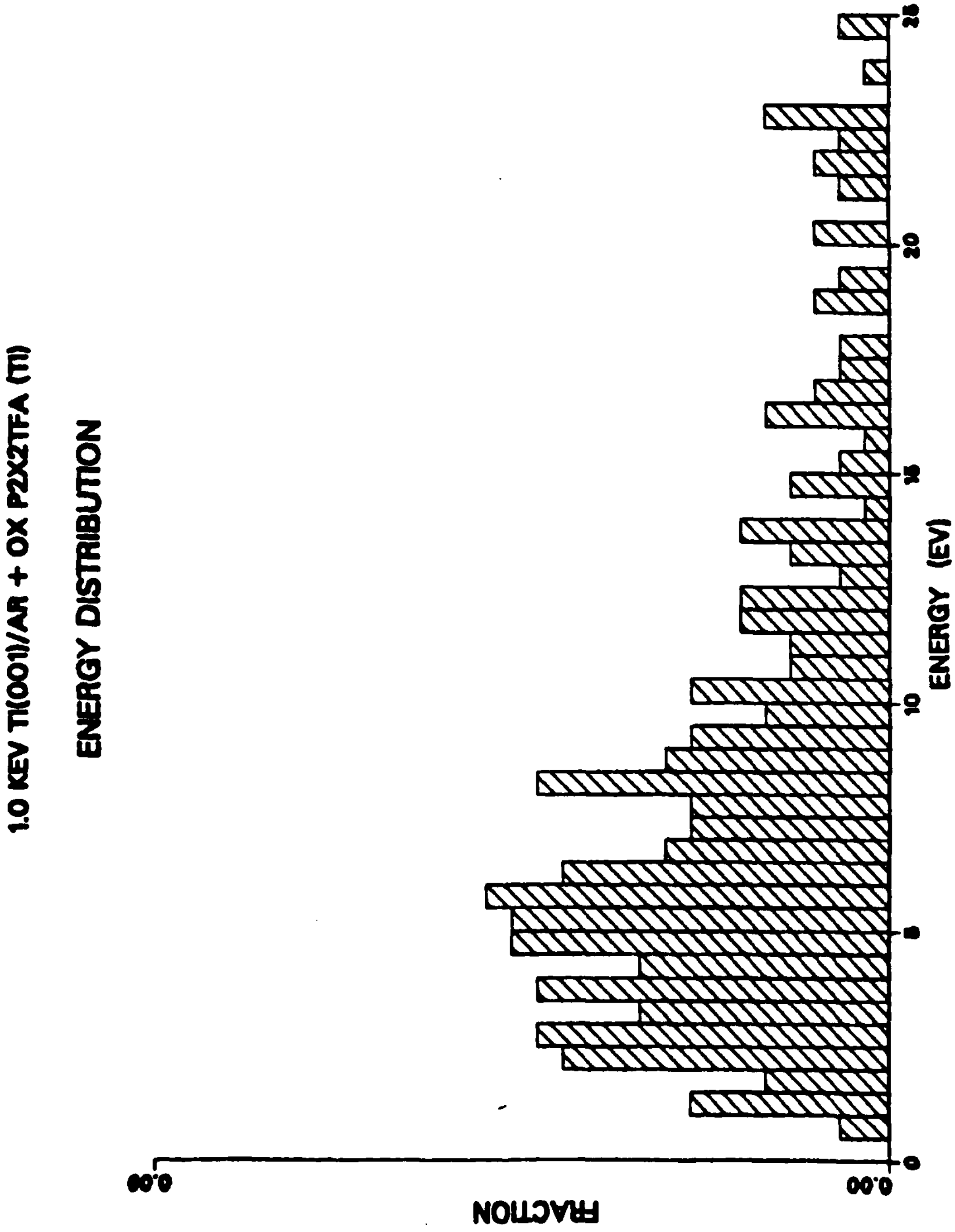
1.0 KEV Ti(001)/AR + OX P2X2TFA (Ti)
ENERGY DISTRIBUTION
FRACTION
0.00
0.09
ENERGY (EV)
0
5
10
15
20
25

Fig. 45.

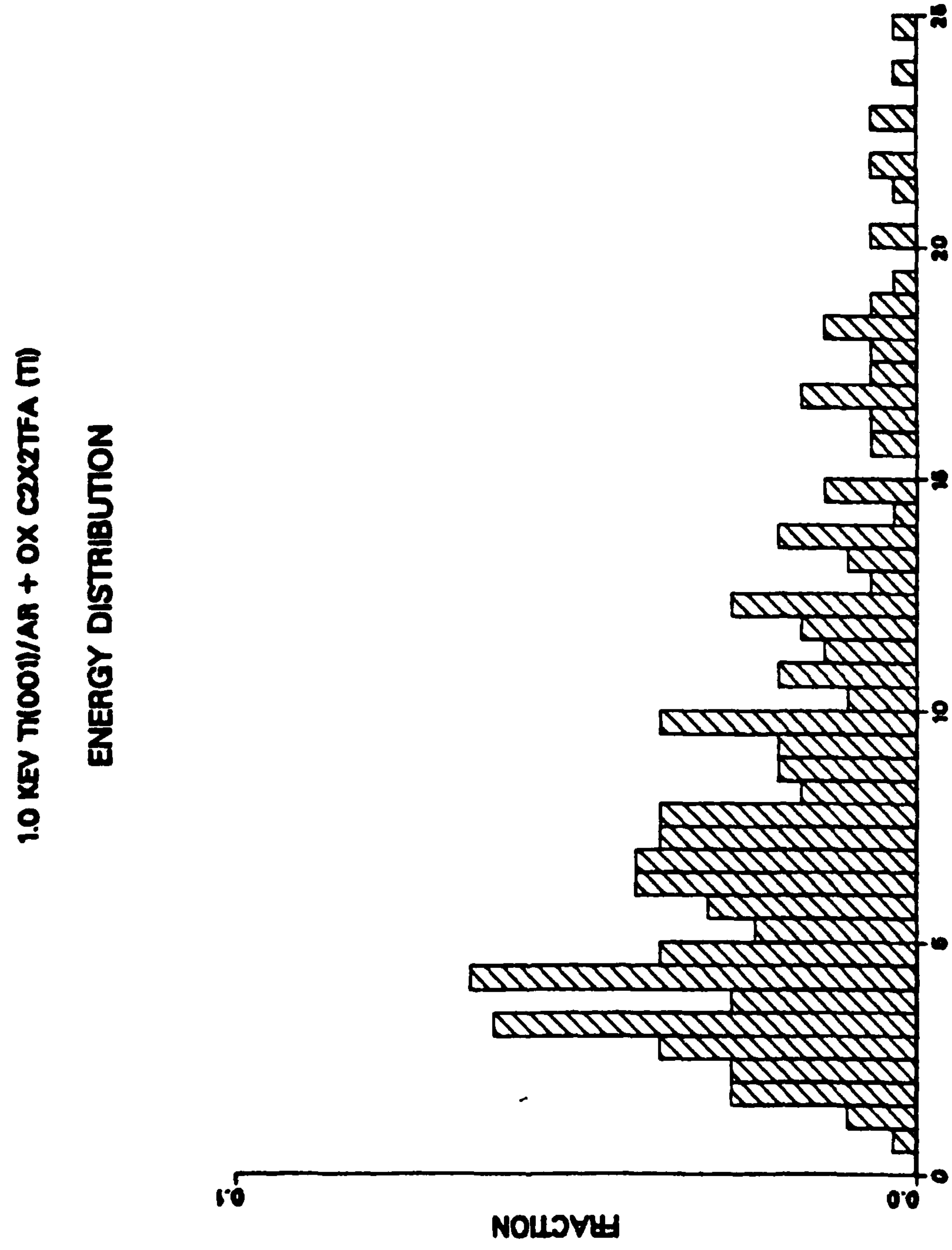
1.0 KEV Ti(001)/AR + OX C2X2TFA (TI)
ENERGY DISTRIBUTION
FRACTION
0.0
0.1
ENERGY (EV)
0
5
10
15
20
25

Fig. 46.

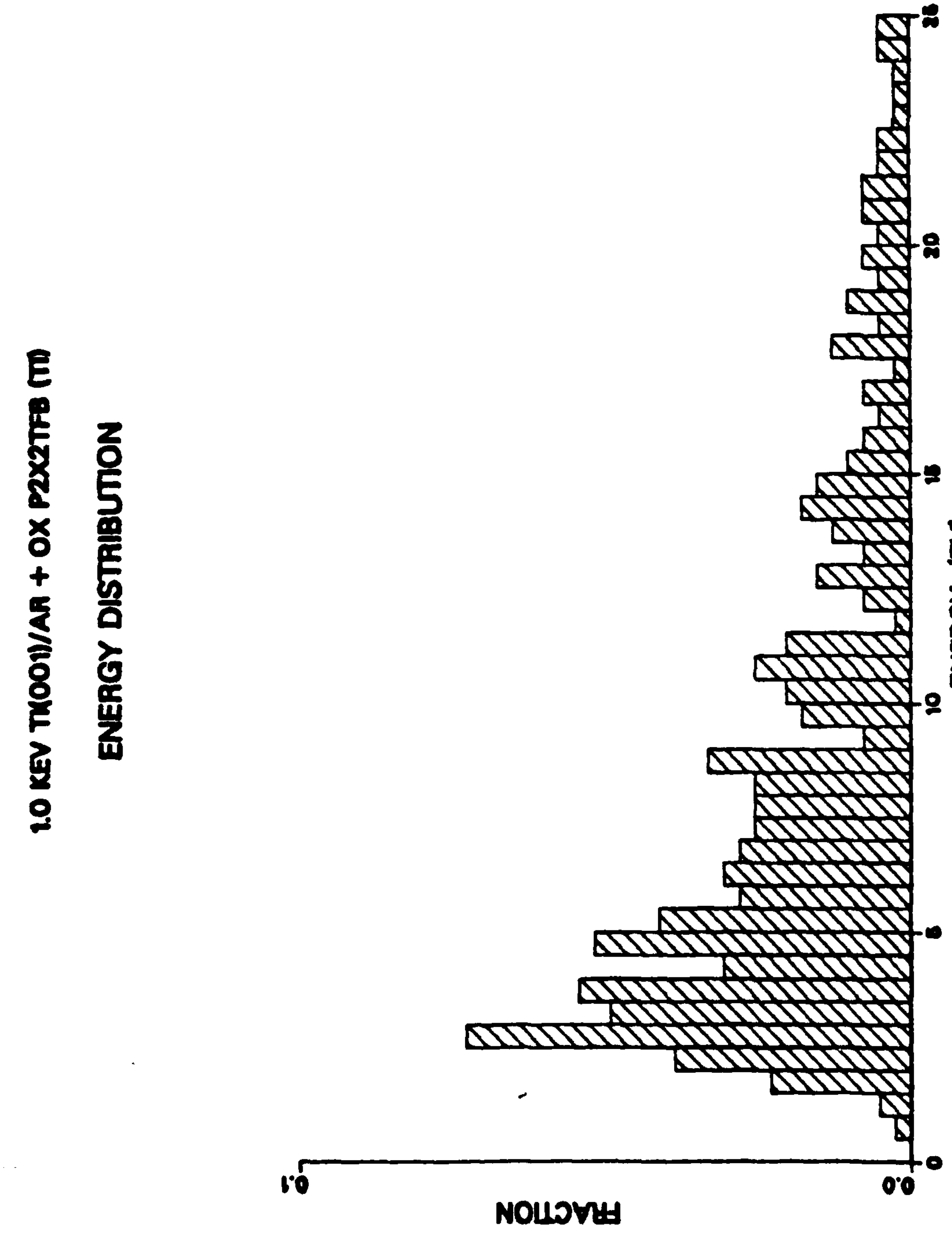
1.0 KEV TI(001)/AR + OX P2X2TFB (TI)
ENERGY DISTRIBUTION
FRACTION
0.1
0.0
0
5
10
15
20
25
ENERGY (EV)

Fig. 47.

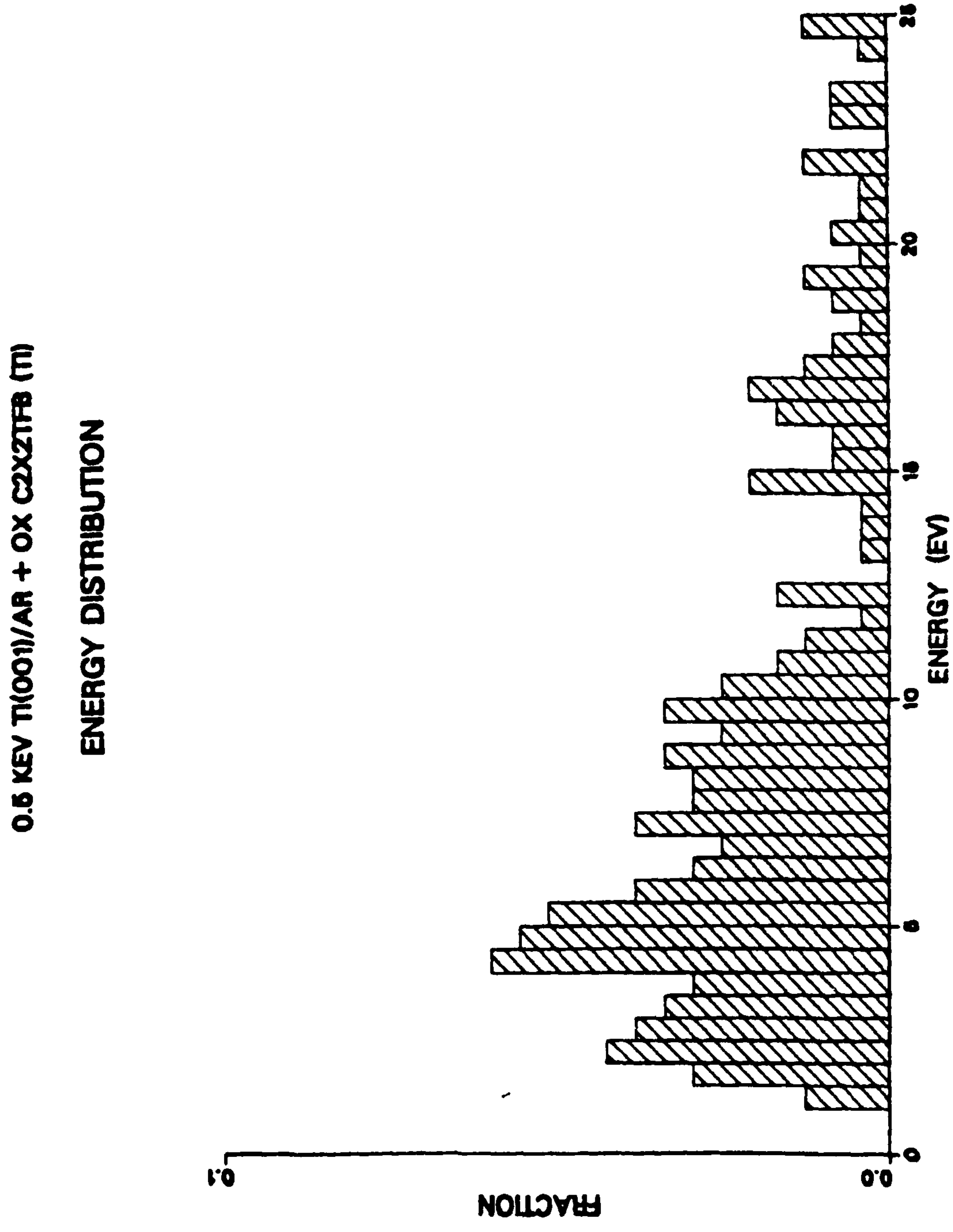
0.5 KEV TI(001)/AR + OX C2X2TFB (TI)
ENERGY DISTRIBUTION
FRACTION
0.0
0.1
ENERGY (EV)
0
5
10
15
20
25

Fig. 48.

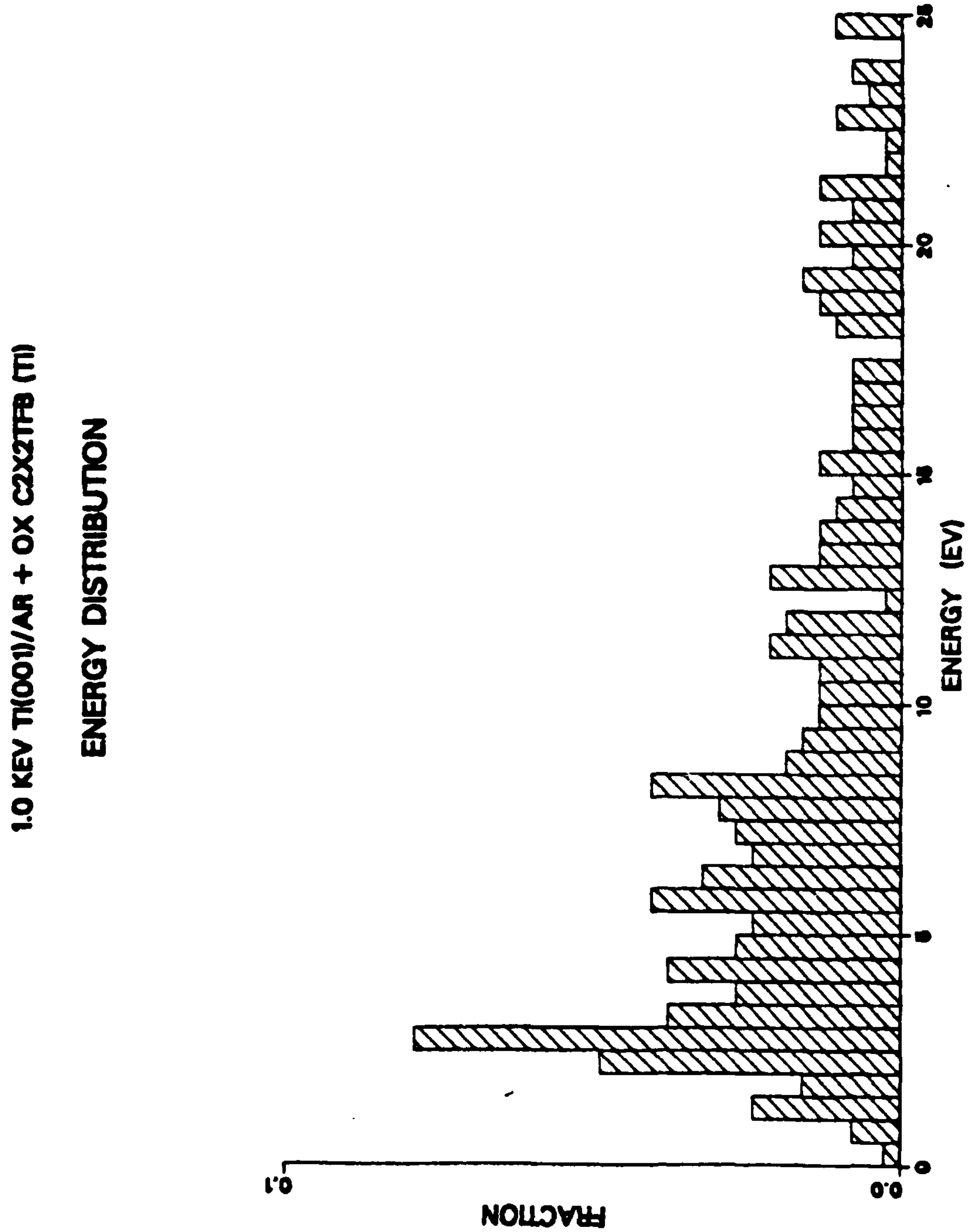
1.0 KEV TI(001)/AR + OX C2X2TFB (TI)
ENERGY DISTRIBUTION
FRACTION
0.0
0.1
ENERGY (EV)
0
5
10
15
20
25

Fig. 49.

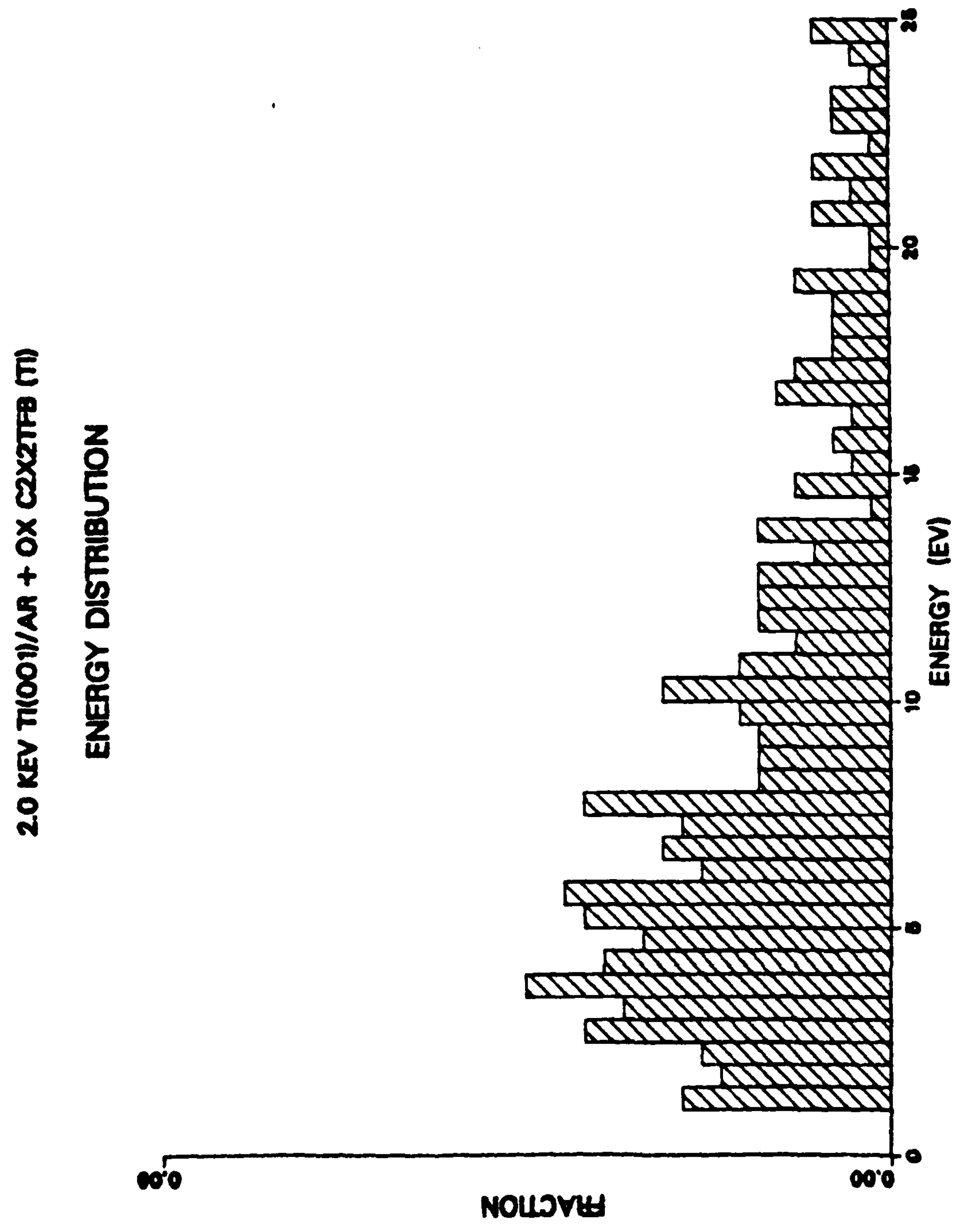
2.0 KEV TI(001)/AR + OX C2X2TFB (TI)
ENERGY DISTRIBUTION
FRACTION
0.00
0.08
ENERGY (EV)
0
5
10
15
20
25

Fig. 50.

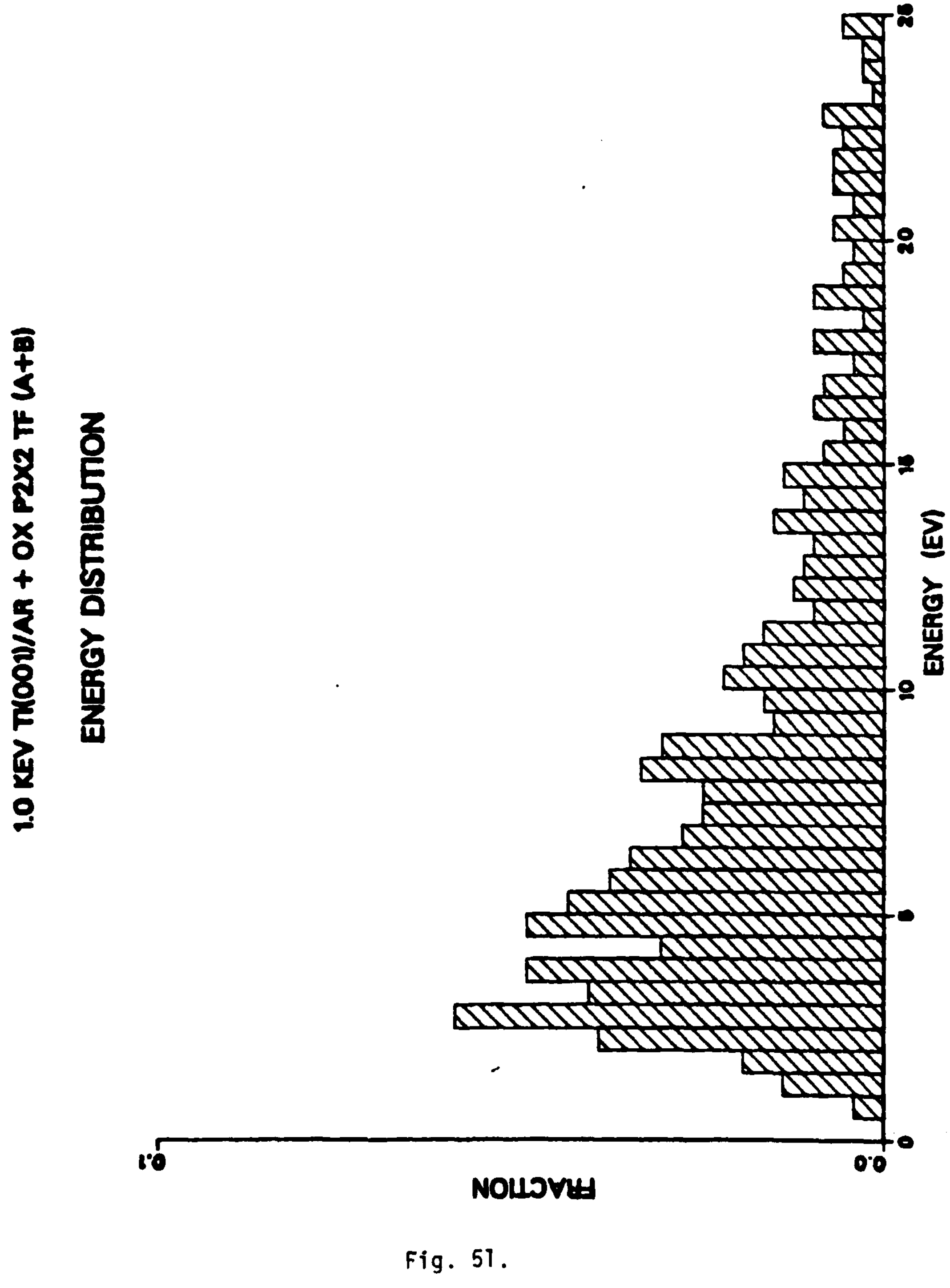
1.0 KEV TI(001)/AR + OX P2X2 TF (A+B)
ENERGY DISTRIBUTION
FRACTION
0.0
0.1
ENERGY (EV)
0
5
10
15
20
25

Fig. 51.

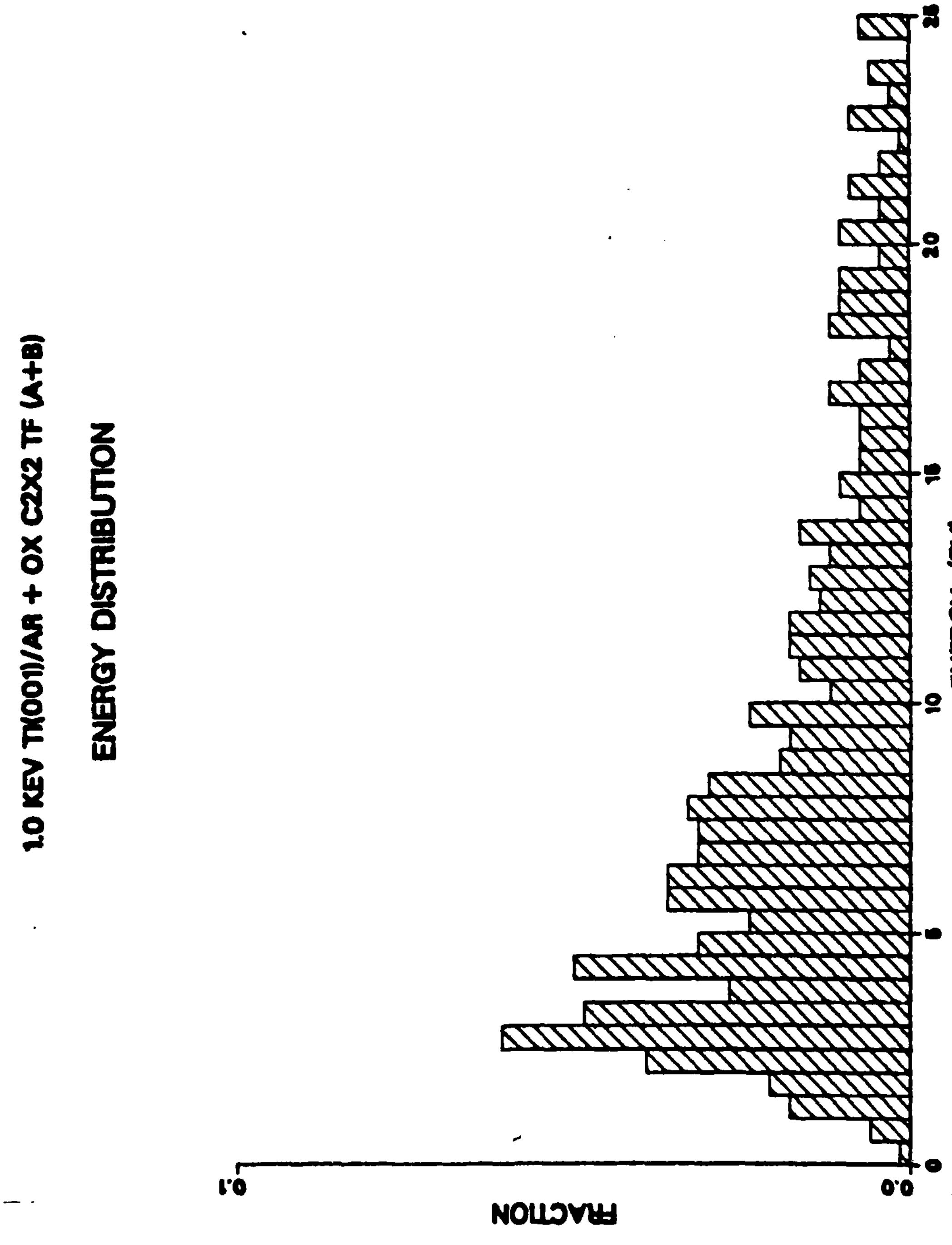
1.0 KEV TI(001)/AR + OX C2X2 TF (A+B)
ENERGY DISTRIBUTION
FRACTION
0.0
0.1
ENERGY (EV)
0
5
10
15
20
25

Fig. 52.

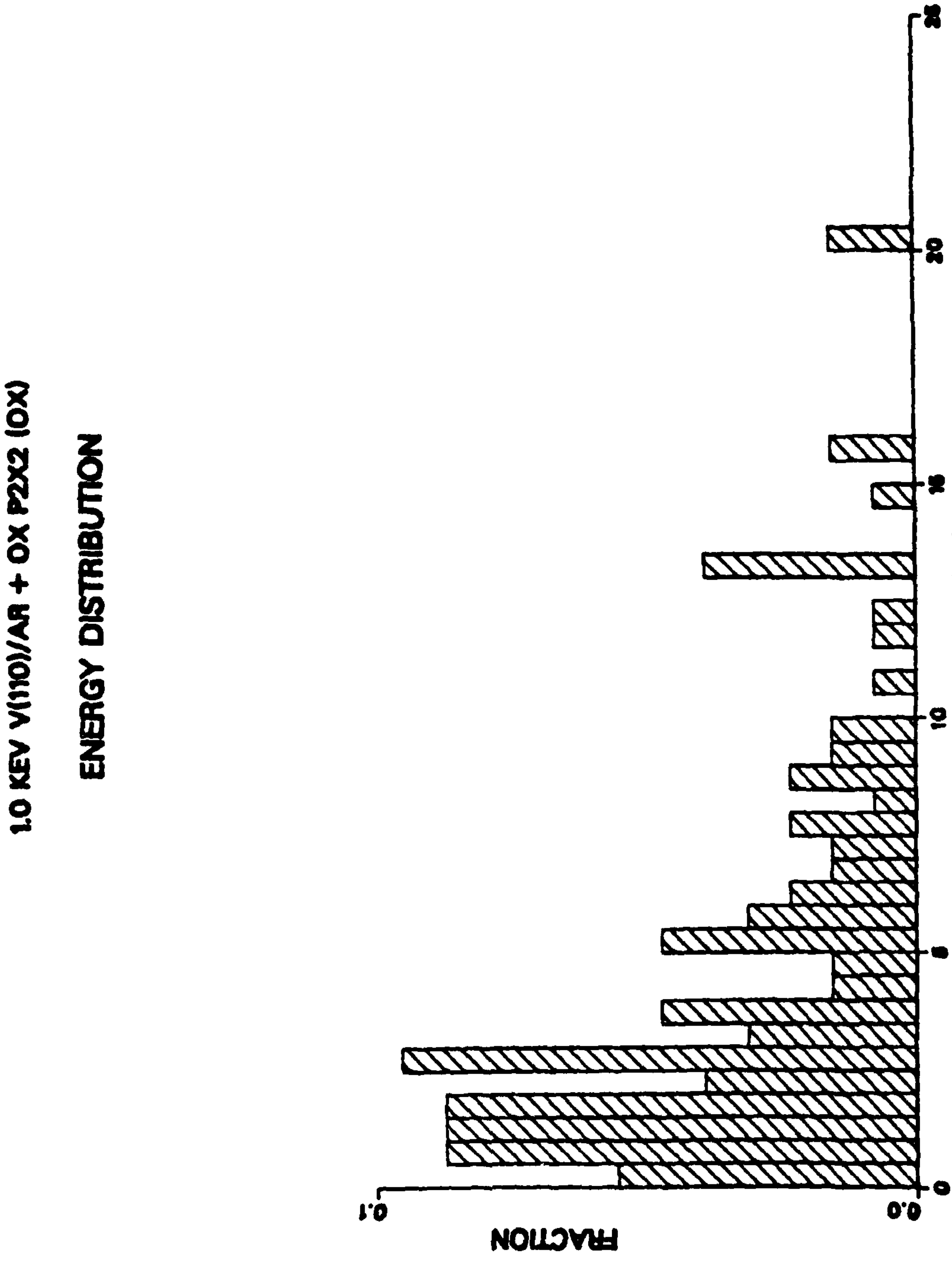
1.0 KEV V(110)/AR + OX P2X2 (OX)
ENERGY DISTRIBUTION
FRACTION
0.0
0.1
ENERGY (EV)
0
5
10
15
20
25

Fig. 53.

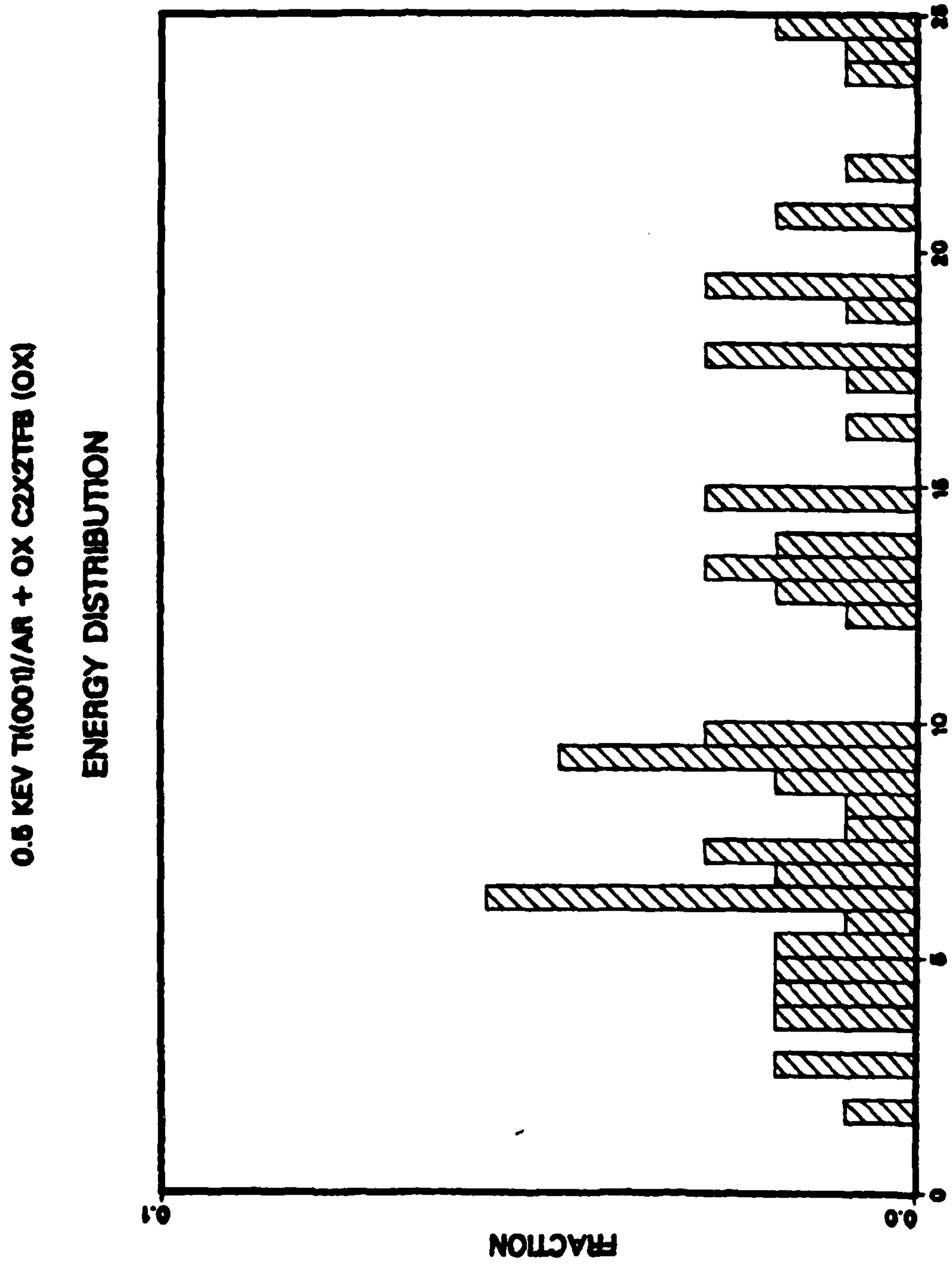
0.5 KEV TI(001)/AR + OX C2X2TFB (OX)
ENERGY DISTRIBUTION
FRACTION
0.0
0.1
ENERGY (EV)
0
5
10
15
20
25

Fig. 54.

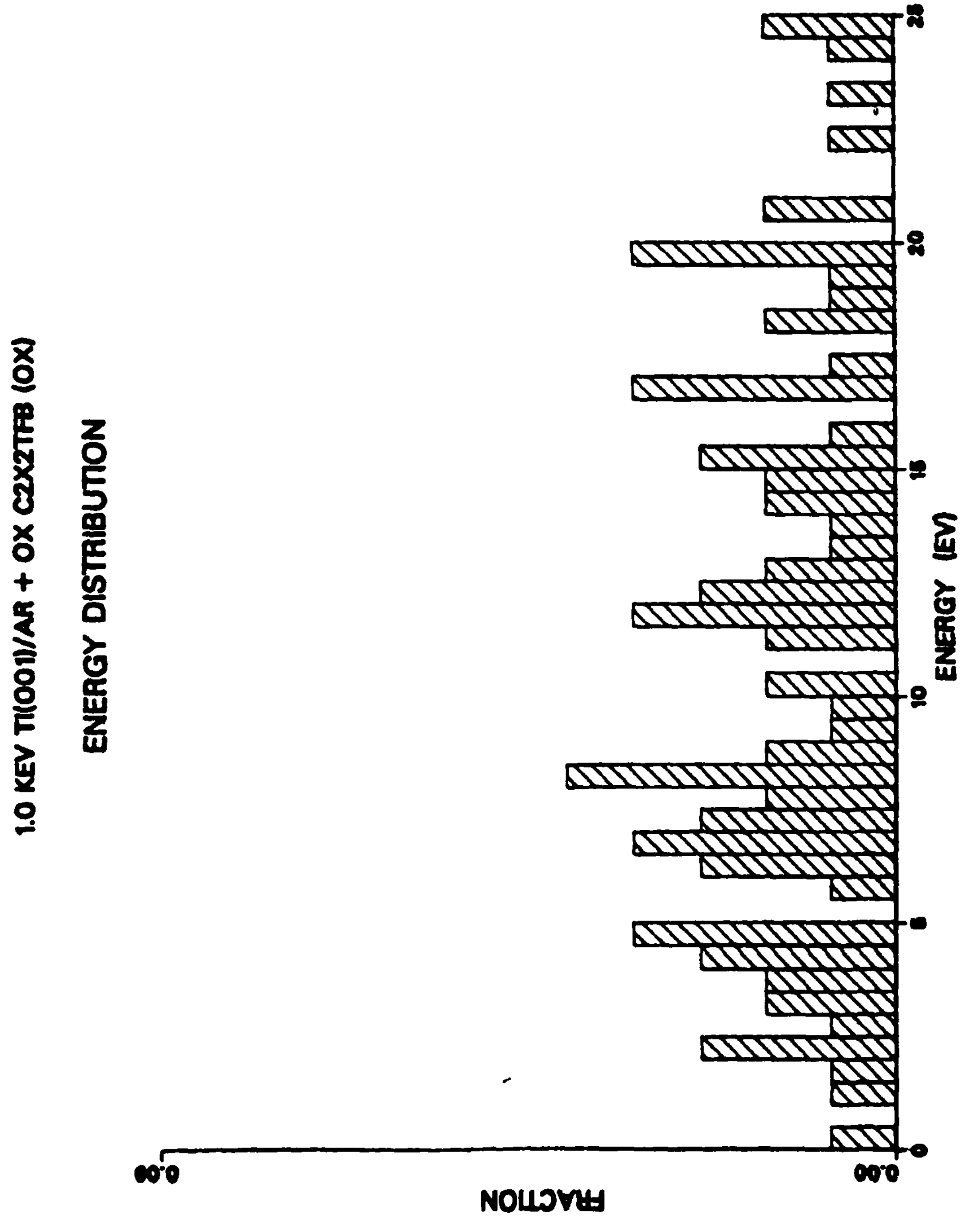
1.0 KEV TI(001)/AR + OX C2X2TFB (OX)
ENERGY DISTRIBUTION
FRACTION
0.00
0.08
ENERGY (EV)
0
5
10
15
20
25

Fig. 55.

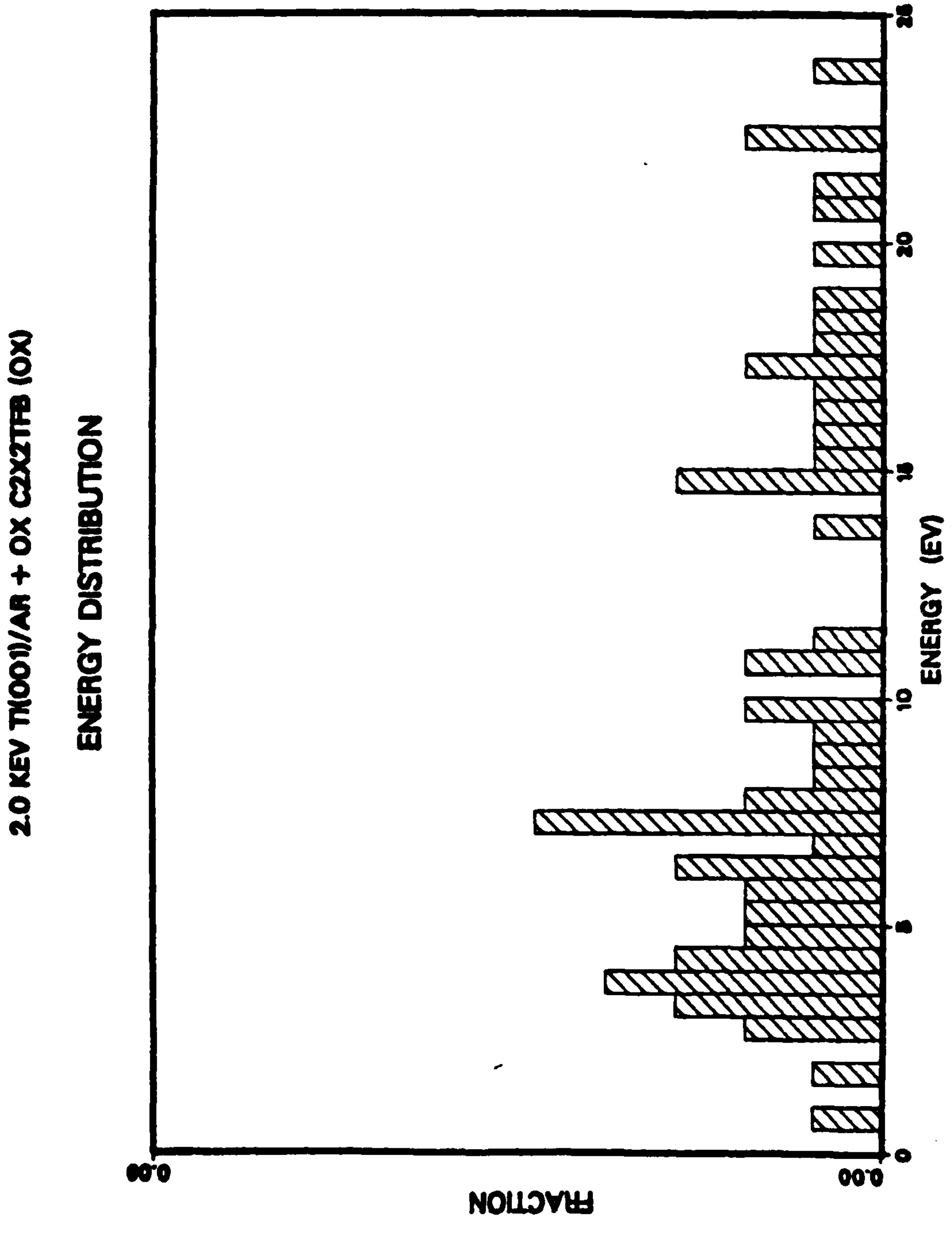
2.0 KEV TI(001)/AR + OX C2X2TFB (OX)
ENERGY DISTRIBUTION
FRACTION
0.00
0.00
ENERGY (EV)
0
5
10
15
20
25

Fig. 56.

APPENDIX D

EJECTION TIME DISTRIBUTION CHARTS

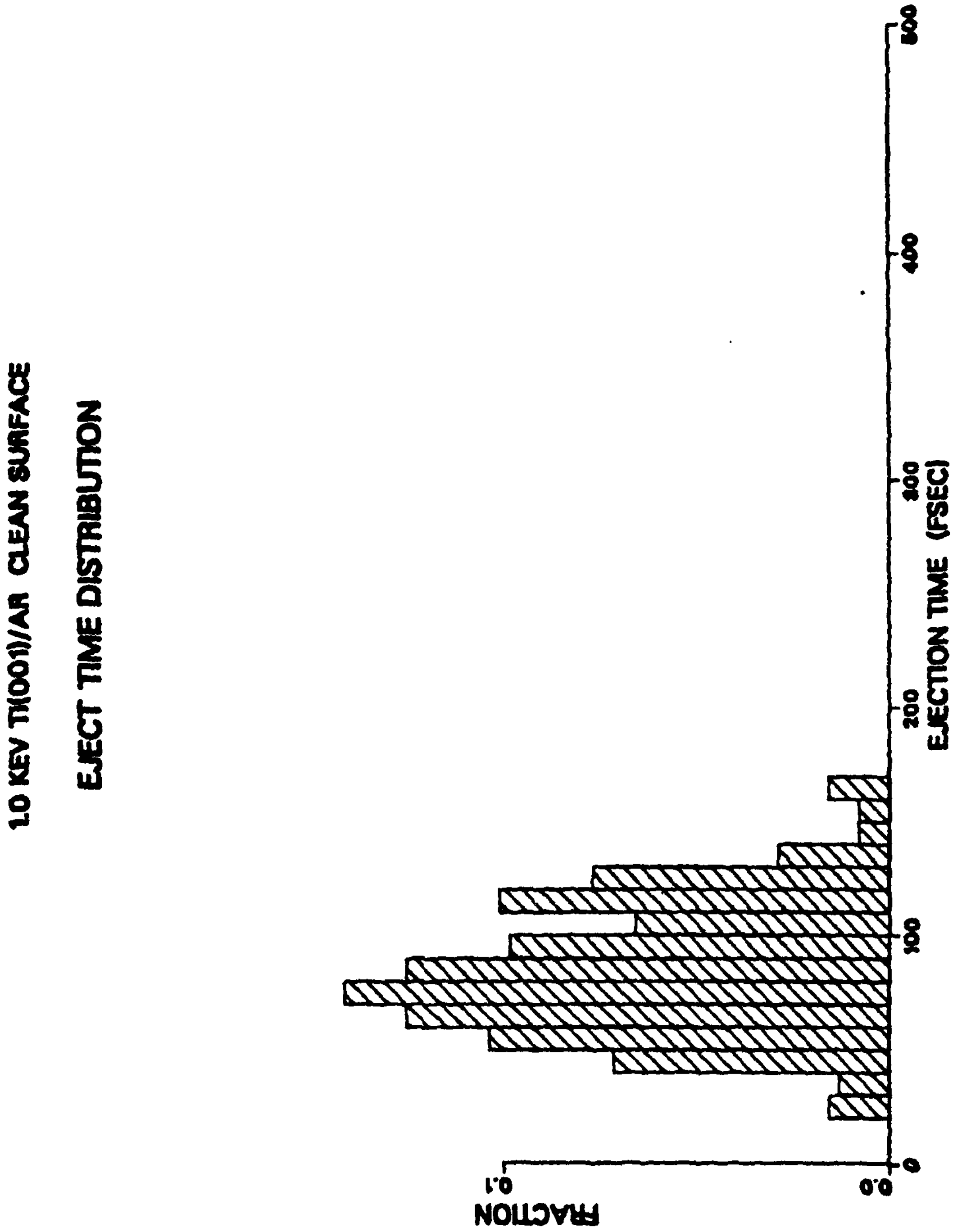

Fig. 57.

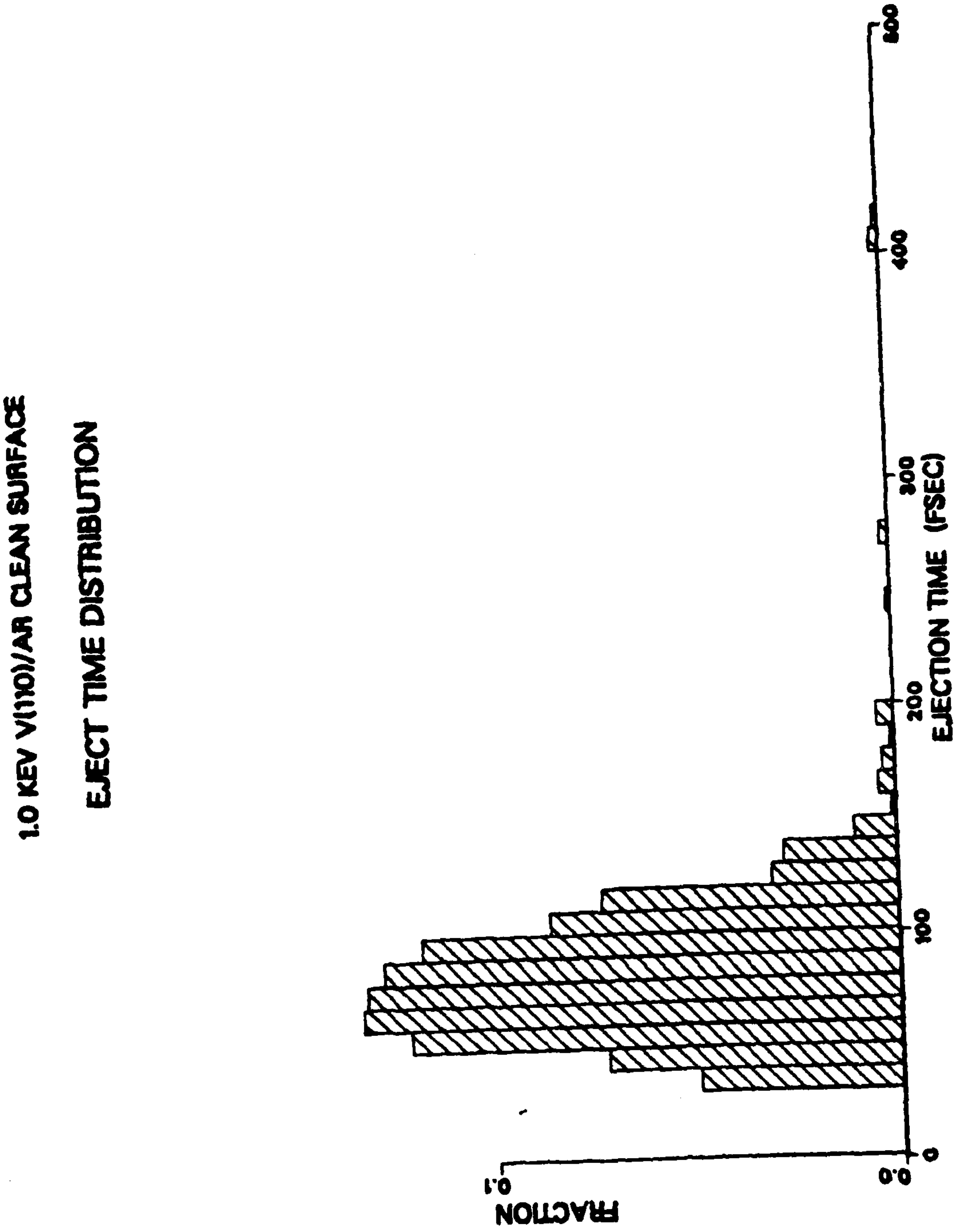
1.0 KEV V(110)/AR CLEAN SURFACE
EJECT TIME DISTRIBUTION
FRACTION
0.1
0.0
0
100
200
300
400
500
EJECTION TIME (FSEC)

Fig. 58.

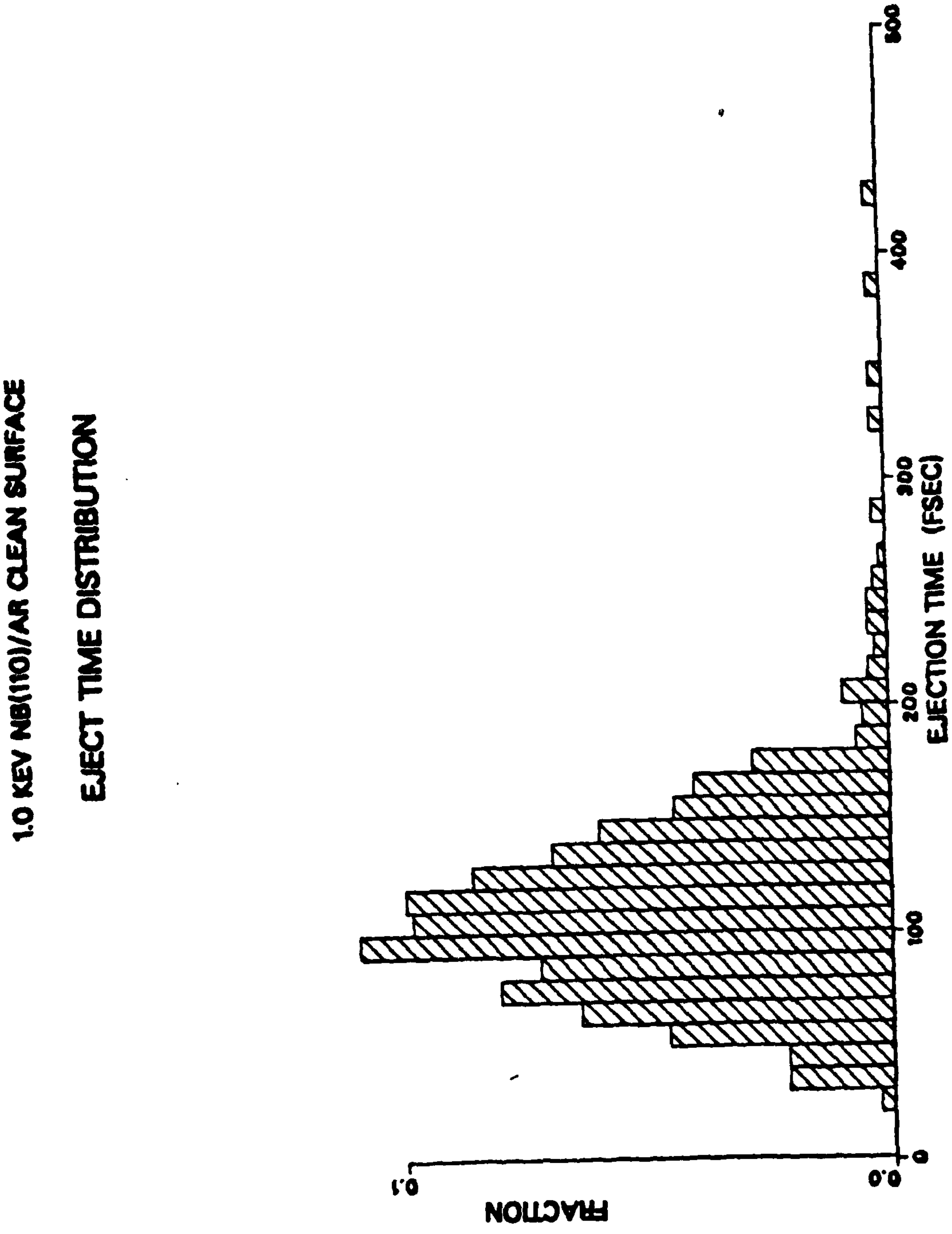
1.0 KEV NB(110)/AR CLEAN SURFACE
EJECT TIME DISTRIBUTION
FRACTION
0.0
0.1
EJECTION TIME (FSEC)
0
100
200
300
400
500

Fig. 59.

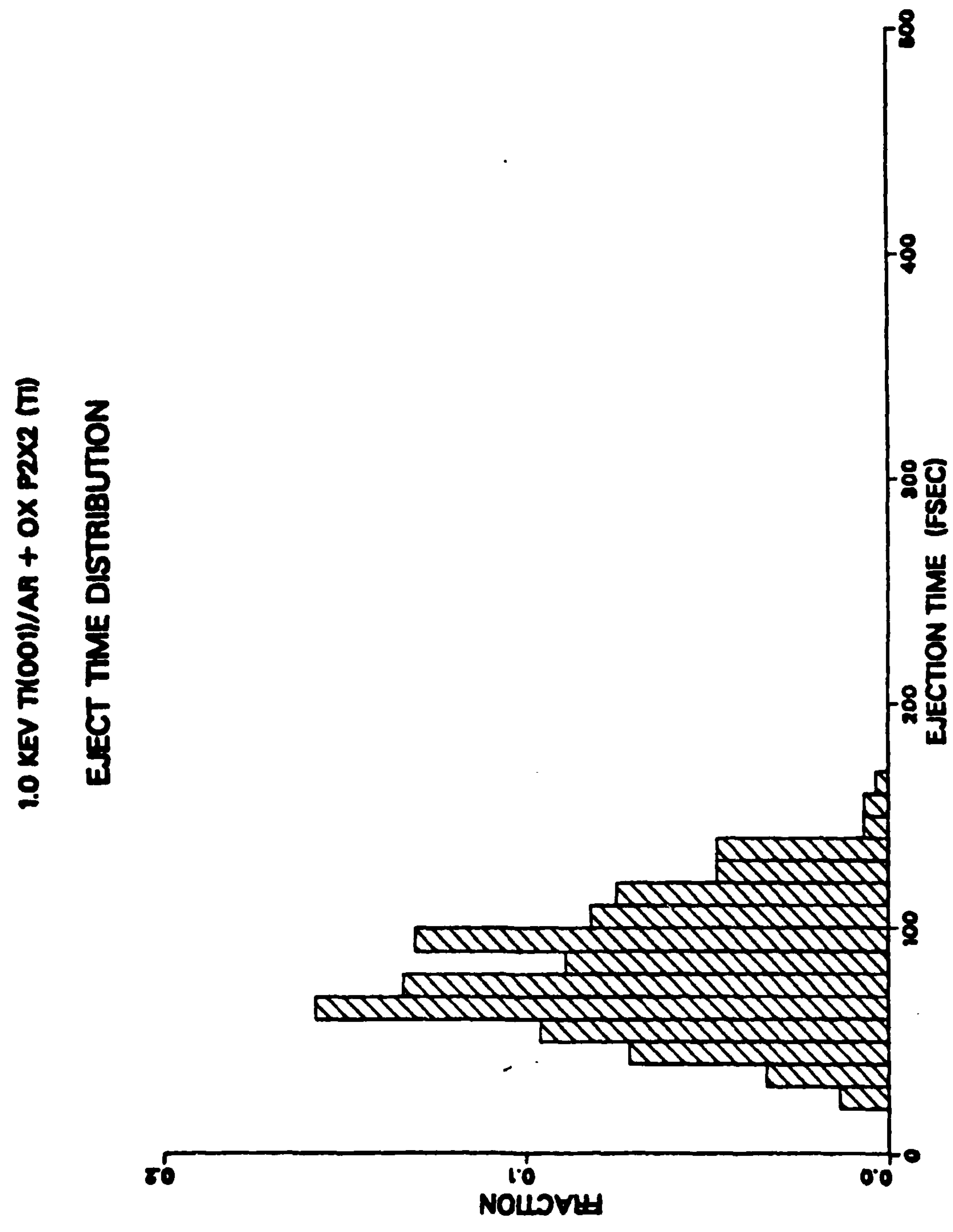
1.0 KEV Ti(001)/AR + OX P2X2 (Ti)
EJECT TIME DISTRIBUTION
FRACTION
0.0
0.1
0.2
0
100
200
300
400
500
EJECTION TIME (FSEC)

Fig. 60.

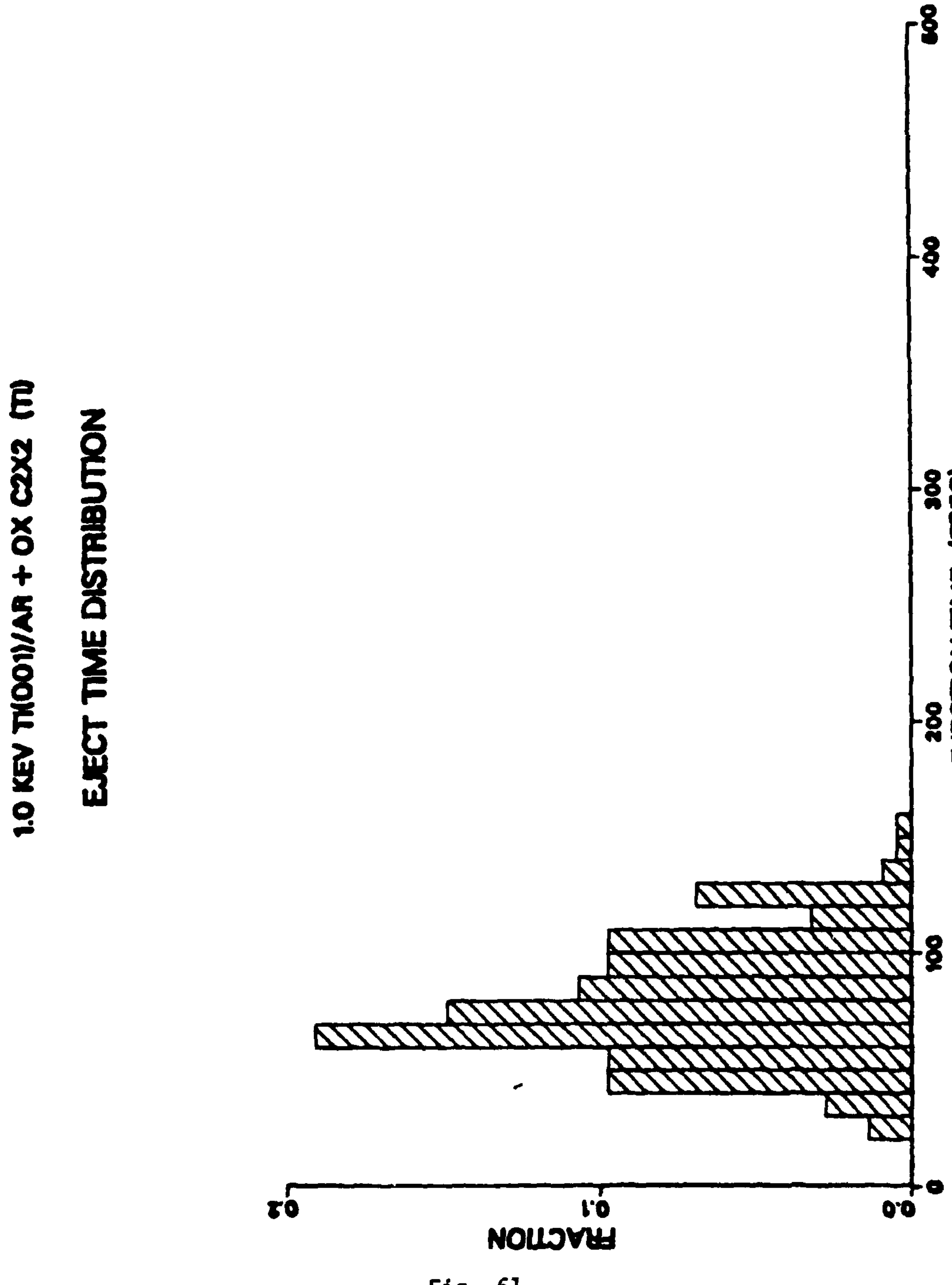
1.0 KEV TI(001)/AR + OX C2X2 (TI)
EJECT TIME DISTRIBUTION
FRACTION
0.0
0.1
0.2
EJECTION TIME (FSEC)
0
100
200
300
400
500

Fig. 61.

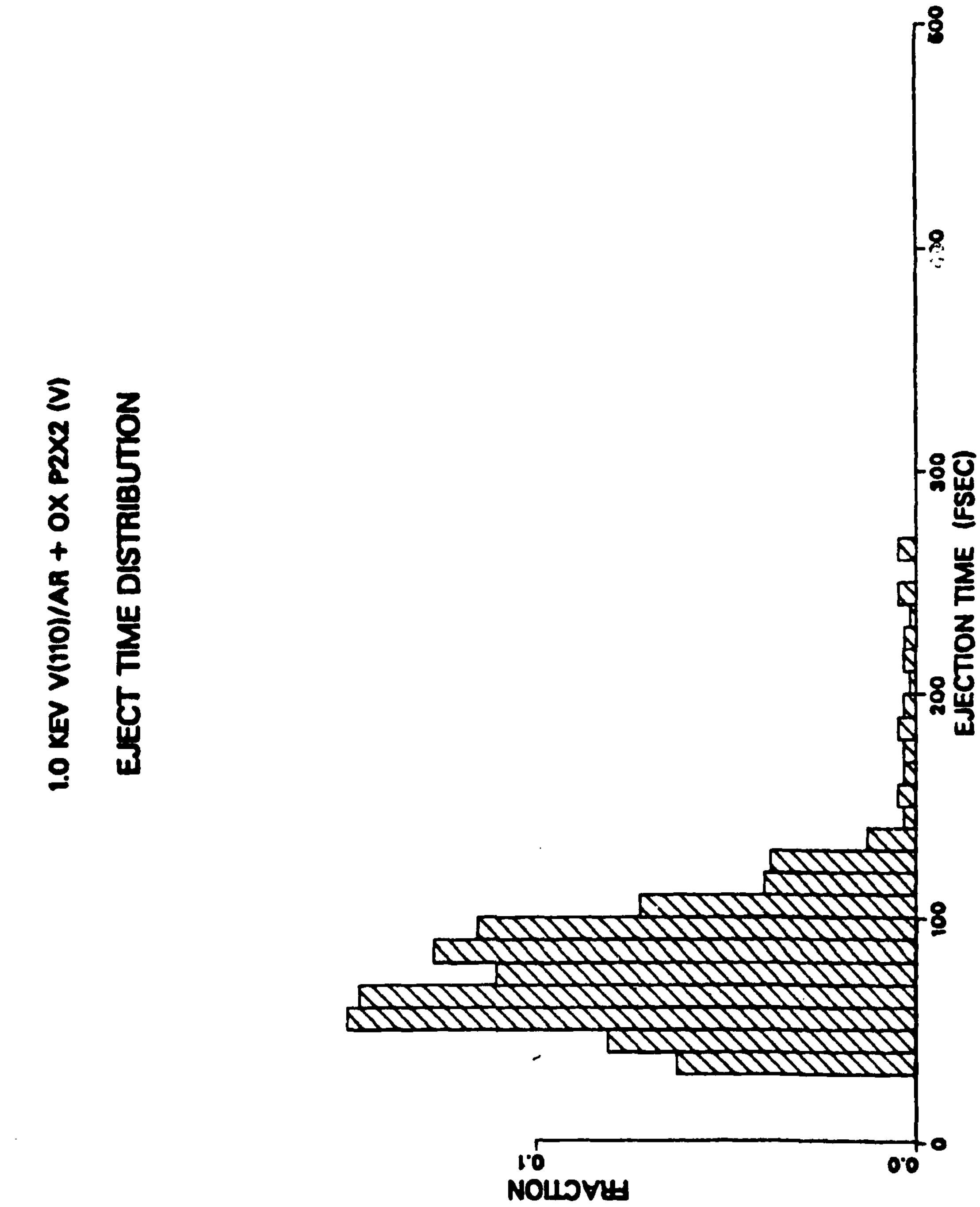
1.0 KEV V(110)/AR + OX P2X2 (V)
EJECT TIME DISTRIBUTION
FRACTION
0.1
0.0
0
100
200
300
400
500
EJECTION TIME (FSEC)

Fig. 62.

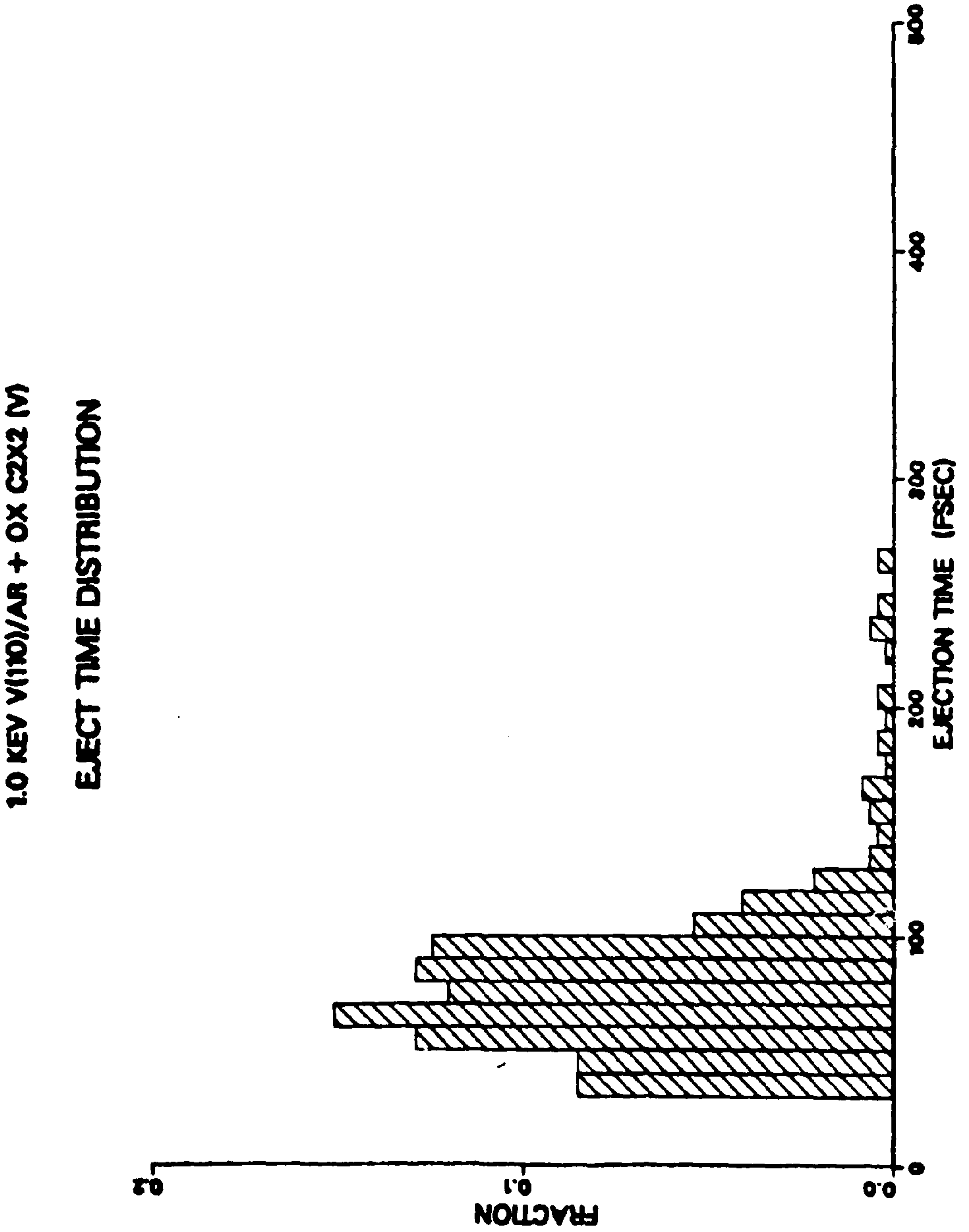
1.0 KEV V(110)/AR + OX C2X2 (V)
EJECT TIME DISTRIBUTION
FRACTION
0.0
0.1
0.2
EJECTION TIME (FSEC)
0
100
200
300
400
500

Fig. 63.

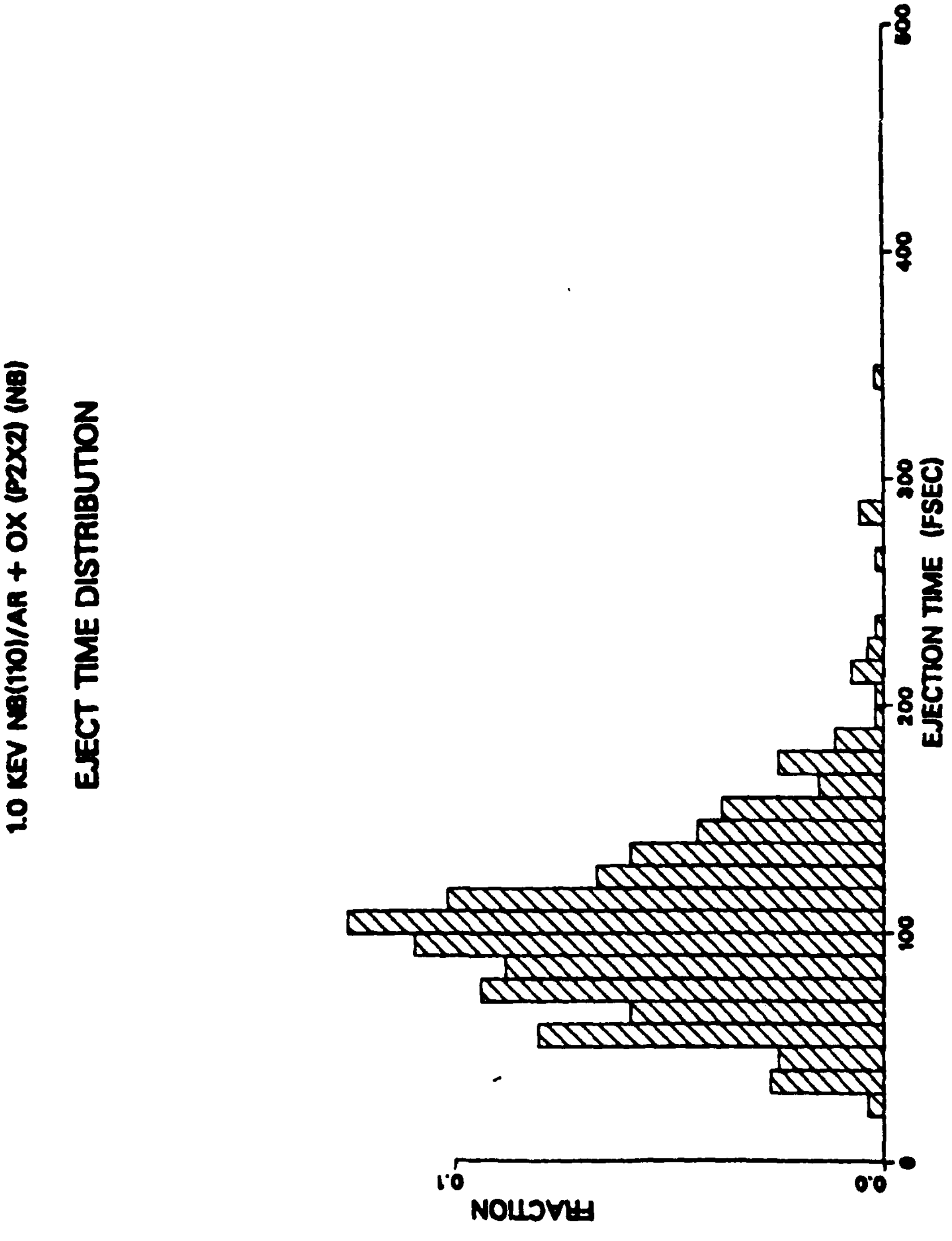
1.0 KEV NB(110)/AR + OX (P2X2) (NB)
EJECT TIME DISTRIBUTION
FRACTION
0.1
0.0
0
100
200
300
400
500
EJECTION TIME (FSEC)

Fig. 64.

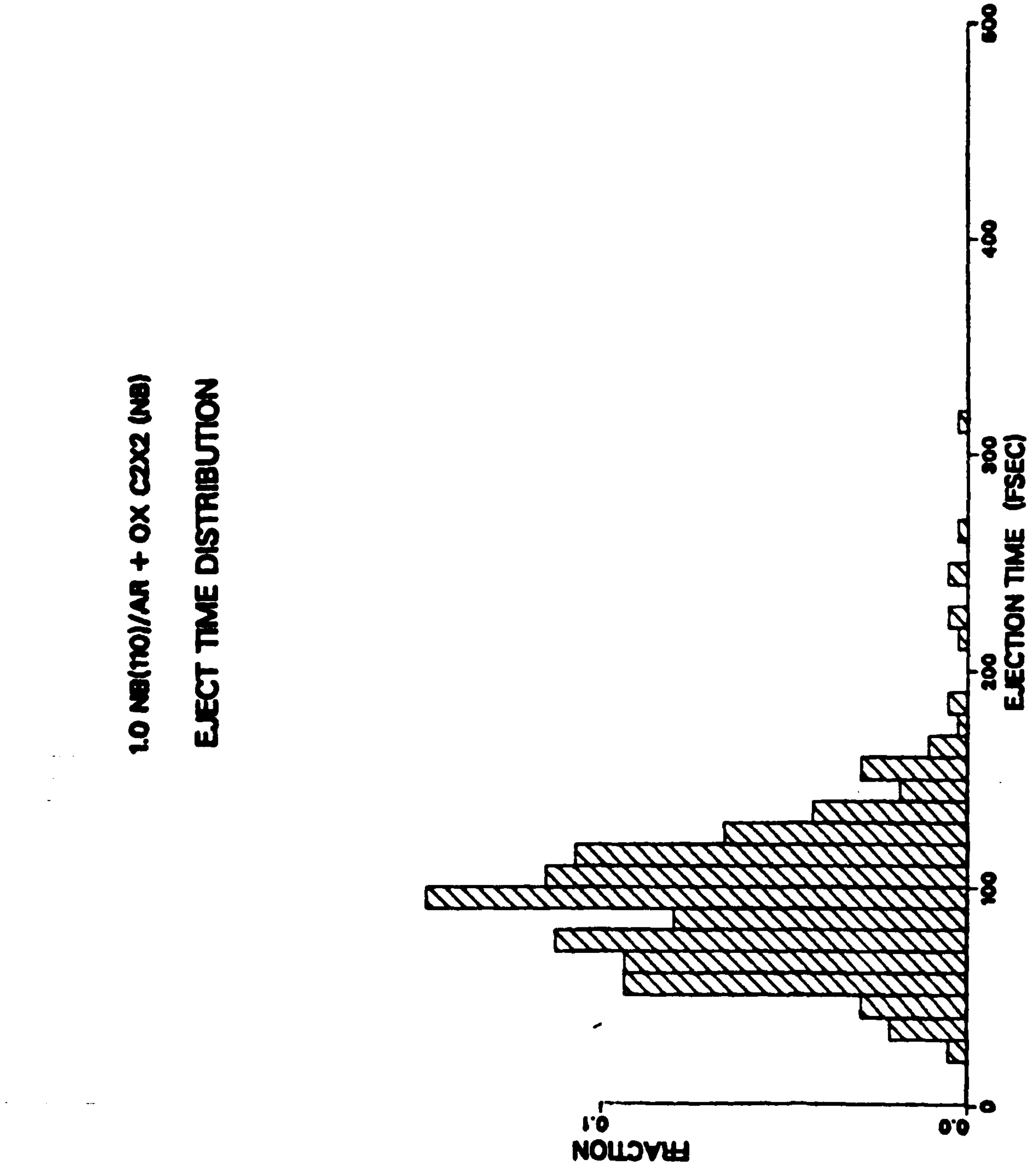
1.0 NB(110)/AR + OX C2X2 (NB)
EJECT TIME DISTRIBUTION
FRACTION
0.1
0.0
0
100
200
300
400
500
EJECTION TIME (FSEC)

Fig. 65.

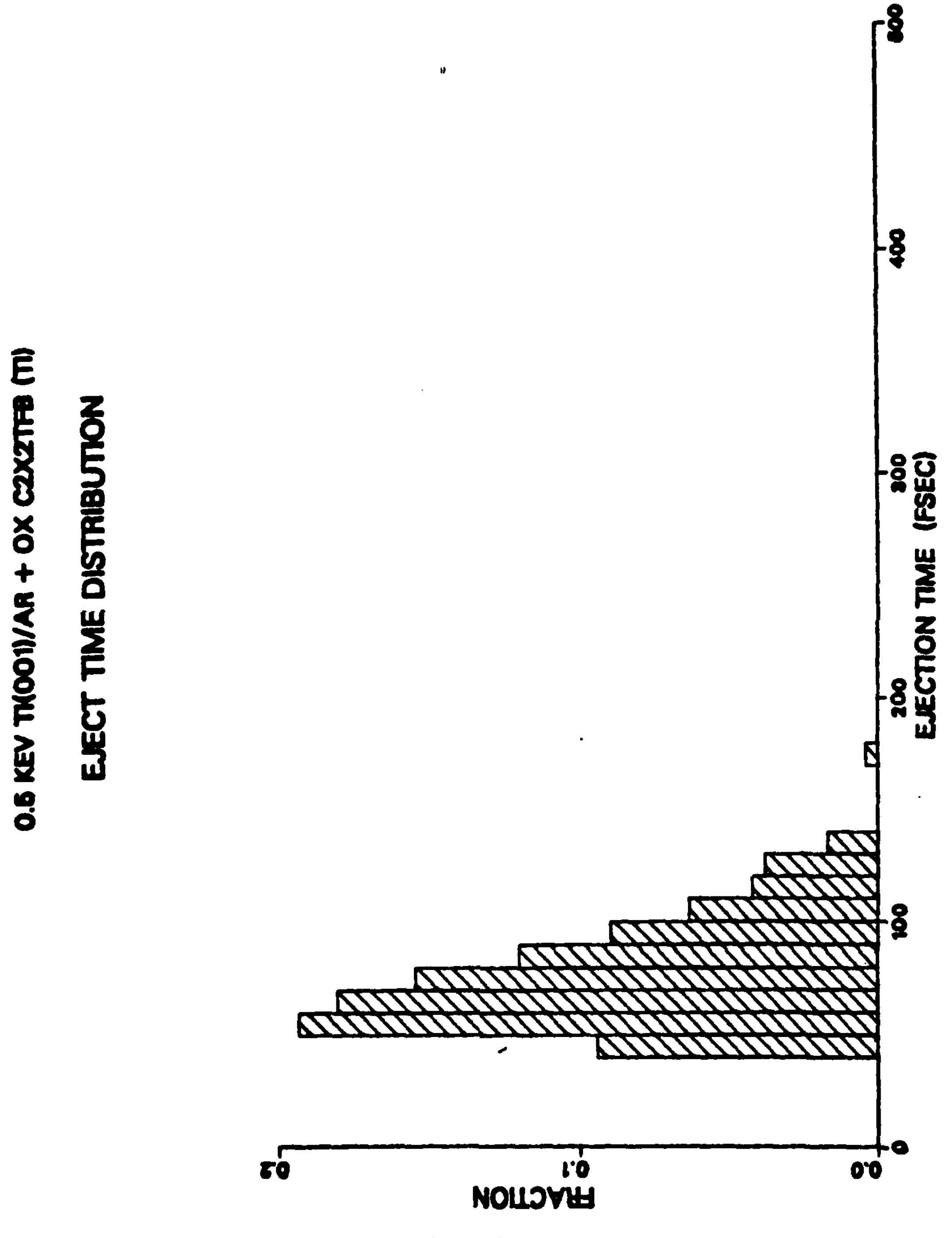
0.5 KEV TI(001)/AR + OX C2X2TFB (TI)
EJECT TIME DISTRIBUTION
FRACTION
0.0
0.1
0.2
EJECTION TIME (FSEC)
0
100
200
300
400
500

Fig. 66.

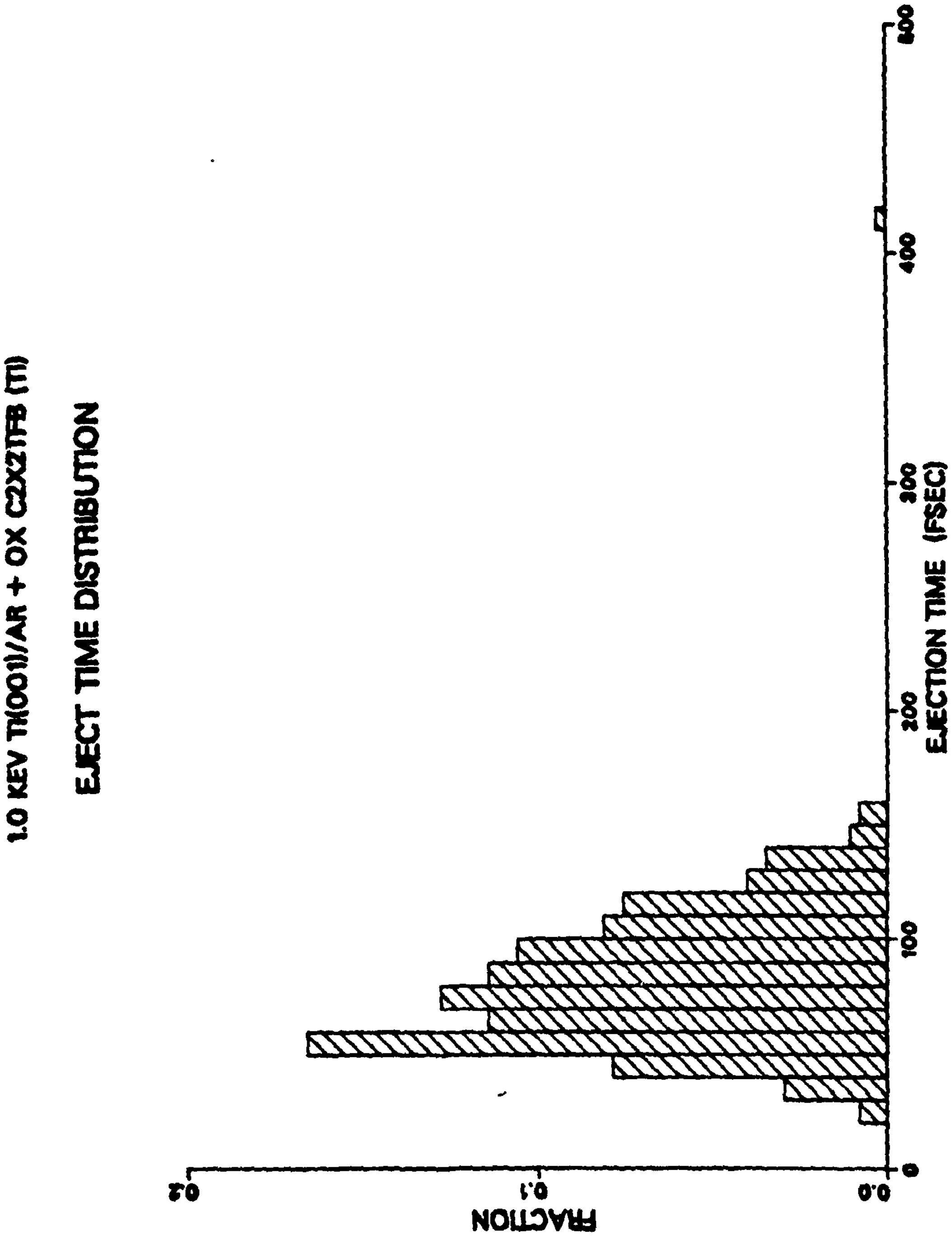
1.0 KEV Ti(001)/AR + OX C2X2TFB (Ti)
EJECT TIME DISTRIBUTION
FRACTION
0.0
0.1
0.2
EJECTION TIME (FSEC)
0
100
200
300
400
500

Fig. 67.

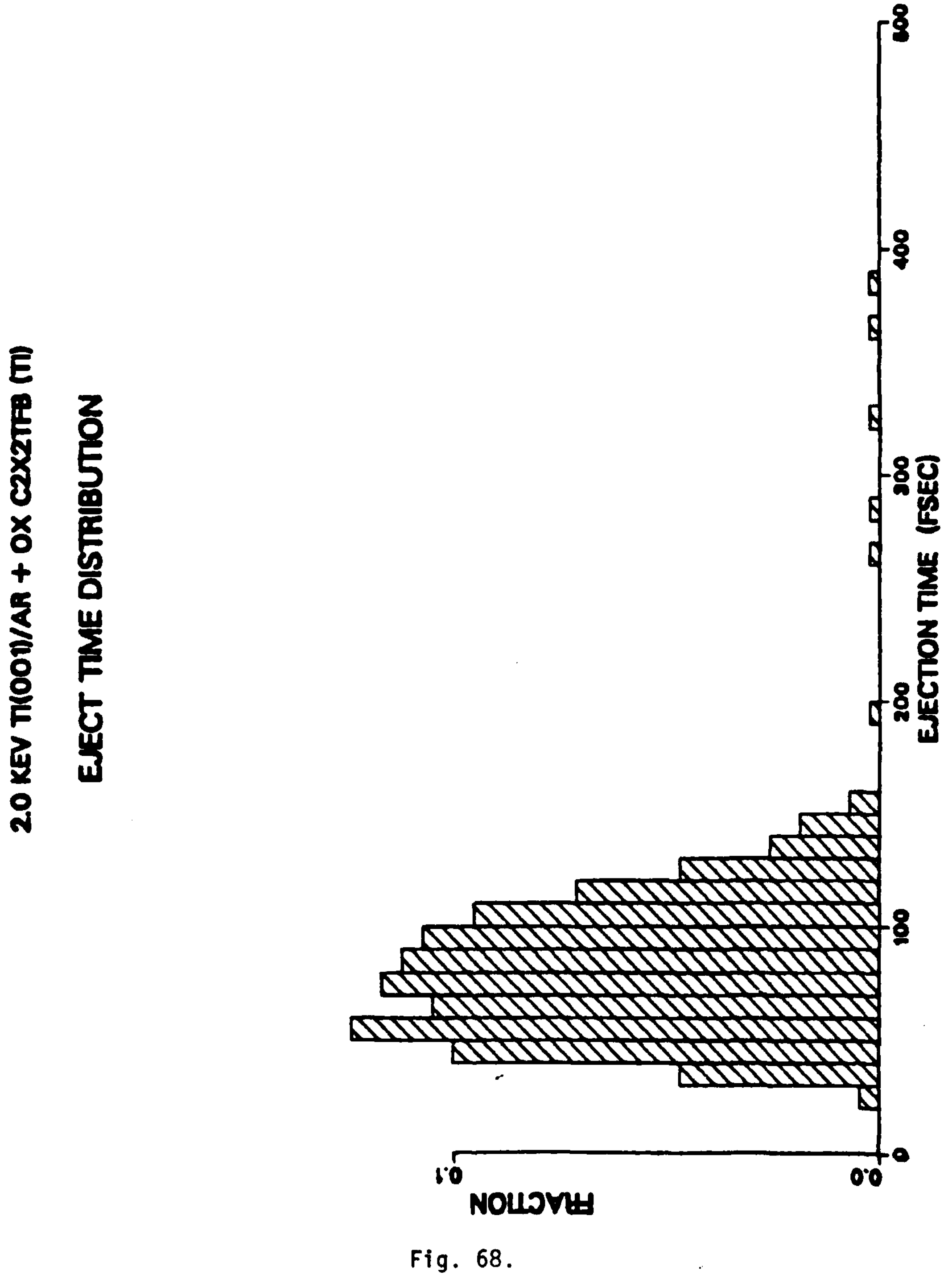
2.0 KEV TI(001)/AR + OX C2X2TFB (TI)
EJECT TIME DISTRIBUTION
FRACTION
0.1
0.0
0
100
200
300
400
500
EJECTION TIME (FSEC)

Fig. 68.

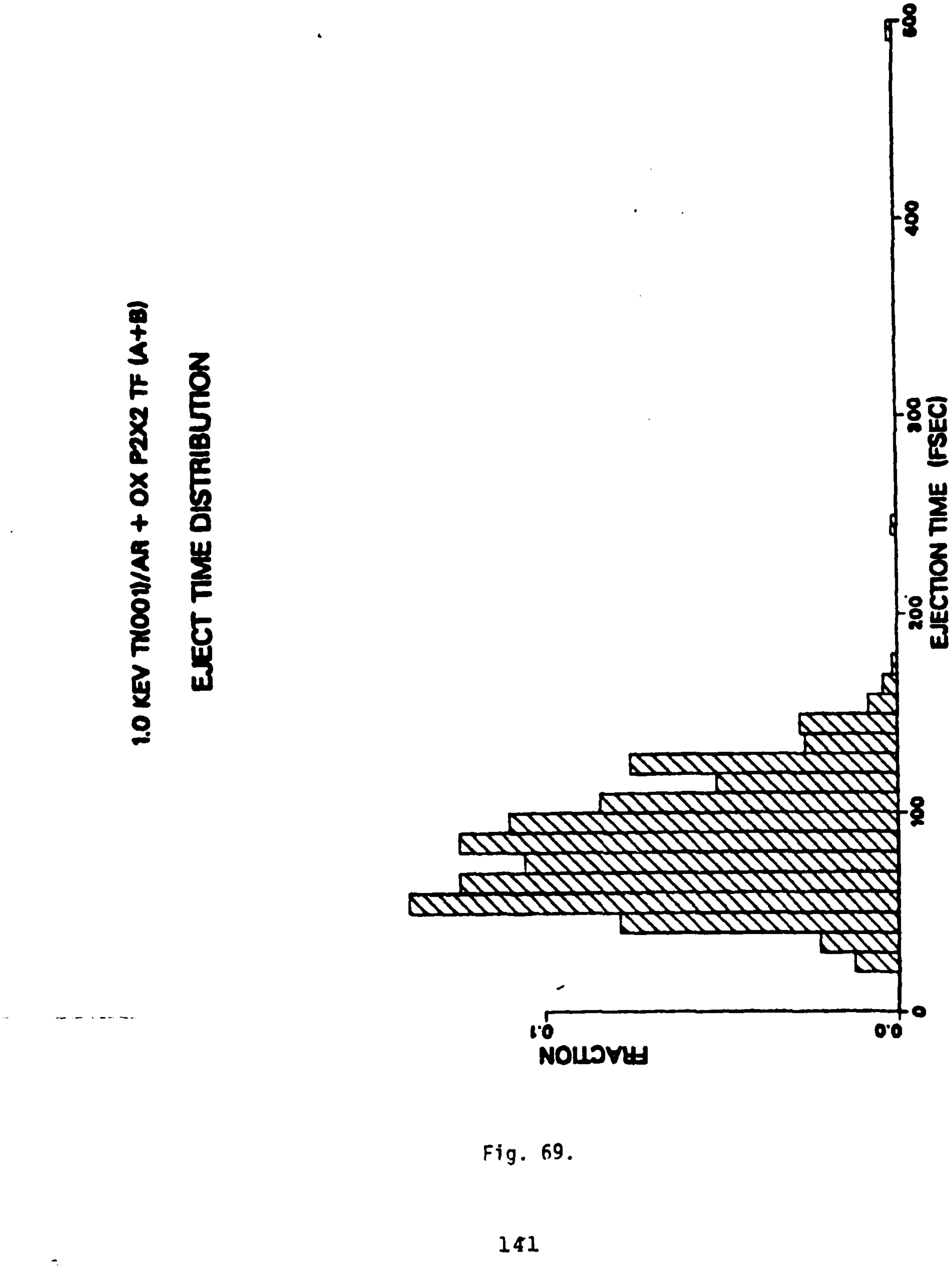
1.0 KEV TI(001)/AR + OX P2X2 TF (A+B)
EJECT TIME DISTRIBUTION
FRACTION
0.0
0.1
EJECTION TIME (FSEC)
0
100
200
300
400
500

Fig. 69.

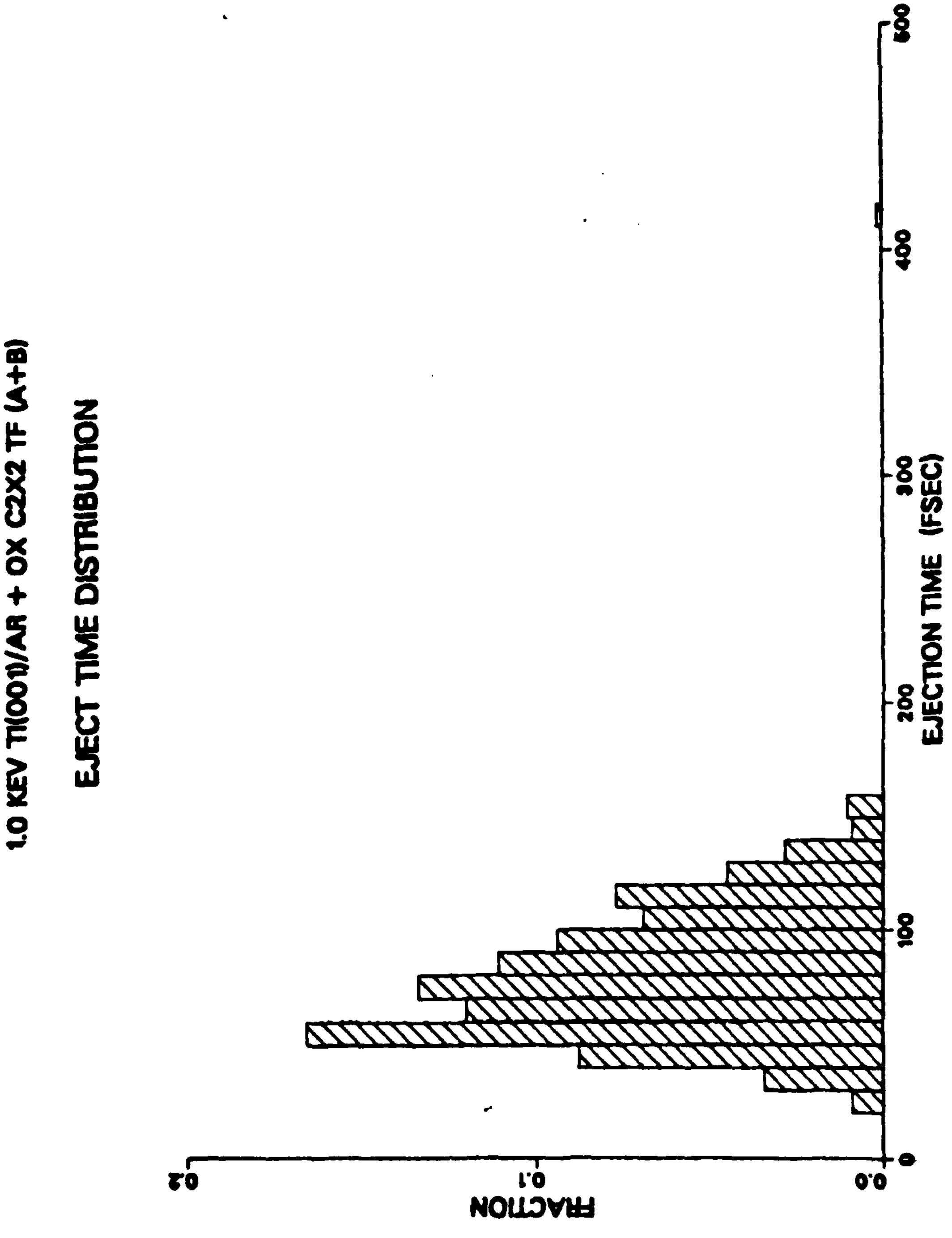
1.0 KEV TI(001)/AR + OX C2X2 TF (A+B)
EJECT TIME DISTRIBUTION
FRACTION
0.0
0.1
0.2
EJECTION TIME (FSEC)
0
100
200
300
400
500

Fig. 70

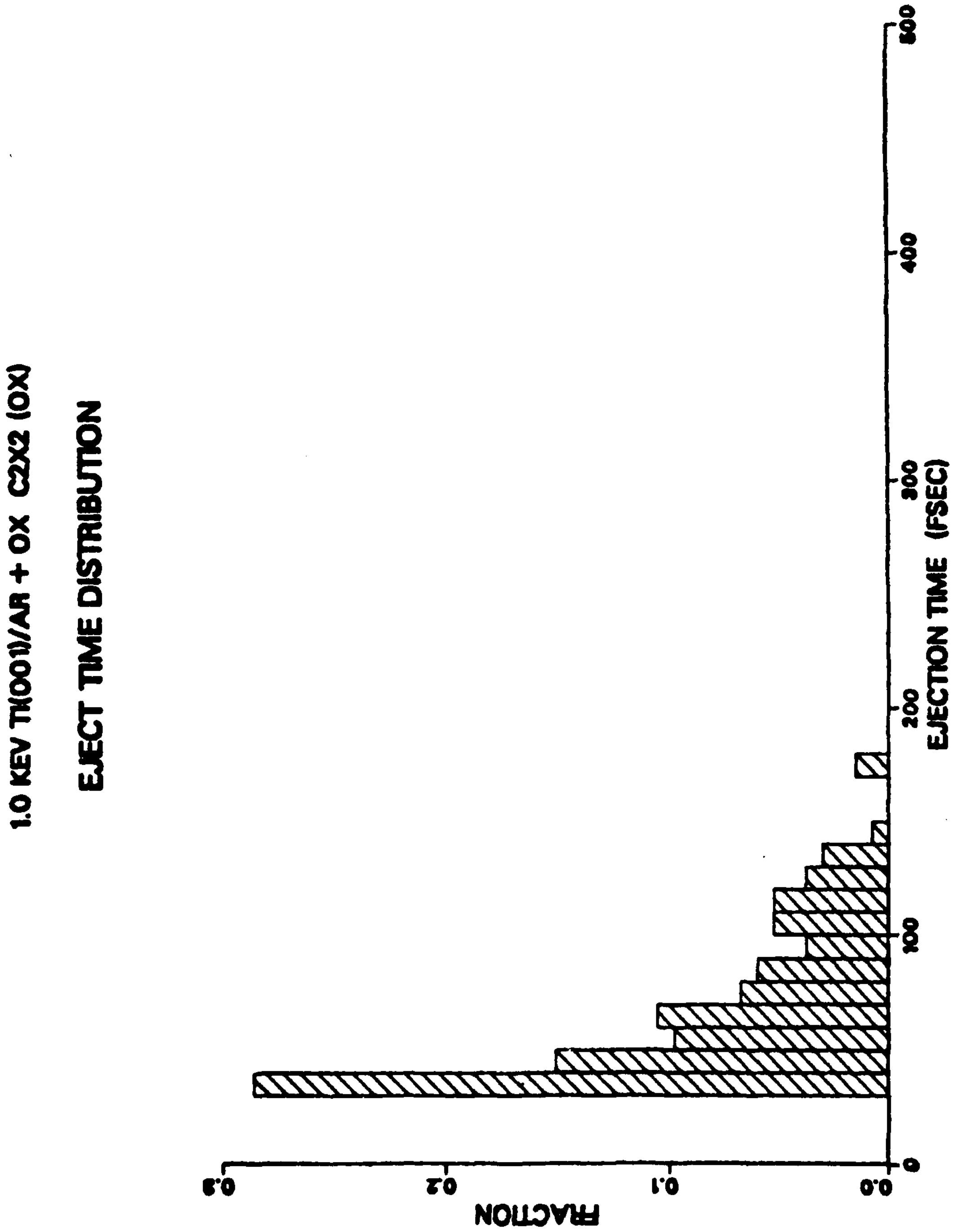
1.0 KEV Ti(001)/AR + OX C2X2 (OX)
EJECT TIME DISTRIBUTION
FRACTION
0.0
0.1
0.2
0.3
0
100
200
300
400
500
EJECTION TIME (FSEC)

Fig. 71.

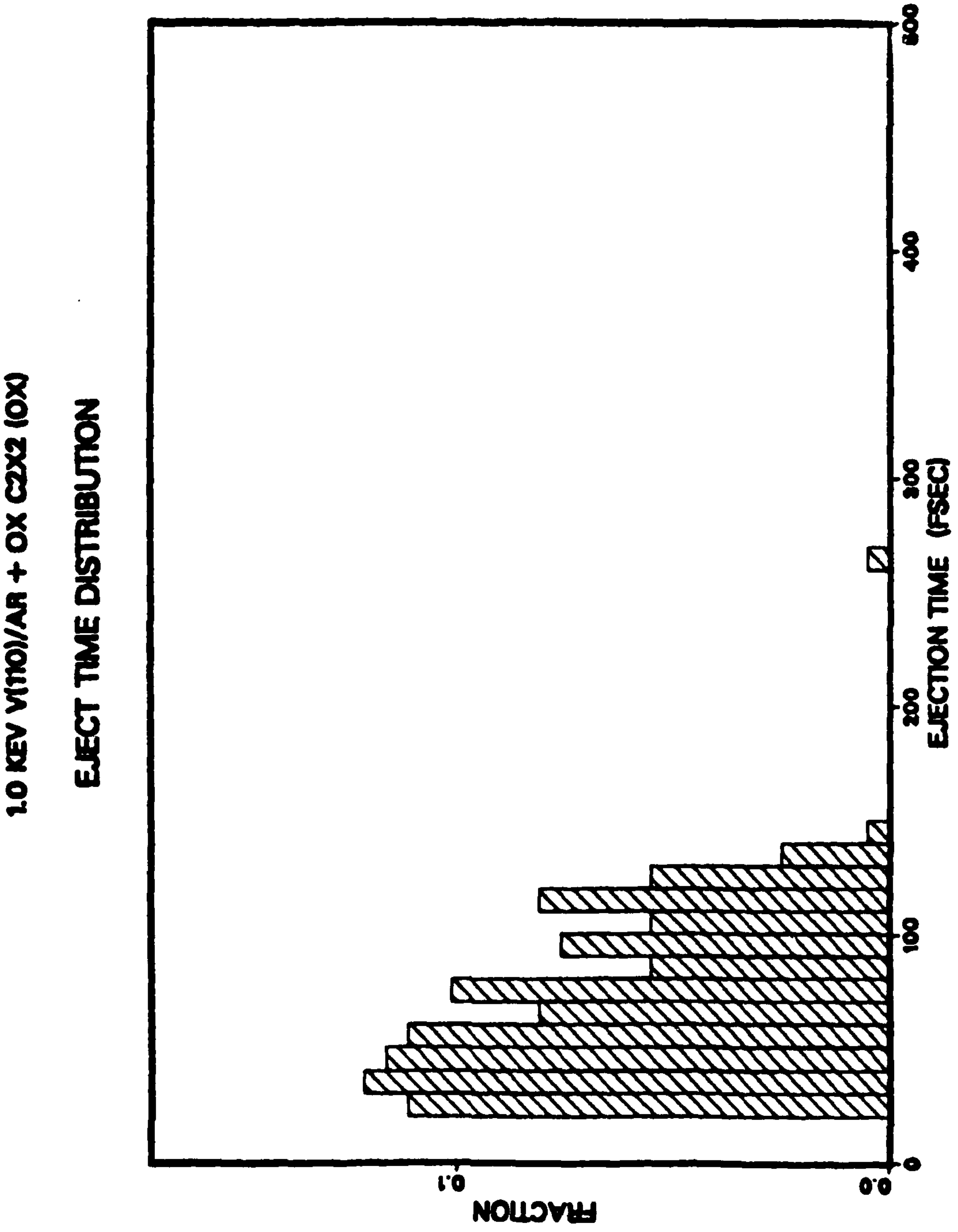
1.0 KEV V(110)/AR + OX C2X2 (OX)
EJECT TIME DISTRIBUTION
FRACTION
0.0
0.1
EJECTION TIME (FSEC)
0
100
200
300
400
500

Fig. 72.

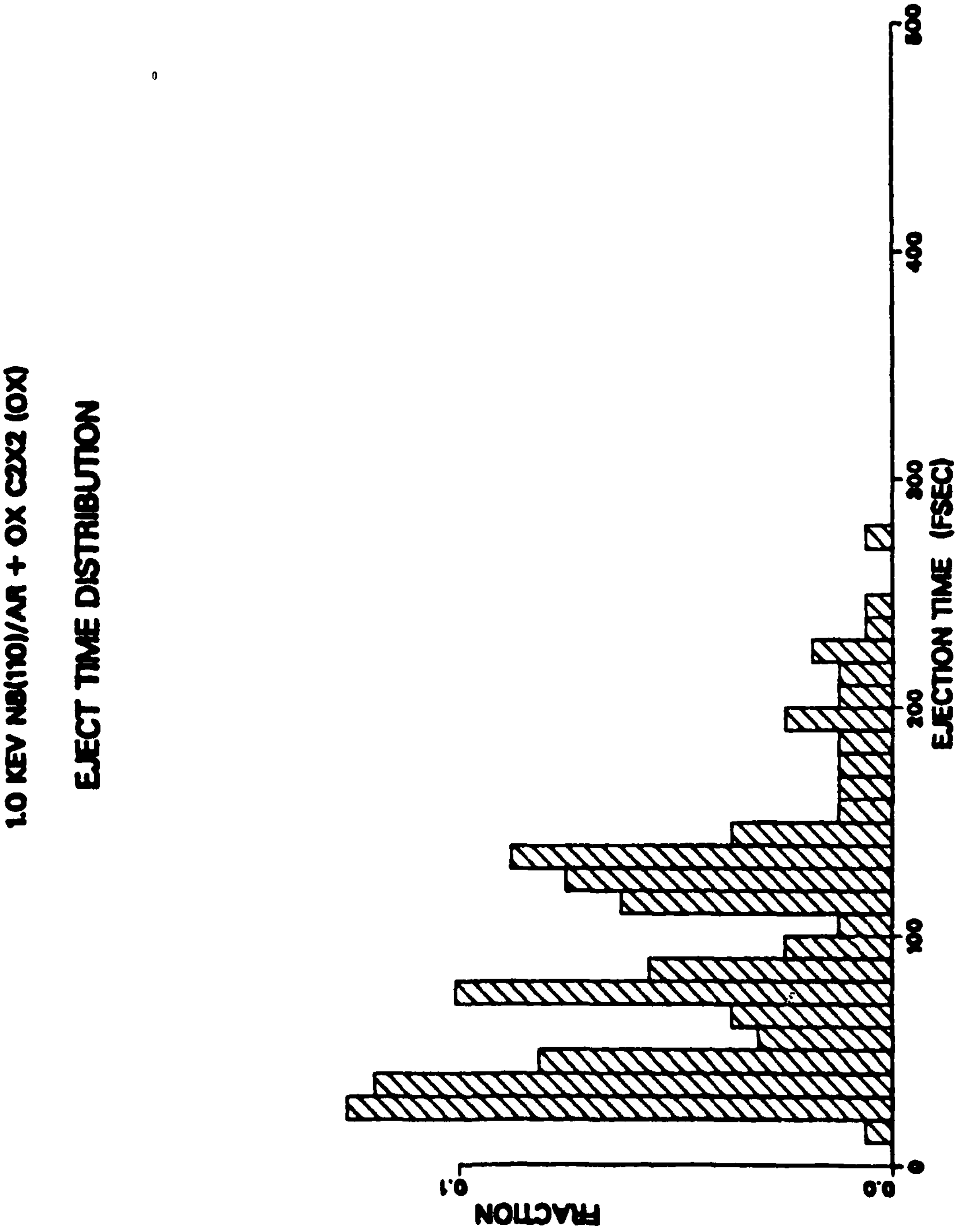
1.0 KEV NB(110)/AR + OX C2X2 (OX)
EJECT TIME DISTRIBUTION
FRACTION
0.0
0.1
0
100
200
300
400
500
EJECTION TIME (FSEC)

Fig. 73.

APPENDIX E

INITIAL LOCATIONS OF EJECTED ATOMS

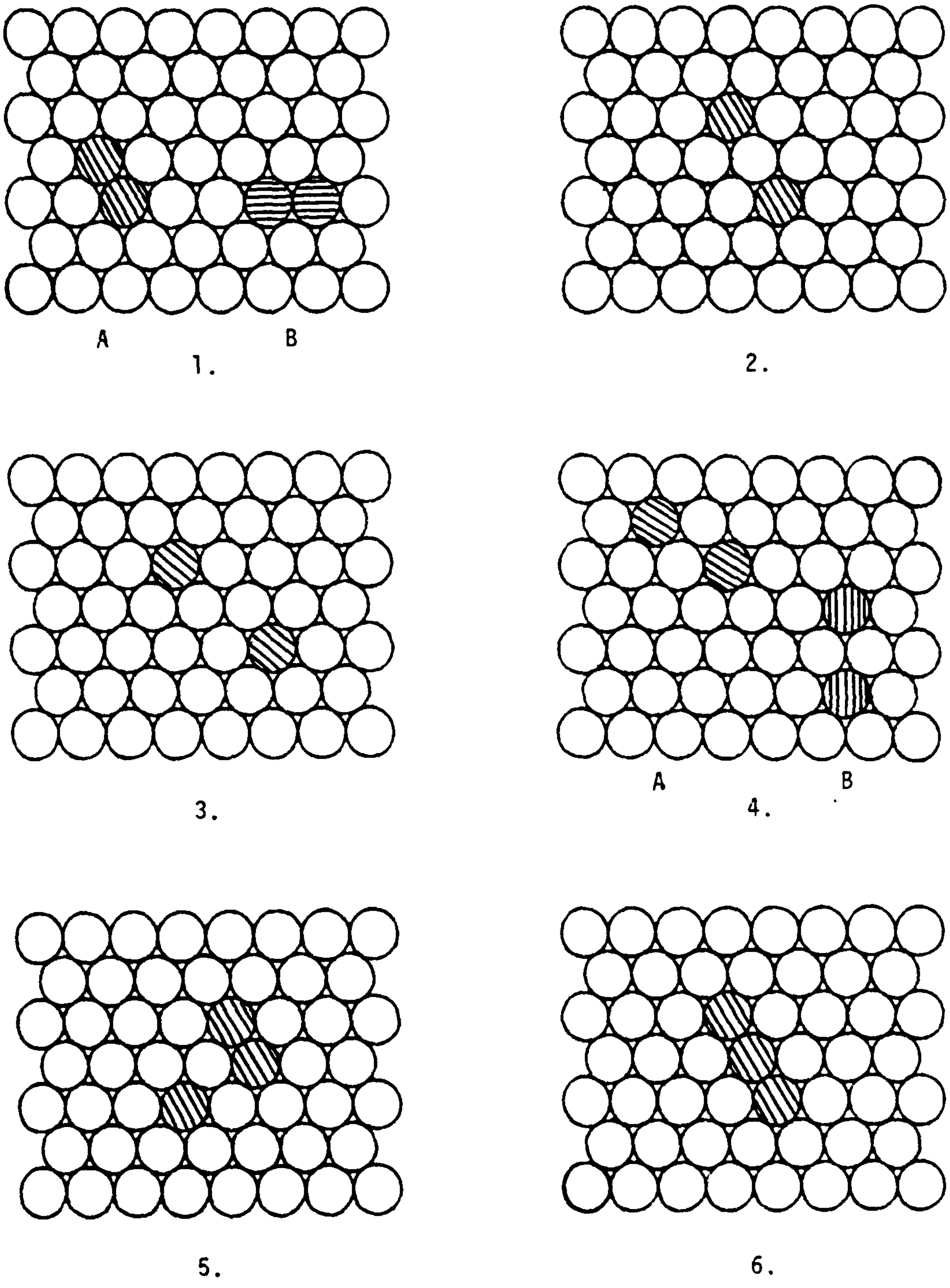

Fig. 74. Origin of sputtered atoms, clean Ti.

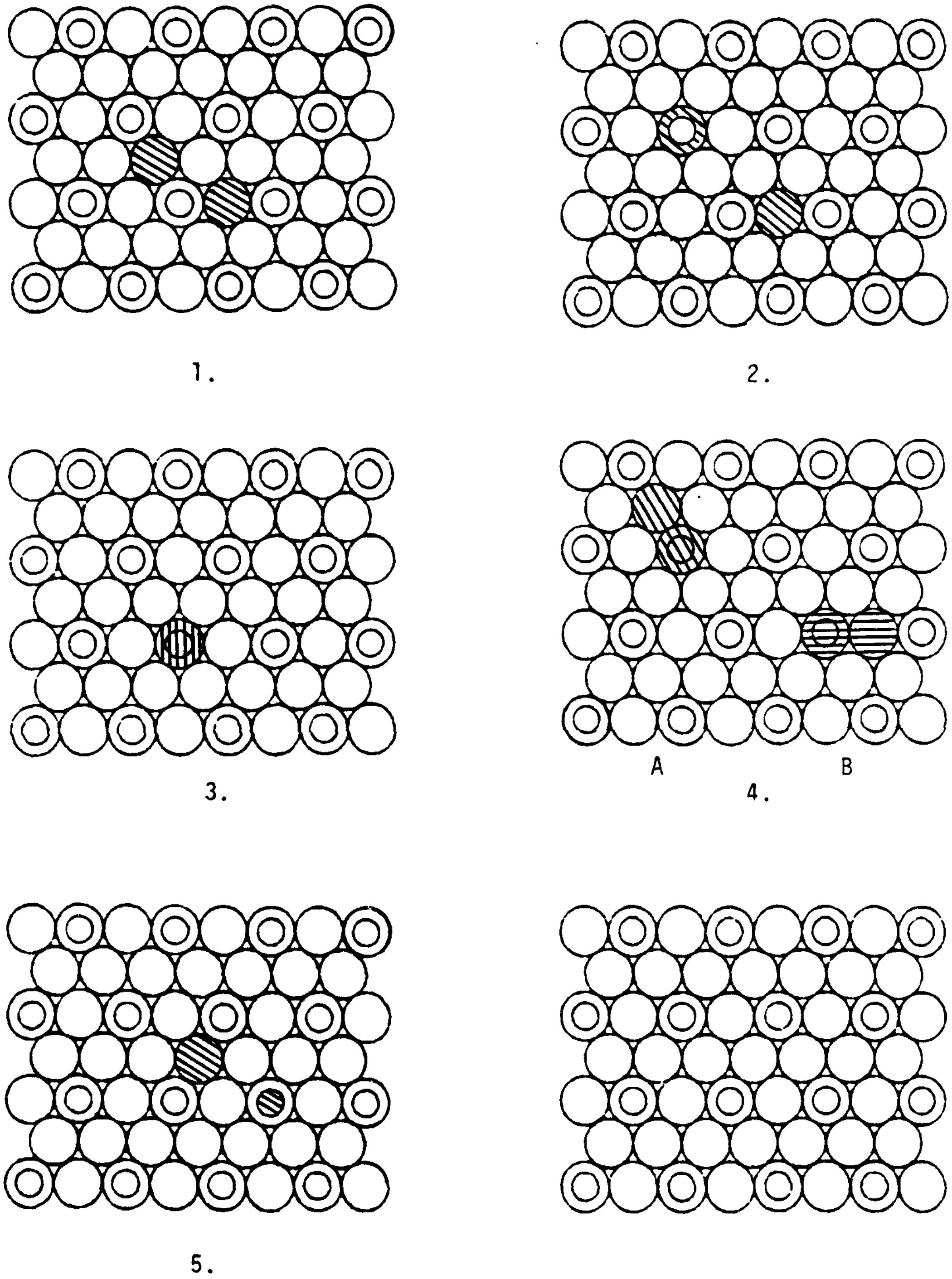

Fig. 75. Origin of sputtered atoms, Ti P(2x2) A-Top.

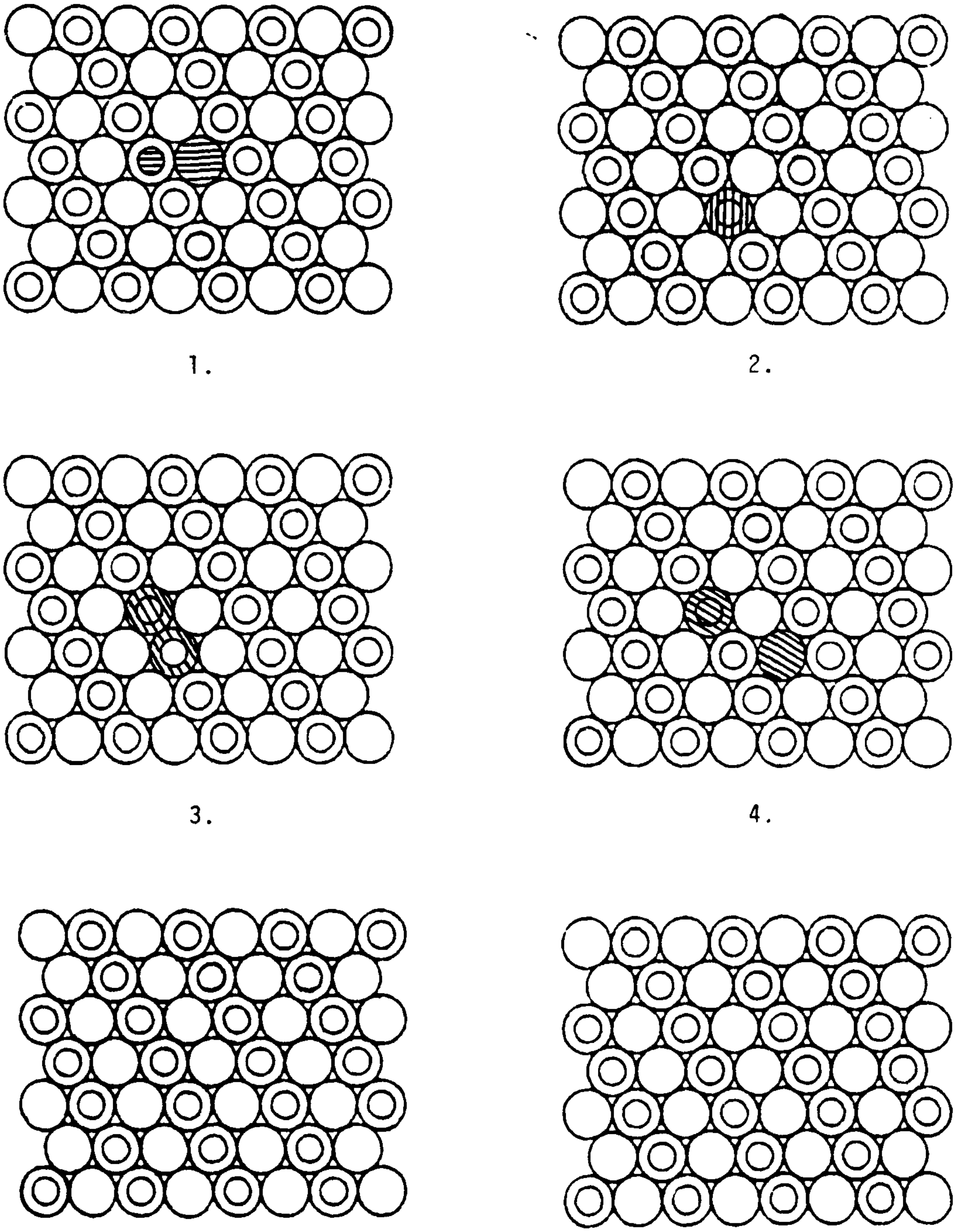

1.

2.

3.

4.

Fig. 76. Origin of sputtered atoms, Ti C(2x2) A-top.

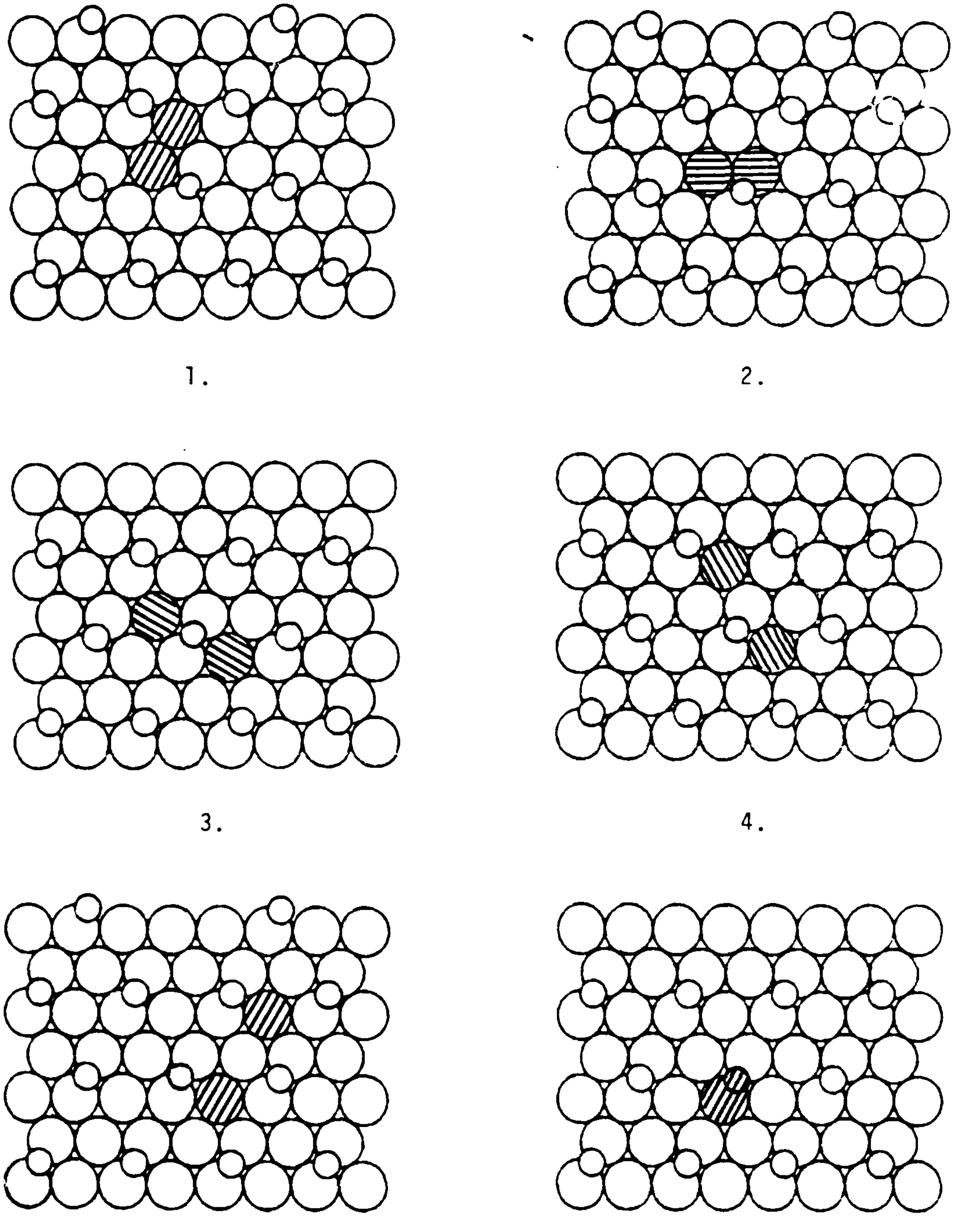

1.

2.

3.

4.

5.

6.

Fig. 77. Origin of sputtered atoms, Ti P(2x2) bridge.

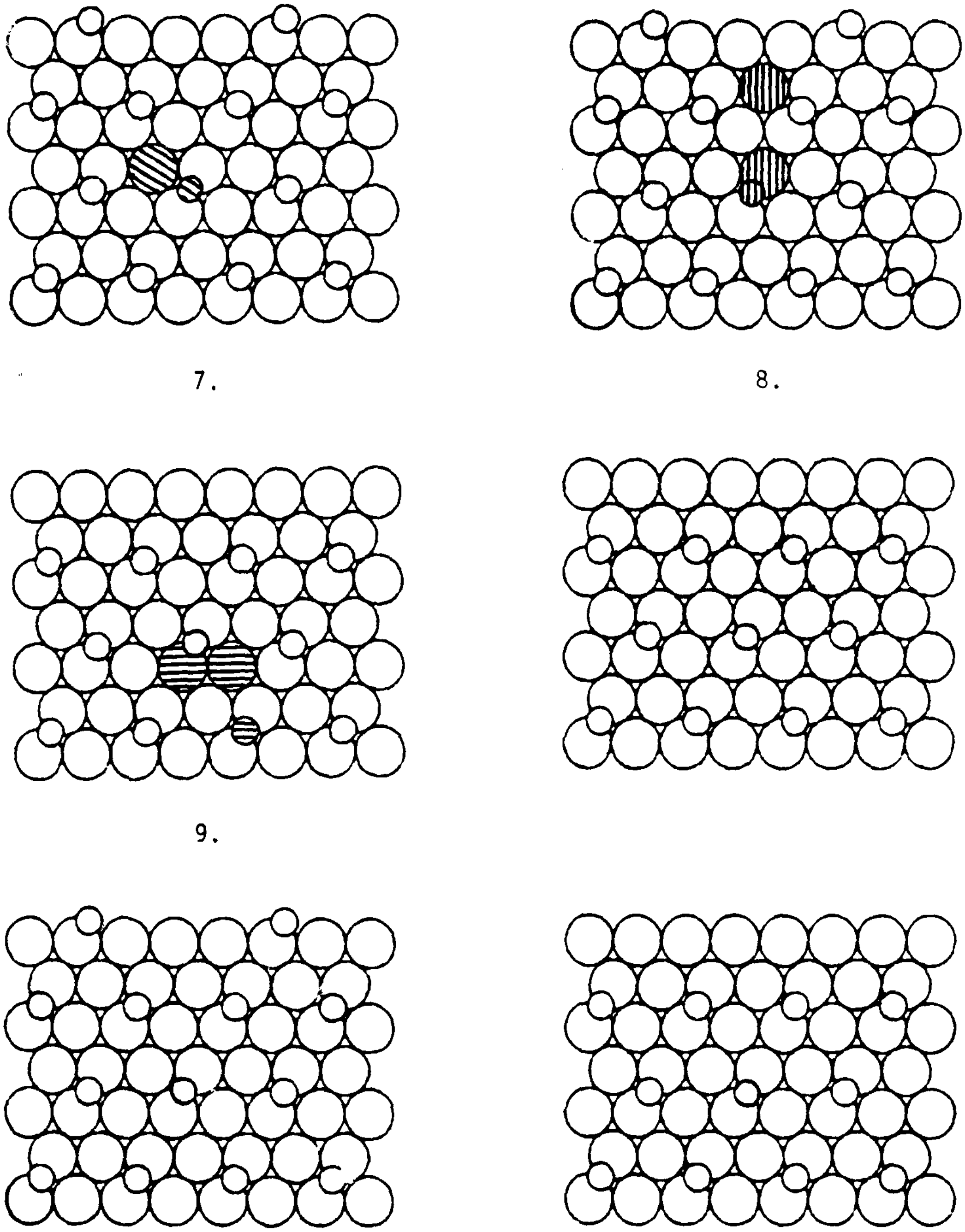
7.

8.

9.

Fig. 77 (cont.).

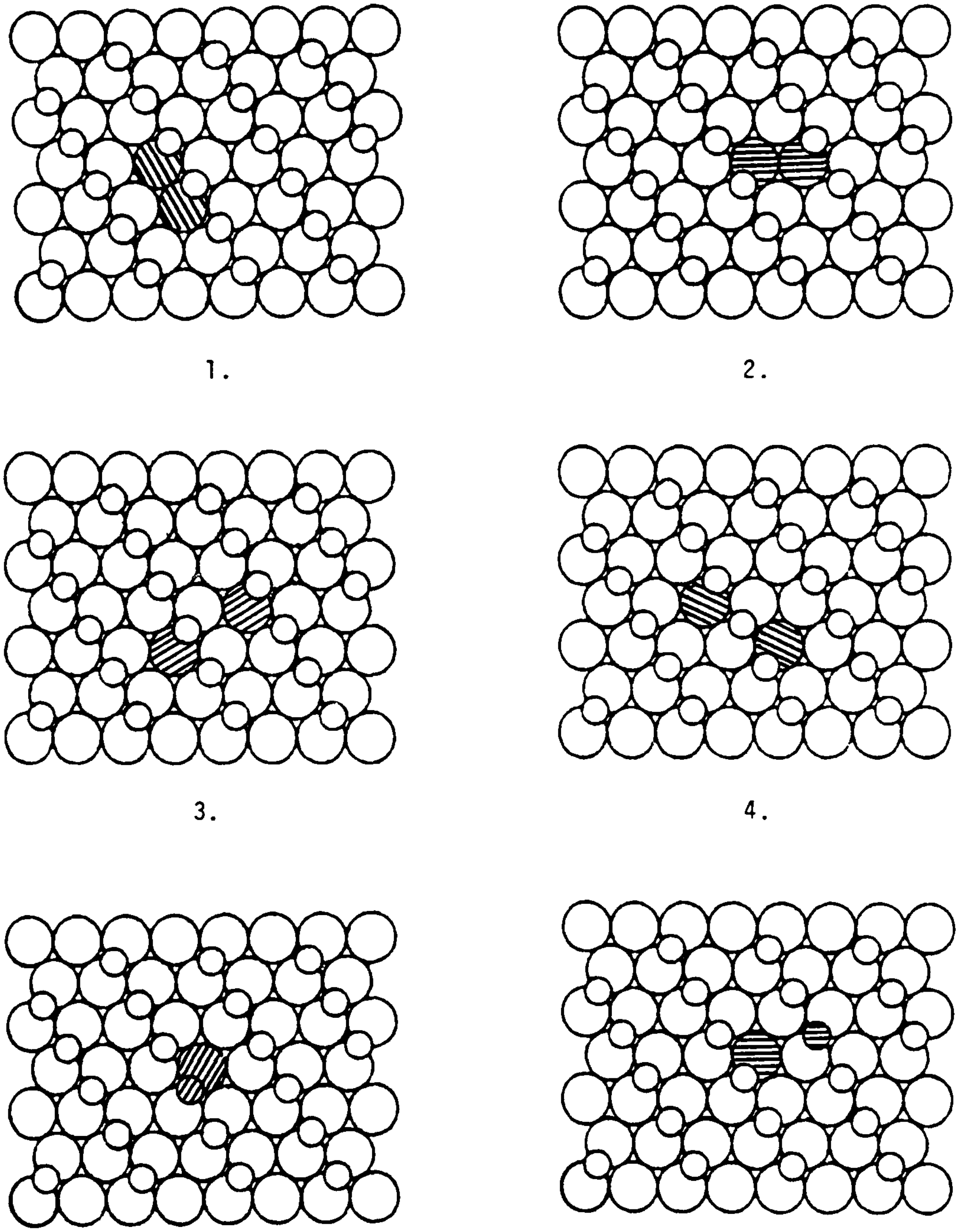

1. 2. 3. 4. 5. 6.

Fig. 78. Origin of sputtered atoms, Ti C(2x2) bridge.

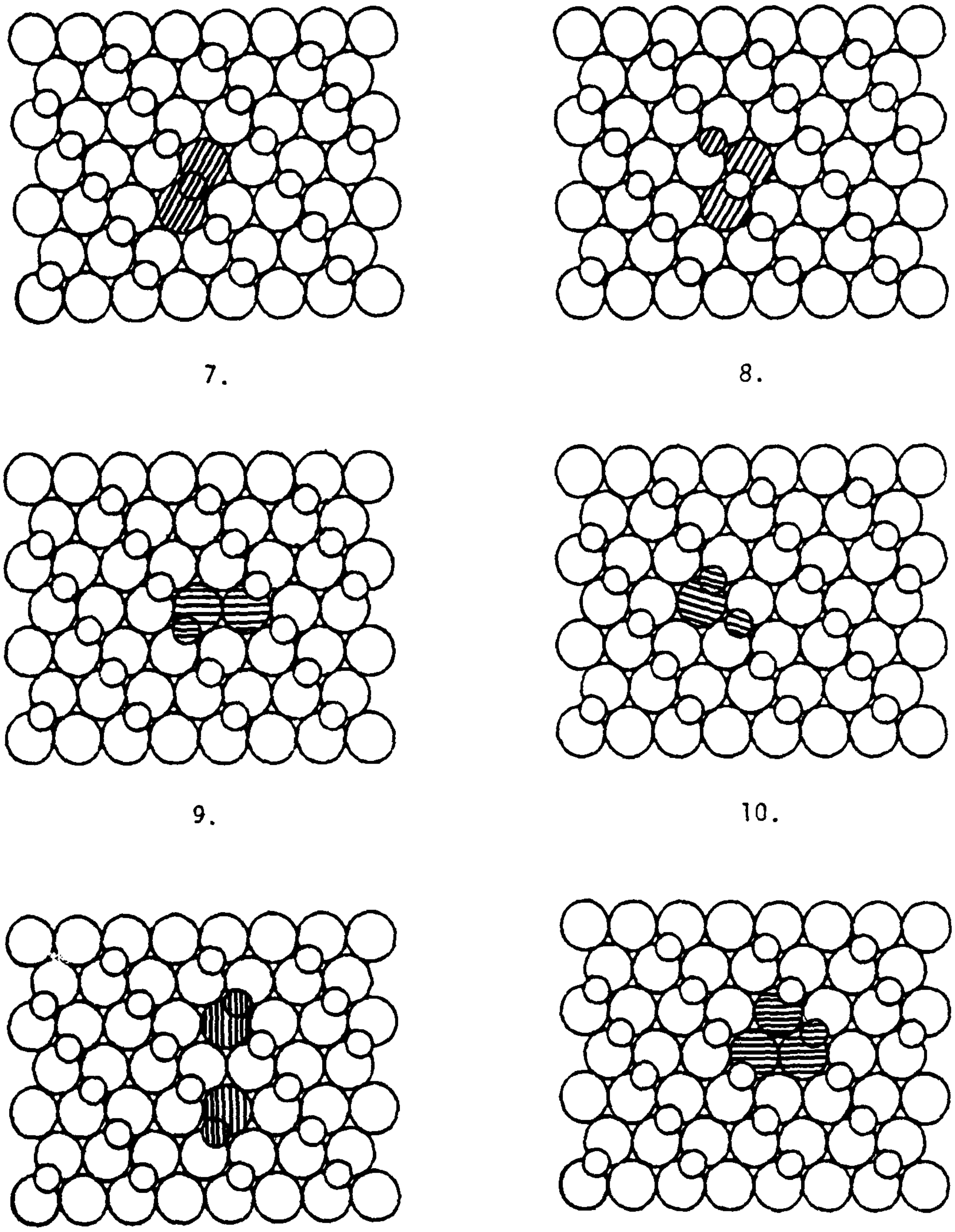

7.

8.

9.

10.

11.

12.

Fig. 78 (cont.).

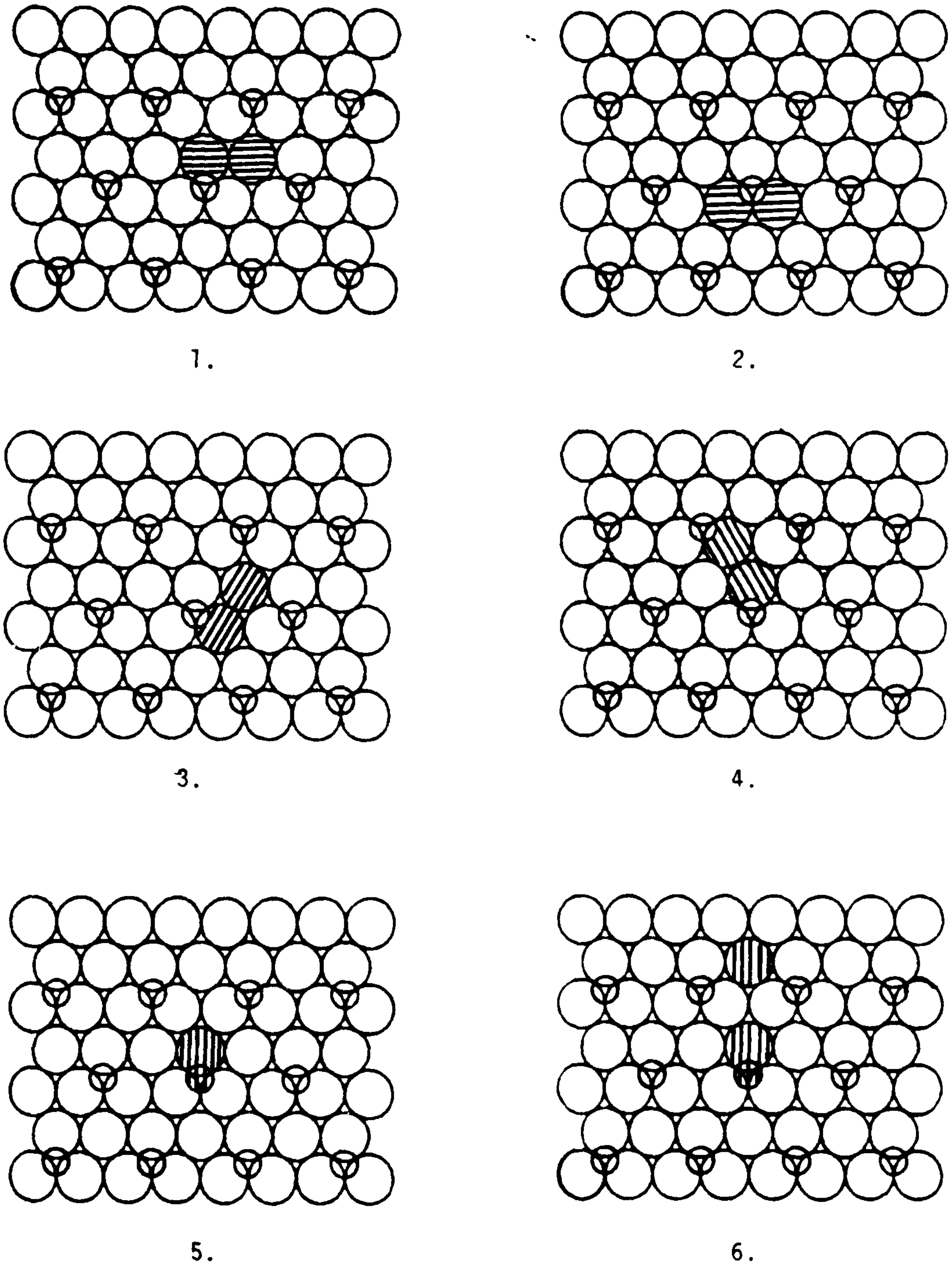

Fig. 79. Origin of sputtered atoms, Ti P(2x2)TFA.

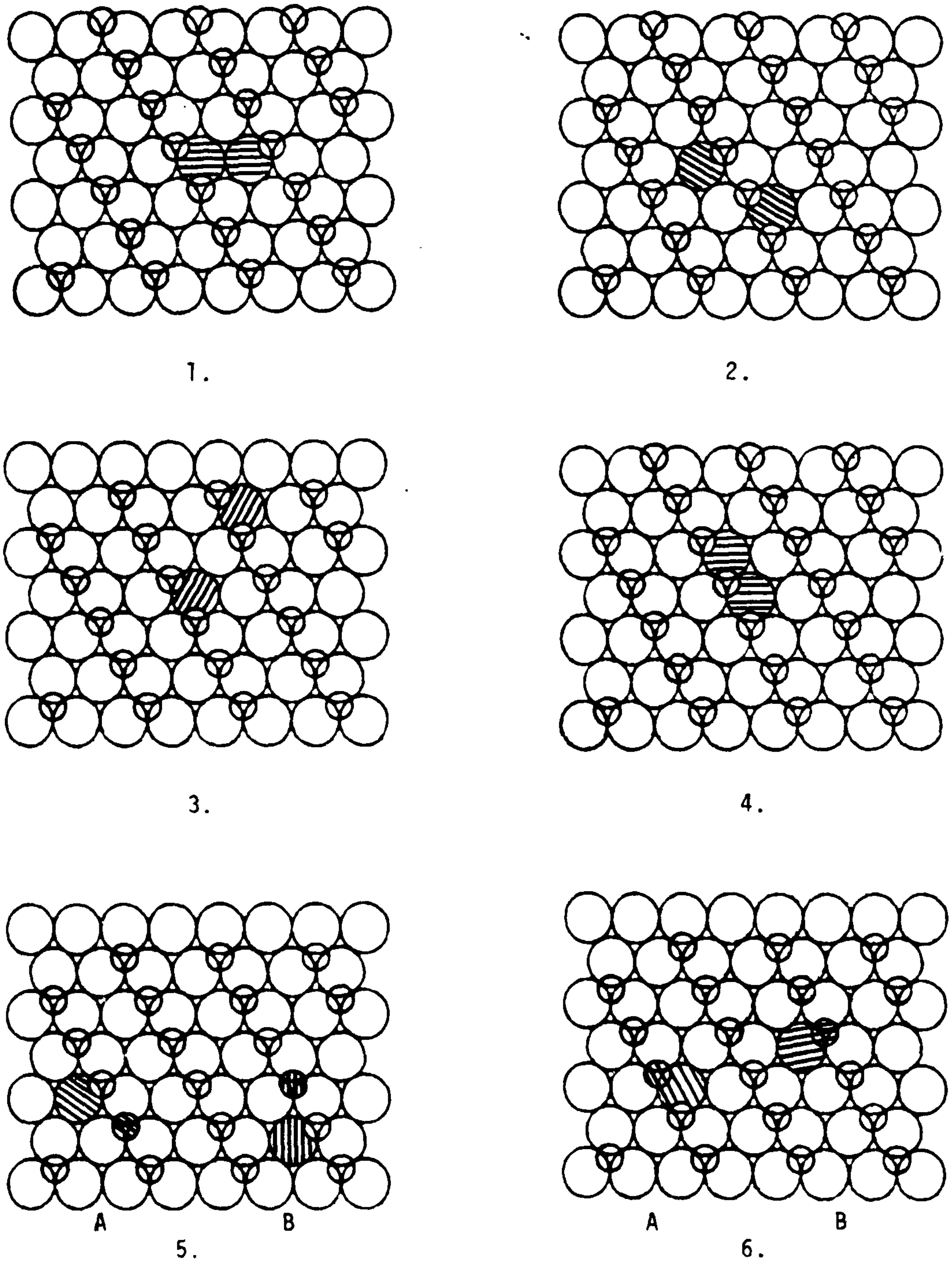

Fig. 80. Origin of sputtered atoms, Ti C(2x2)TFA

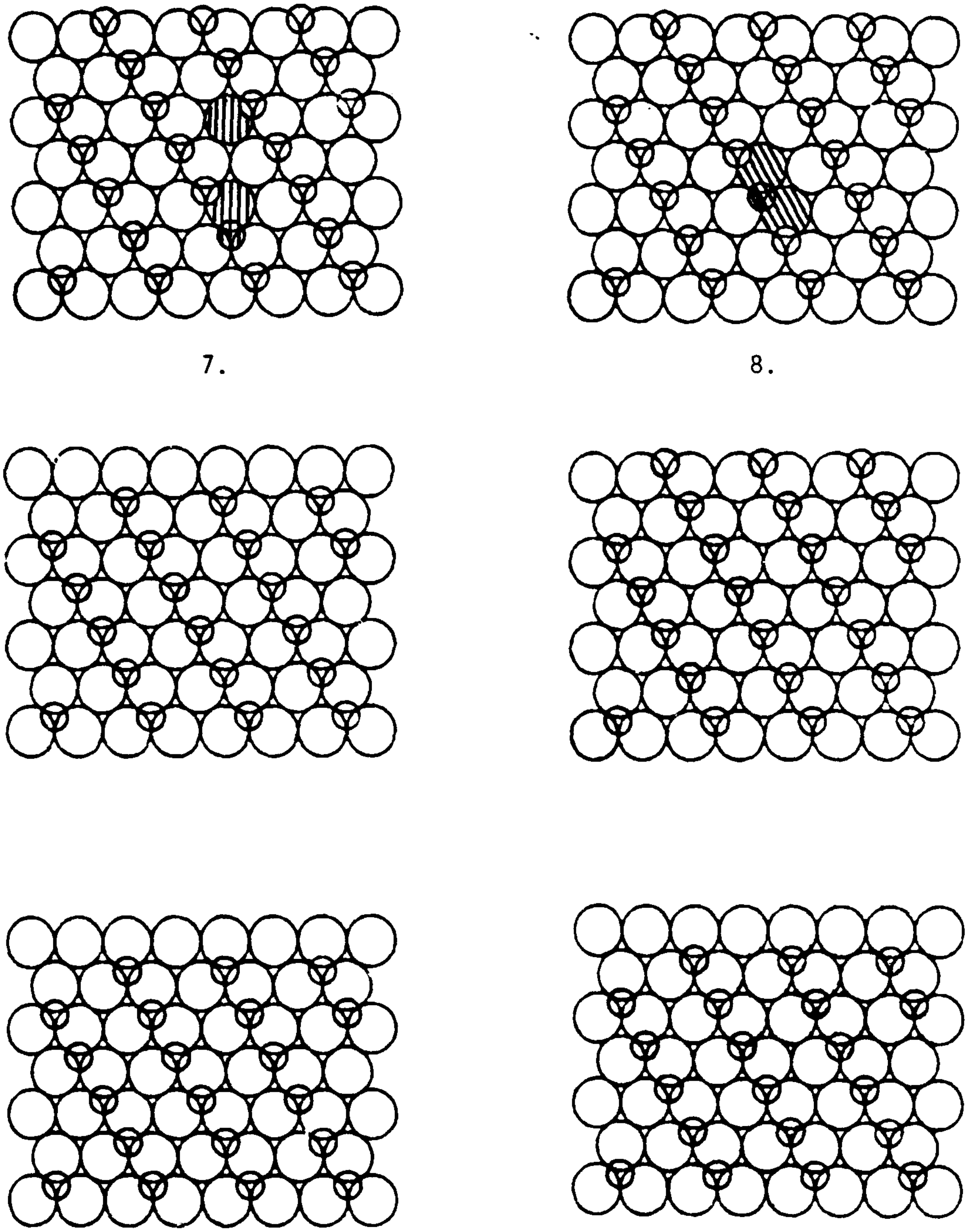

7.

8.

Fig. 80 (cont.).

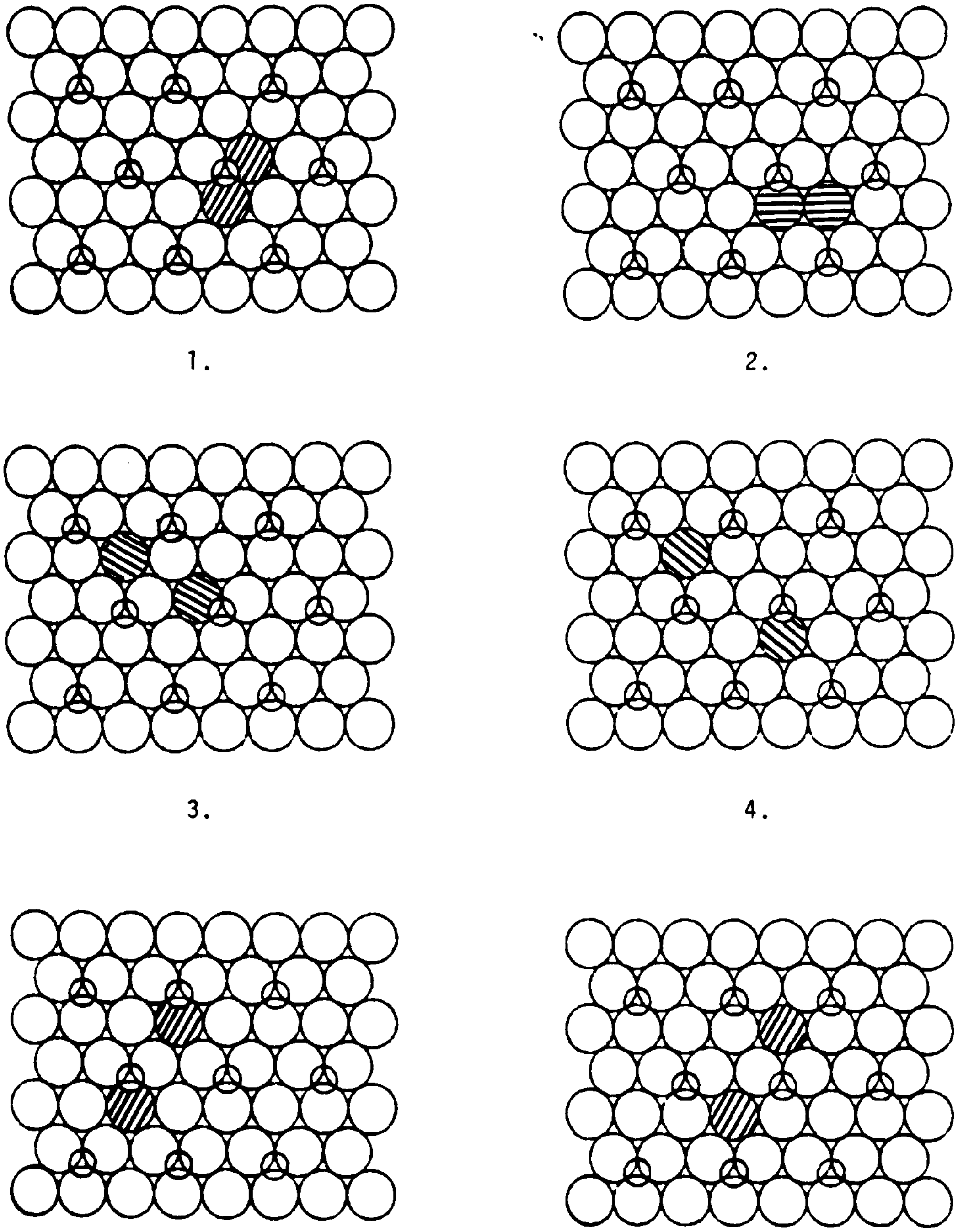

1.

2.

3.

4.

5.

6.

Fig. 81. Origin of sputtered atoms, Ti P(2x2)TFB.

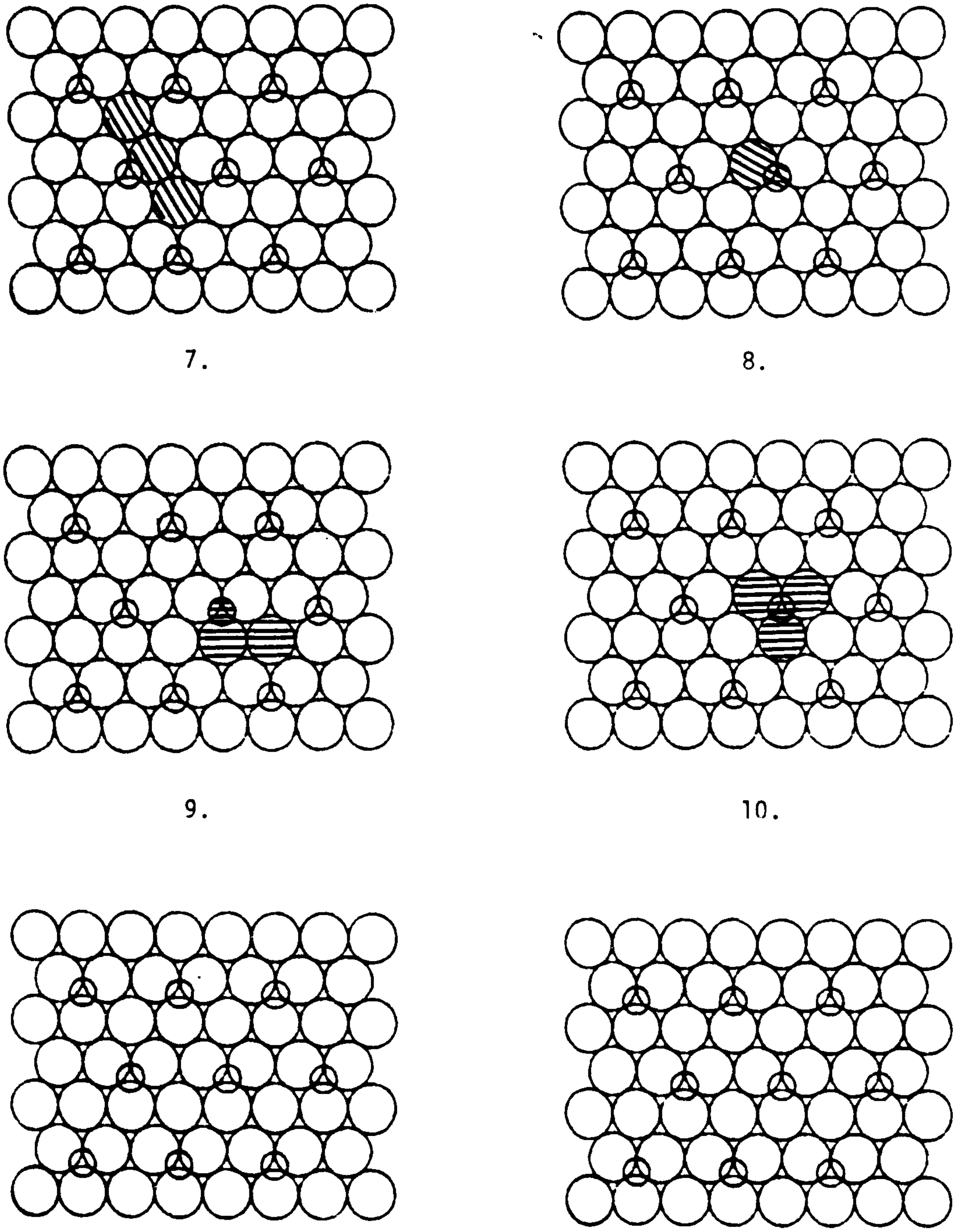

Fig. 81 (cont.).

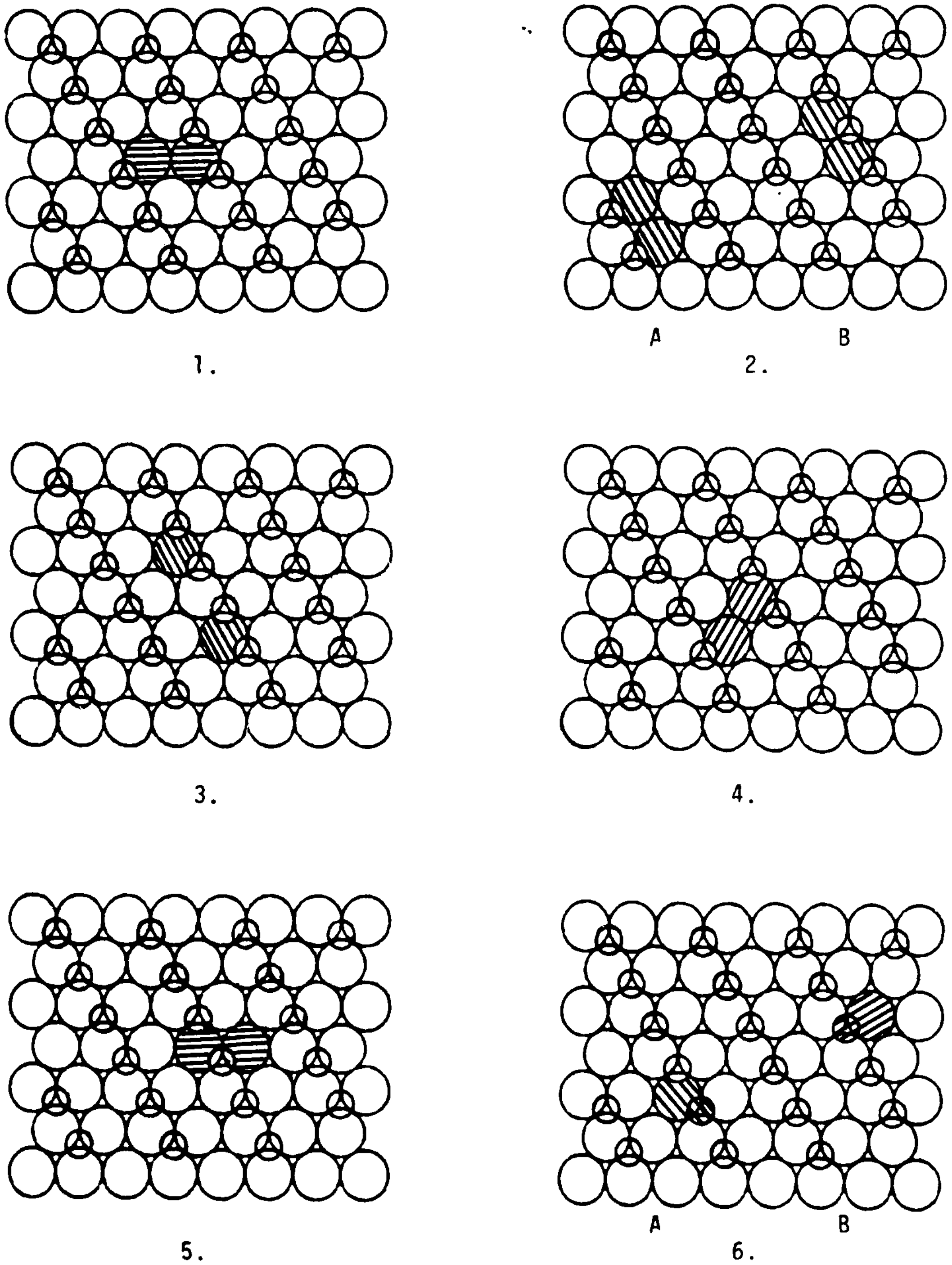

1.

2.

3.

4.

5.

6.

Fig. 82. Origin of sputtered atoms, Ti C(2x2)TFB, 1.0 keV.

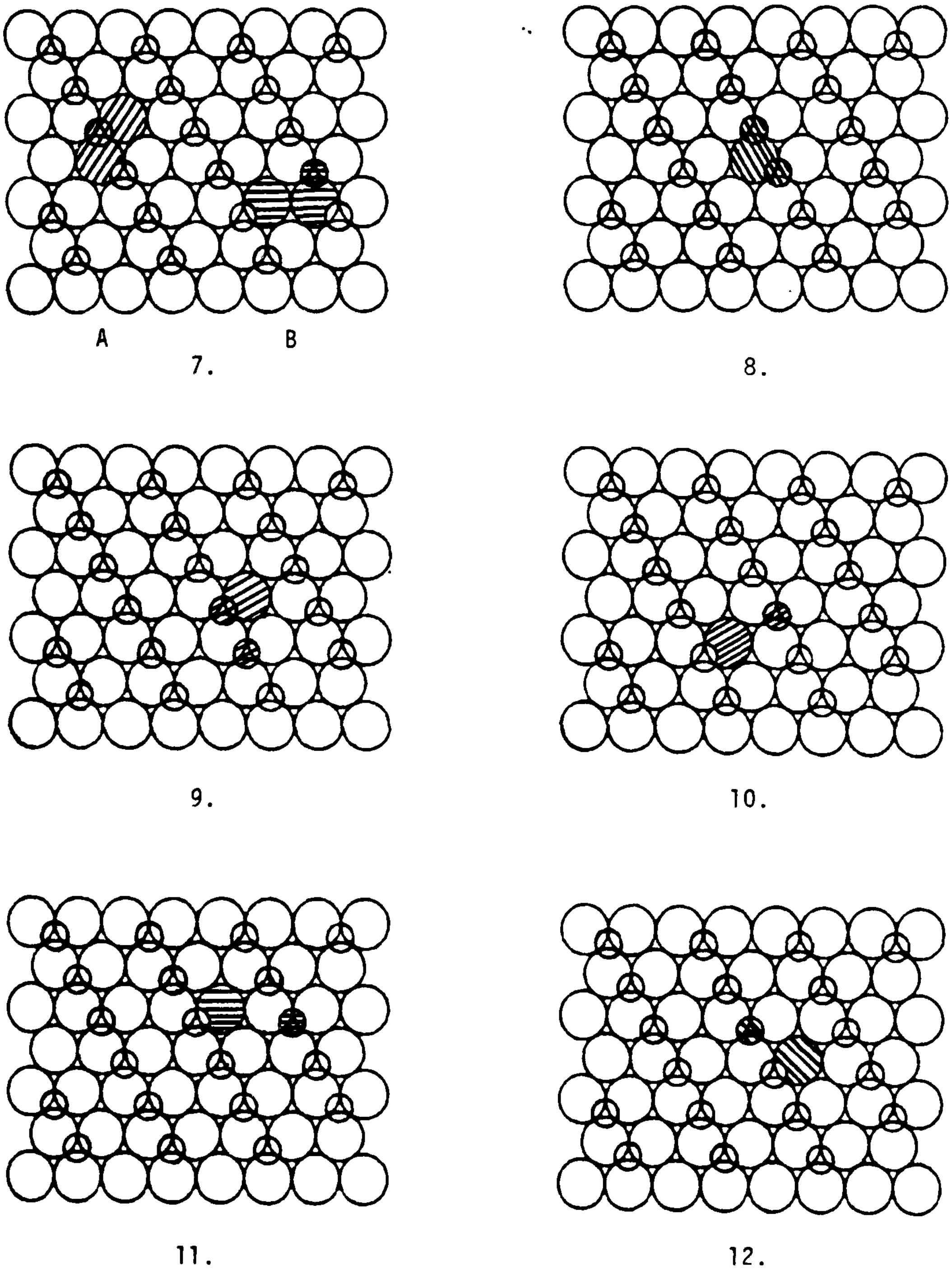

7.

8.

9.

10.

11.

12.

Fig. 82 (cont.).

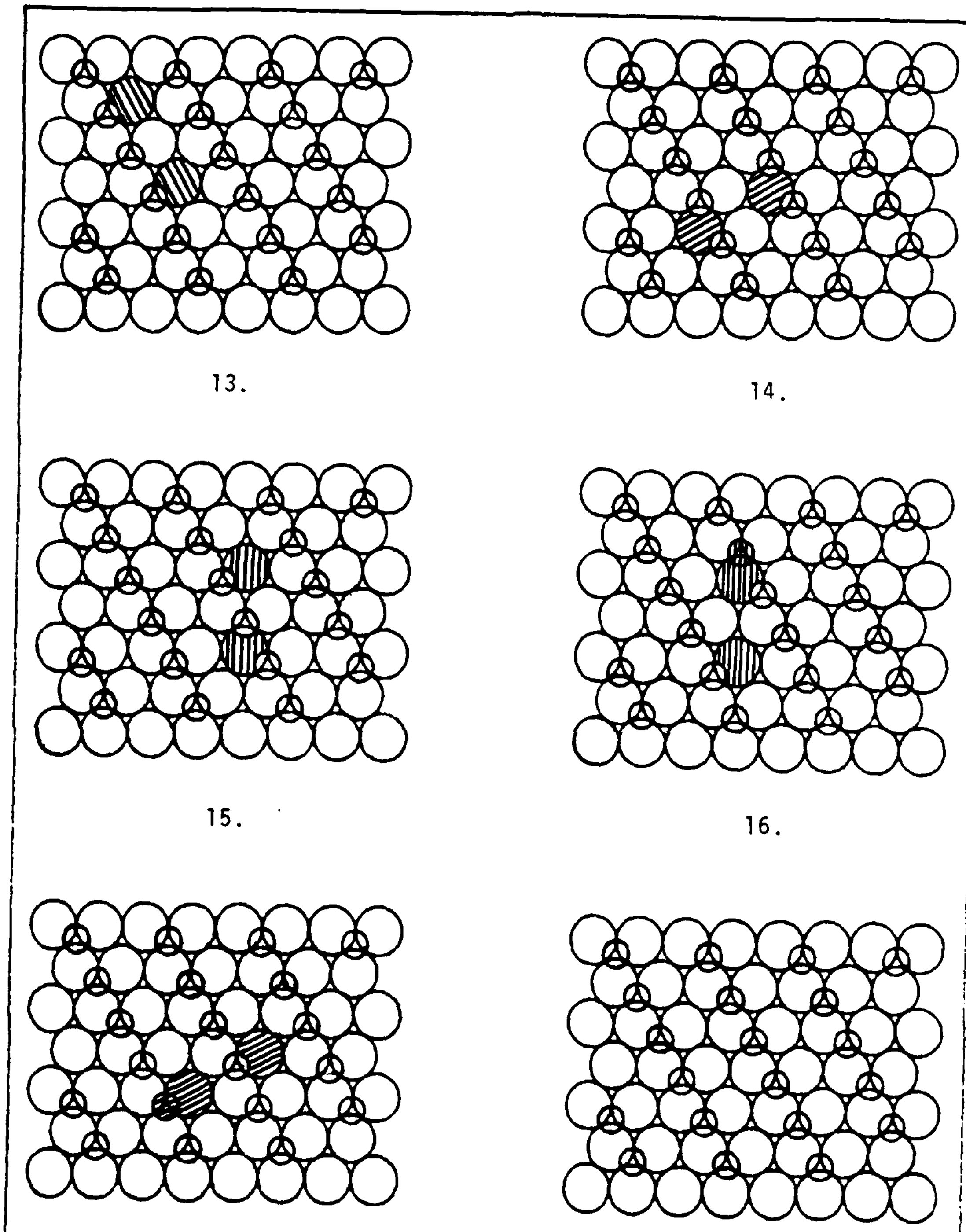

13.

14.

15.

16.

17.

18.

Fig. 82 (cont.).

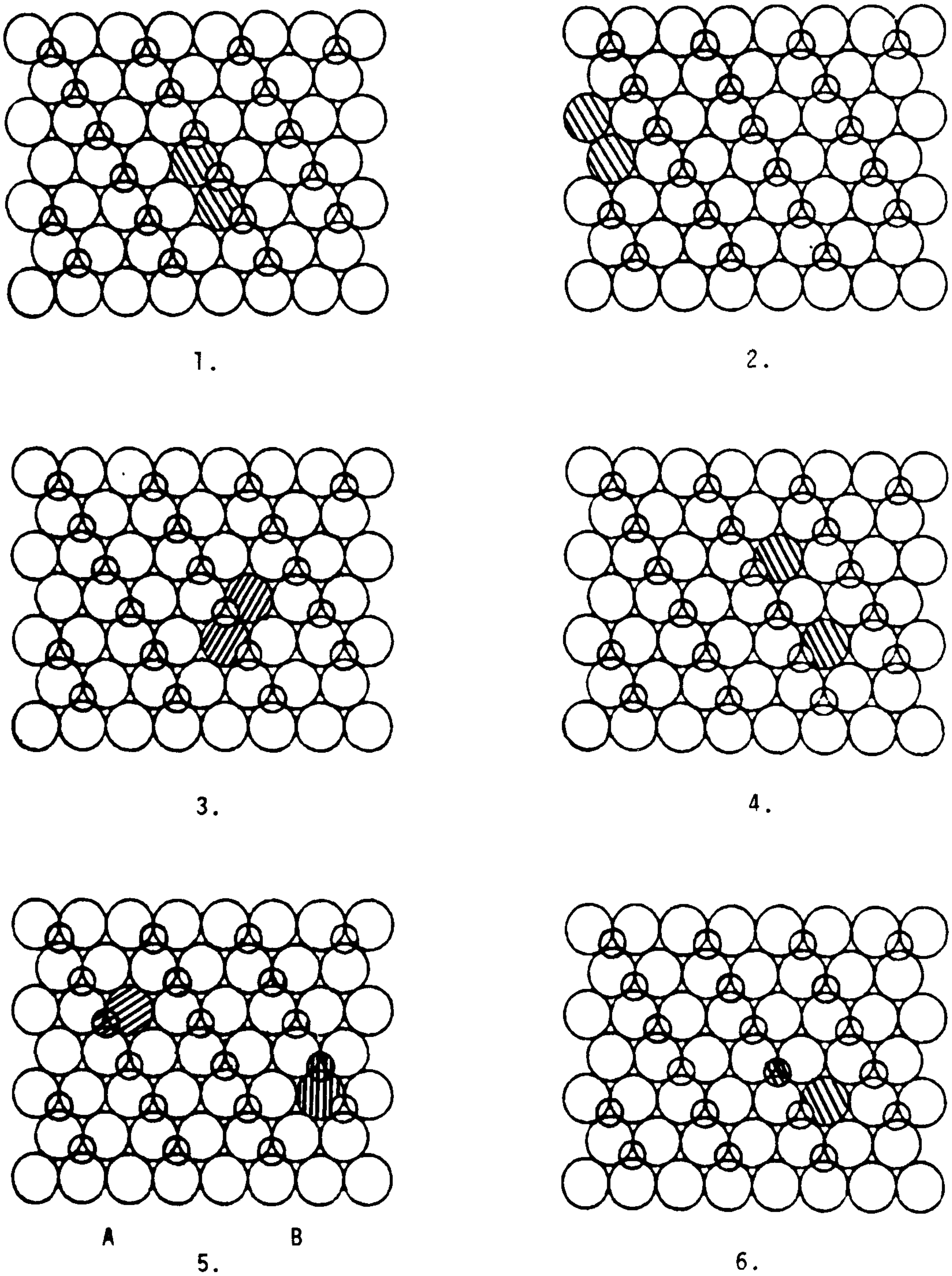

1. 2. 3. 4. 5. 6.

Fig. 83. Origin of sputtered atoms, Ti C(2x2)TFB, 0.5 keV.

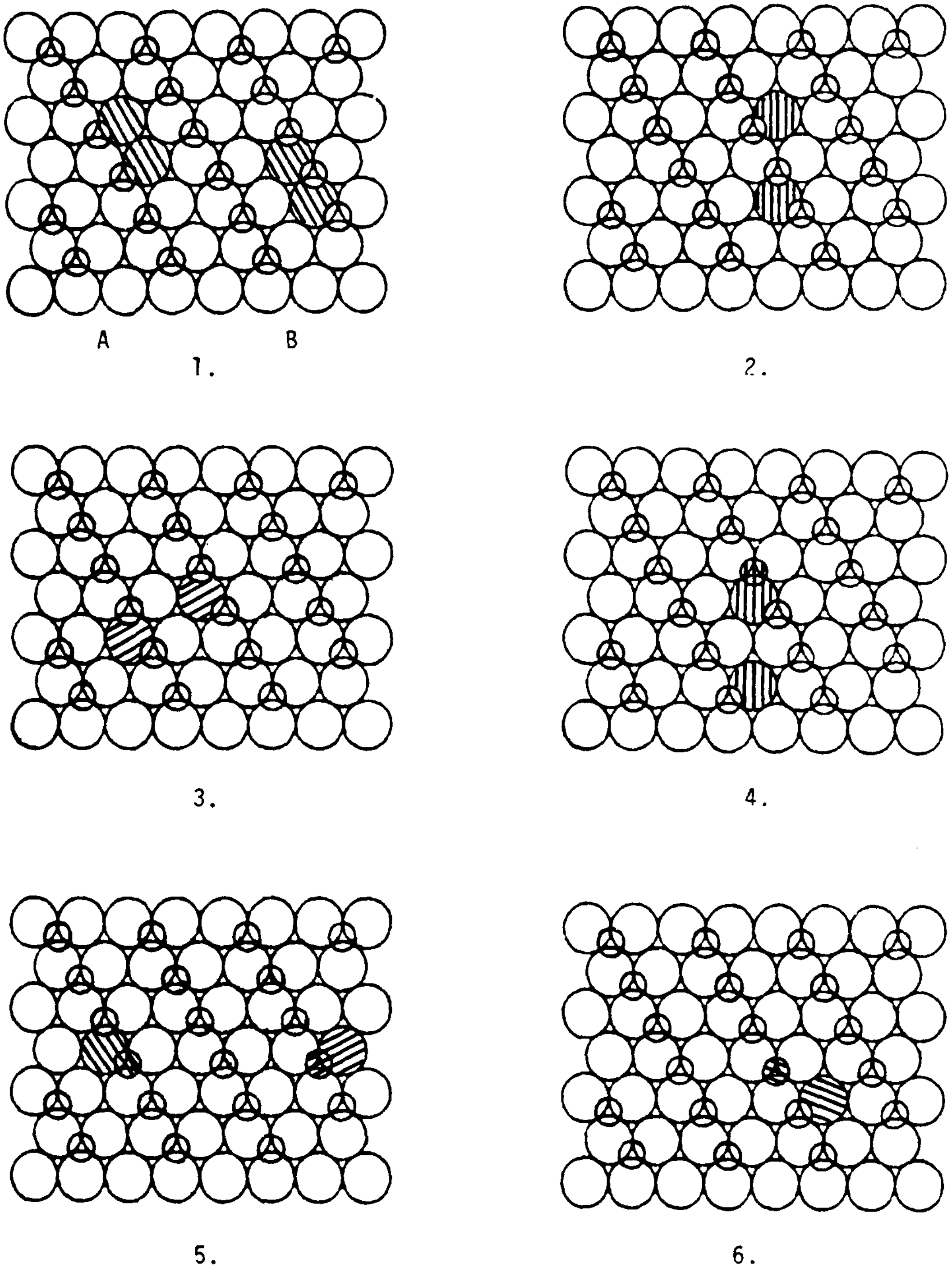

1.

2.

3.

4.

5.

6.

Fig. 84. Origin of sputtered atoms, Ti C(2x2)TFB, 2.0 keV.

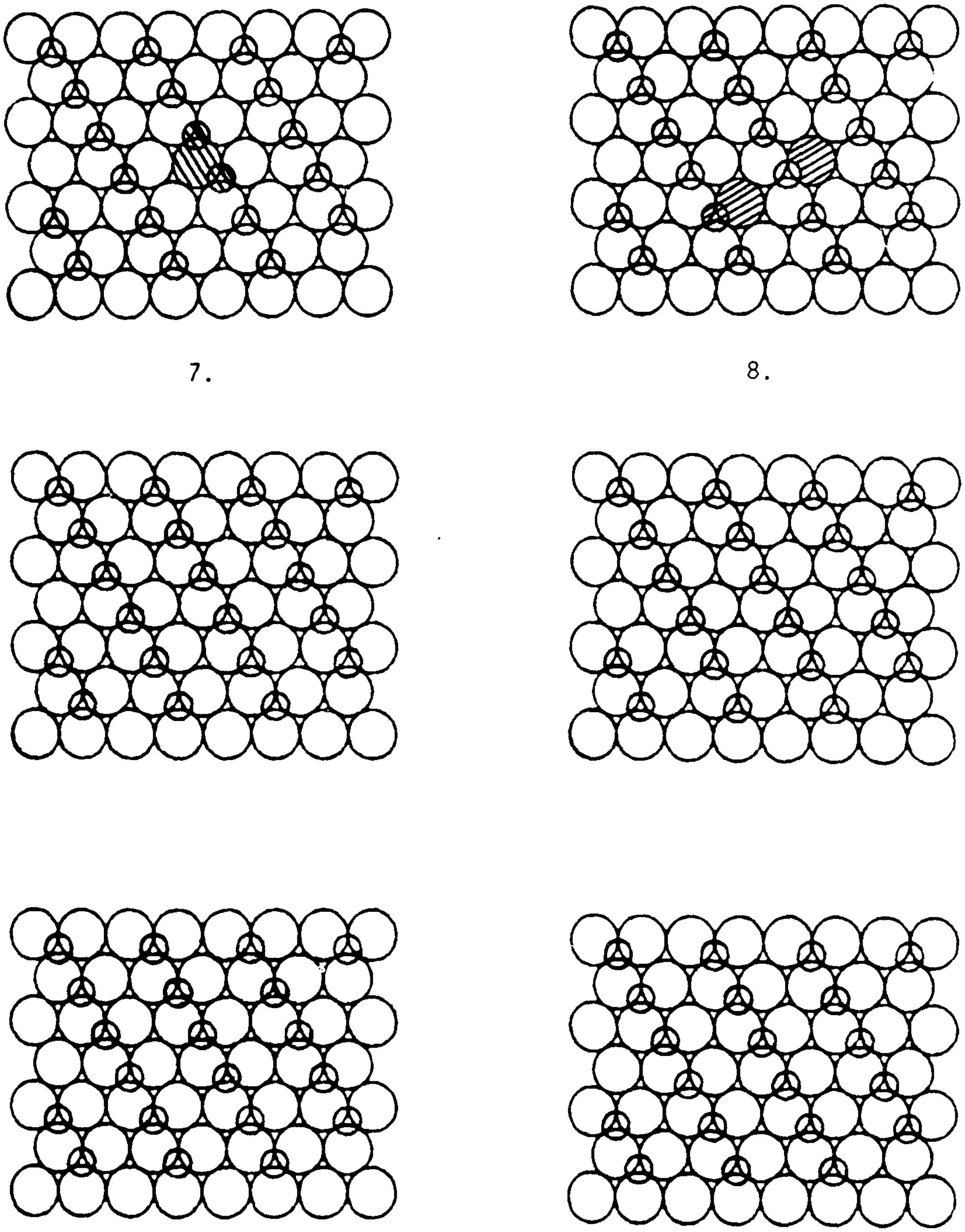

7.

8.

Fig. 84 (cont.).

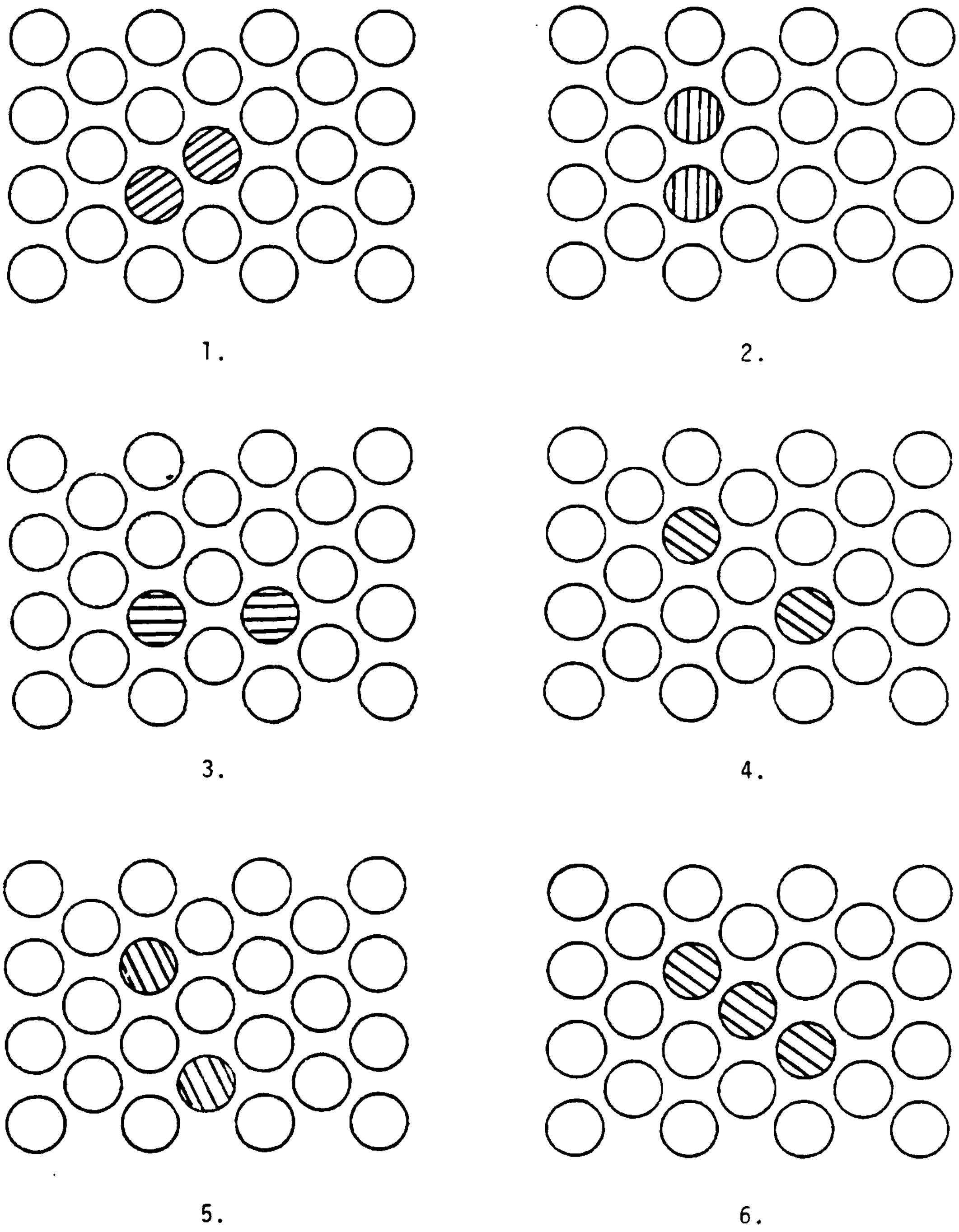

Fig. 85. Origin of sputtered atoms, V and Nb clean surface.

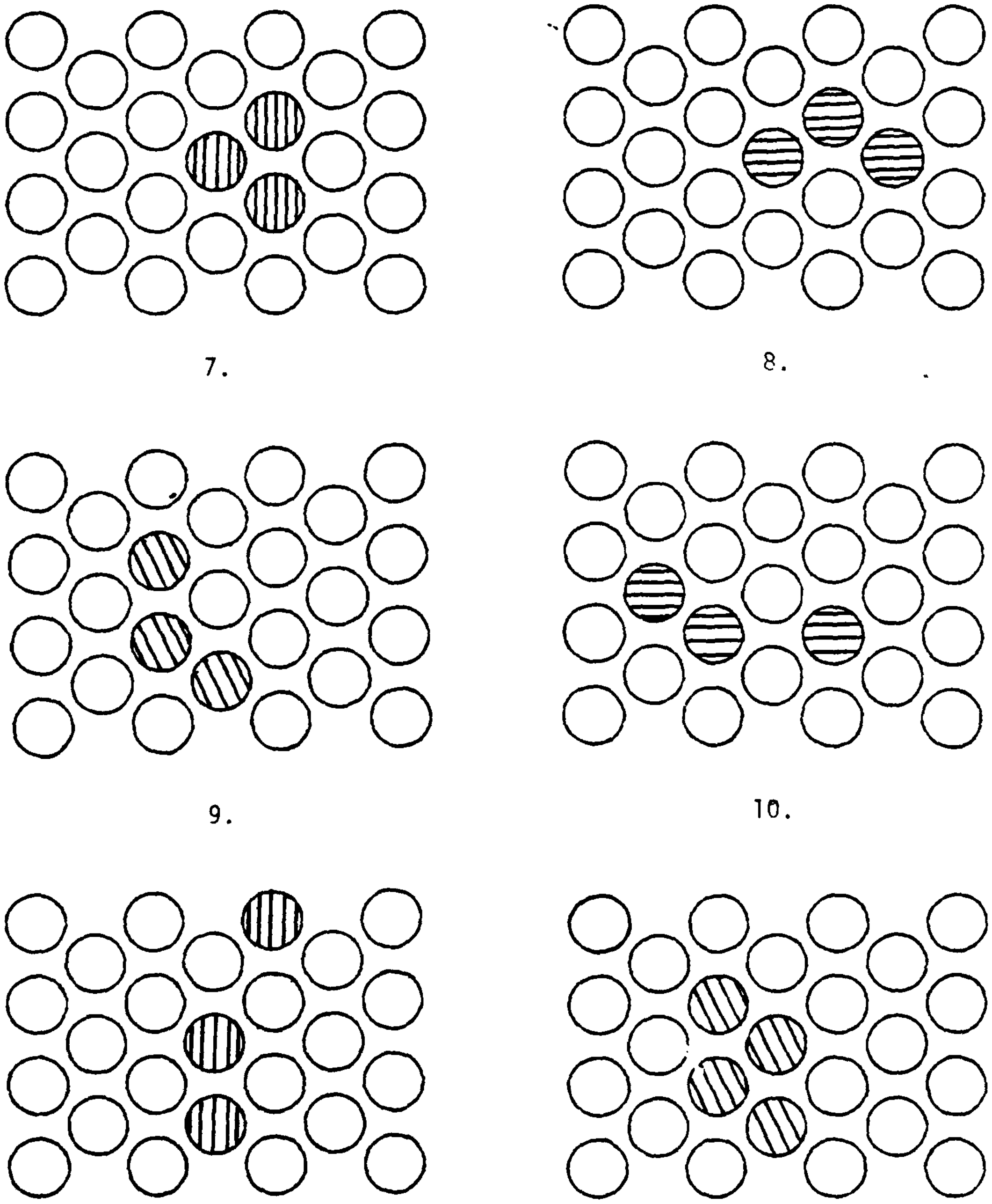

7. 8. 9. 10. 11. 12.

Fig. 85 (cont.).

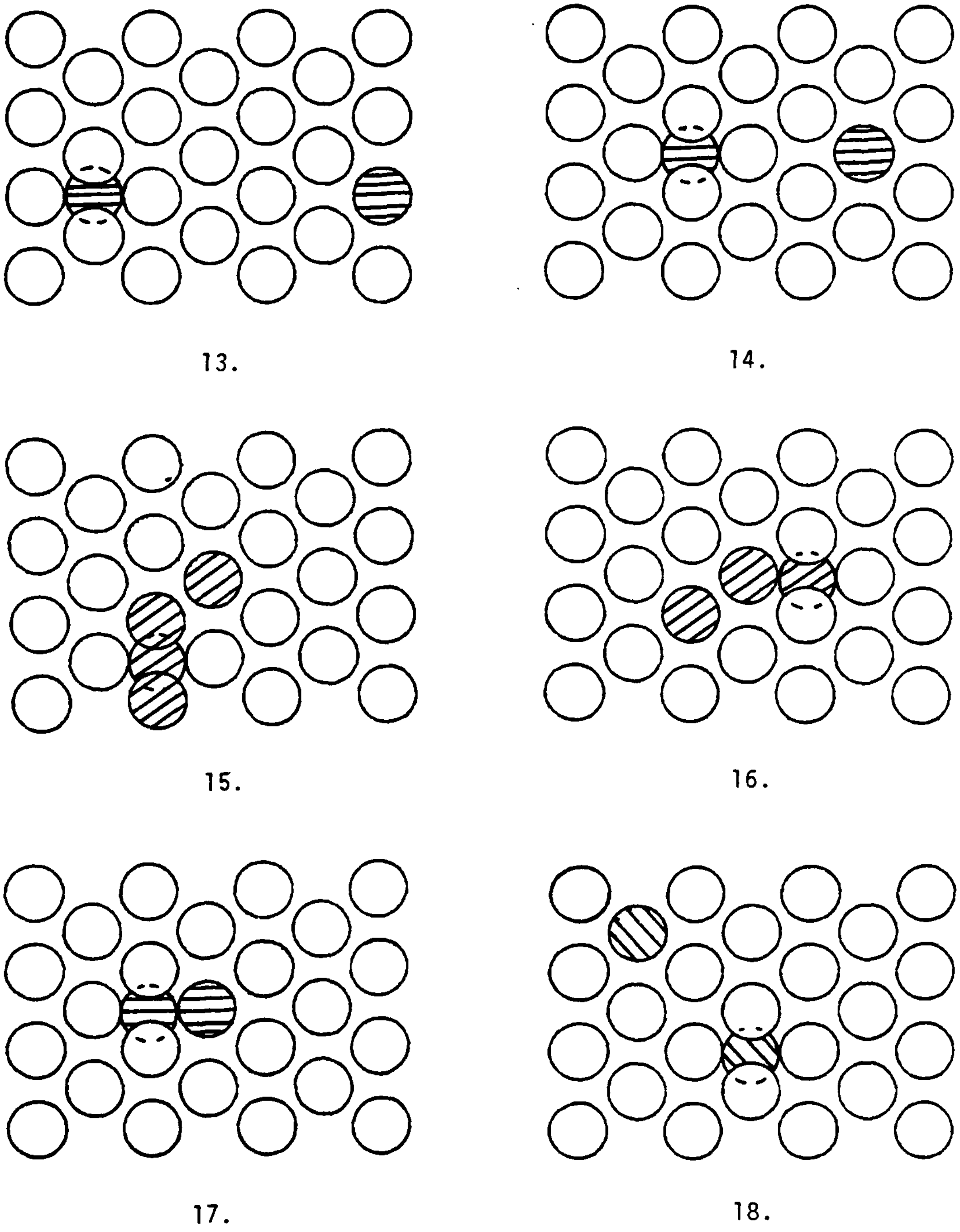

Fig. 85 (cont.). Dashed lines indicate second layer atoms.

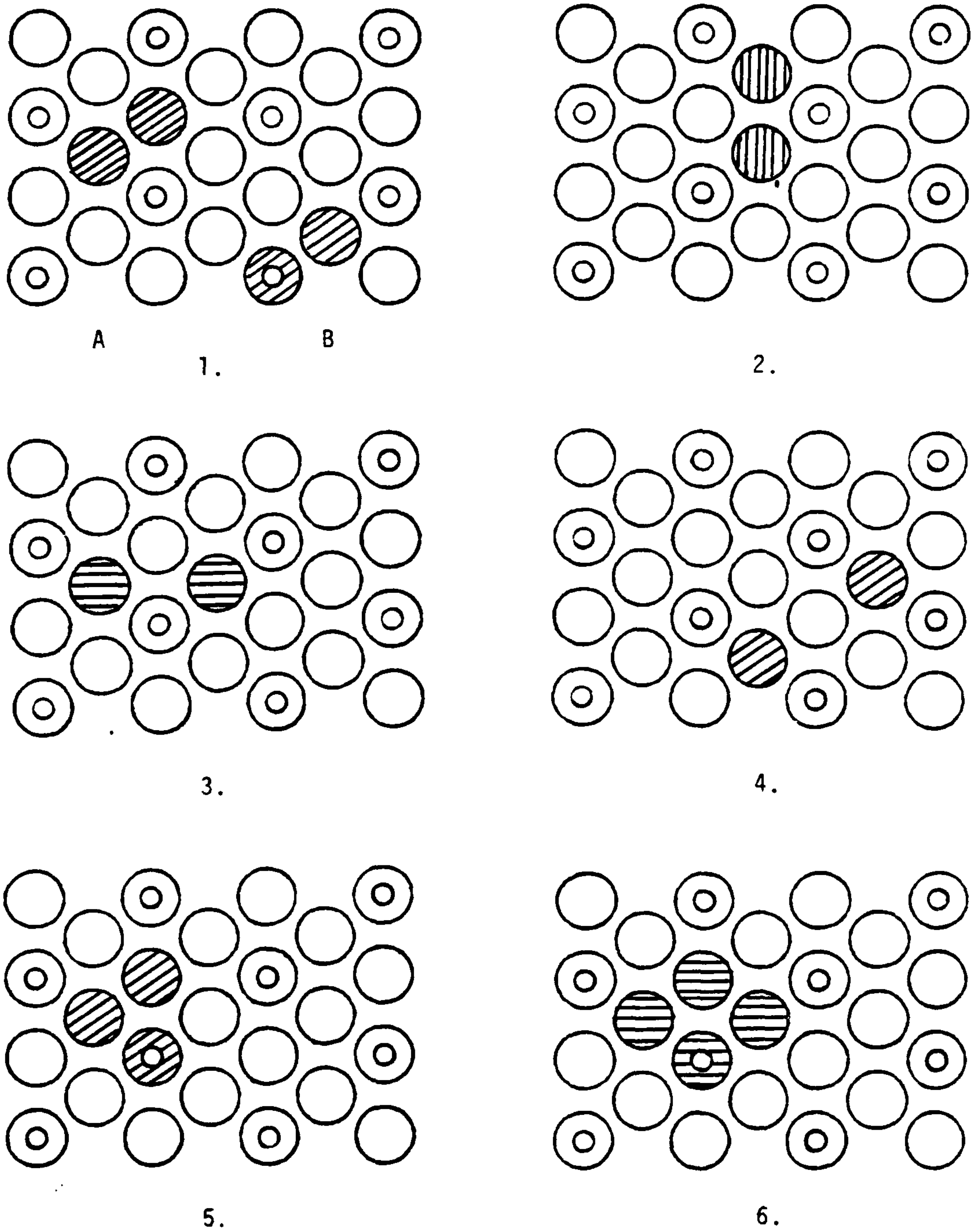

Fig. 86. Origin of sputtered atoms, V and Nb P(2x2) A-top.

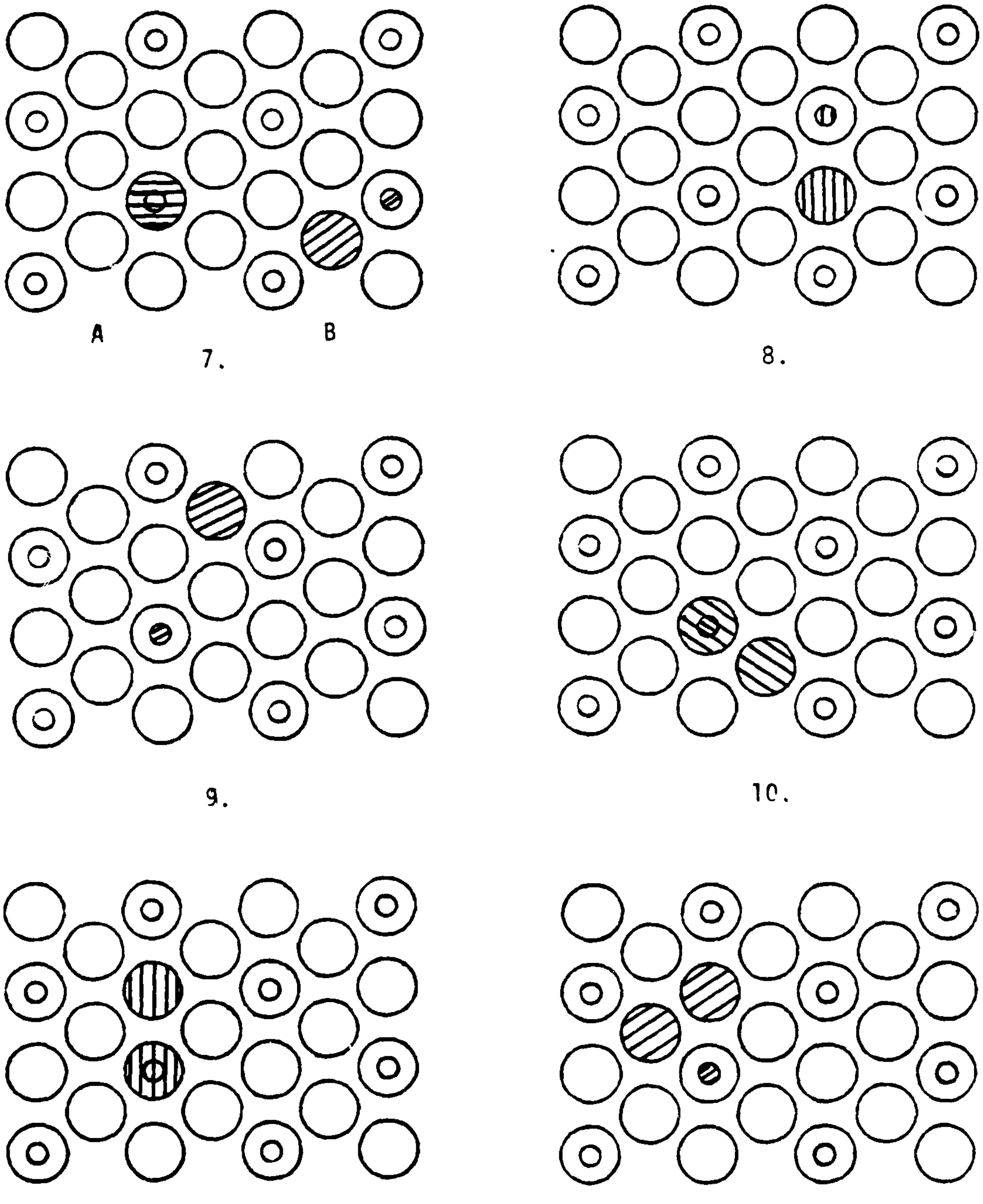

7.

8.

9.

10.

11.

12.

Fig. 86 (cont.).

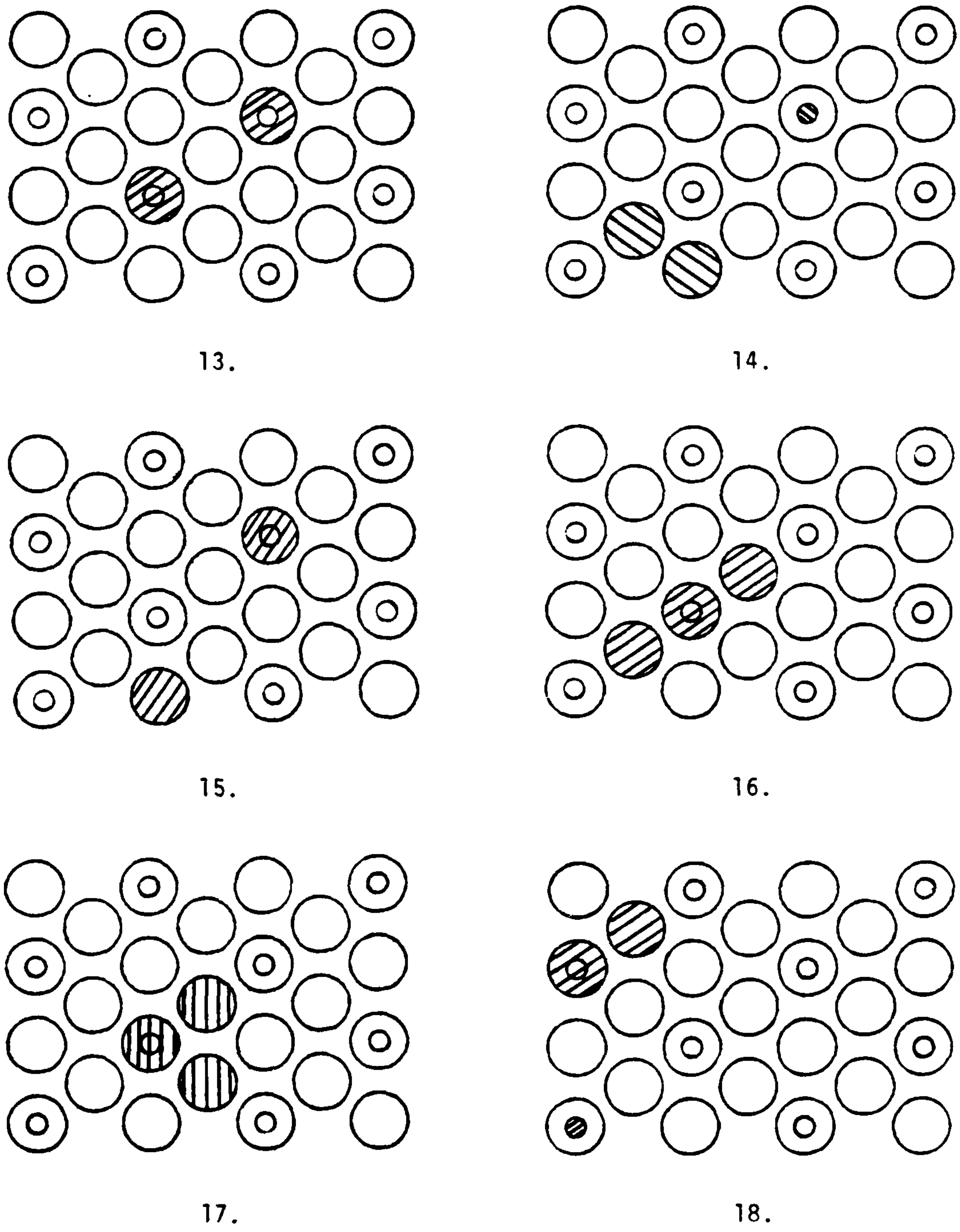

13. 14. 15. 16. 17. 18.

Fig. 86 (cont.).

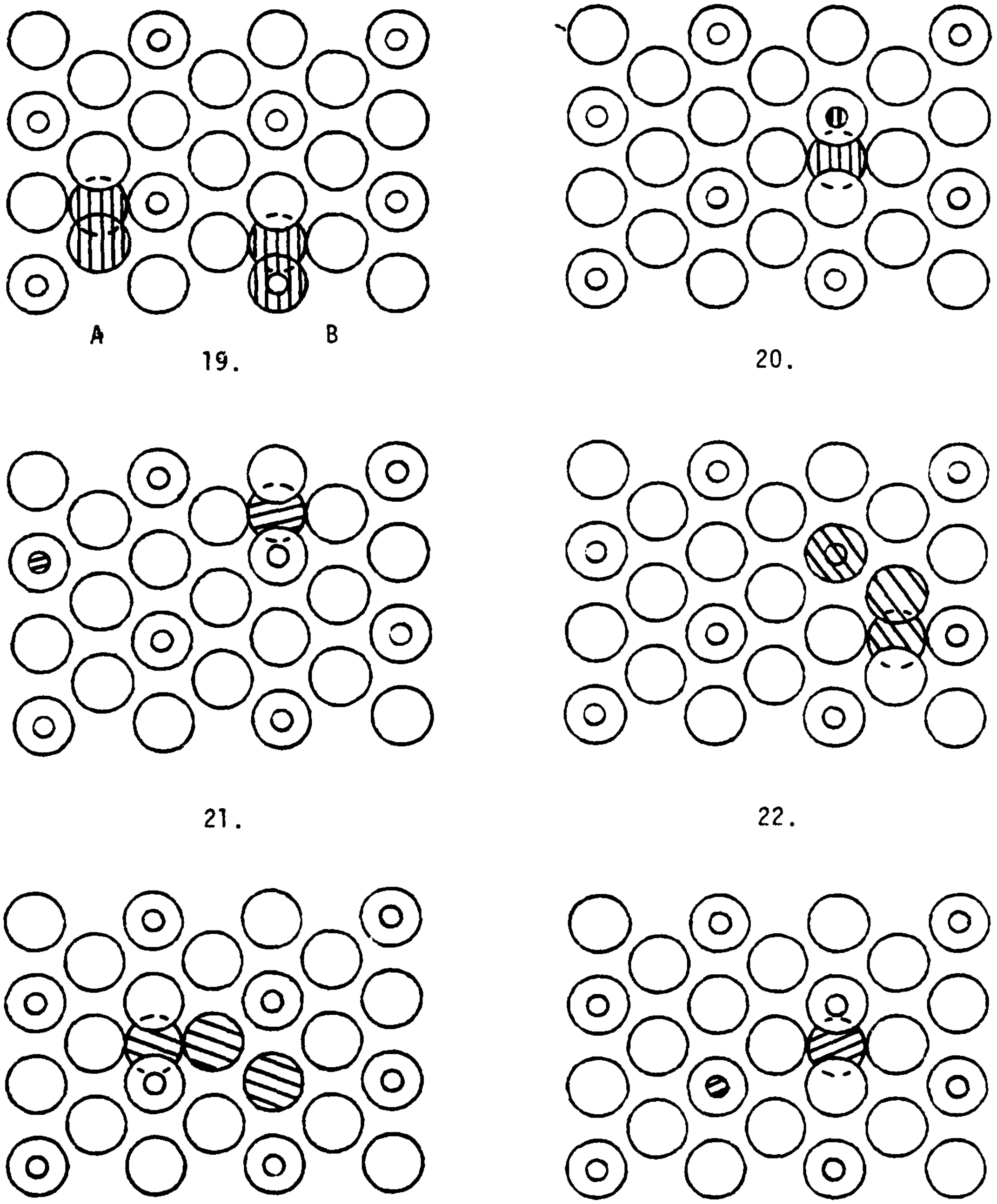

19.

20.

21.

22.

23.

24.

Fig. 86 (cont.).

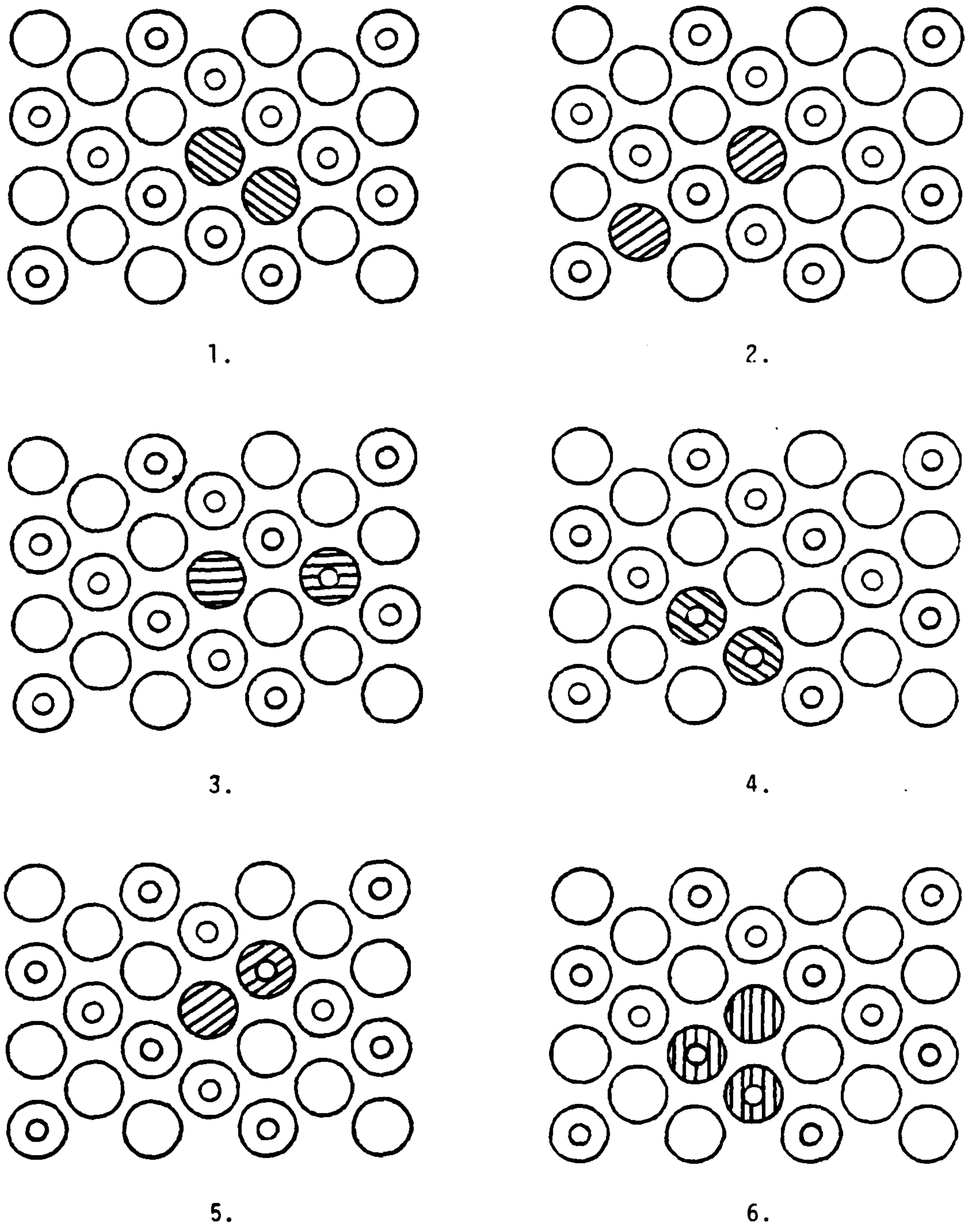

Fig. 87. Origin of sputtered atoms, V and Nb C(2x2) A-top.

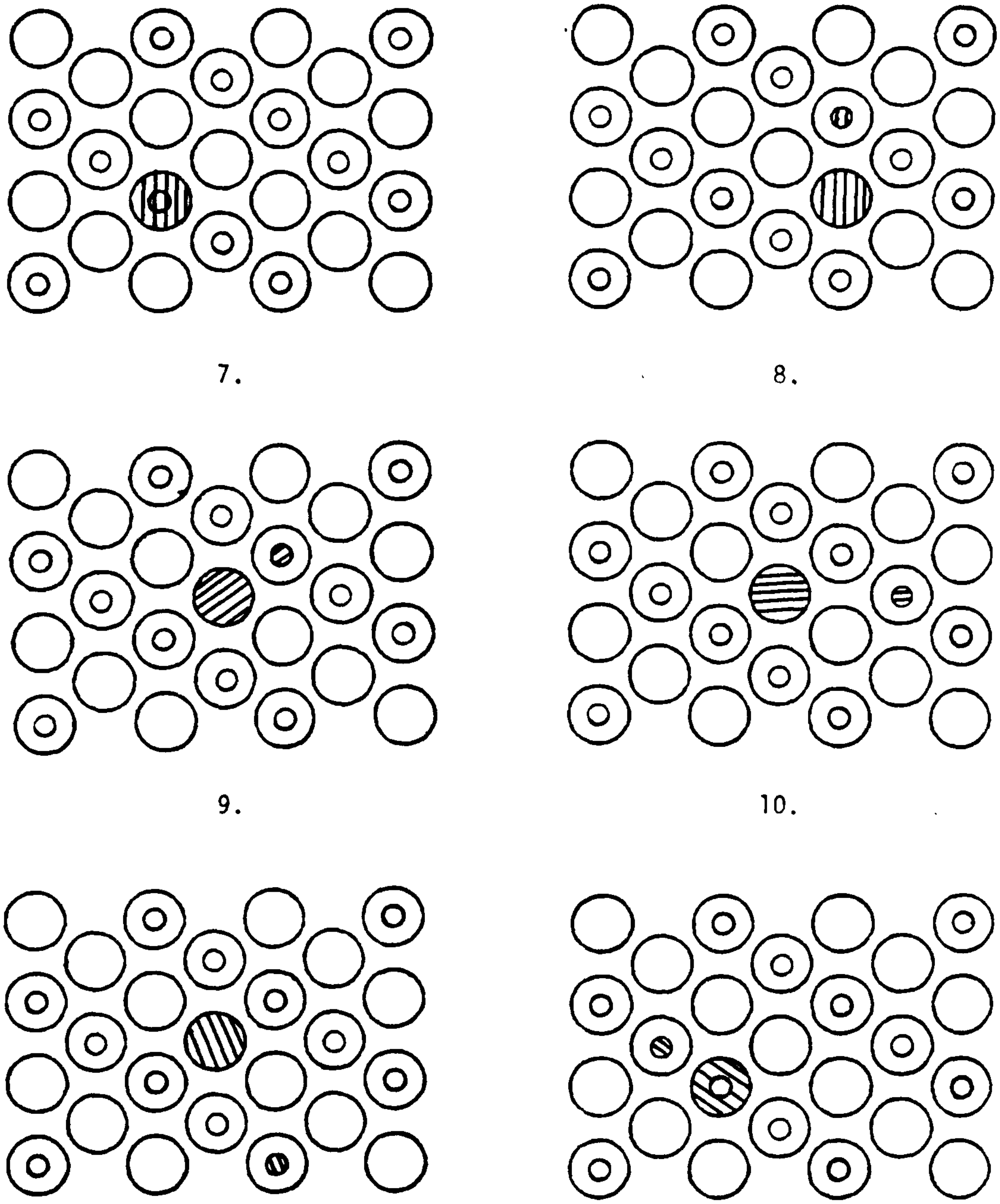

7. 8. 9. 10. 11. 12.

Fig. 87 (cont.).

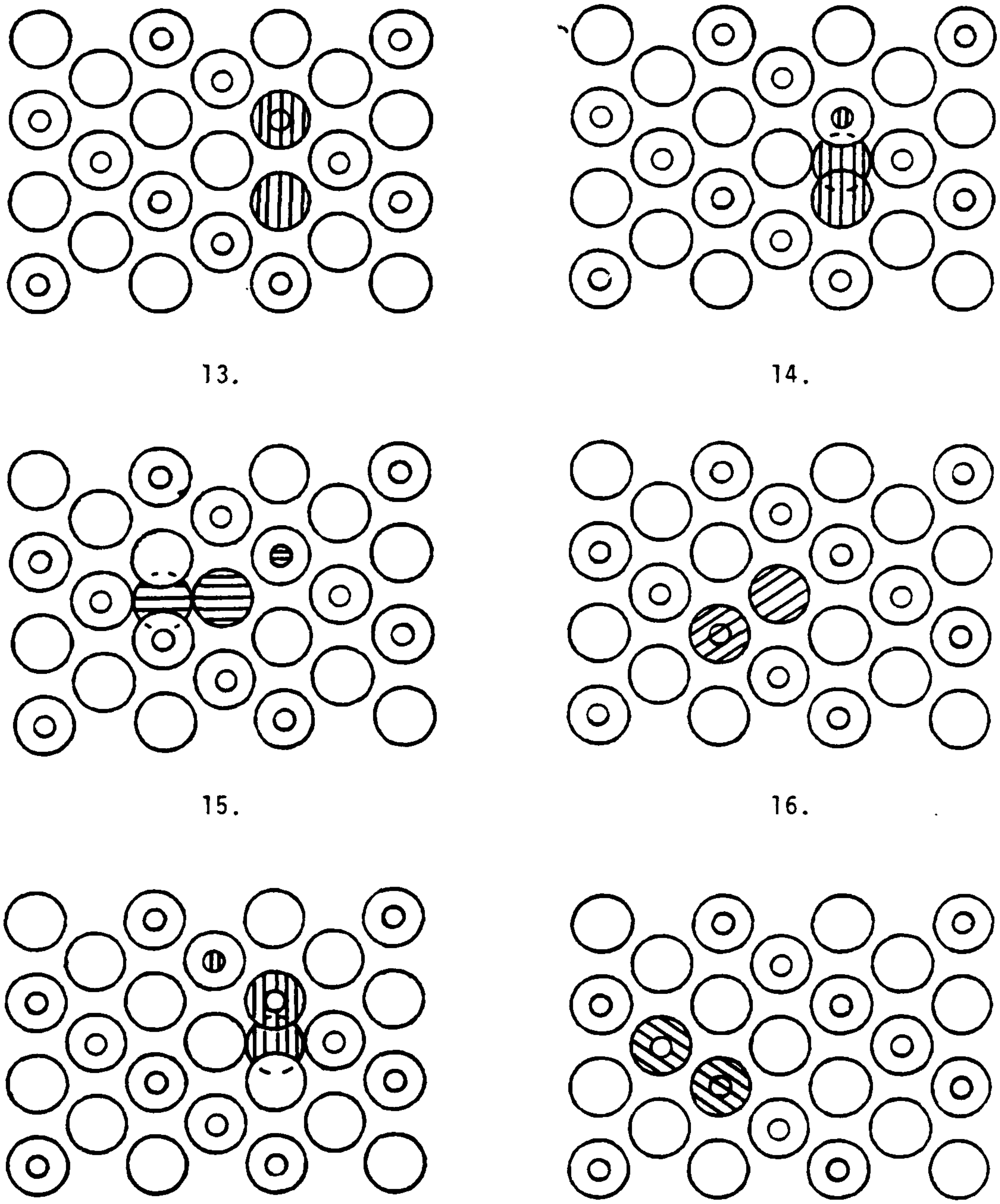

13. 14.

15. 16.

17. 18.

Fig. 87 (cont.).

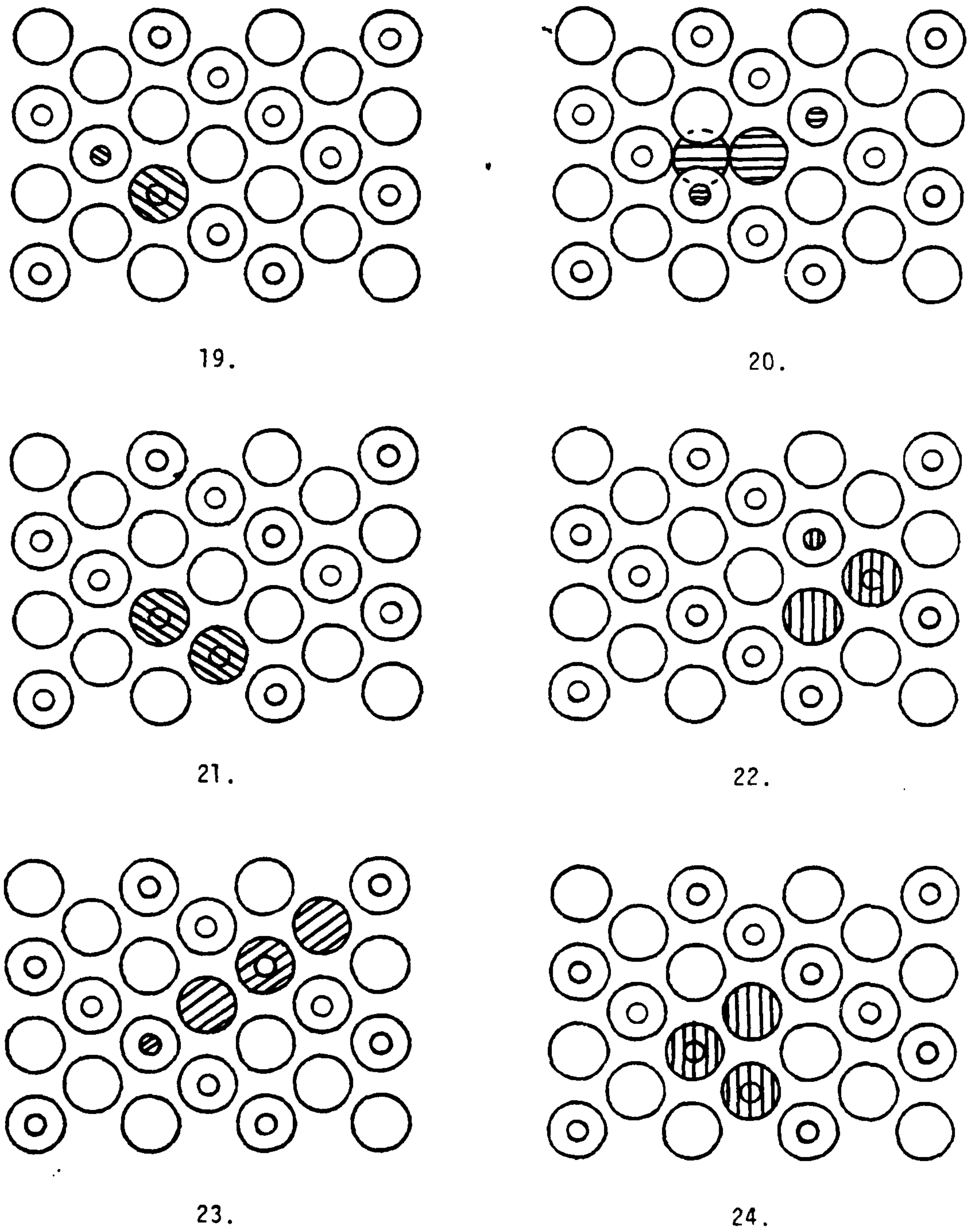

19.

20.

21.

22.

23.

24.

Fig. 87 (cont.).

APPENDIX F

EJECTION TIME DIFFERENCE CHARTS

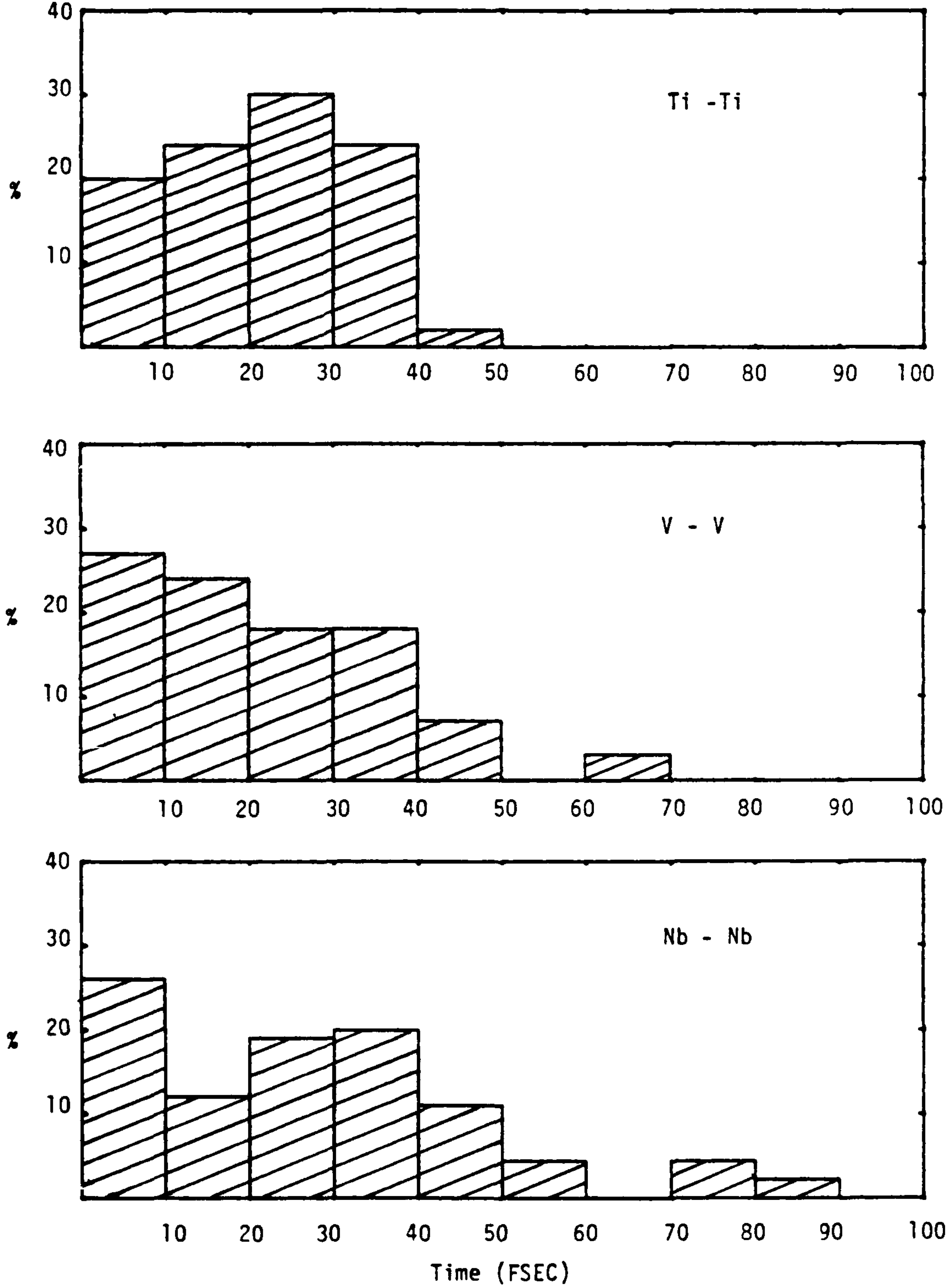

Fig. 88. Ejection time difference for dimers formed from clean metal surfaces.

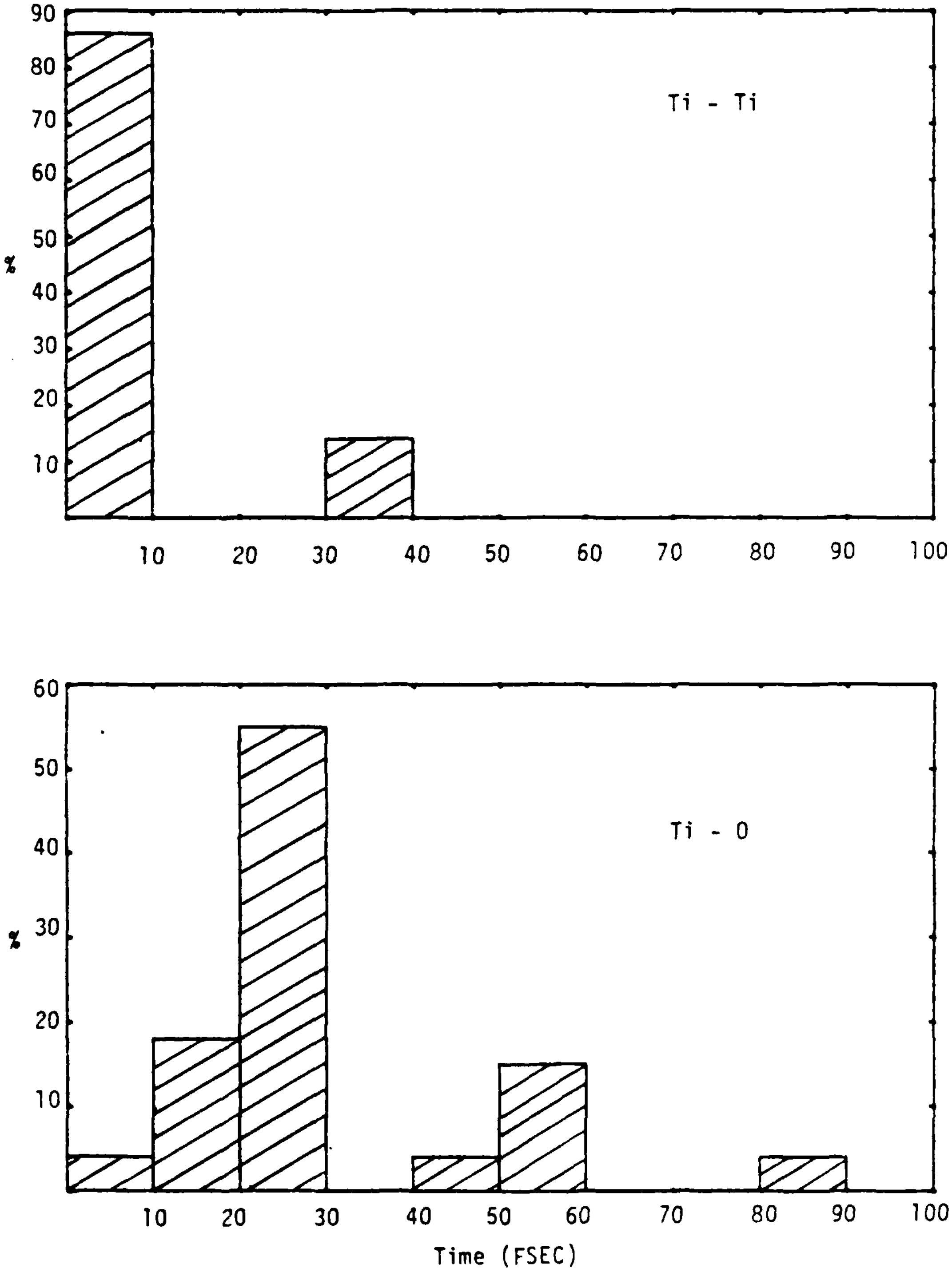

Fig. 89. Ejection time difference for Ti P(2x2) A-top.

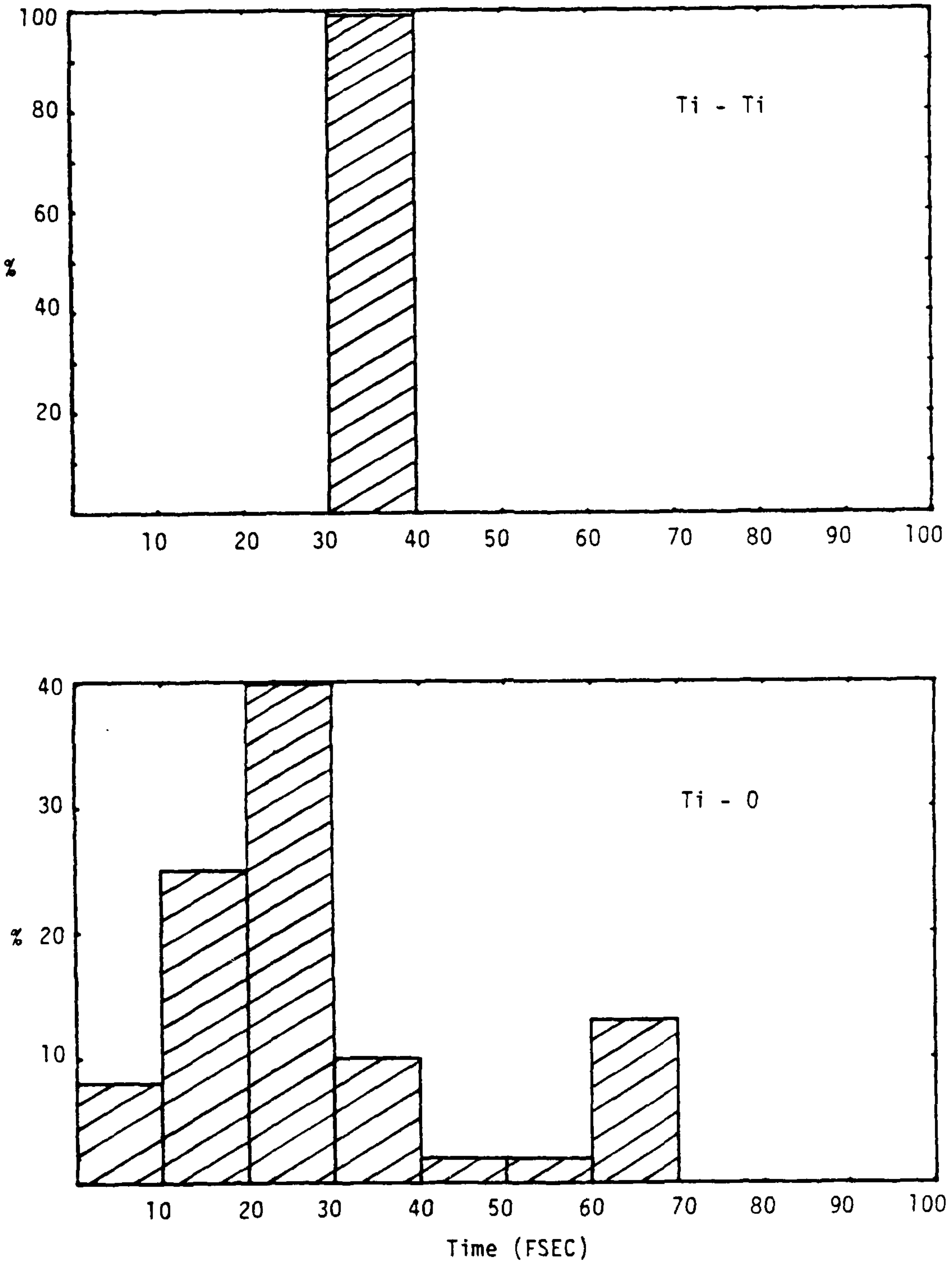

Fig. 90. Ejection time difference for Ti C(2x2) A-top.

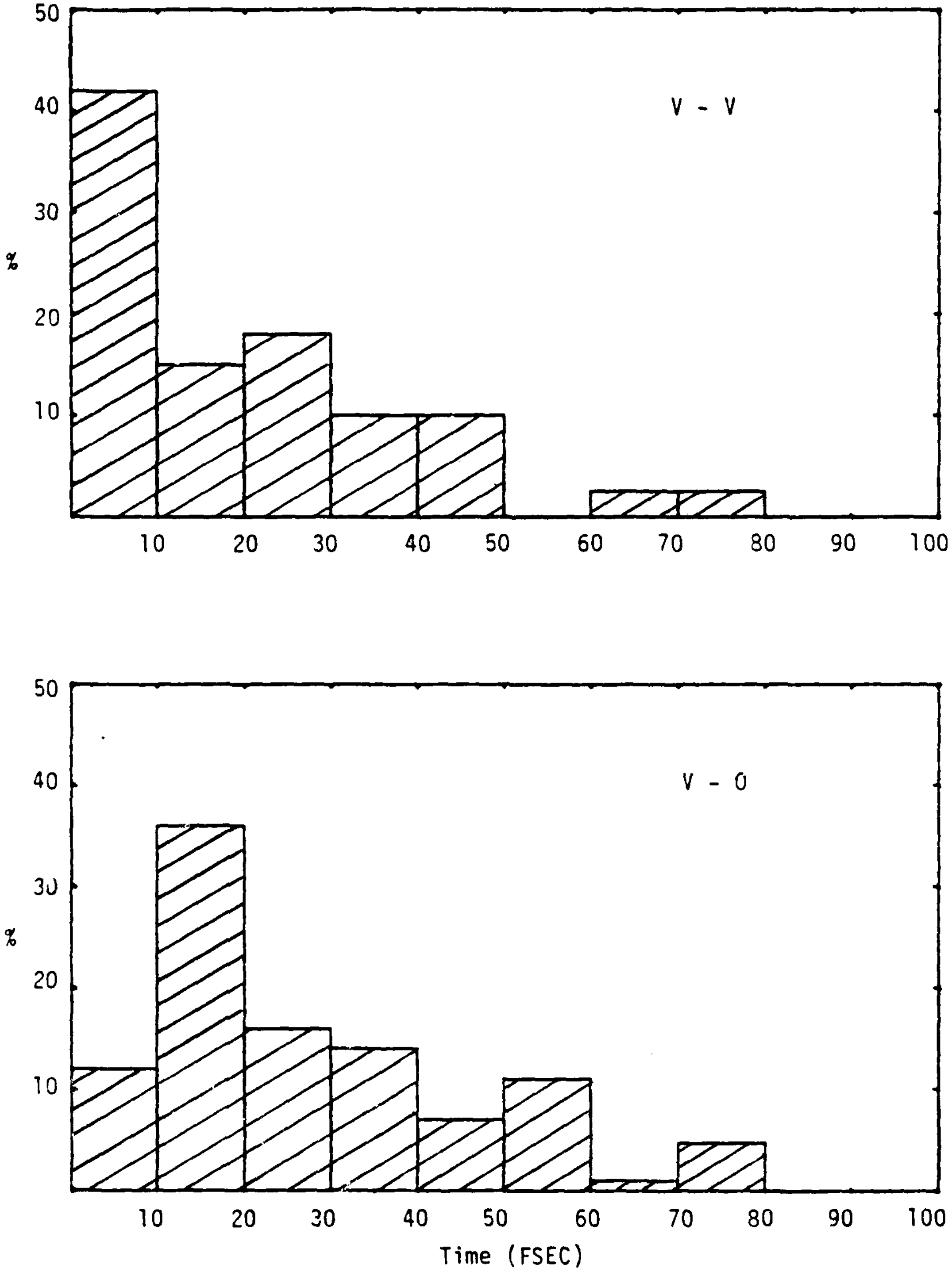

Fig. 91. Ejection time difference for V P(2x2) A-top.

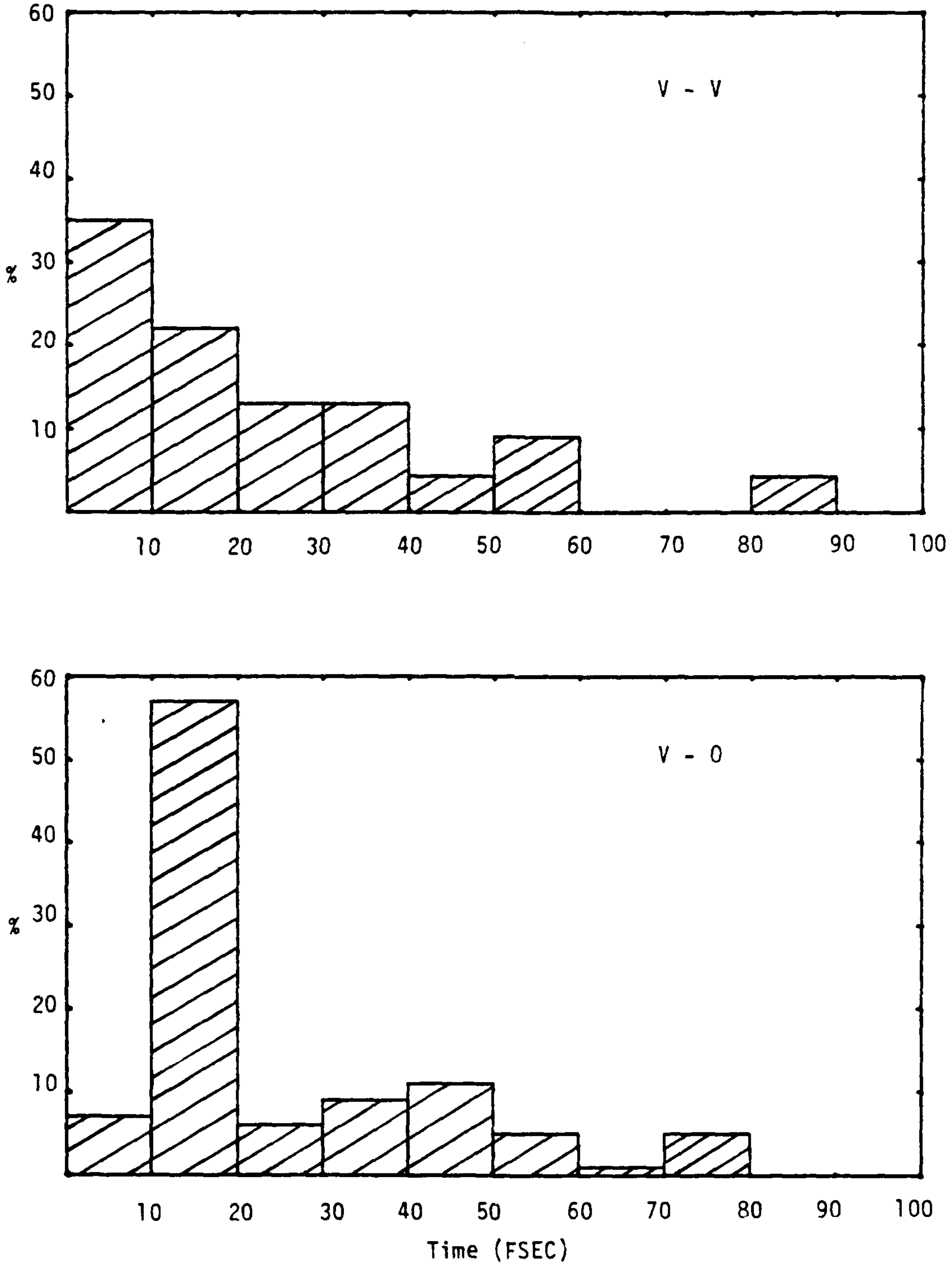

Fig. 92. Ejection time difference for V C(2x2) A-top.

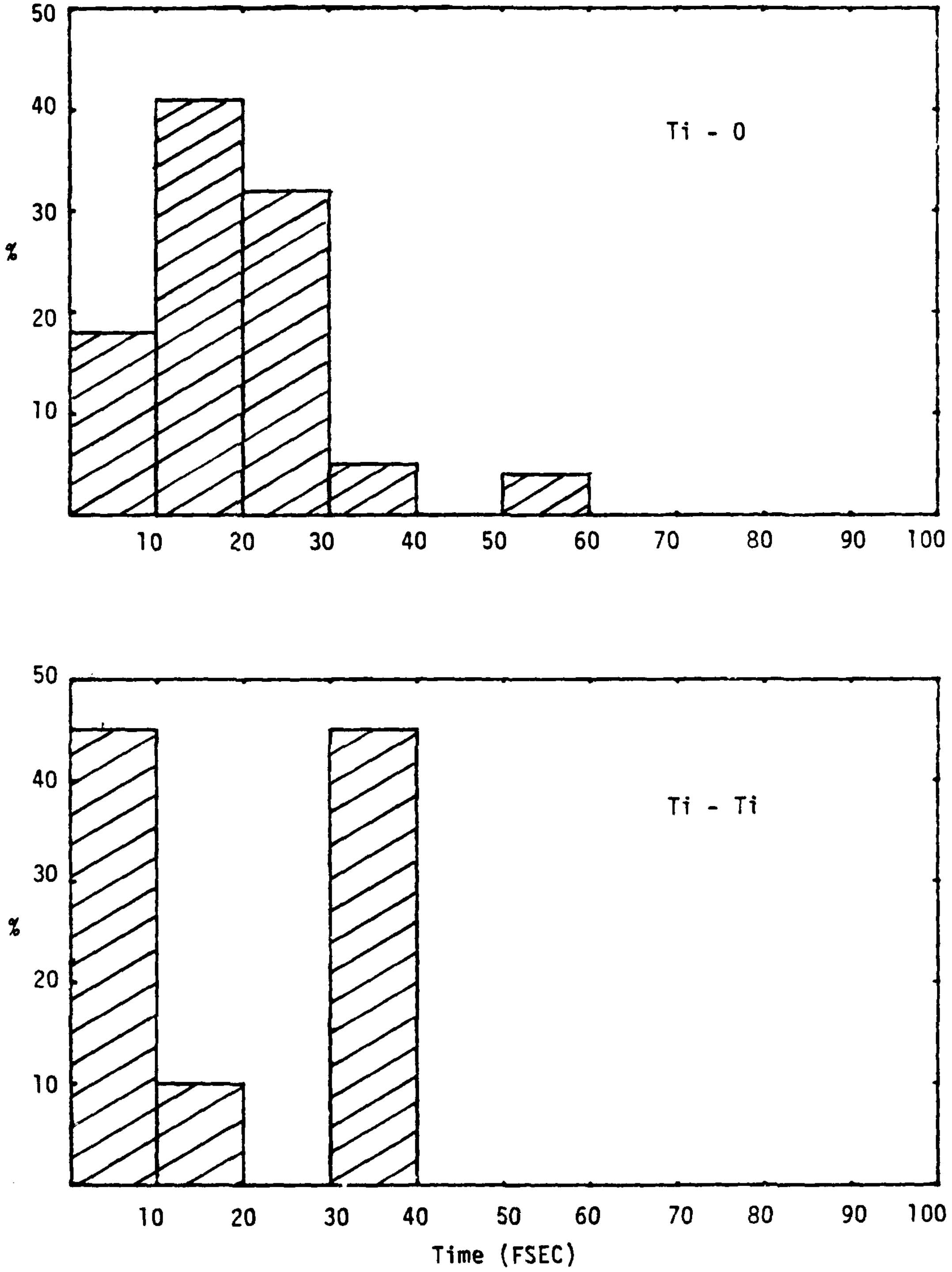

Fig. 93. Ejection time difference for Ti P(2x2) bridge.

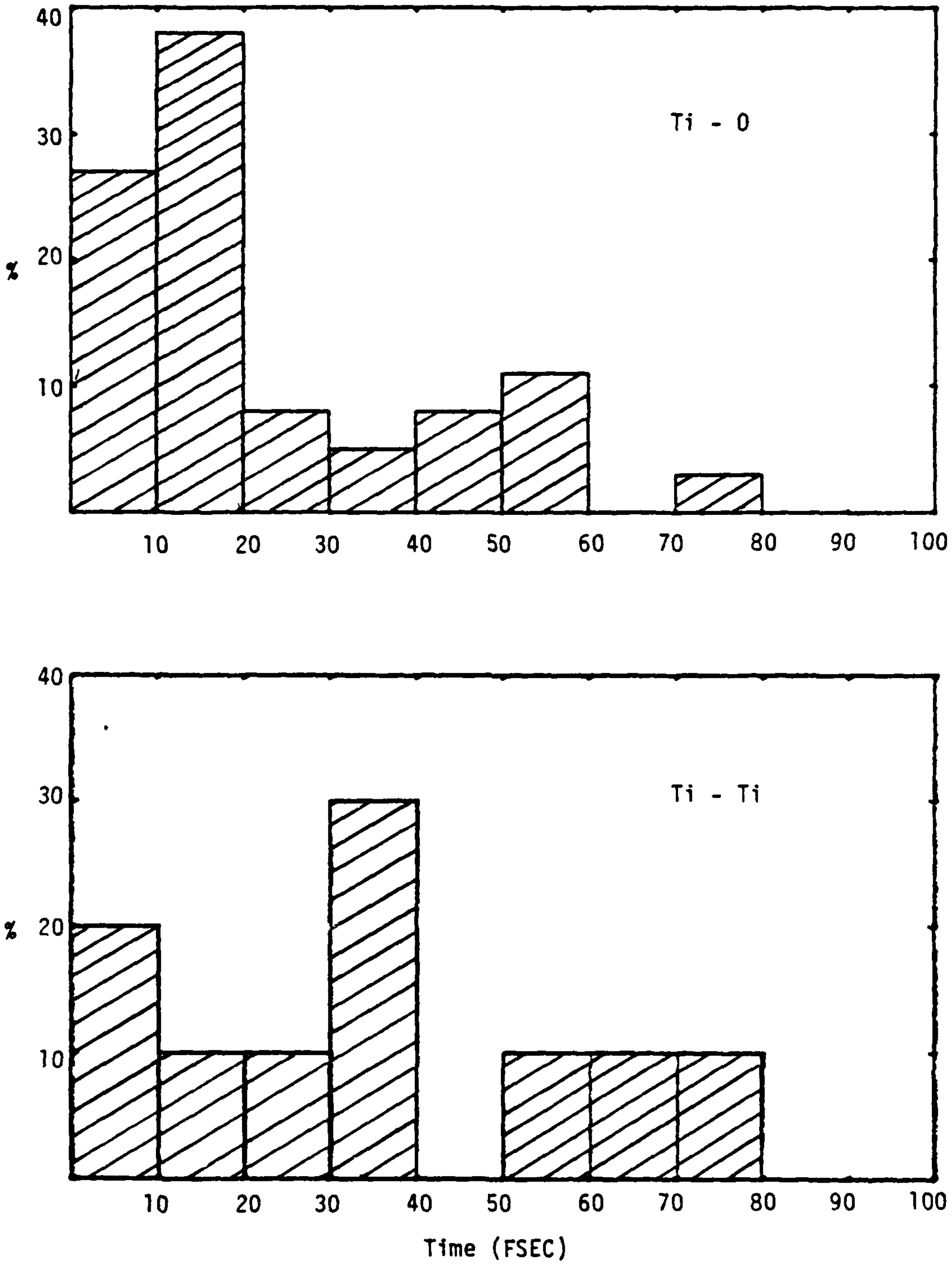

Fig. 94. Ejection time difference for Ti C(2x2) bridge.

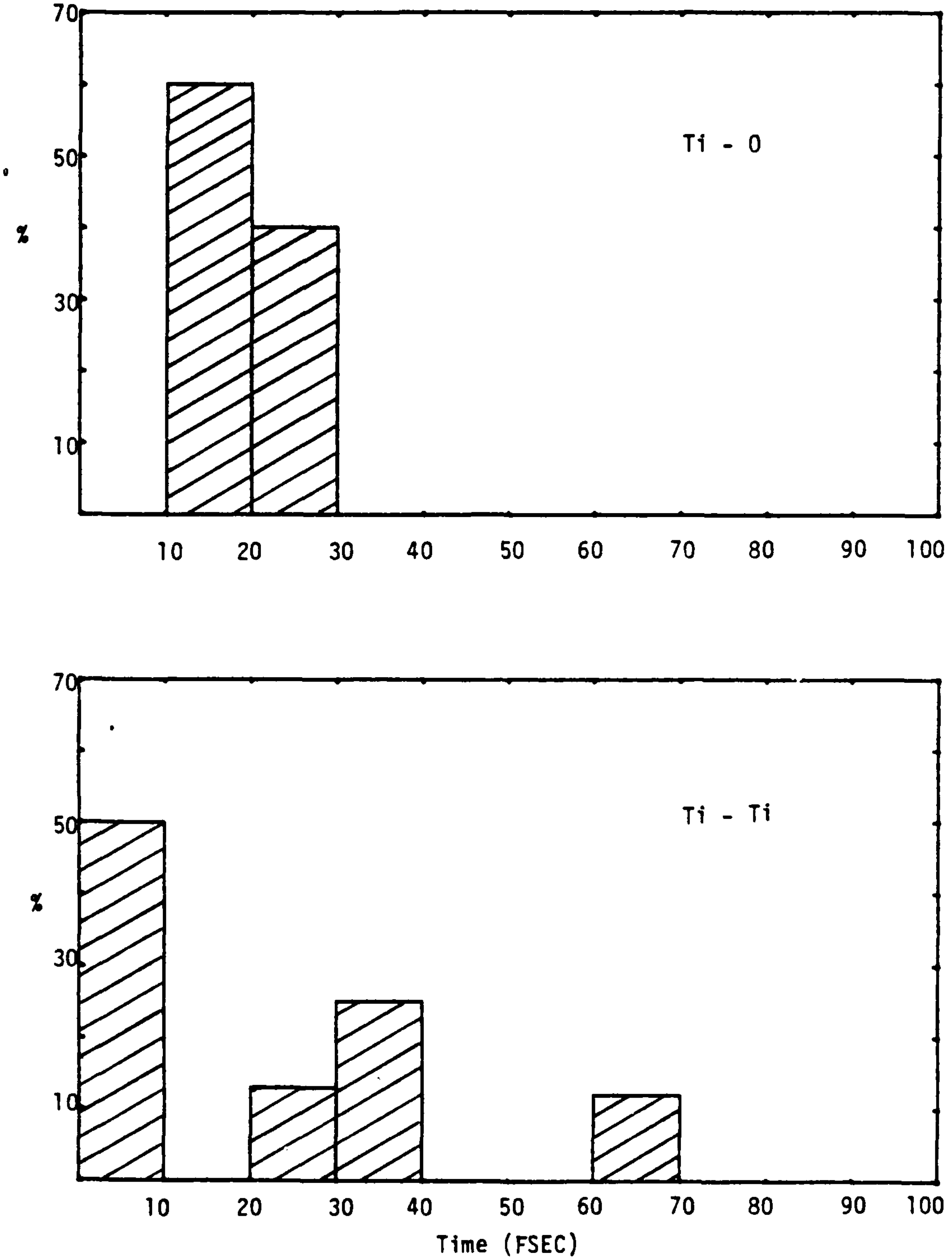

Fig. 95. Ejection time difference for P(2x2)TFA.

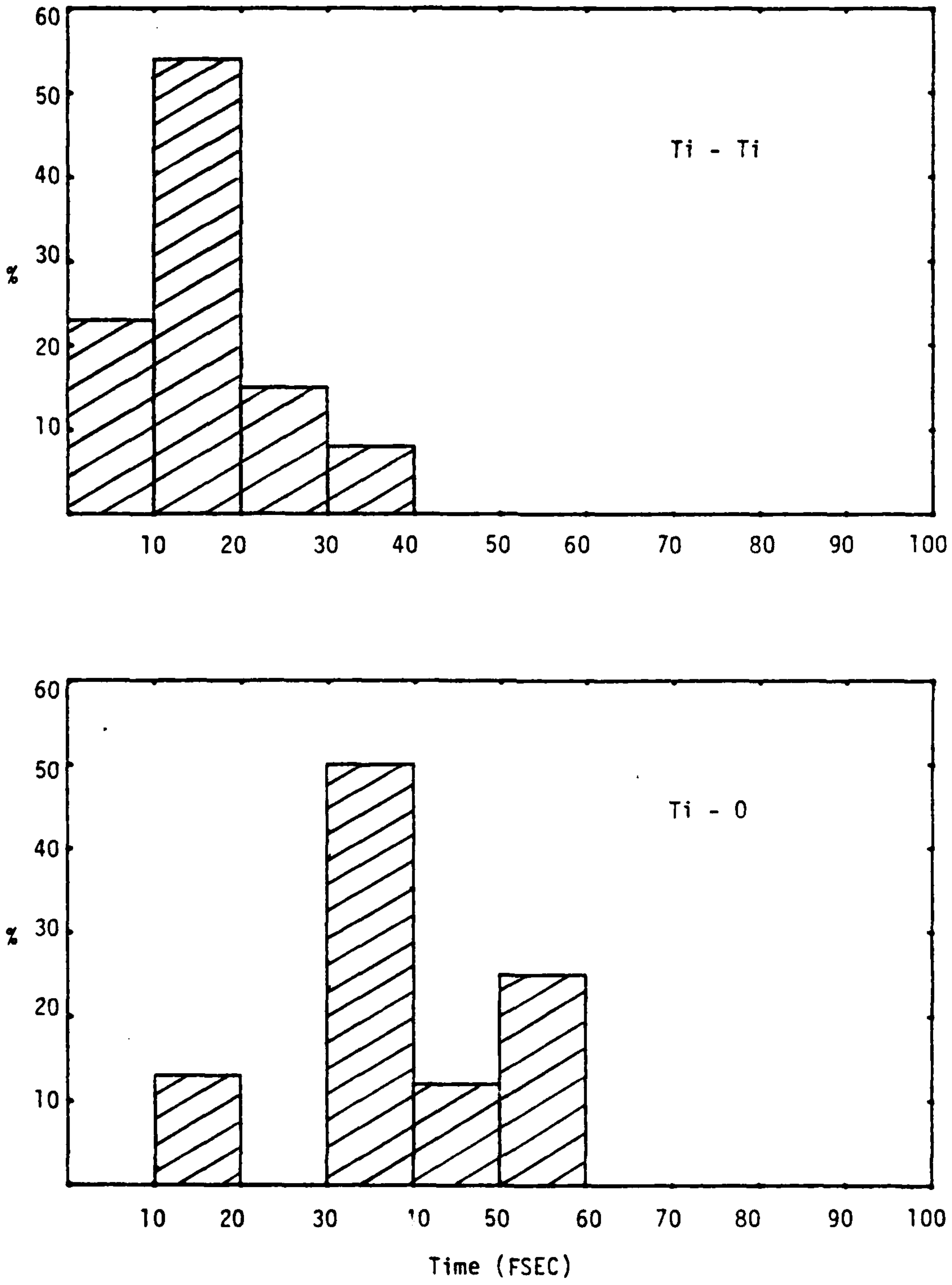

Fig. 96. Ejection time difference for Ti C(2x2)TFA.

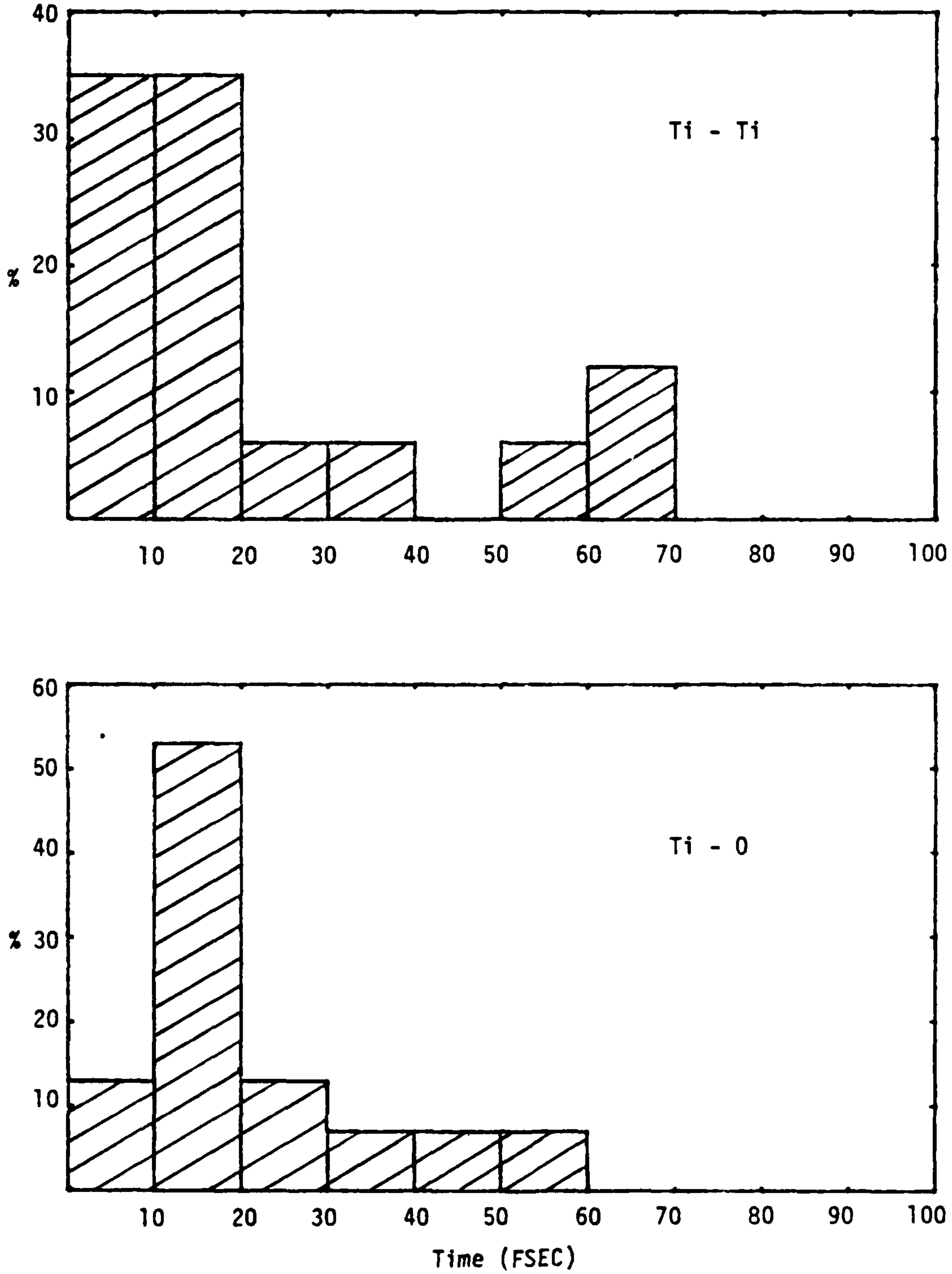

Fig. 97. Ejection time difference for Ti P(2x2)TFB.

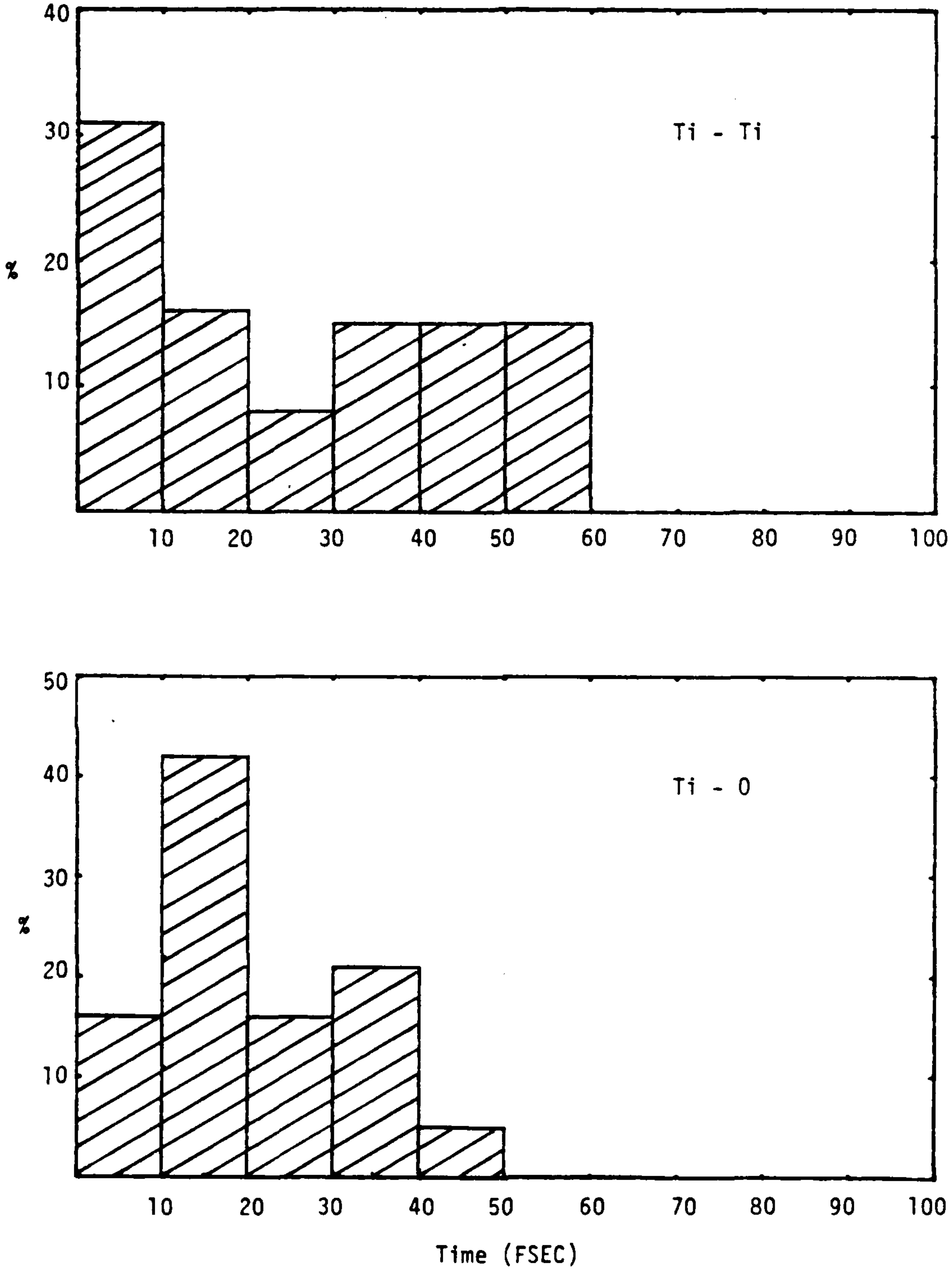

Fig. 98. Ejection time difference for Ti C(2x2)TFB.

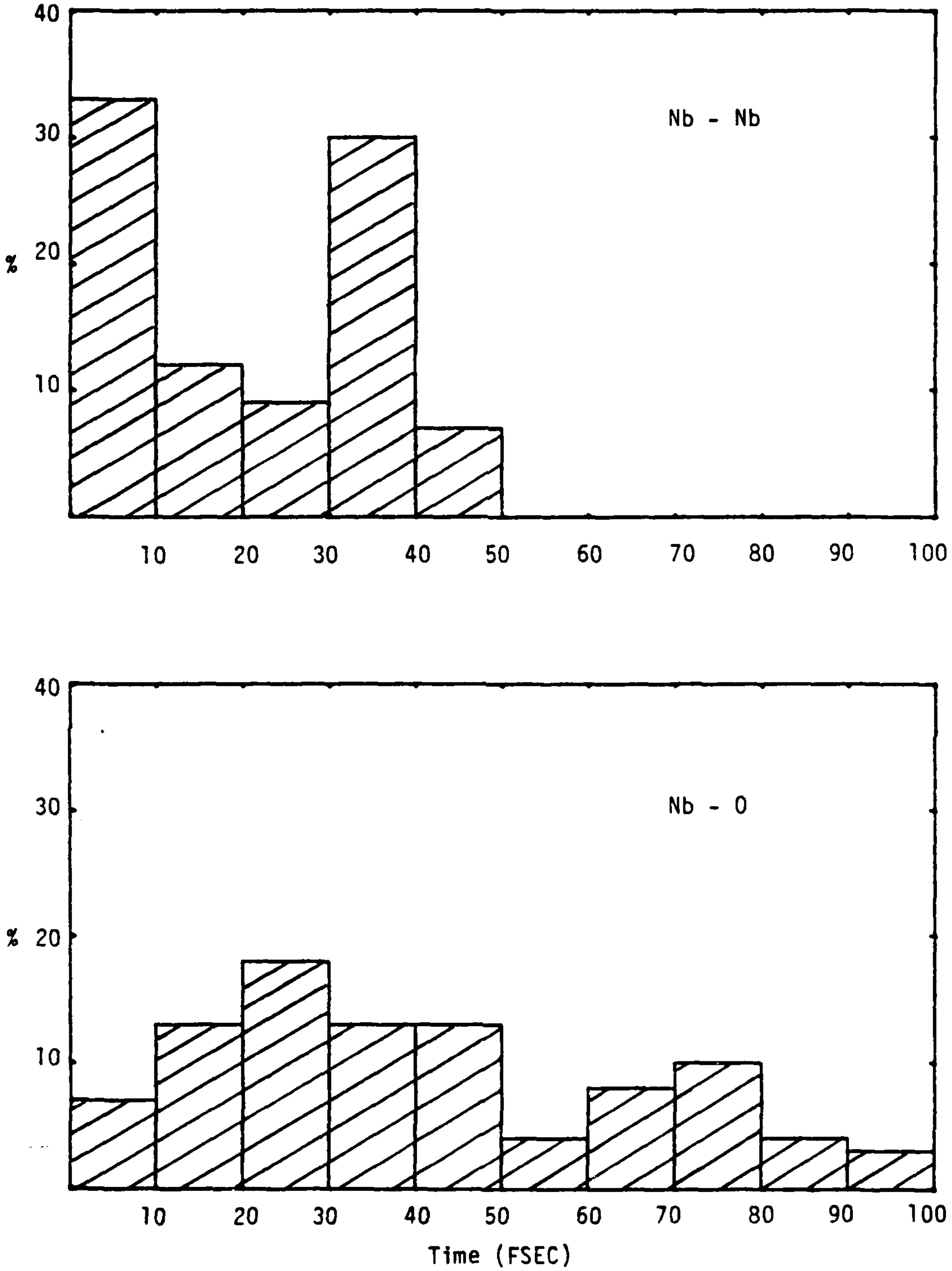

Fig. 99. Ejection time difference for Nb P(2x2) A-top.

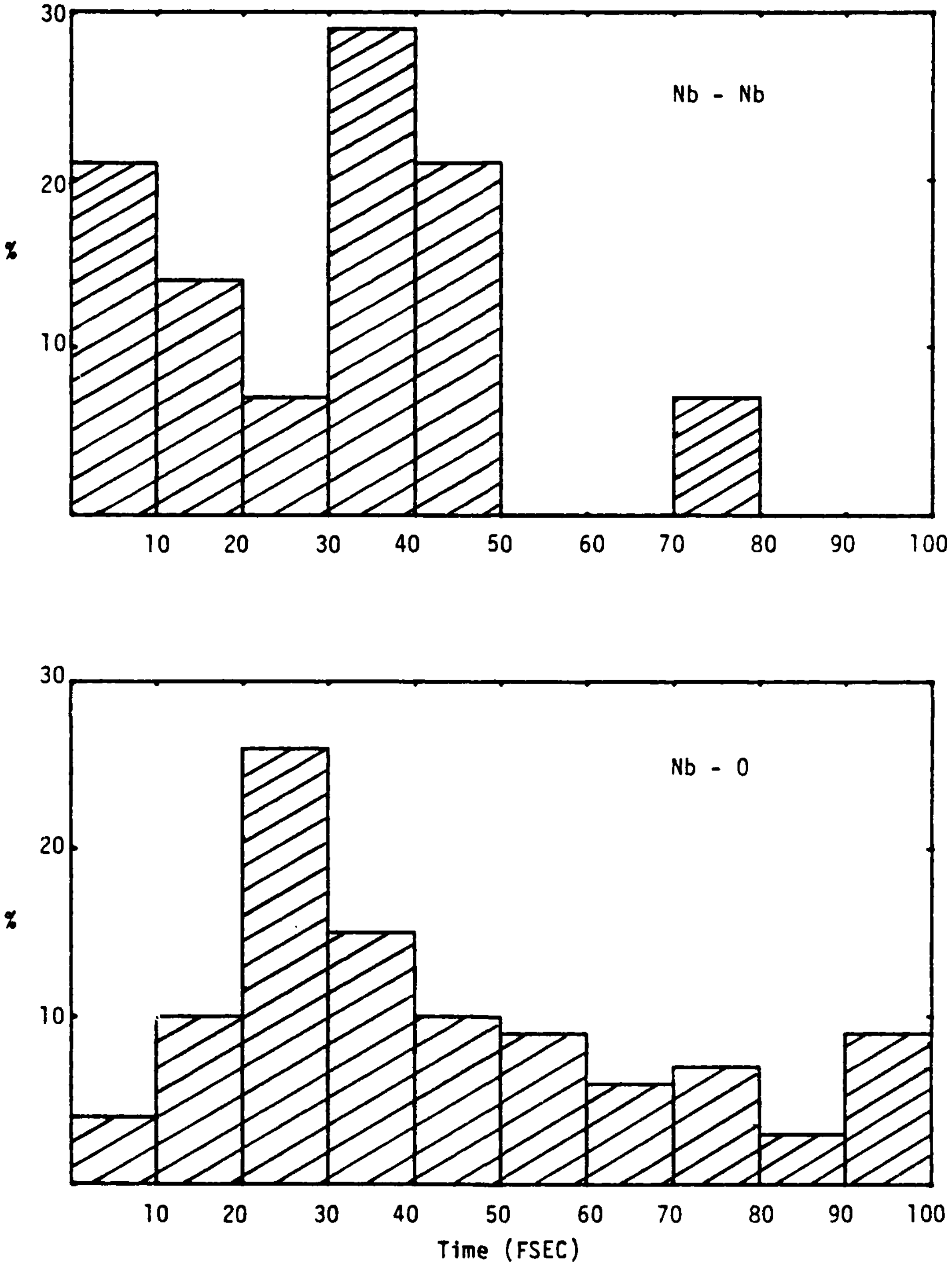

Fig. 100. Ejection time difference for Nb C(2x2) A-top.

APPENDIX G

SPOT PATTERNS

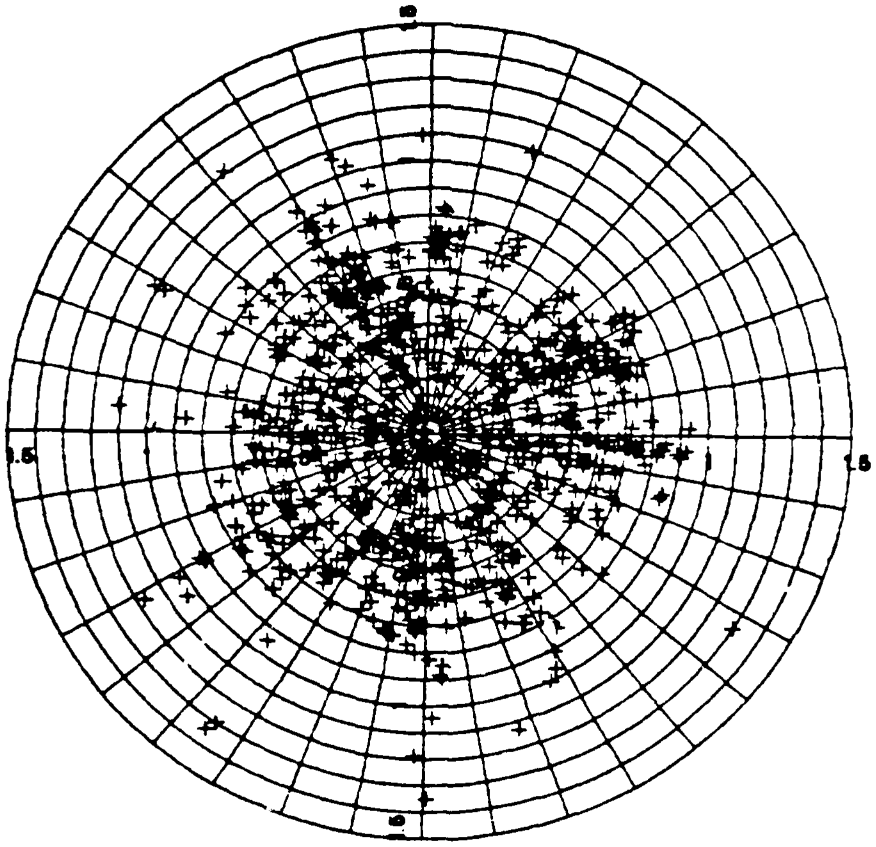

1.0 KEV TI(001)/AR CLEAN SURFACE IPX5

SPOT PATTERN

Fig. 101.

1.0 KEV V(110)/AR CLEAN SURFACE

SPOT PATTERN

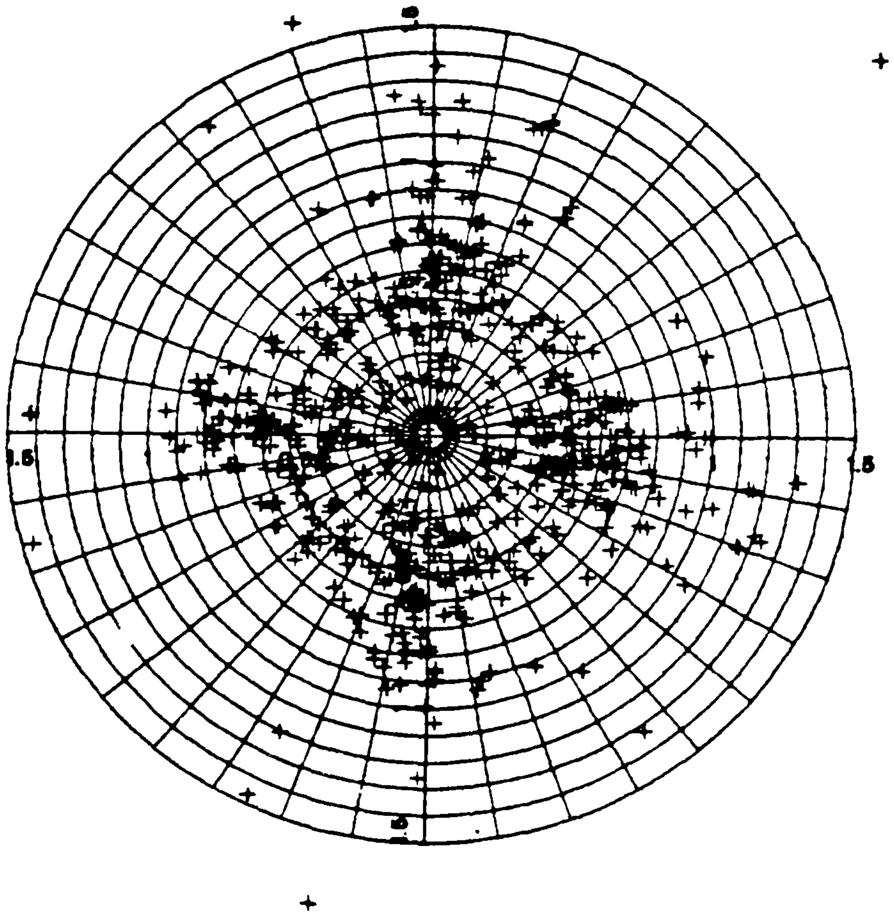

Fig. 102.

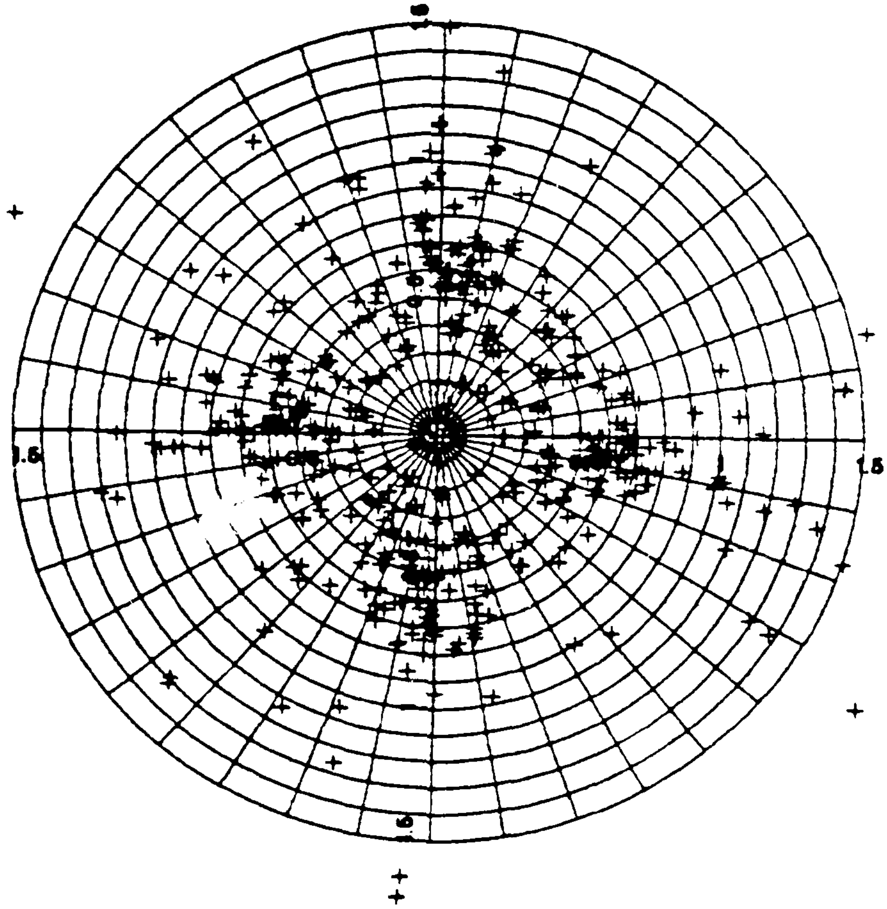

1.0 KEV NB(110)/AR CLEAN SURFACE

SPOT PATTERN

Fig. 103.

1.0 KEV TI(001)/AR + OX P2X2TFB (TI)

SPOT PATTERN

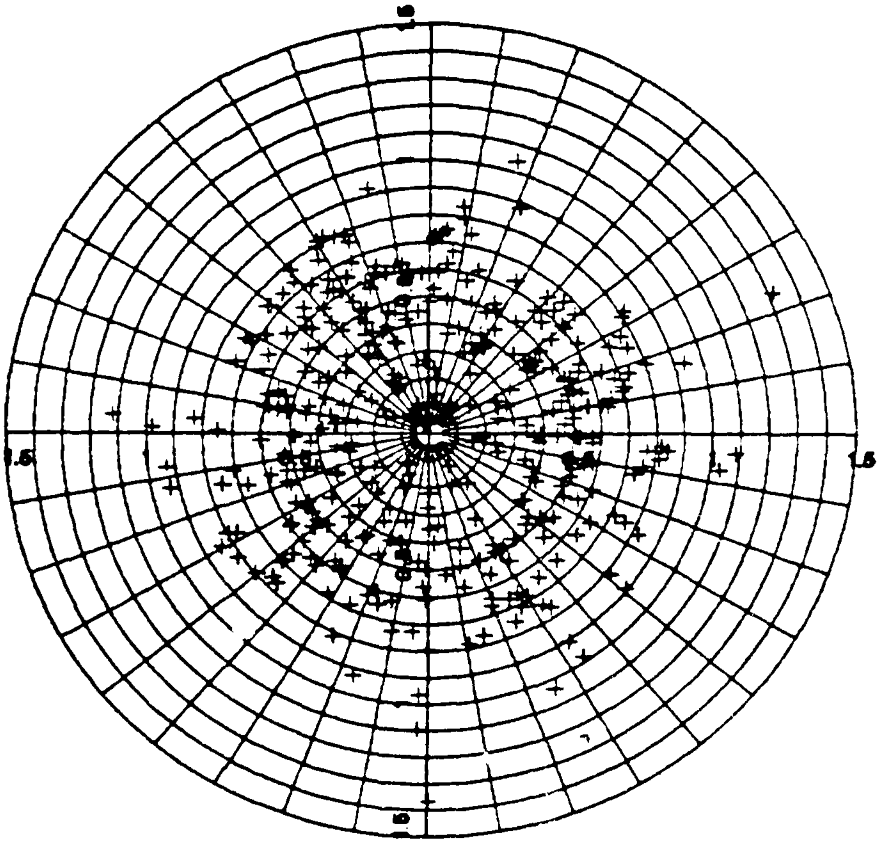

Fig. 104.

AD-A141 998 COMPUTER SIMULATION STUDIES OF SPUTTERING AND MULTIMER FORMATION FROM CLE..(U) NAVAL POSTGRADUATE SCHOOL MONTEREY CA M G MATHIS DEC 83 3/3

UNCLASSIFIED F/G 20/12 NL

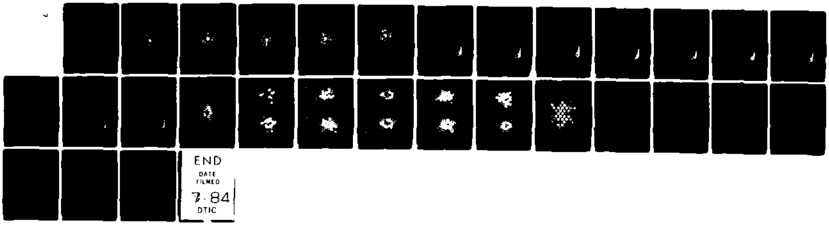

END
DATE
FILMED
7-84
DTIC

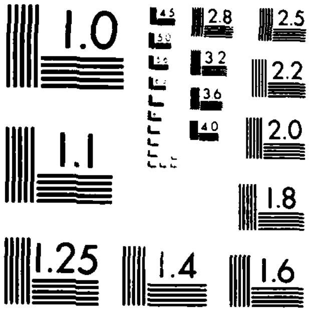

MICROCOPY RESOLUTION TEST CHART
NATIONAL BUREAU OF STANDARDS-1963-A

0.5 KEV TI(001)/AR + OX C2X2TFB (TI)

SPOT PATTERN

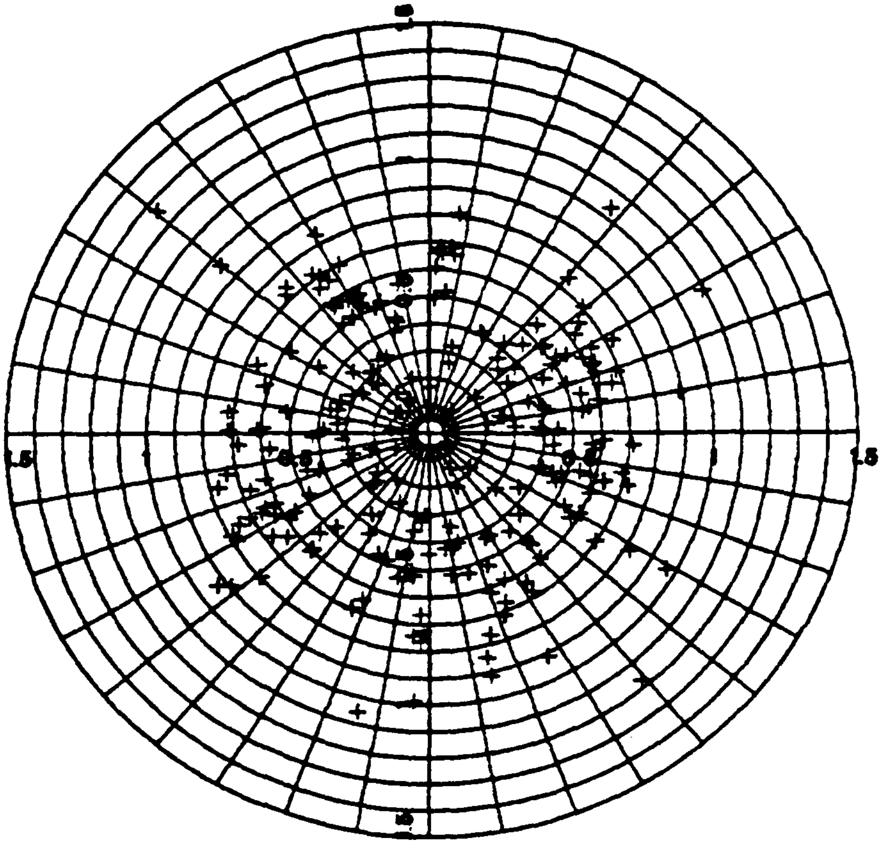

Fig. 105.

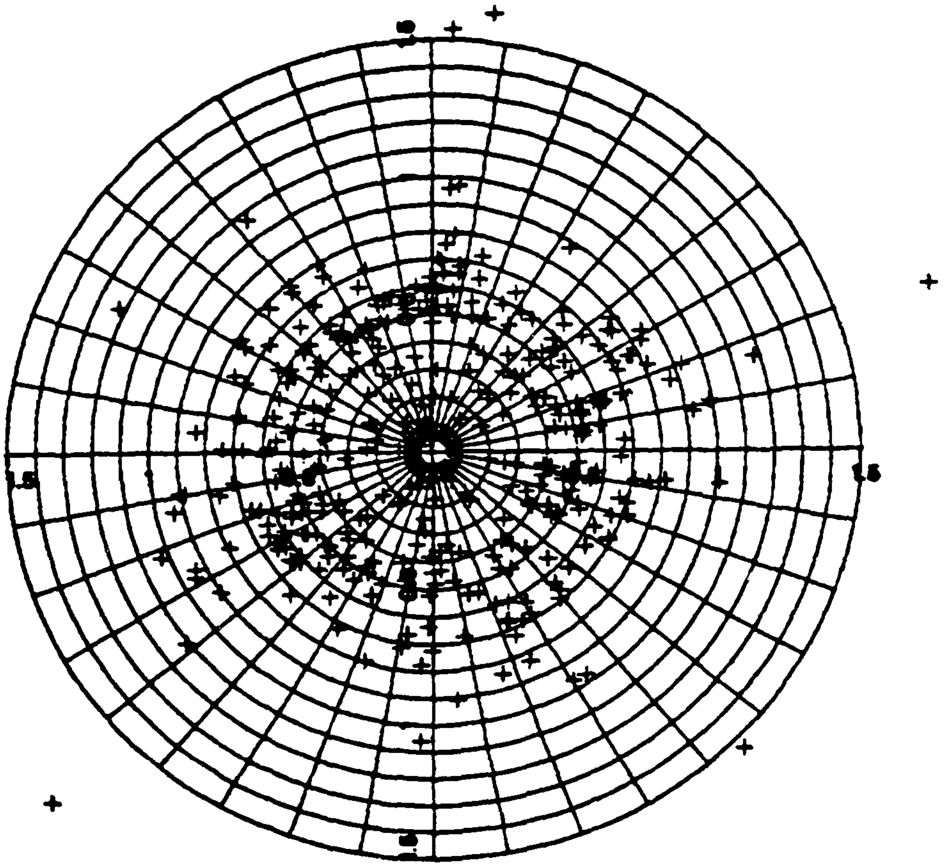

1.0 KEV TI(001)/AR + OX C2X2TFB (TI)

SPOT PATTERN

Fig. 106.

2.0 KEV TI(001)/AR + OX C2X2TFB (TI)

SPOT PATTERN

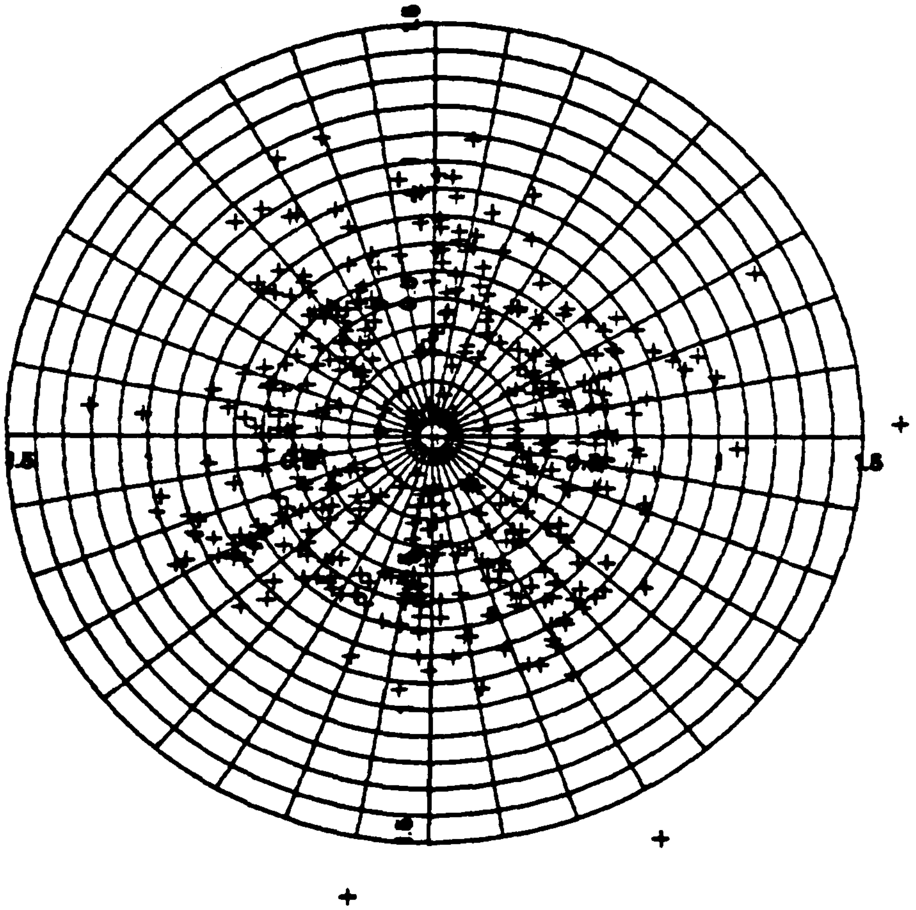

Fig. 107.

1.0 KEV TI(001)/AR + OX P2X2 TF (A+B)

SPOT PATTERN

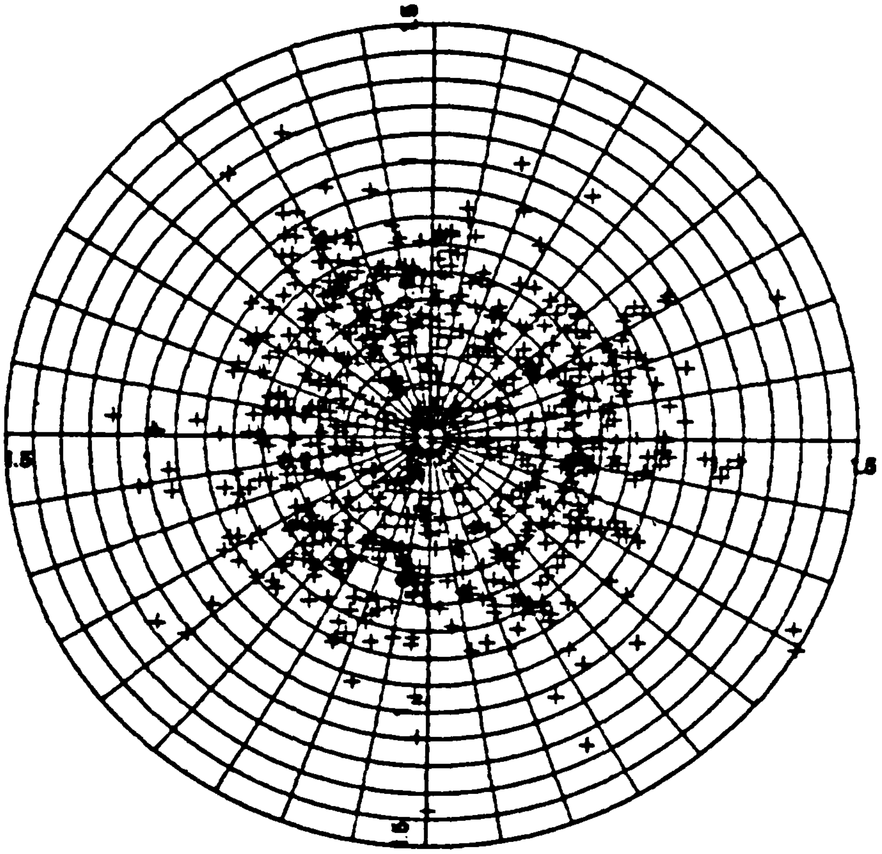

Fig. 108.

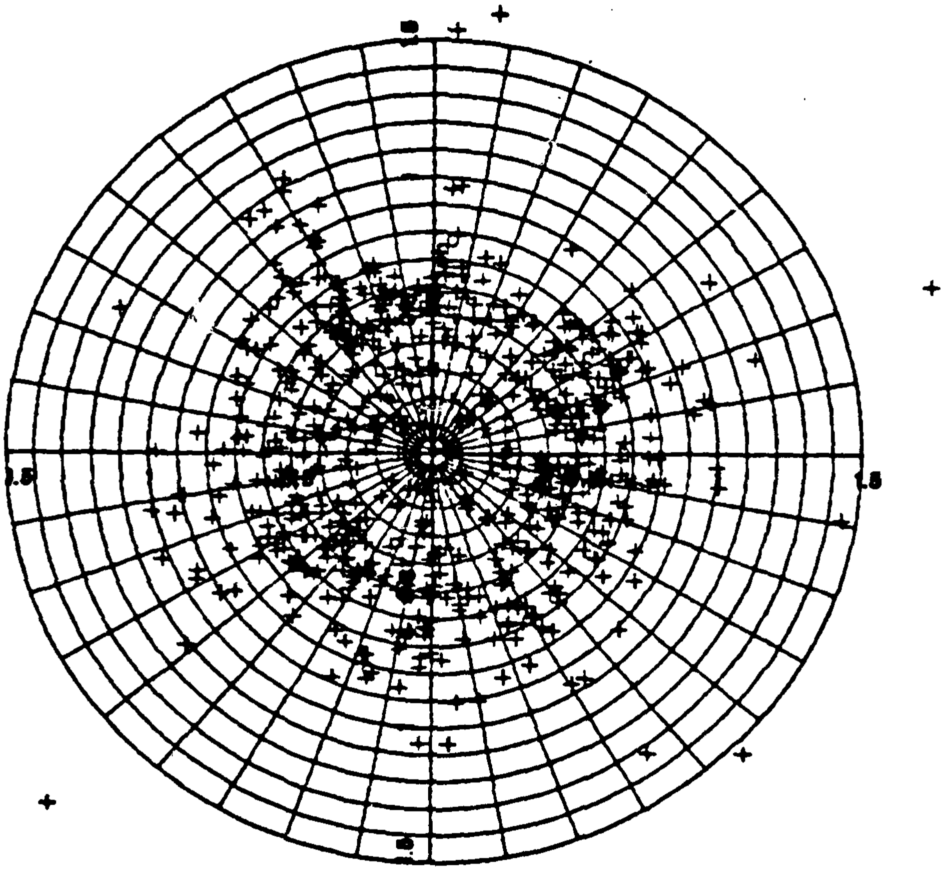

1.0 KEV TI(001)/AR + OX C2X2 TF (A+B)

SPOT PATTERN

Fig. 109.

APPENDIX H

EJECTION TIME VERSUS ENERGY CHARTS

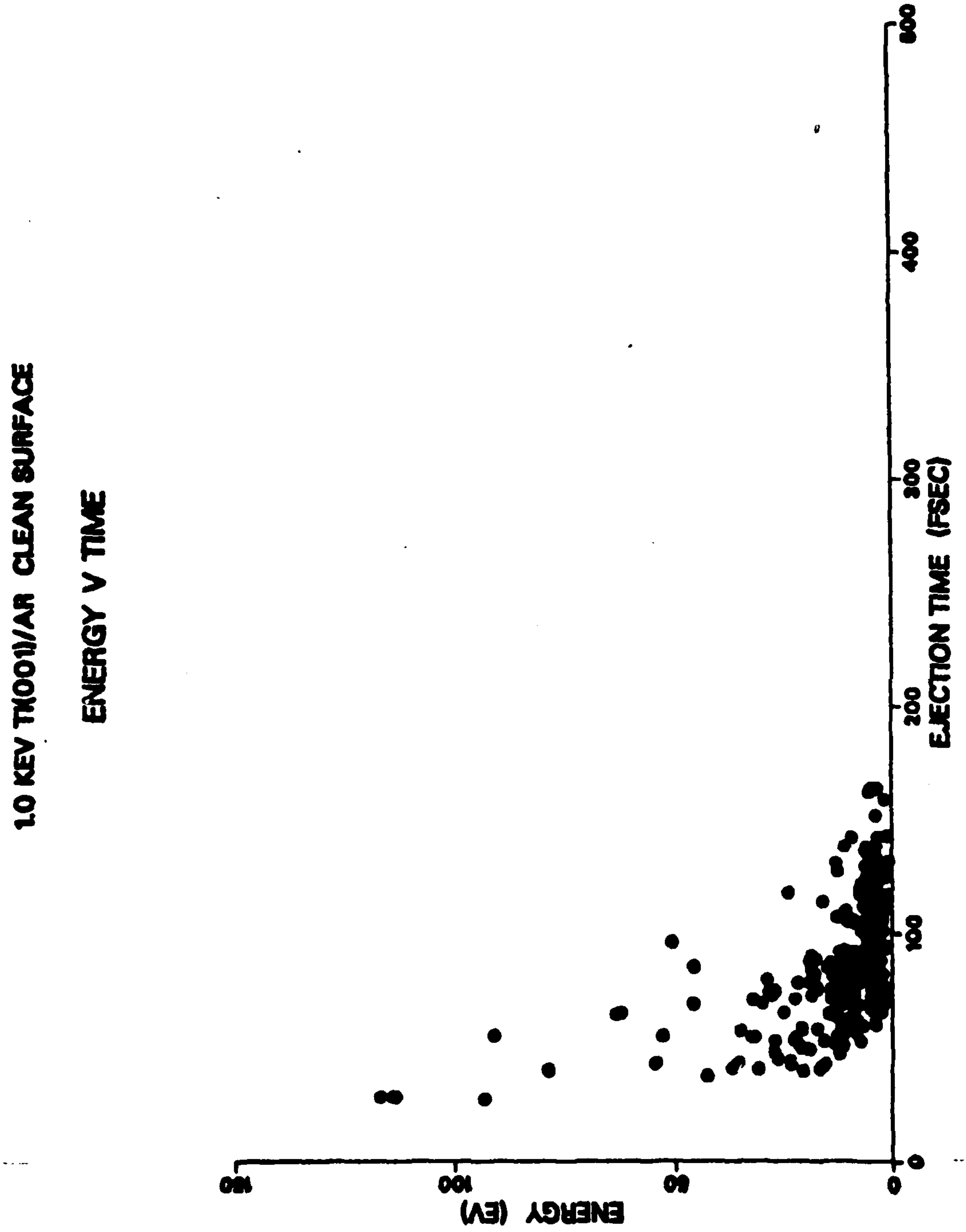

Fig. 110.

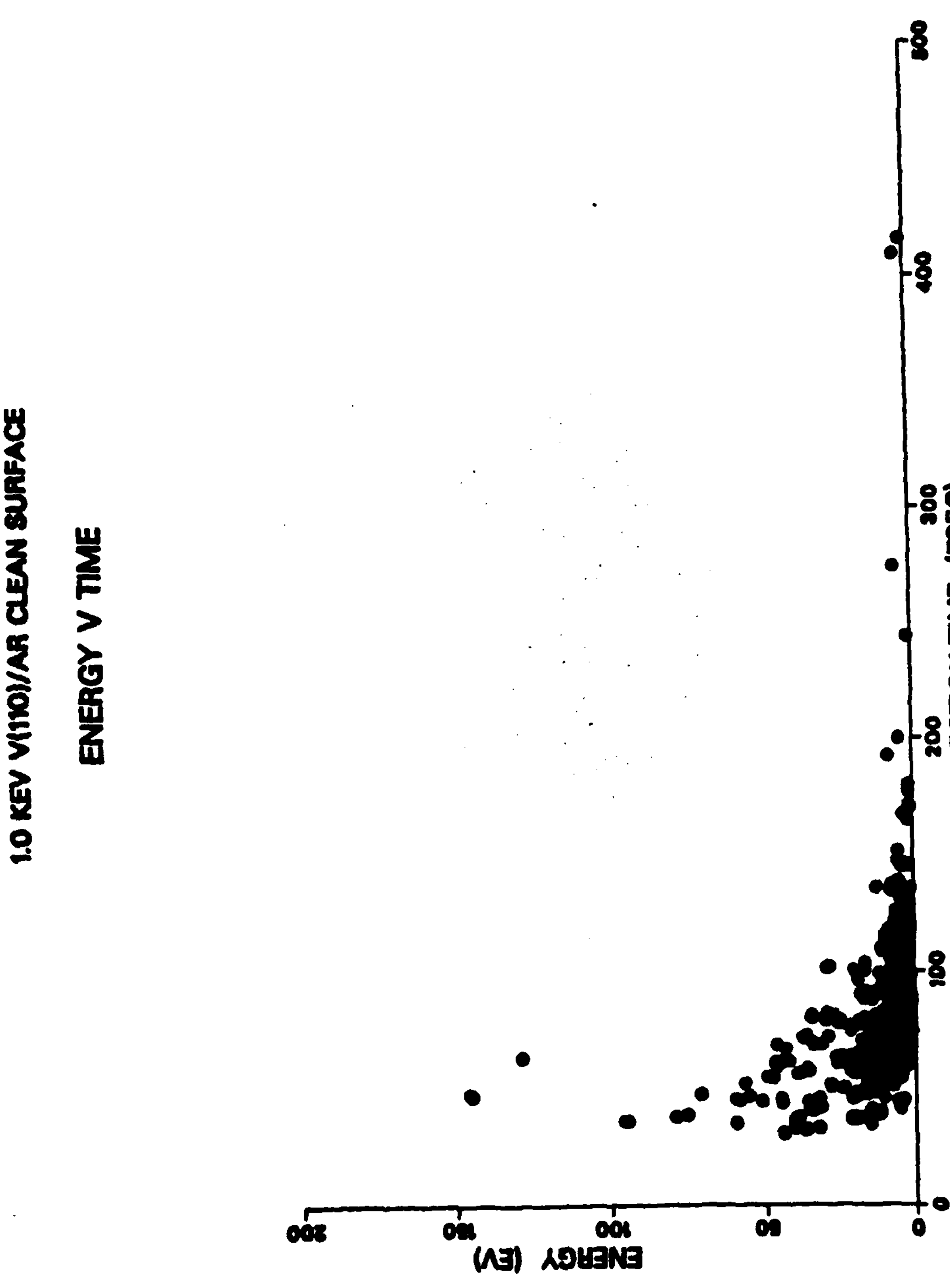
1.0 KEV V(110)/AR CLEAN SURFACE
ENERGY V TIME
EJECTION TIME (FSEC)
0
100
200
300
400
500
ENERGY (EV)
0
50
100
150
200

Fig. 111.

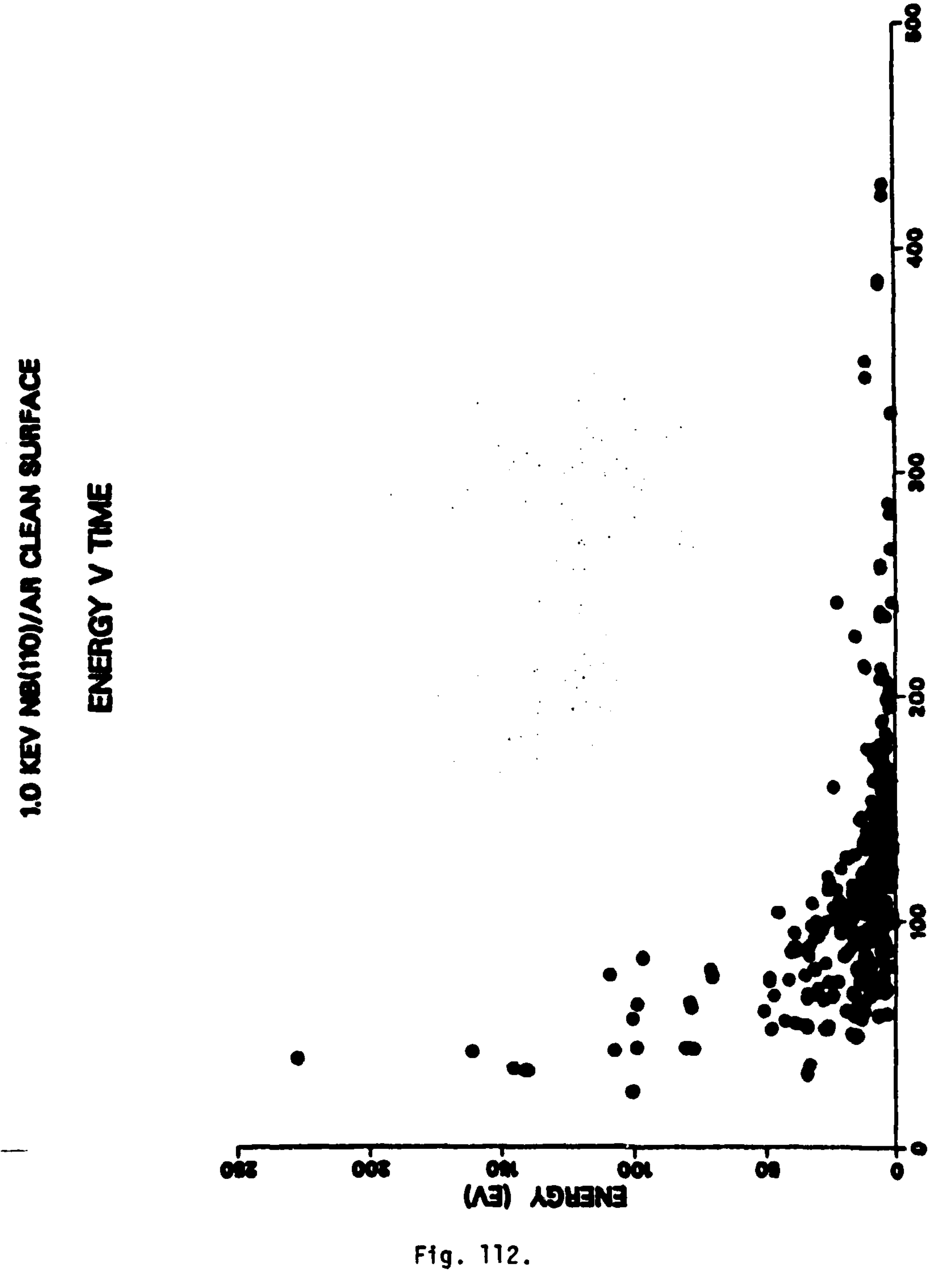
1.0 KEV NB(110)/AR CLEAN SURFACE
ENERGY V TIME
EJECTION TIME (FSEC)
0
100
200
300
400
500
ENERGY (EV)
0
50
100
150
200
250

Fig. 112.

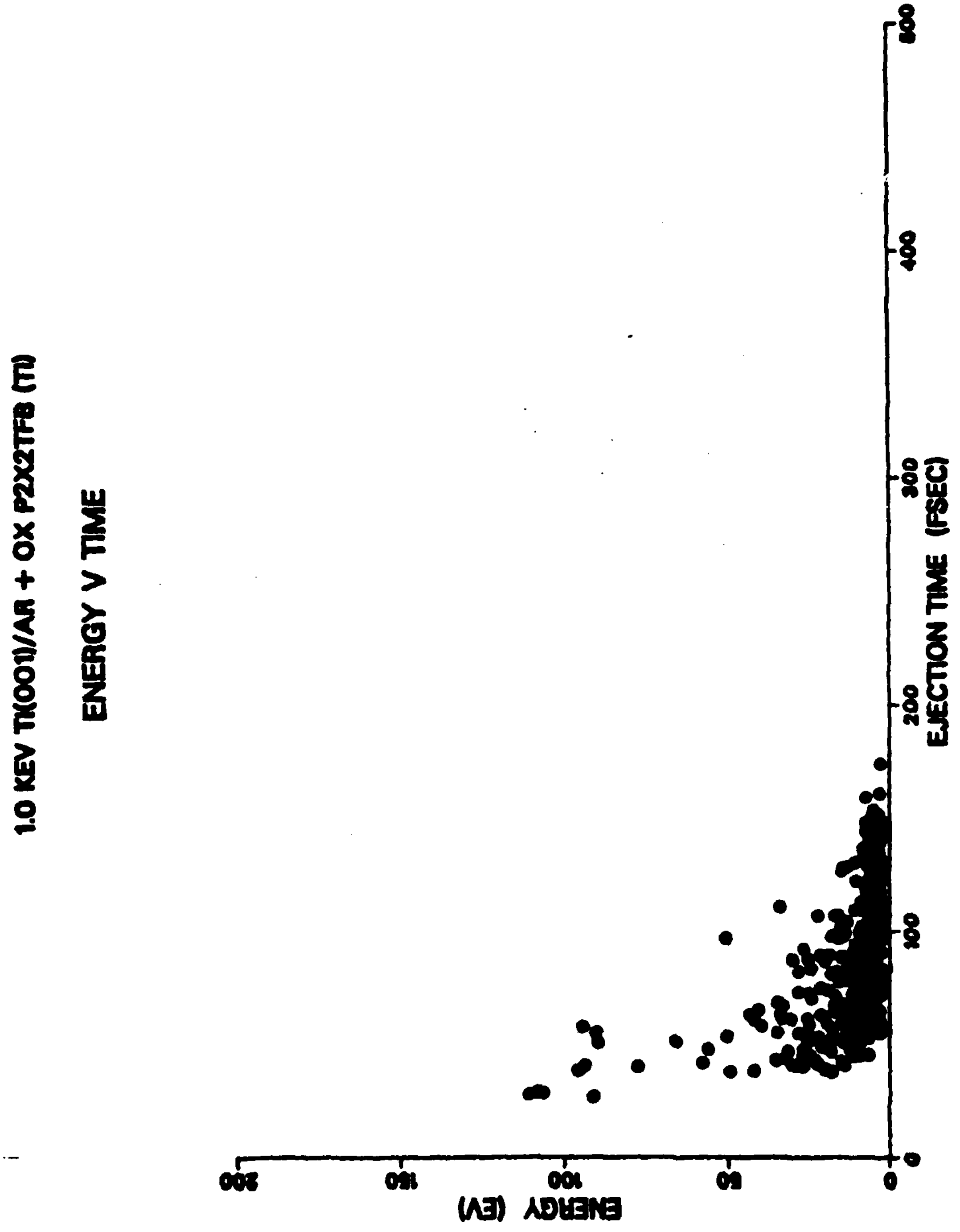
1.0 KEV TI(001)/AR + OX P2X2TFB (TI)
ENERGY V TIME
EJECTION TIME (FSEC)
0
100
200
300
400
500
ENERGY (EV)
0
50
100
150
200

Fig. 113.

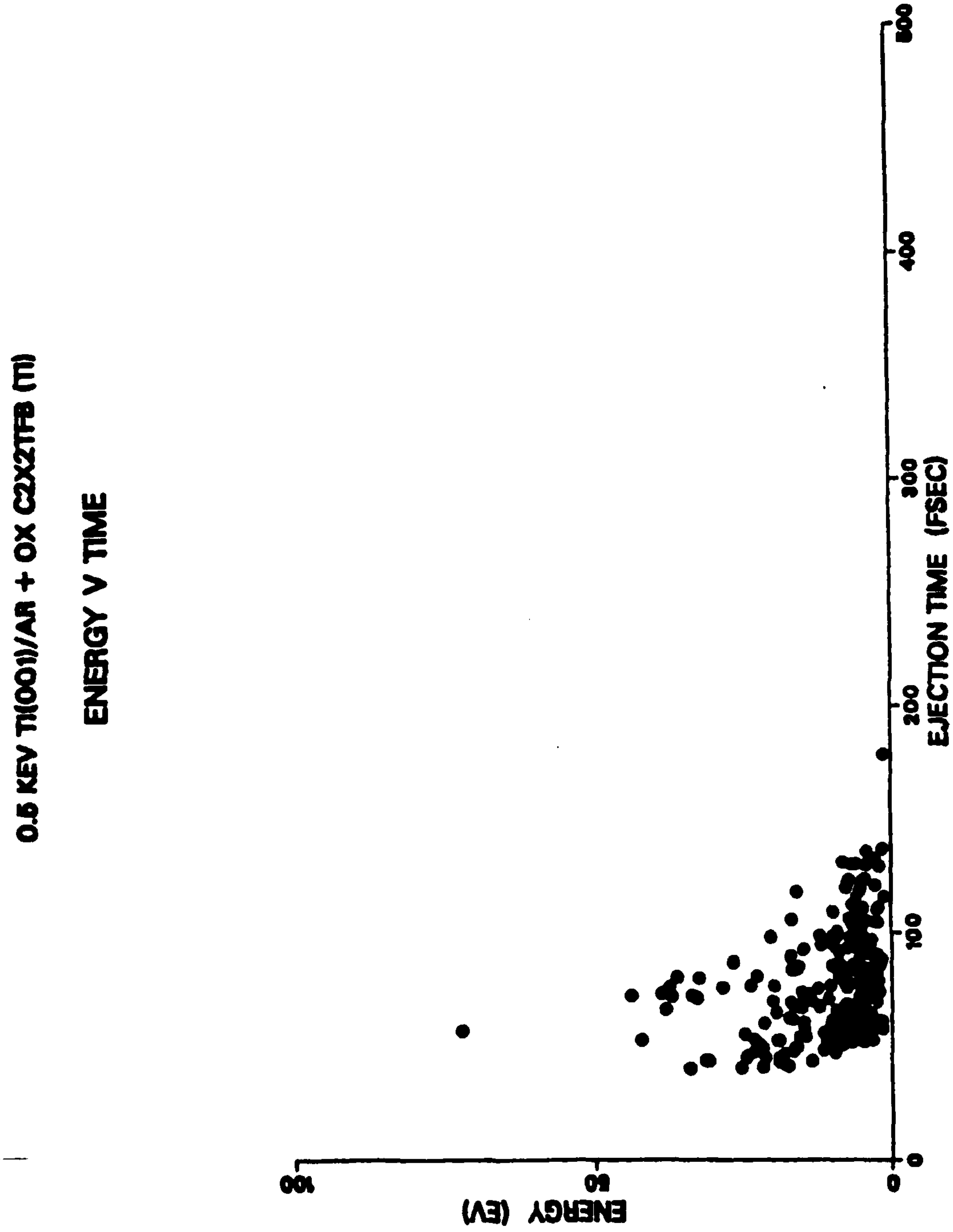

0.5 KEV TI(0001)/AR + OX C2X2TFB (TI)

ENERGY V TIME

Fig. 114.

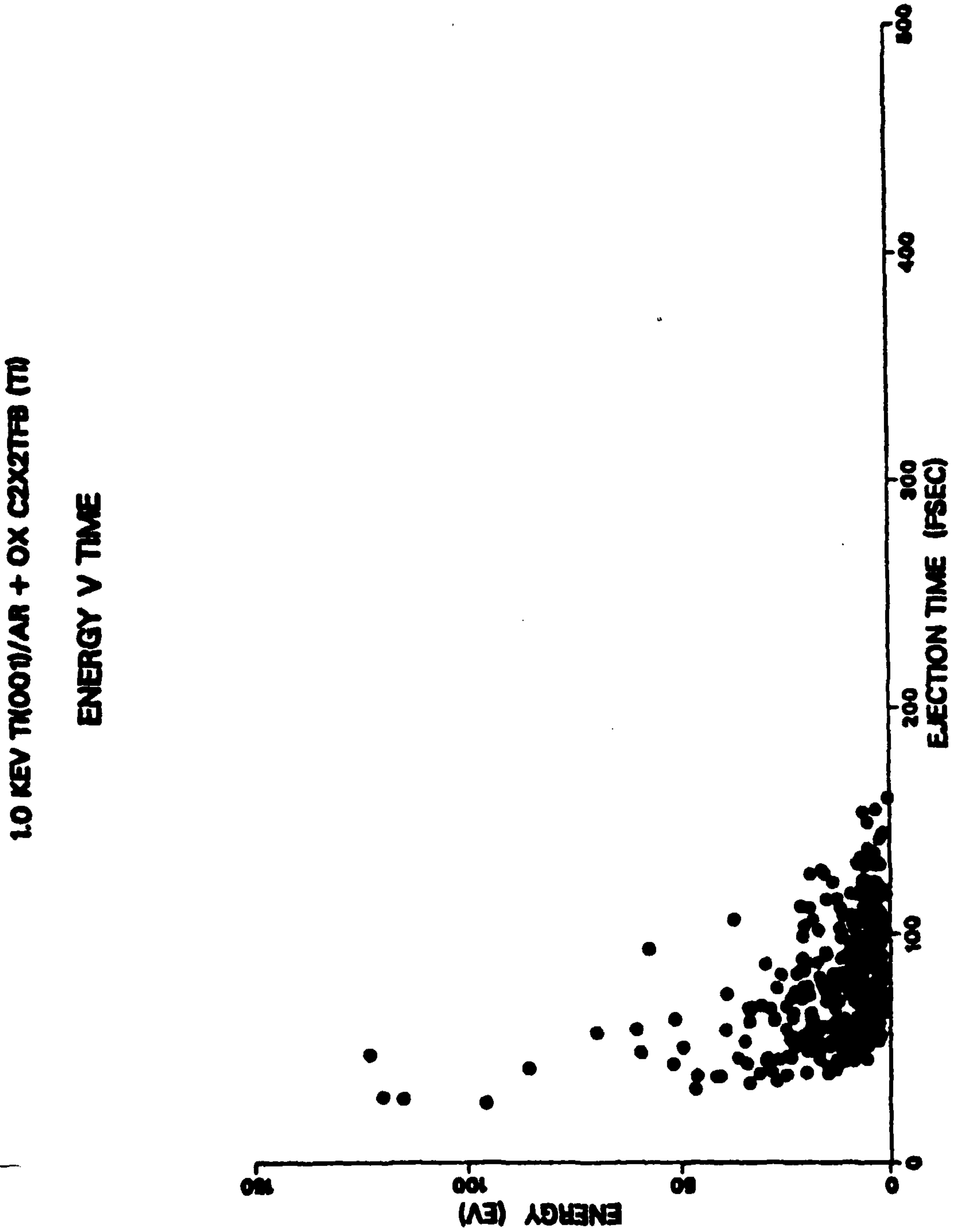
1.0 KEV Ti(001)/AR + OX C2X2TFB (Ti)
ENERGY V TIME
EJECTION TIME (FSEC)
0
100
200
300
400
500
ENERGY (EV)
0
50
100
150

Fig. 115.

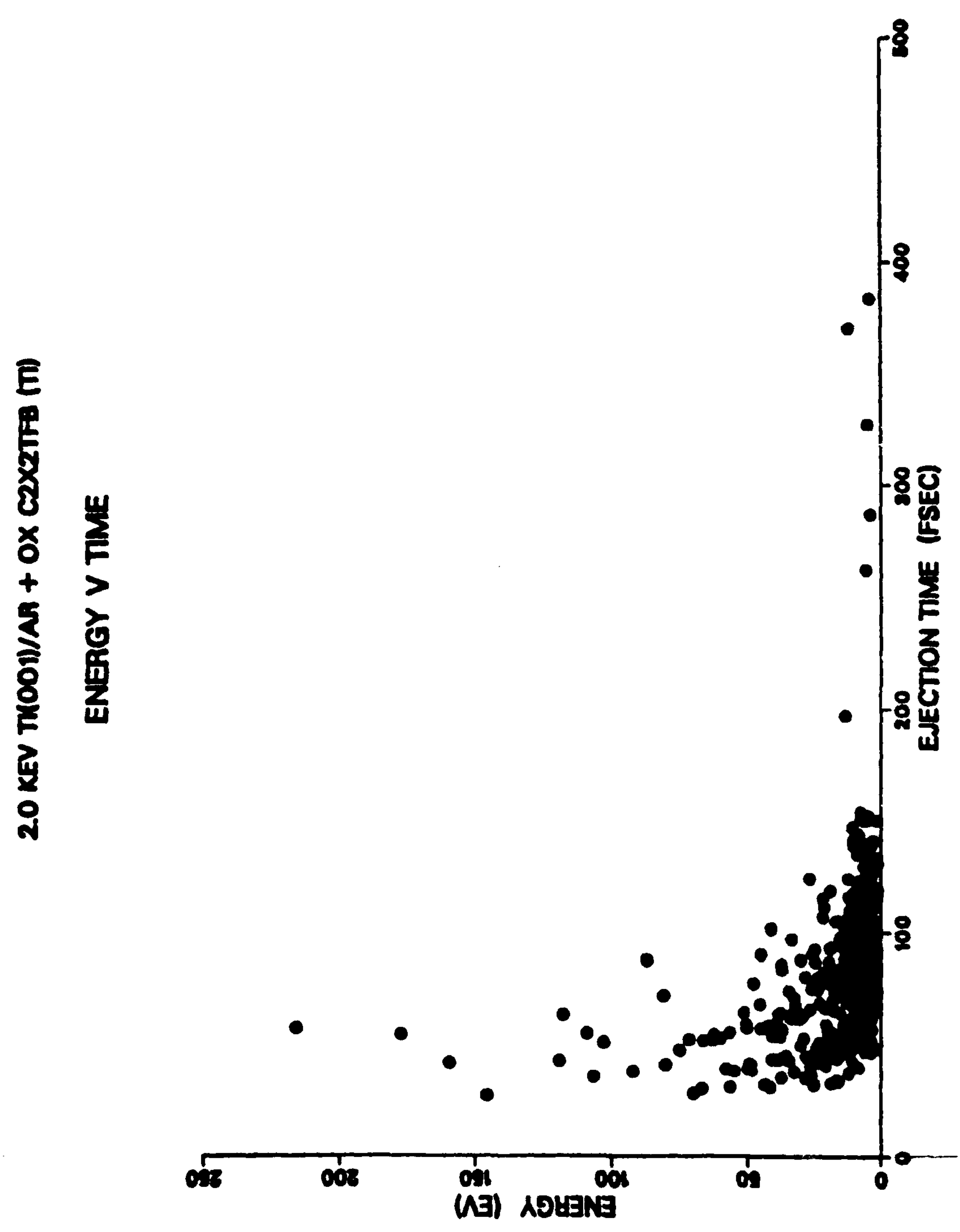
2.0 KEV TI(001)/AR + OX C2X2TFB (TI)
ENERGY V TIME
EJECTION TIME (FSEC)
0
100
200
300
400
500
ENERGY (EV)
0
50
100
150
200
250

Fig. 116.

1.0 KEV TI(001)/AR + OX P2X2TFB (OX)

ENERGY V TIME

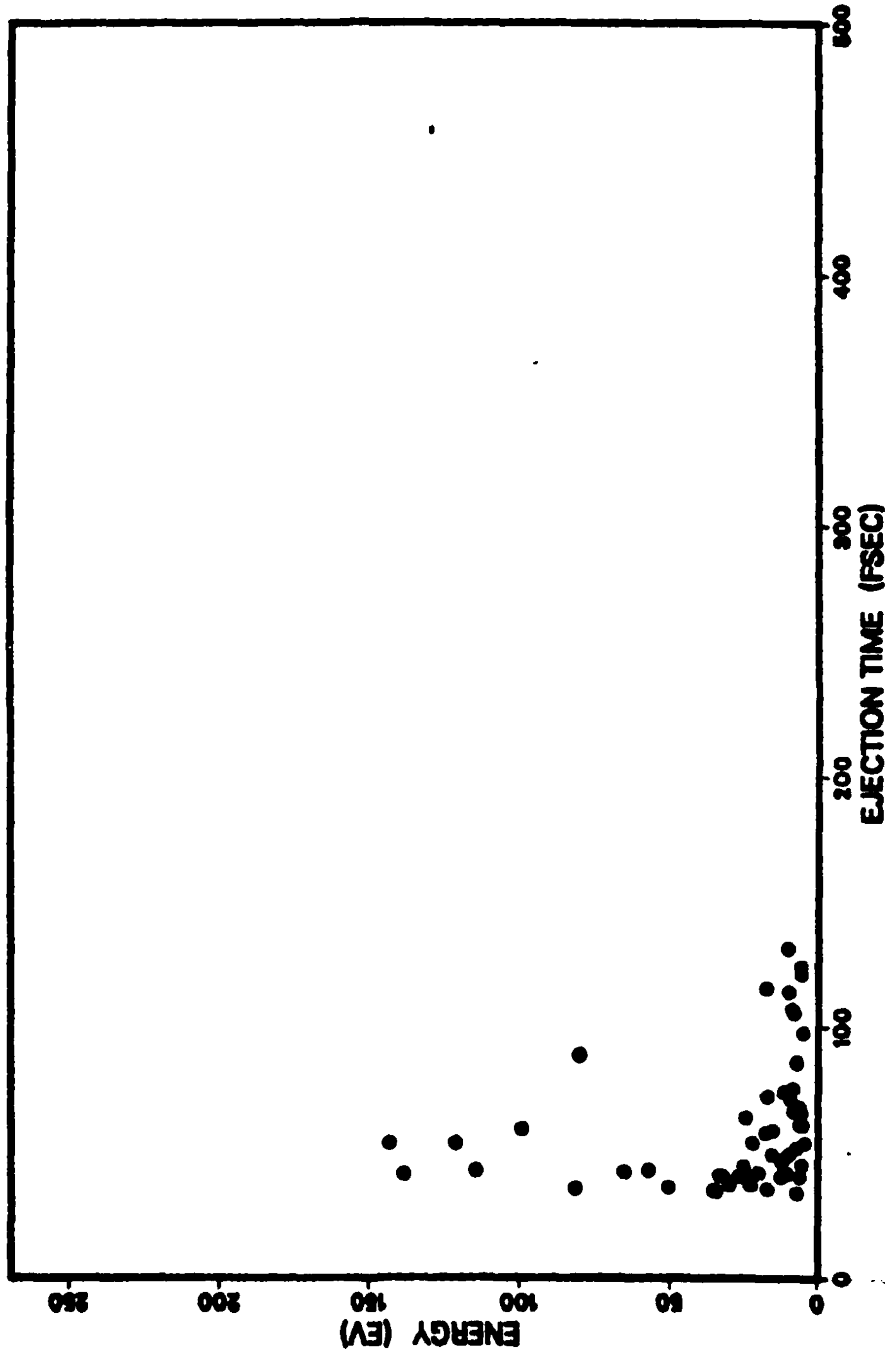

Fig. 117.

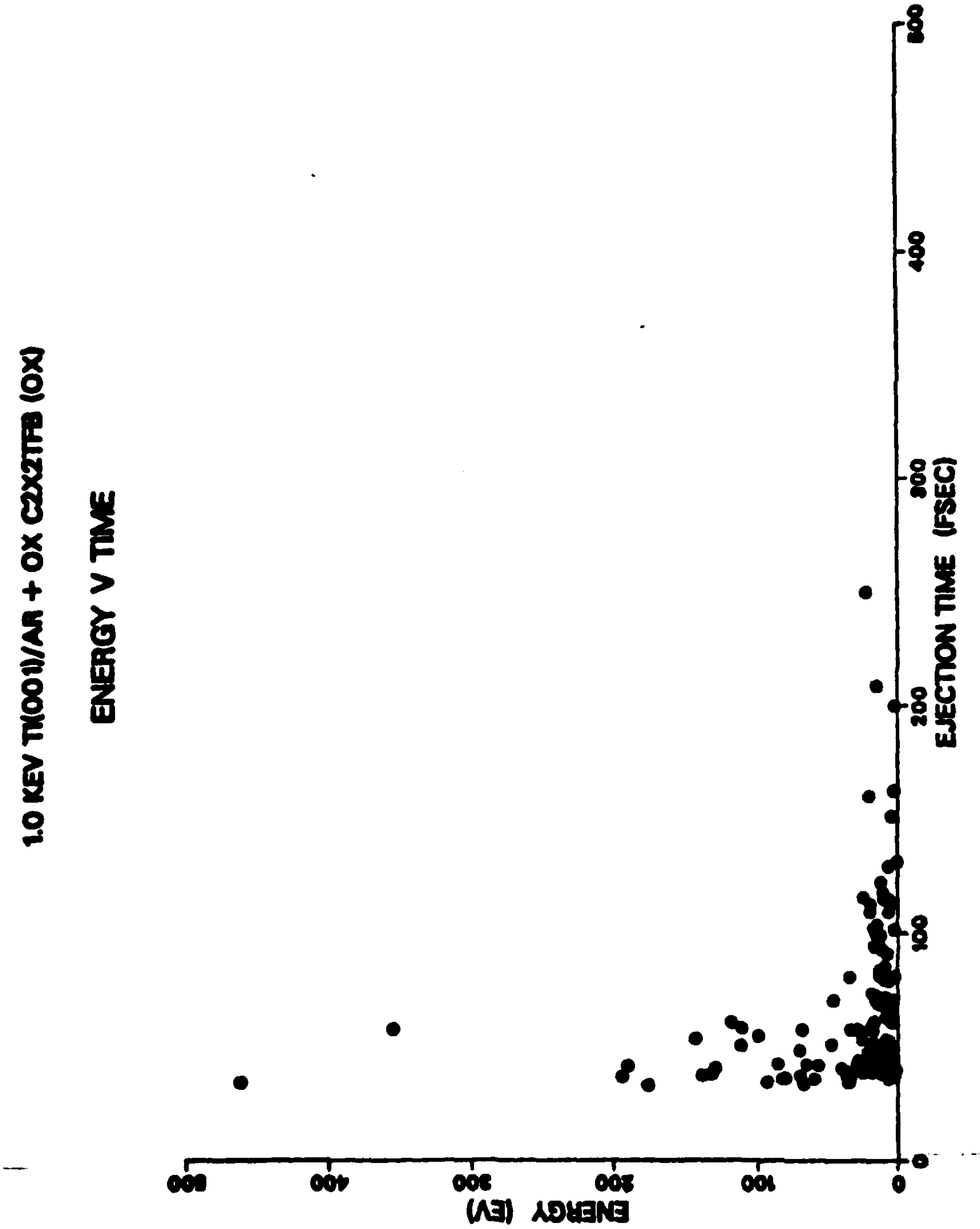
1.0 KEV TI(001)/AR + OX C2X2TFB (OX)
ENERGY V TIME
EJECTION TIME (FSEC)
0
100
200
300
400
500
ENERGY (EV)
0
100
200
300
400
500

Fig. 118.

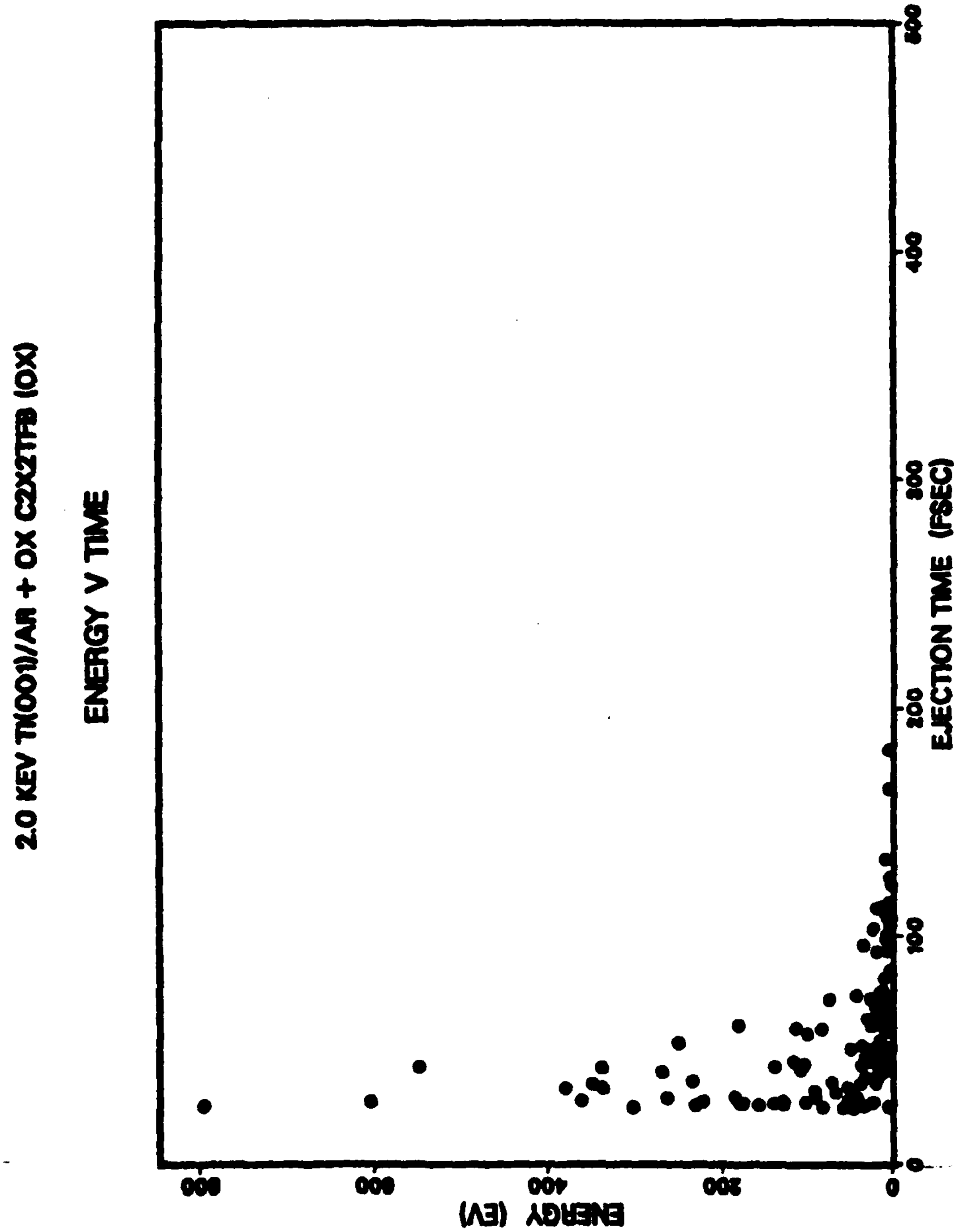
2.0 KEV TI(001)/AR + OX C2X2TFB (OX)
ENERGY V TIME
EJECTION TIME (FSEC)
0
100
200
300
400
500
ENERGY (EV)
0
200
400
600
800

Fig. 119.

APPENDIX I

SURFACE LAYER EJECTION FREQUENCY PLOTS

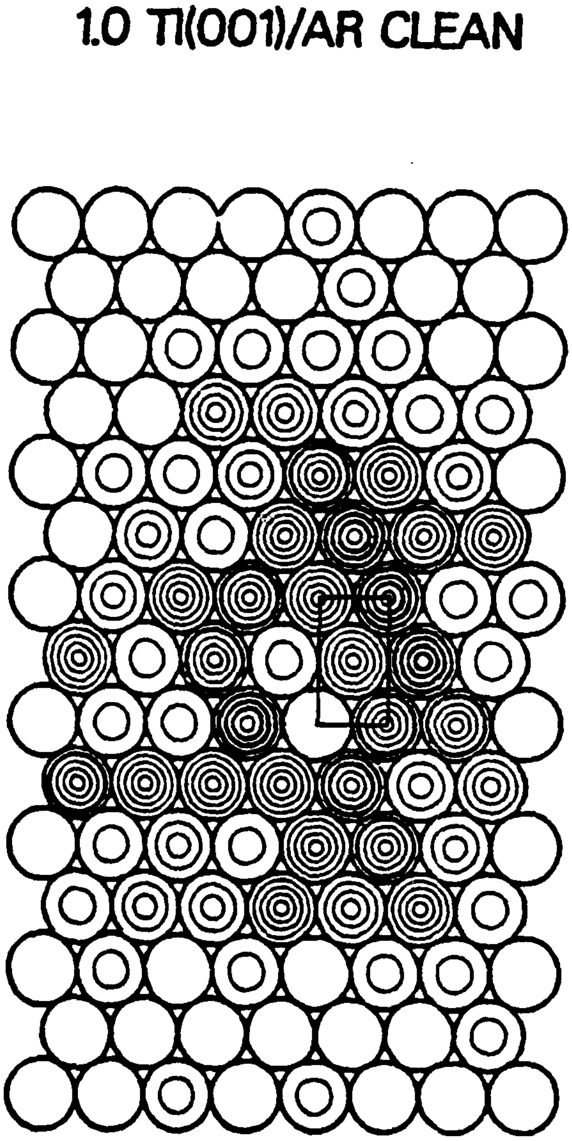

Fig. 120. Relative surface layer ejection frequency.

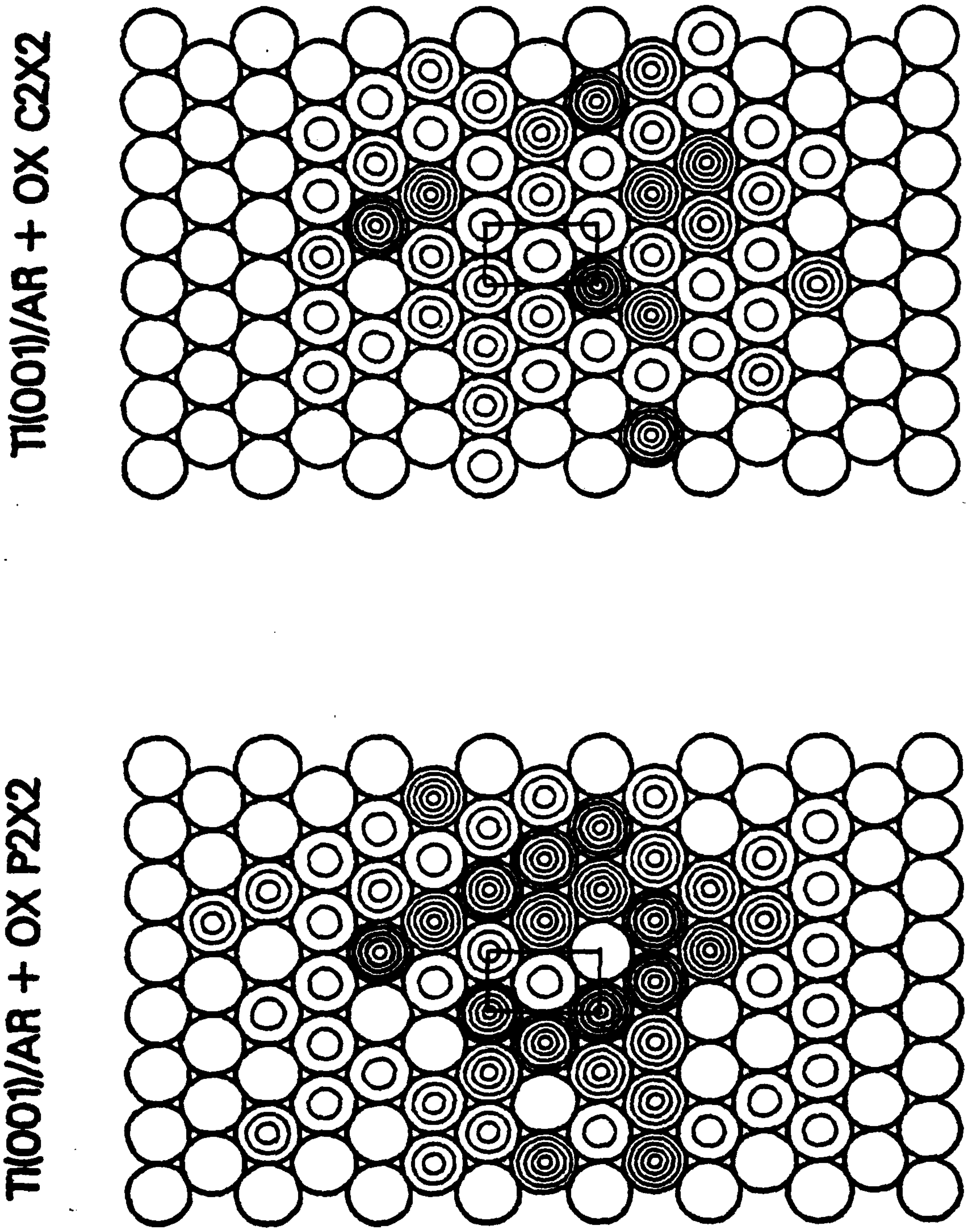

TI(001)/AR + OX C2X2

TI(001)/AR + OX P2X2

Fig. 121. Relative surface layer ejection frequency.

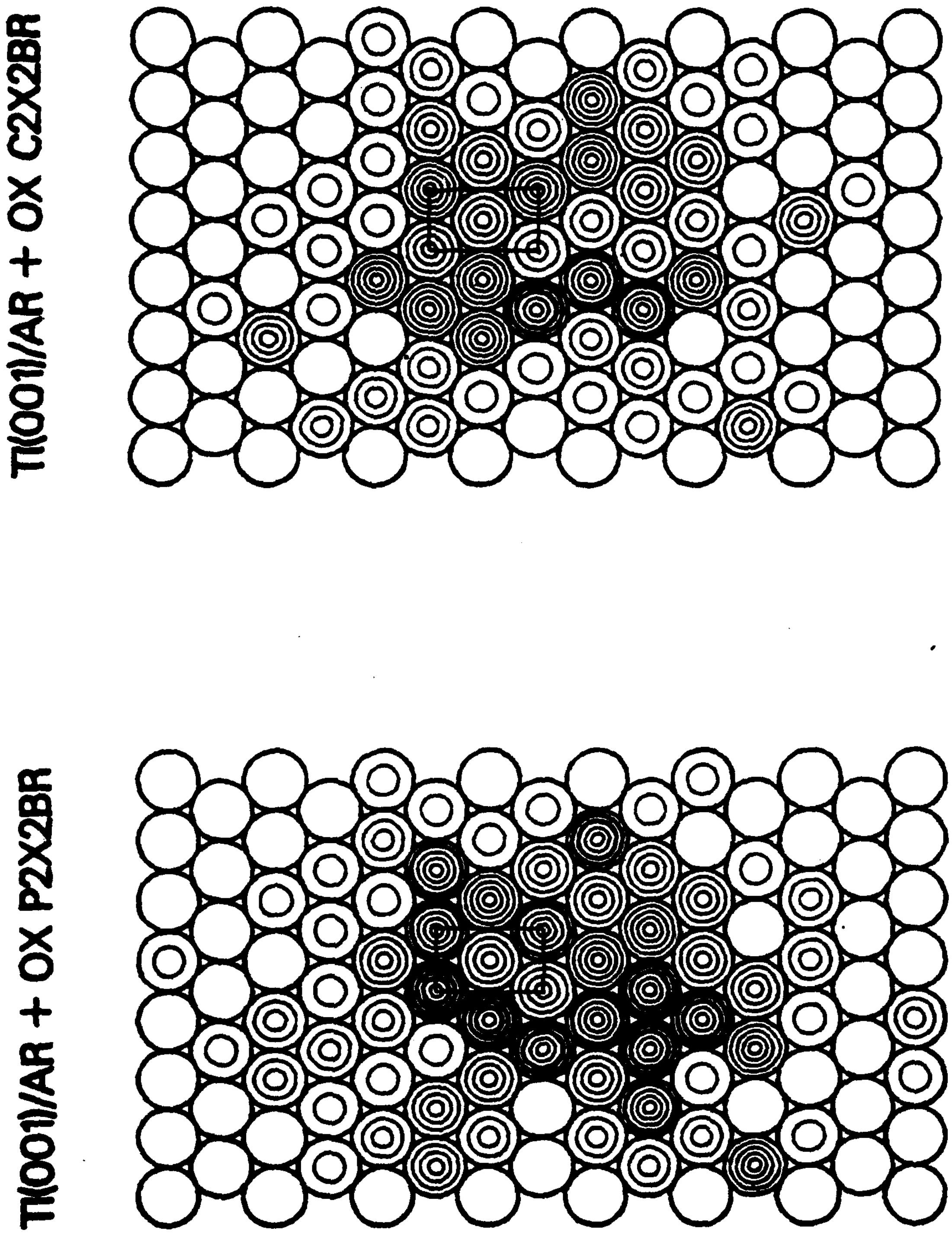

Ti(001)/AR + OX C2X2BR

Ti(001)/AR + OX P2X2BR

Fig. 122. Relative surface layer ejection frequency.

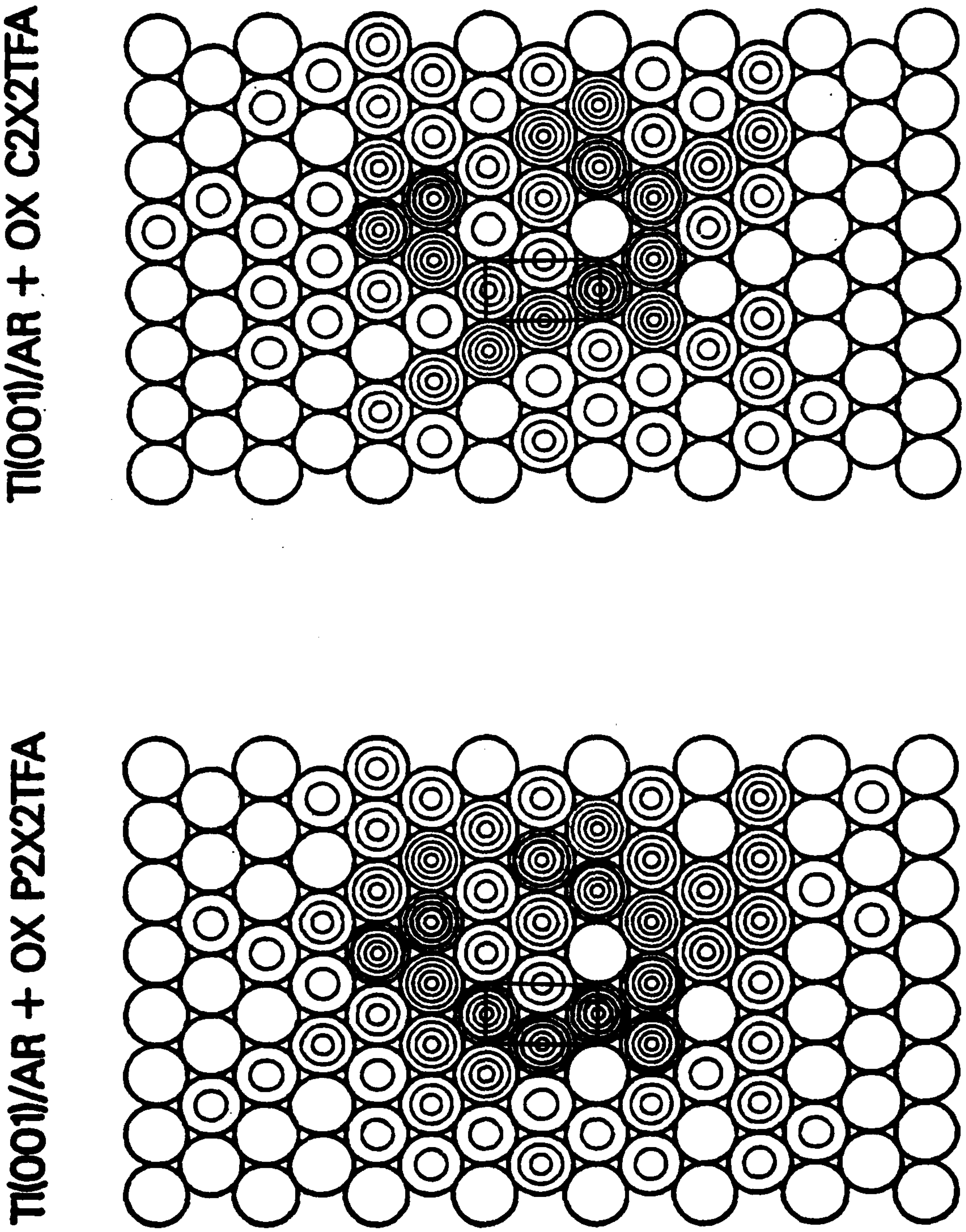

Fig. 123. Relative surface layer ejection frequency.

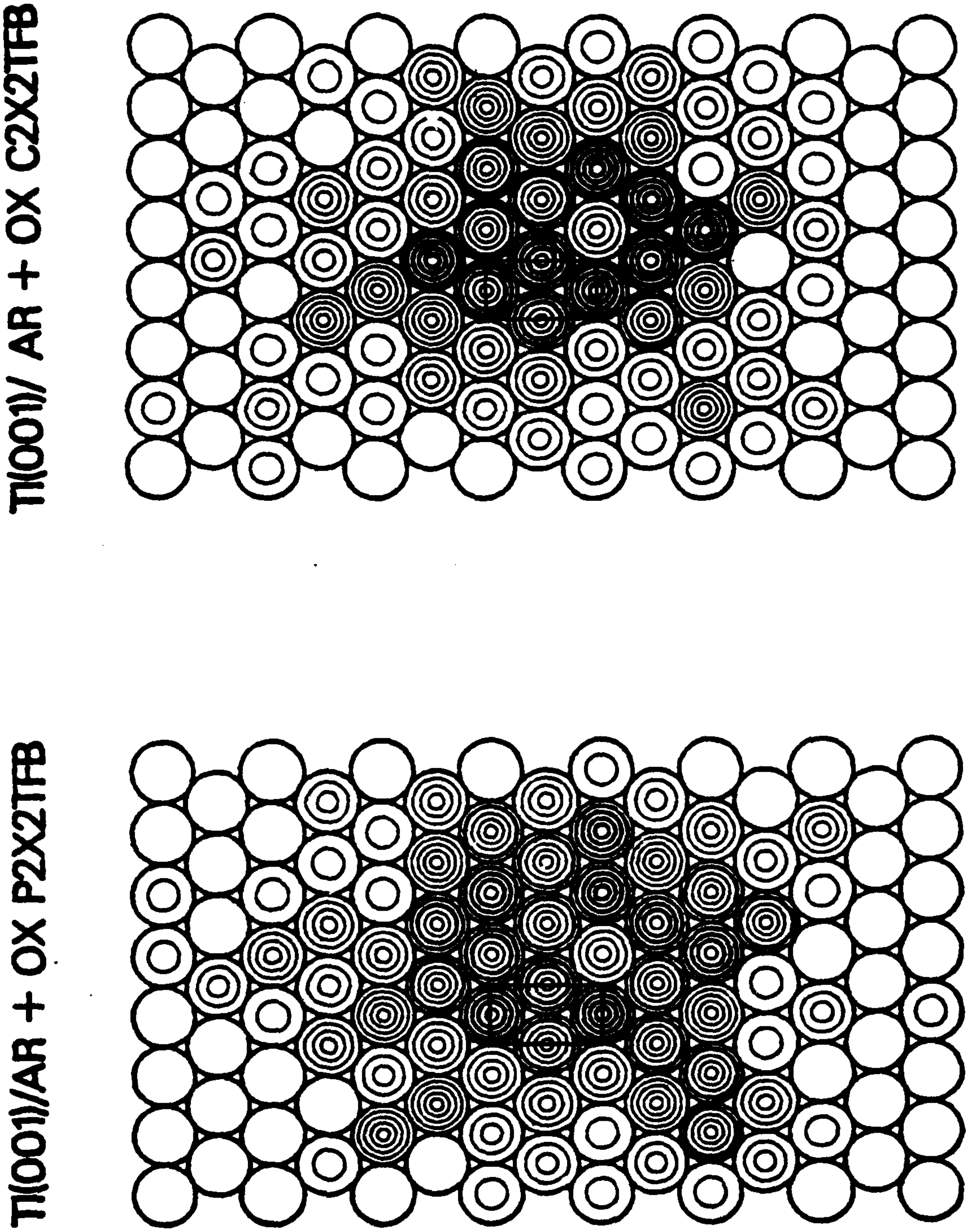

Fig. 124. Relative surface layer ejection frequency.

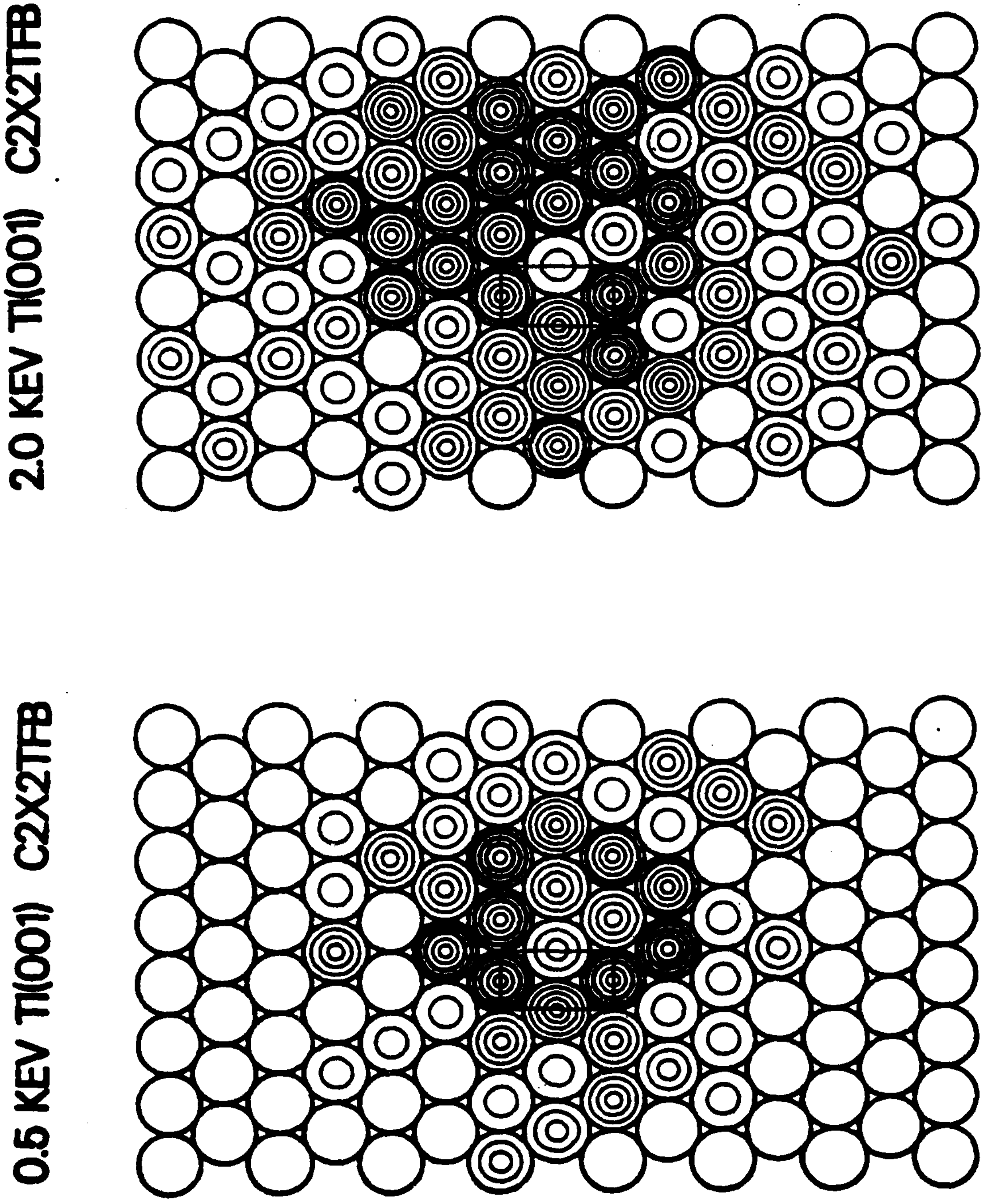
2.0 KEV Ti(001) C2X2TFB

0.5 KEV Ti(001) C2X2TFB

Fig. 125. Relative surface layer ejection frequency.

1.0 KEV NB(110)/AR + OX (P2X2)

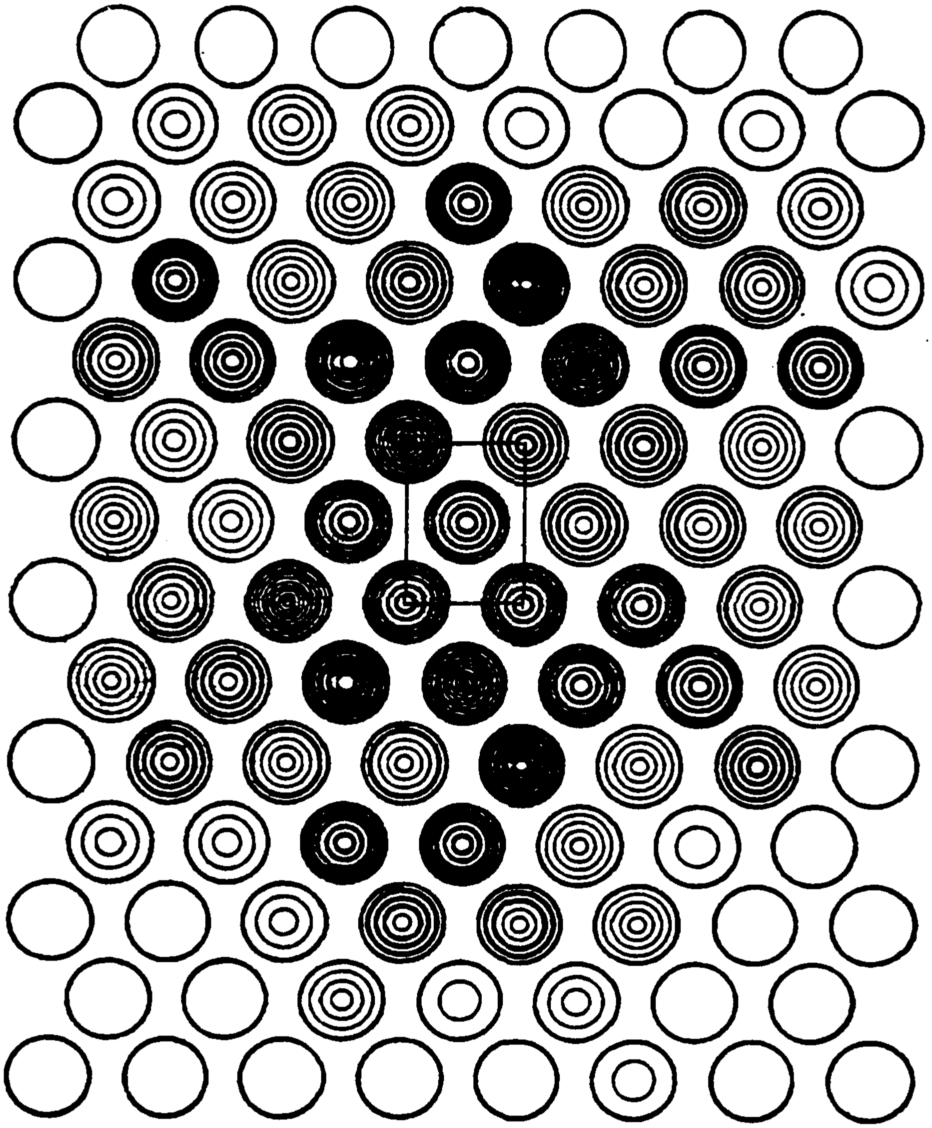

Fig. 126. Relative surface layer ejection frequency.

APPENDIX J

EXPERIMENTAL RESULTS

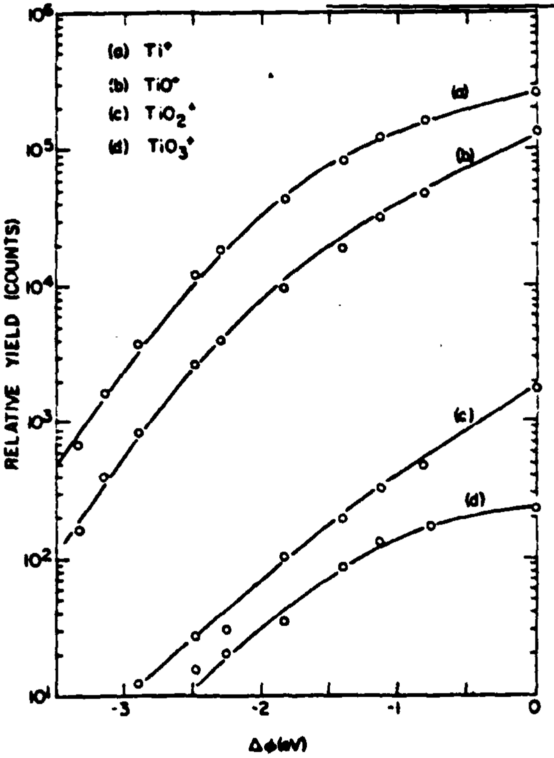

Work-function dependence of the yield of Ti^+, TiO^+, TiO_2^+, and TiO_3^+ at high oxygen coverage. The Auger ratio for [O]/[Ti] is 1.24 (see text). The primary ion was 500-eV Ne^+.

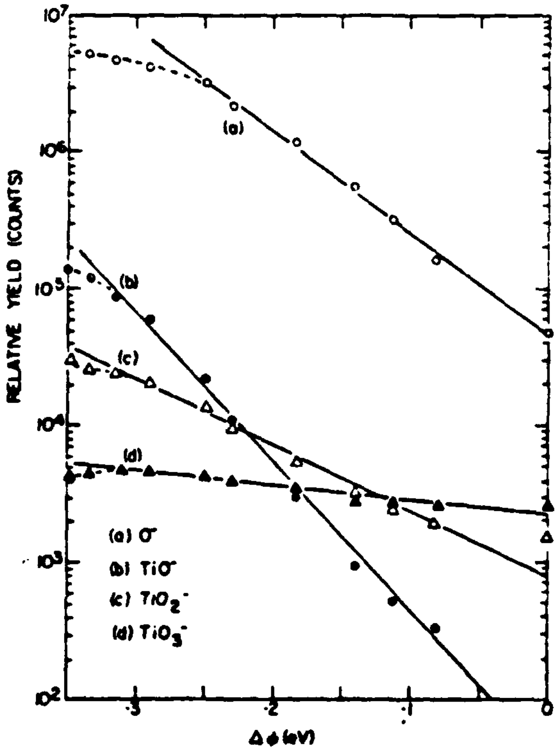

Work-function dependence of the yield of O^-, TiO^-, TiO_2^-, and TiO_3^- at high oxygen coverage. The Auger ratio for [O]/[Ti] is 1.24 (see text). The exponential behavior was similar at all other oxygen coverages. The primary ion was 500-eV Ne^+.

Fig. 127. (From ref. [22]).

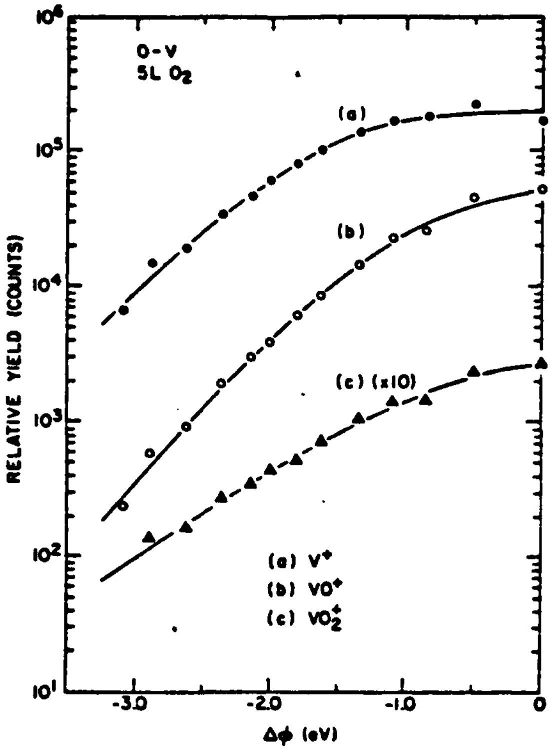

Work function dependence of the V$^+$, VO$^+$, and VO$_2$$^+$ yields at 5-L O$_2$ exposure. The primary ion was 500-eV Ne$^+$.

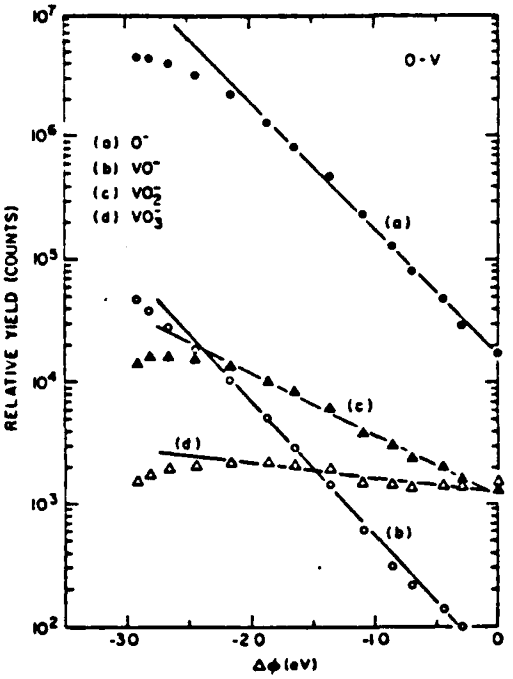

Work function dependence of the O$^-$, VO$^-$, VO$_2$$^-$, and VO$_3$$^-$ yields. The O$_2$ exposure was 4 L. The primary ion was 500 -eV Ne$^+$.

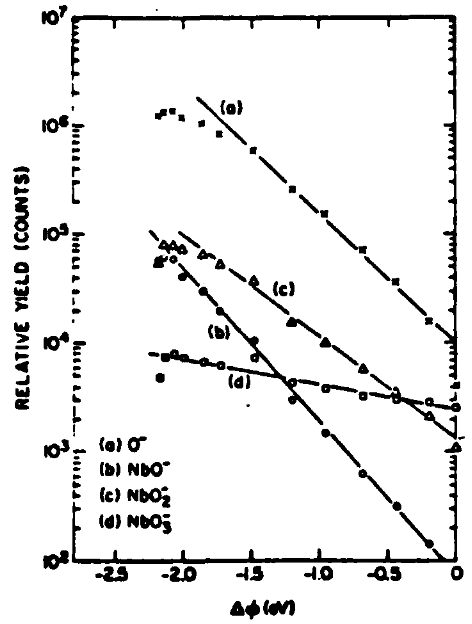

Work function dependence of the O$^-$, NbO$^-$, NbO$_2$$^-$, and NbO$_3$$^-$ yields. The O$_2$ exposure was 4 L. The primary ion was 500 -eV Ar$^+$.

Fig. 128. (From ref. [23]).

LIST OF REFERENCES

1. Goldstein, E., Verh. Dtsch. Phys. Ges., v. 4, pp. 22-37, 1902.

2. Penning, F.M. and Moubis, J.H.A., "Cathode Sputtering in a Magnetic Field," Koninkl. Ned. Akad. Wetenschap, Proc., v. 43, no. 1, pp. 41-56, 1940.

3. Arifov, U.A., "A Method of Investigating the Secondary Electron Energy Distribution when a Metal is Bombarded by Electrons," Radiotekhnika i Elektronika, v. 8, no. 1, pp. 138-144, January 1963.

4. Yonts, O.C., and Harrison, D.E., Jr., "Surface Cleaning by Cathode Sputtering," Journal of Applied Physics, v. 31, no. 9, pp. 1583-4, September 1960.

5. Stark, J., "Volatilisation by Atom Rays," Zeitschr. Elektrochem., v. 15, pp. 509-512, 15 July 1909.

6. von Hipple, A., "Uber die Natur und den Ladungszustand der bei Kathodeenzerstaubung emittierten Metallteilchen," Annalen der Physik, v. 80, no. 15, pp. 672-706, 1926.

7. Wehner, G.K., "Momentum Transfer in Sputtering by Ion Bombardment," Journal of Applied Physics, v. 25, no. 1, pp. 270-271, January 1954.

8. Keywell, F., "Radiation Damage Theory of High Vacuum Sputtering," Physical Review, v. 97, no. 6, pp. 1611-1619, 15 March 1955.

9. Harrison, D.E., Jr., "Theory of Sputtering Processes," Physical Review, v. 102, no. 6, pp. 1473-1480, 15 June 1956.

10. Silsbee, R.H., "Focusing in Collision Problems in Solids," Journal of Applied Physics, v. 28, pp. 1246-1250, November 1967.

11. Sigmund, P., "Theory of Sputtering. I. Sputtering Yield of Amorphous and Polycrystalline Targets," Physical Review, v. 184, no. 2, pp. 383-416, 10 August 1969.

12. Thompson, M.W., "The Energy Spectrum of Ejected Atoms During High-Energy Sputtering of Gold," Philosophy Magazine, v. 18, pp. 377-414, August 1968.

13. Robinson, M.T., "The Energy Spectra of Atoms Slowing Down in Structureless Media," Philosophy Magazine, v. 12, pp. 145-156, July 1965.

14. Gibson, J.B., et al., "Dynamics of Radiation Damage," Physical Review, v. 1028, no. 4, pp. 1229-1253, 15 November 1960.

15. Robinson, M.T. and Den, O.S., "The Channeling of Energetic Atoms in Crystal Lattices," Applied Physics Letters, v. 2, no. 2, pp. 30-32, 15 January 1963.

16. Harrison, D.E., Jr., et al., "Computer Simulation of Sputtering," Journal of Applied Physics, v. 39, no. 8, pp. 3742-3761, July 1968.

17. Harrison, D.E., Jr., Moore, W.L., Jr., and Holcombe, H.T., "Computer Simulation of Sputtering II," Radiation Effects, v. 17, pp. 167-183, 1973.

18. Harrison, D.E., Jr. and Delaplain, C.B., "Computer Simulation of the Sputtering of Clusters," Journal of Applied Physics, v. 47, no. 6, pp. 2252-2259, June 1976.

19. Gay, W.L. and Harrison, D.E., Jr., "Machine Simulation of Collisions between a Cu Atom and a Cu Lattice," Physical Review, v. 135, no. 6A, p. A1780, 14 September 1964.

20. Harrison, D.E., Jr., "Additional Information of Computer Simulation of Sputtering," Journal of Applied Physics, v. 40, no. 9, pp. 3870-3872, August 1969.

21. Garrison, B.J., Winograd, N. and Harrison, D.E., Jr., "Atomic and Molecular Ejection from Ion Bombarded Reacted Single-Crystal Surfaces: Oxygen on Cu(100)," Physical Review B, v. 18, no. 11, pp. 6000-6010, 1 December 1978.

22. Yu, M.L., "Emission Mechanisms of Titanium Oxide Ions during Sputtering," Physical Review B, v. 24, no. 2, pp. 1147-1150, 15 July 1981.

23. Yu, M.L., "Formation of Molecular Ions during Sputtering," Physical Review B, v. 24, no. 10, pp. 2586-2595, 15 November 1981.

24. Benningshoven, A., "Investigation of Surface Reactions by SIMS," Surface Science, v. 35, pp. 427-432, June 1973.

25. Konner, G.P. and Tip, A., "Electron Transfer and Reactive Ionization in CO_2," Radiation Effects, v. 26, pp. 23-32, 1975.

26. Harrison, D.E., Jr., Gay, W.L., and Effron, H.M., "Algorithm for the Calculation of the Classical Equations of Motion of an N-Body System," Journal of Applied Physics, v. 10, no. 7, pp. 1179-1184, July 1969.

27. Garrison, B.J., Winograd, N. and Harrison, D.E., Jr., "Formation of Small Metal Clusters by Ion Bombardment of Single Crystal Surfaces," Journal of Chemical Physics, v. 69, no. 4, pp. 1440-1444, 15 August 1978.

28. Harrison, D.E., Jr., "Sputtering Models--A Synoptic View," Radiation Effects, v. 70, pp. 1-64, 1983.

29. Barksdale, J., Titanium, 2nd Edition, Ronald Press, New York 1966.

30. Handbook of Chemistry and Physics, 63rd. Edition, Chemical Rubber Company, 1983.

31. Donnay, J.D.H., and Ondik, H.M., Crystal Data, National Bureau of Standards, 3rd. Edition, 1973.

32. Metals Handbook, 8th Edition, v. 1, American Society for Metals, Cleveland, 1961.

33. Kittel, C., Introduction to Solid State Physics, 5th Edition, John Wiley & Sons, New York, 1976.

34. Herzberg, G., Spectra of Diatomic Molecules, 2nd Edition, D. Van Nostrand Co., New York, 1950.

35. Huber, K.P., and Herzberg, G., Molecular Spectra and Structure, D. Van Nostrand Co., New York, 1979.

36. Kant, A. and Lin, S.S., "Dissociation Energies of Ti and V," Journal of Chemical Physics, v. 51, no. 4, pp. 1644-1647, 15 August 1969.

37. Hanson, D.M., Stockbauer, R., and Madey, T.E., "Photon-stimulated Description and other Spectroscopic Studies of the Interaction of Oxygen with a Titanium (001) Surface," Physical Review B, v. 24, no. 10, pp. 5513-5521, 15 November 1981.

38. Plateau, A., et al., "Oxidation of Cerium and Titanium Studies by Photoelectron Spectroscopy," Surface Science, v. 63, pp. 153-161, 1977.

39. Jonker, B.T., Morar, J.F. and Park, R.L., "Surface States and Oxygen Chemisorption on Ti(0001)," Physical Review B, v. 24, no. 6, pp. 2951-2957, 15 September 1981.

40. Kawasaki, K., "Adsorption of CO, O_2 and CO_2 on Titanium Film," Japanese Journal of Applied Physics, v. 10, no. 10, pp. 1359-1364, October 1971.

41. Madey, T.E., "The Role of Steps and Defects in Electron Stimulated Desorption: Oxygen on W(110) Surfaces," Surface Science, v. 94, no. 2-3, pp. 483-506, April 1980.

42. Harrison, D.E., Jr. and Webb, R., "A Molecular Dynamics Simulation Study of the Influence of the Lattice Atom Potential Function upon Atom Ejection Processes," Journal of Applied Physics, v. 53, no. 6, pp. 4193-4201, June 1982.

43. Singh, B., Muller, J. and Supplice, N.A., "Adsorption of Oxygen and Carbon Monoxide by Films of Titanium," Thin Solid Films, v. 21, pp. 255-265, 1974.

44. Haas, T.W., Jackson, A.G. and Hooker, M.P., "Adsorption on Niobium (110), Tantalum (110) and Vanadium (110) Surfaces," Journal of Chemical Physics, v. 46, no. 8, pp. 3035-3033, 15 April 1967.

45. Wood, E.A., "Vocabulary of Surface Crystallography," Journal of Applied Physics, v. 35, no. 4, pp. 1306-1312, April 1964.

46. Foley, K., Surface Characterization with SIMS: CO Adsorption on Ni Surfaces, Ph.D. Dissertation, Purdue University, (unpublished), 1981.

47. Barrow, G.M., Molecular Spectroscopy, McGraw-Hill, New York, 1962.

INITIAL DISTRIBUTION LIST

		No. Copies
1.	Defense Technical Information Center Cameron Station Alexandria, VA 22314	2
2.	Library, Code 0142 Naval Postgraduate School Monterey, CA 93943	2
3.	Department Chairman, Code 61 Department of Physics Naval Postgraduate School Monterey, CA 93943	2
4.	Dr. D.E. Harrison, Jr., Code 61Hx Department of Physics Naval Postgraduate School Monterey, CA 93943	5
5.	LCDR M.G. Mathis, USN 2417 E. Balboa Dr. Tempe, AZ 85282	2


7